UNIVERSITY OF ILLINOIS
URBANA

AERONOMY REPORT
NO. 99

THEORETICAL AND LIDAR STUDIES OF THE DENSITY RESPONSE OF THE MESOSPHERIC SODIUM LAYER TO GRAVITY WAVE PERTURBATIONS

by

J. D. Shelton
C. S. Gardner

November 1, 1981

Library of Congress ISSN 0568-0581

Supported by
National Aeronautics and Space Administration
National Science Foundation

Aeronomy Laboratory
Department of Electrical Engineering
University of Illinois
Urbana, Illinois

UILU-ENG-81 2505

AERONOMY REPORT

NO. 99

THEORETICAL AND LIDAR STUDIES OF THE DENSITY RESPONSE OF THE MESOSPHERIC SODIUM LAYER TO GRAVITY WAVE PERTURBATIONS

by

J. D. Shelton
C. S. Gardner

November 1, 1981

Supported by
National Aeronautics and
Space Administration
Grant NGR 14-005-181
National Science Foundation
Grant ATM 79-20726

Aeronomy Laboratory
Department of Electrical Engineering
University of Illinois
Urbana. Illinois

ABSTRACT

Laser radar observations of the mesospheric sodium layer often reveal wavelike density fluctuations moving through the layer. It is often assumed that these features are a layer density response to gravity waves. The density response of atmospheric layers to gravity waves is developed in two forms; an exact solution and a perturbation series solution. The degree of nonlinearity in the layer density response is clearly described by the series solution whereas the exact solution gives insight into the nature of the response. It is shown that density perturbations in an atmospheric layer can be substantially greater than the atmospheric density perturbations associated with the propagation of a gravity wave. Because of the density gradients present in atmospheric layers, interesting effects are observed such as a phase reversal in the linear layer response which occurs near the layer peak. Once the layer response is understood, the sodium layer can be used as a tracer of atmospheric wave motions.

In order to increase the resolution of lidar data, a two-dimensional digital signal processing technique has been developed. Both spatial and temporal filtering are utilized to enhance the resolution by decreasing shot noise by more than 10 dB. Many of the features associated with a layer density response to gravity waves are observed in high resolution density profiles of the mesospheric sodium layer. These include nonlinearities as well as the phase reversal in the linear layer response.

TABLE OF CONTENTS

PAGE

LIST OF FIGURES

1. INTRODUCTION

The availability of lasers has made it much easier to take advantage of resonant scattering in the remote detection of atmospheric constituents. One of the initial remote sensing applications of tunable dye lasers was in the study of the mesospheric sodium layer. The layer has been investigated since its discovery in the late 1930's. A review of the early measurements and theory of the sodium layer chemistry is contained in Brown [1973]. Mesospheric sodium is believed to be of meteoric origin [Richter and Sechrist, 1979a; Gadsden, 1970]. In addition to providing a source of atomic sodium, recent work indicates meteoric dust may also contribute to the removal of atomic sodium from the mesosphere [Hunten, 1981].

Before dye laser based lidar systems became available as a tool for remote sensing, sodium measurements were largely restricted to studying resonantly scattered sunlight. Ground-based measurements of this type [Blamont and Donahue, 1961; Gadsden and Purdy, 1970] were able to define seasonal variations in column abundance, but the sharp layer boundaries were not revealed until rocket-born dayglow measurements were made [Hunten and Wallace, 1967; Donahue and Meier, 1967]. Lidar observations of the vertical structure of the sodium layer were first made in England [Bowman et al., 1969]. Since then, similar measurements have been reported from a variety of locations including France [Blamont et al., 1972], Brazil [Kirchhoff and Clemesha, 1973], California [Hake et al., 1972], Illinois [Rowlett et al., 1978] and at high latitudes (Franz Joseph Land, USSR) [Juramy et al., 1981]. Because the daytime sky produces unacceptably high background photon rates in most sodium lidar receivers, almost all lidar observations of the sodium layer have been restricted to the nighttime. In addition, most lidar observations of the sodium layer are zenith measurements. Steerable measurements have been made [Thomas et al., 1976; Clemesha et al., 1980] in an attempt to determine the horizontal structure of the layer and the direction of propagation of wavelike features in the layer.

The mesospheric sodium layer is generally confined to an altitude range of 80-100 km with a sharply defined peak near 90 km where the maximum number density is usually about 10^9-10^{10} m^{-3}. The upper boundary typically has a scale height that is less than that of the atmosphere (3-4 km compared to about 7 km for the atmosphere at this altitude). The lower layer boundary is even more sharply defined; the sodium density drops an order of magnitude within a few km at about 80 km in altitude. Seasonal as well as daily and hourly variations in the layer are observed. A winter increase in column abundance has been observed in both dayglow [Hunten, 1967; Gault and Rundle, 1969] and lidar [Gibson and Sandford, 1971; Megie and Blamont, 1977] observations. Current theories of sodium layer chemistry [Richter and Sechrist, 1979b] appear to explain the annual abundance variations. Diurnal variations in column abundance were observed in ground-based [Gadsden and Purdy, 1970] and rocket-born [Donahue and Meier, 1967] dayglow measurements. Daytime lidar measurements [Gibson and Sandford, 1972] have failed to confirm these observations. However, a pre-sunrise increase in column abundance has been detected in nighttime observations made at Urbana, Illinois and is reported in this thesis. These variations are not fully explained by current theories of the sodium layer.

Short term variations in sodium density are often observed [Kirchhoff and Clemesha, 1973; Rowlett et al., 1978; Juramy et al., 1980] and are attributed to tidal and gravity wave oscillations. To understand the effects of atmospheric dynamics on the sodium layer, the response of layers to atmospheric wave motions must be understood. Fortunately, chemical effects are reduced in the nighttime sodium layer so that it can more readily be used as a tracer of atmospheric motions. The linear density response of minor constituents to gravity wave perturbations has been investigated by several researchers [Dudis and Reber, 1976; Chiu and Ching, 1978]. These results have been applied to $O_2('\Sigma)$ airglow measurements [Weinstock, 1978], measurements of the green line airglow at 557.7 nm [Battaner and Moliva, 1980], and the nightglow emission of the hydroxyl radical [Frederick, 1979]. It also appears that many of the wavelike features observed in the sodium layer are associated with a linear layer response to atmospheric waves [Shelton et al., 1980]. An expression for the total layer response to atmospheric waves is derived in this thesis. Many of the features in experimental data are consistent with such a layer density response to gravity waves. Features often observed in the linear response of the layer include a phase reversal and differing perturbation amplitudes above and below the layer peak. Nonlinearities in the layer response have also been observed. In regions of large density gradients or where the linear response is small (i.e. at the point of phase reversal), nonlinear effects become important. Sodium density perturbations associated with a double frequency response to gravity waves are consistently observed in these regions. Because of the nonlinear nature of the sodium layer response, density oscillations with short temporal periods and small vertical wavelengths can be present.

A detailed study of the nonlinearities in the layer response to gravity waves requires high temporal and spatial resolution. Although shot noise places a practical limit on lidar resolution, appropriate filtering can reduce the shot noise and significantly improve the resolution in lidar profiles. The spatial filtering technique of Rowlett and Gardner [1979] is expanded in this thesis to include temporal filtering. As a consequence, spatial and temporal resolution have been increased and many of the nonlinear features in the layer response to atmospheric waves have been observed.

In Chapter 2, the Urbana lidar system is described and the principles of its operation are presented. Chapter 3 contains a description of the spectral analysis and two-dimensional filtering techniques utilized to process the received photocount profiles. The sodium layer response to atmospheric wave motions is developed in Chapter 4. In addition to explaining many of the wavelike features observed in sodium density profiles, the layer response influences column abundance and must be understood in interpreting the spatial periodograms used in data processing. Observations of the sodium layer made at Urbana, Illinois between October, 1979 and March, 1981 are presented in Chapter 5. The wavelike perturbations in density found in many of these data exhibit the characteristics of a layer response to gravity waves developed in Chapter 4. All of these measurements were restricted to zenith observations and, as a result, it is difficult to deduce the horizontal structure of the sodium layer. Since the horizontal layer structure can be influential in determining the layer response to atmospheric waves it is sometimes difficult to interpret lidar data when only the vertical variations in sodium density are known. In Chapter 6, initial results of steerable observations of the sodium layer are shown. These observations, made at Goddard Space Flight Center, illustrate a technique which may be used to determine the horizontal structure of the layer. Chapter 7 describes the stratospheric dust layers observed over Urbana following the volcanic eruptions of Mt. St. Helens in 1980. Although these observations are not directly related to observations of the mesospheric sodium layer, they illustrate the flexibility and the many uses of ground-based lidar facilities. Conclusions and recommendations for further work are outlined in Chapter 8. The appendix contains a description of some of the lidar system hardware.

2. LIDAR SYSTEM DESCRIPTION AND OPERATION

2.1 OVERVIEW

The Urbana sodium lidar facility consists of a Fresnel lens telescope and the associated receiving electronics, a pulsed organic dye laser, and a microprocessor system which coordinates the data collection process and stores the received data. The output of the dye laser is tuned to the sodium D2 line at 5890 Å in order to induce fluorescence in the atomic sodium of the mesospheric sodium layer. This increases the effective backscattering cross section of atomic sodium substantially. Backscattered photons are collected by the Fresnel lens telescope where the detected photons are counted. By periodically sampling these counts, a record of photocounts versus height is obtained which may be used to determine estimates of the density profile of sodium with altitude. The processing required to obtain these estimates is performed off-line on the University of Illinois Control Data CYBER 175 computer.

2.2 RECEIVING SYSTEM

The major elements comprising the receiving system are a Fresnel lens telescope, photomultiplier tube (PMT) and its associated electronics, and a counter interface. Each of these items is included in the lidar system block diagram (Figure 2.1).

2.2.1 RECEIVING TELESCOPE

The collecting element of the receiving system telescope is a 1.22 meter diameter f/1.56 acrylic Fresnel lens. The lens as well as the remainder of the telescope are discussed in some detail by Rowlett and Gardner [1979]. A

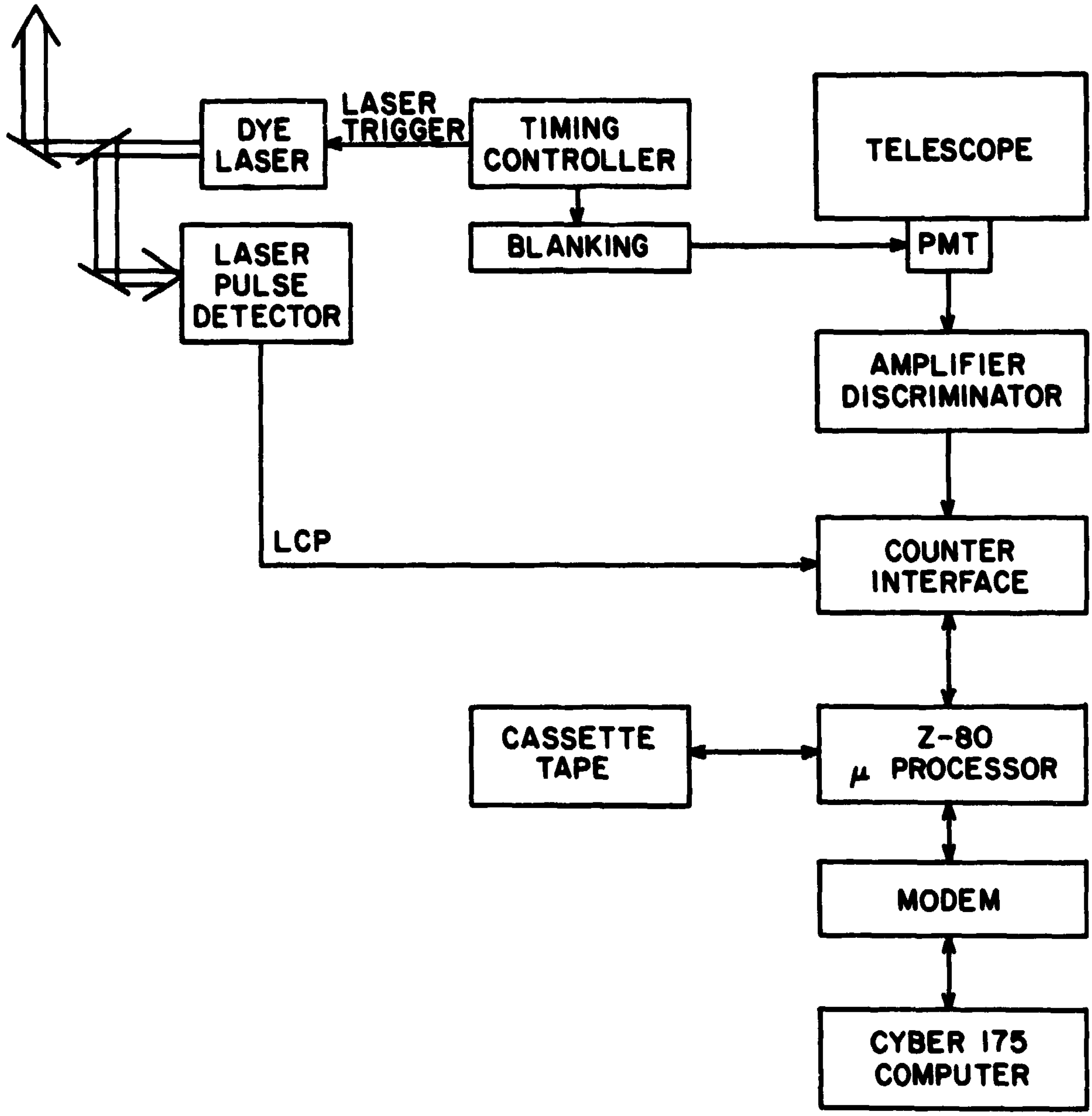

Figure 2.1 Block diagram of the Urbana lidar system. Double lines indicate light paths while single lines represent electrical connections. Angled lines in light path symbolize beamsplitters and mirrors.

block diagram of the receiving telescope is shown in Figure 2.2. The Fresnel lens focuses the collected photons onto the plane of a field-stop iris. Following the iris, a Nikon 35 mm f/1.4 lens collimates the beam prior to its passage through an interference filter. Because of the 5 nm bandpass of this filter, the number of photons due to background sky illumination is reduced substantially. A focusing lens contained in the PMT cooled housing focuses the photons which are passed by the interference filter onto the cathode of an RCA C31034A high quantum efficiency PMT. This PMT is thermoelectrically cooled by a Products for Research Model TE-206TS-RF cooled housing. Table 2.1 contains a list of parameters for the telescope. All data presented in this thesis, with the exception of the measurements presented in Chapter 6, were collected with this telescope. Mechanical considerations have restricted the use of the telescope to zenith measurements.

TABLE 2.1 RECEIVING TELESCOPE PARAMETERS

Diameter of objective	1.22 m
Area of objective	1.17 m^2
Focal length of objective	1.90 m
Bandwidth	5 nm
Field of view	3 mrad

2.2.2 PMT ELECTRONICS

The output of the PMT is discriminated by a Princeton Applied Research Amplifier-Discriminator (Model 1121). The discriminator compares the amplitude of pulses generated by the PMT to a preset threshold. If the pulse exceeds the threshold, a 12 nanosecond pulse is generated which is counted by the counter interface. Discriminator output pulses are NIM standard, i.e. -18 ma minimum into a 50 ohm line terminated in a 50 ohm load. Another mode of operation for the discriminator is the Pulse Height Analyzer (PHA) mode. The

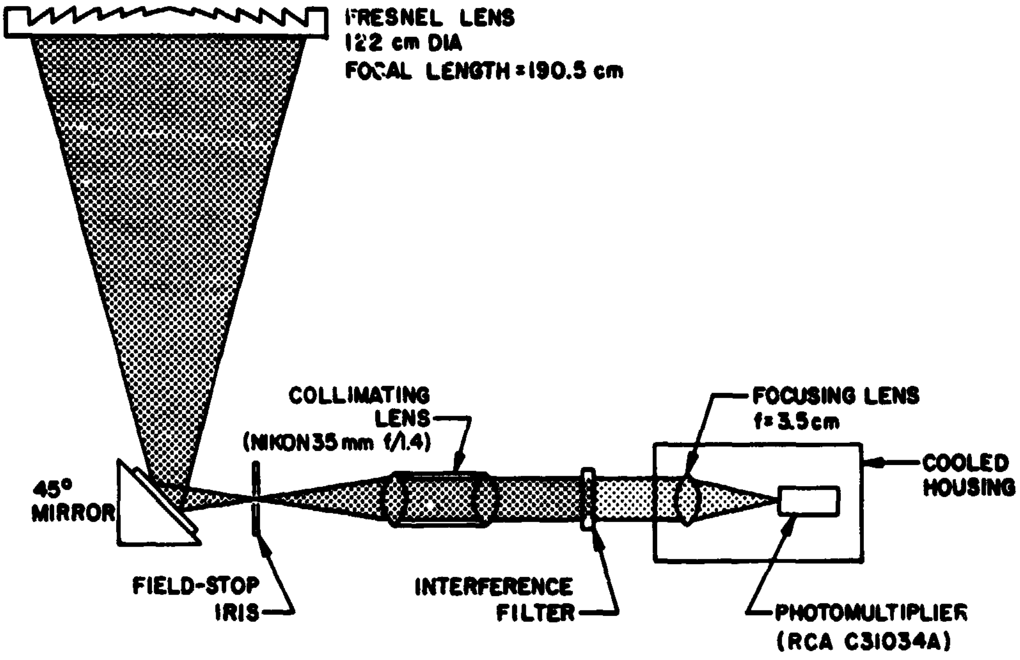

Figure 2.2 Schematic diagram of telescope optics [Rowlett and Gardner, 1979].

principal utility of the PHA mode is that the amplitude distribution of pulses arriving from the PMT can be displayed permitting the determination of the proper threshold level. In addition, this mode can be used to optimize the PMT high voltage setting in order to maximize the output signal to dark count ratio.

There are several possible sources of error in photon counting systems which may introduce significant error at very high counting rates. One such source is "pulse pile-up". The PMT output pulse has finite width, usually on the order of 10-40 nanoseconds. As a result, the PMT can act as a paralyzable detector in that two or more output pulses separated by less than the resolving time of the tube will result in one larger and generally wider pulse. Another source of error arises from signal induced noise. It has been shown that such noise is proportional to signal strength and inversly proportional to t^2, where t is the elapsed time from the signal pulse [Pettifer, 1975]. To minimize these problems and to protect the PMT from overloading conditions which are possible due to strong Rayleigh scattering from below 30 km altitude, a gain switching or gating capability has been added to the receiving system. Prior to its installation, the receiving system overloaded at low altitudes and required at least 100 microseconds to recover. As a result, Rayleigh scattering from 30 to 40 km could not be observed. Since the calibration procedure requires these data, the sodium data could not be calibrated to yield estimates of the absolute sodium density.

Gating of the PMT is achieved by controlling the voltage on the first PMT dynode. When the dynode voltage is reduced from its normal state (which is positive with respect to the cathode) to the cathode potential or slightly negative with respect to the cathode potential, a significant decrease in overall PMT gain is achieved. Measurements with this system indicate that the gain is decreased by approximately 3 orders of magnitude. In addition, the recovery time is short, on the order of 6 to 10 microseconds. Thus, the PMT may be electronically switched on and off rapidly enough to permit observation of Rayleigh scatter from 30-40 km without suffering from overloading as a result of strong scattering from below 30 km.

In order to synchronize the firing of the laser and the PMT gating, a timing controller was constructed. This element contains a triggering circuit for the laser and the blanking circuits as well as a free running oscillator which establishes the laser pulse repetition rate. The timing is adjusted so that the PMT is blanked 5 microseconds before a laser pulse is initiated. This insures that the PMT will be completely blanked immediately after the laser fires when the strongest return signal is present. Approximately 200 microseconds later (corresponding to an altitude of 30 km), the PMT is unblanked and data collection proceeds. Both the blanking and the timing circuits are described in greater detail in the appendix.

Figures 2.3 and 2.4 show photocount profiles which illustrate the effectiveness of PMT blanking. In Figure 2.3, overloading has severly distorted returns from below 40 km and data calibration, which depends on Rayleigh returns from 30 to 40 km, is not possible. In Figure 2.4, returns from below 30 km have been attenuated by blanking. Above 30 km, however, there is sufficient Rayleigh scattering to permit calibration of the spatial profile and therefore estimates of the absolute sodium density are possible.

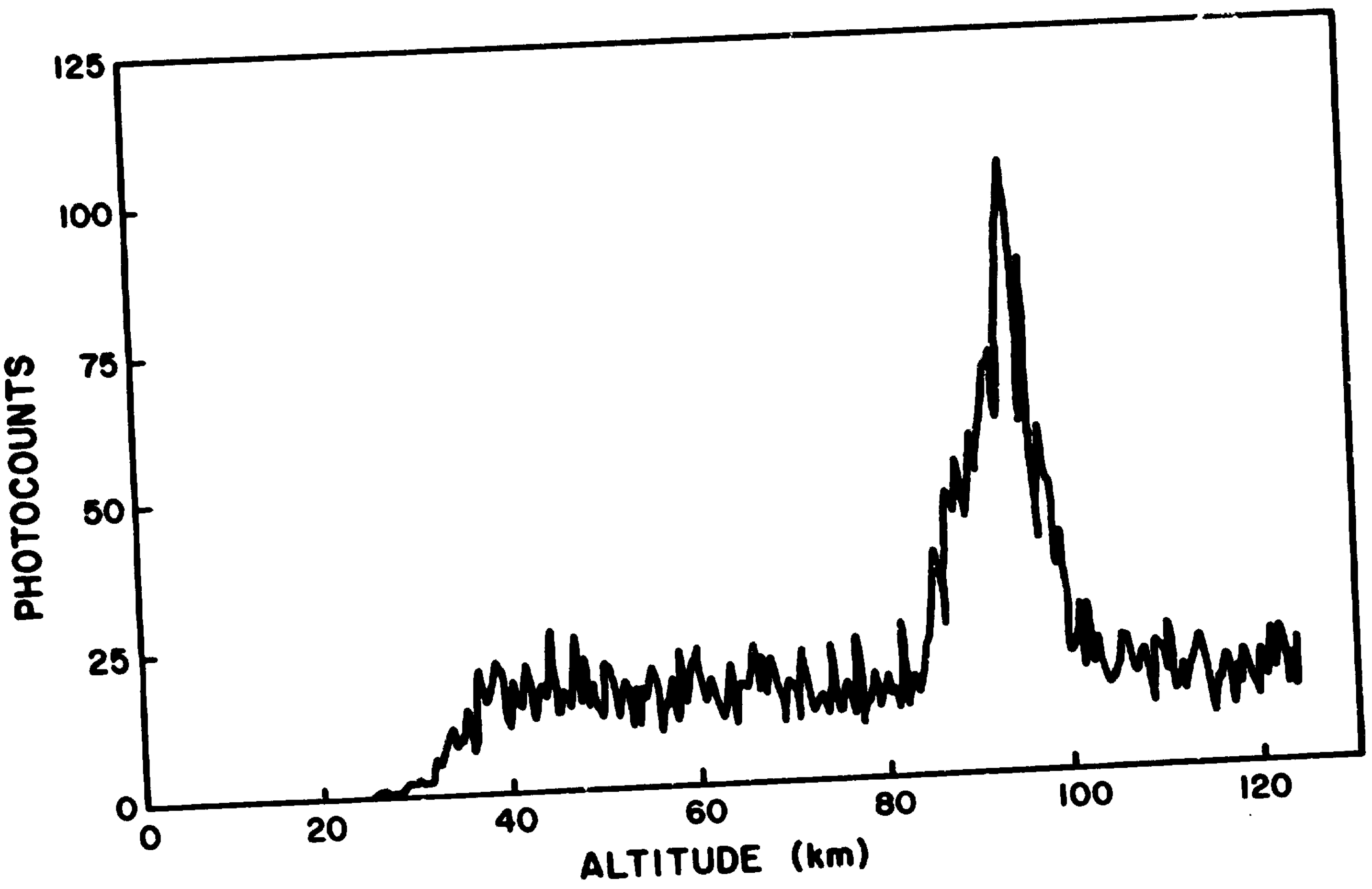

Figure 2.3 Sodium lidar returns showing extreme overloading of the PMT below 40 km. [Cerny and Sechrist, 1980].

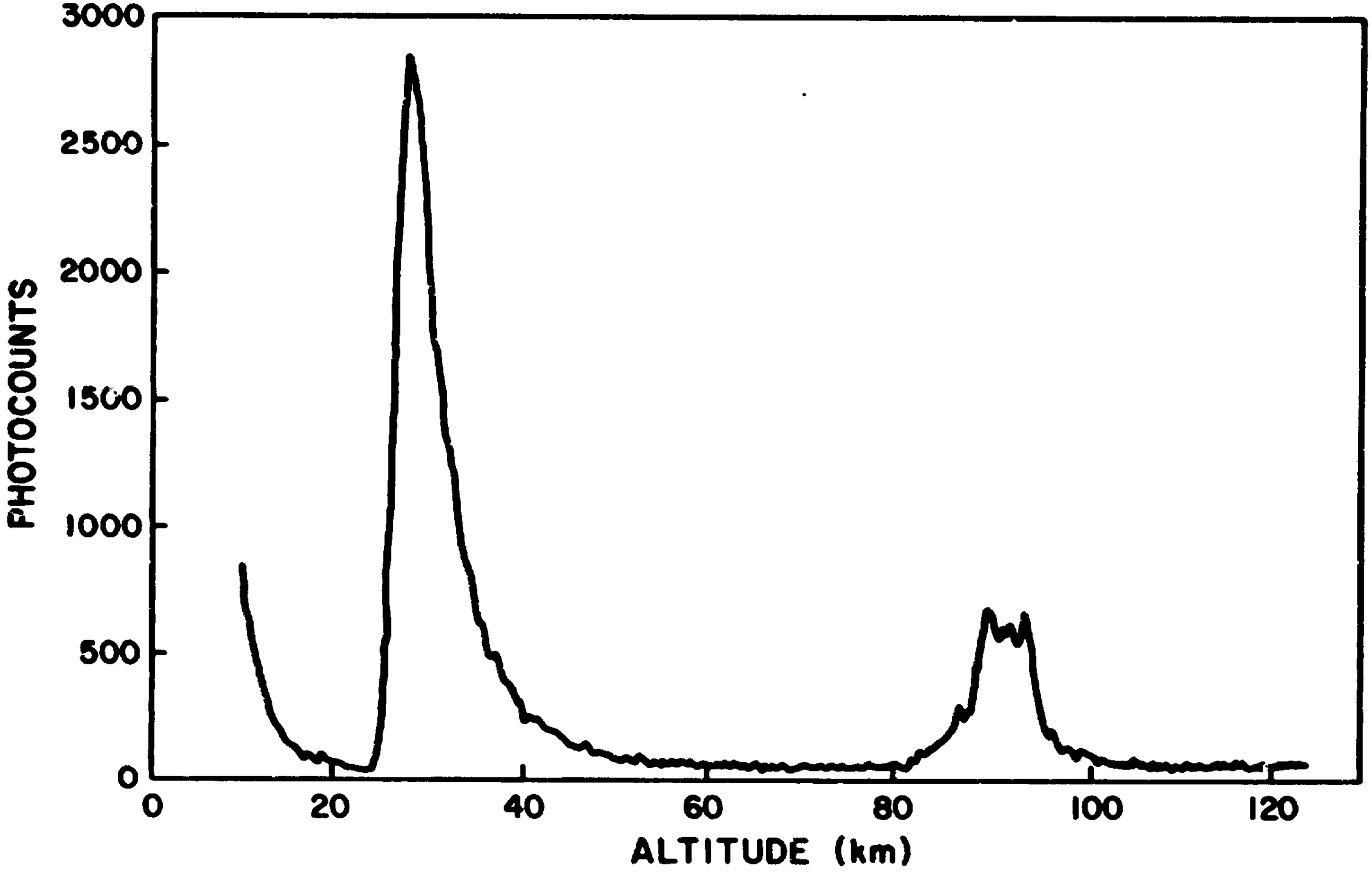

Figure 2.4 Sodium lidar returns after the implementation of PMT blanking. The PMT gain below 25 km is approximately 3 orders of magnitude less than the gain above 28 km. The PMT recovers to its normal gain between 25 and 28 km.

2.2.3 COUNTER INTERFACE

The discriminated pulses from the amplifier-discriminator are counted by a free running 8 bit counter in the counter interface. This device, described by Kinter [1977], contains the logic necessary to periodically sample and store the contents of the counter. Counter interface operation is synchronized with the laser firing by a pulse from a photodiode detector (the Laser Command Pulse, LCP). The counter sampling interval, or range gate width, is software controlled and may be varied from 1 to 128 microseconds in 1 microsecond increments. All the sodium data presented in this thesis were collected with a 3 microsecond range gate. In addition to the range gate, a delay factor must be specified. This determines the delay between laser firing and the point at which counter sampling begins. Because only 256 photocount samples are available, such a delay may be required to insure that the sodium layer is included in the sampled region. A 12 bit word is used to communicate these parameters as well as commands from the lidar microprocessor system to the counter interface. Any return data, such as photocount samples, are returned in an 8 bit word. Two additional lines provide handshaking between the counter interface and the microprocessor system.

2.3 MICROPROCESSOR SYSTEM

A Digital Group Z-80 microprocessor system forms the heart of the microprocessor system. This system was initially implemented to control the data collection process, provide a control system which insured that the laser tuning remained stable, and to monitor the laser spectral linewidth and output energy [Teitlebaum and Sechrist, 1979]. As the lidar system has evolved, so has the function of the microprocessor system. Currently, the microprocessor controls data collection and provides a permanent record of the data on cassette tape.

The Z-80 system permits alignment of receiver and laser, controls data collection and storage, and transmits the acquired data to the CDC CYBER 175 computer for off-line processing. Rayleigh scattering and returns from the sodium layer are displayed to facilitate the alignment process. During the data collection process, the range bin, delay and number of laser pulses per profile are specified by the user. This permits a great deal of flexibility in system operation. After each spatial profile of data is collected, it is stored on cassette tape. Thus, a power or equipment outage will never result in the loss of more than one profile of data. Data is transmitted to the CYBER 175 computer via a telephone line at 300 baud. When operated in this mode, the Z-80 system emulates a remote terminal tied to the CYBER 175.

2.4 LASER

Two lasers were used to collect the data presented in this thesis. Both lasers are flashlamp pumped, organic dye lasers utilizing Rhodamine 6G perchlorate in an alcohol and water solution. Photographs of the two systems are included in Figures 2.5 and 2.6. Prior to January, 1981, a laser utilizing a double elliptical cavity was used [Richter and Sechrist, 1978]. The dye cavity was at the common focus of the two ellipses and a flashlamp was located at each of the remaining focii. During operation, the quartz walls of the flashlamps were ablated. Because of a build-up of ablation products, the flashlamp lifetime was limited to approximately 5000 pulses. The pulse repetition rate for this laser was only 0.5 hertz. This rate could not be exceeded without jeopardizing laser stability.

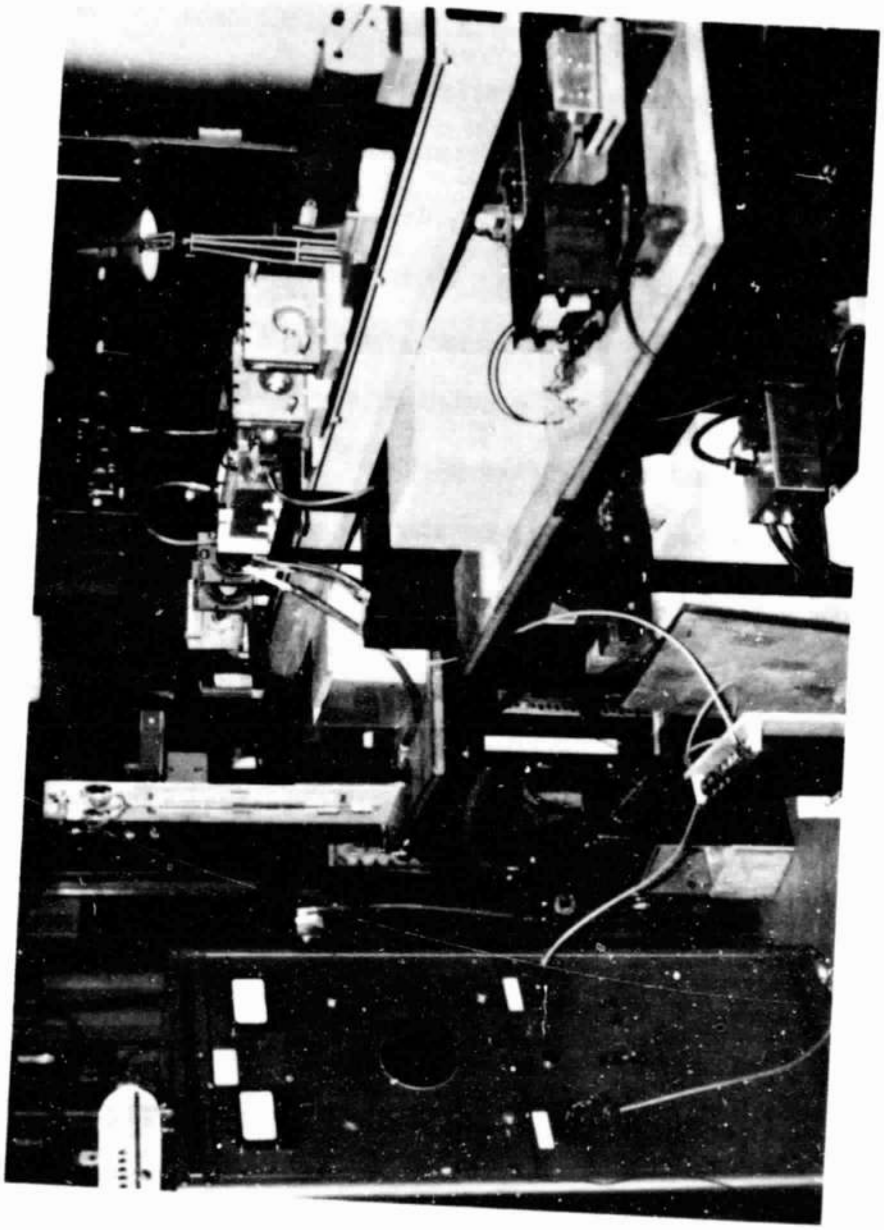

Figure 2.5 Photograph of the dye laser used to collect data prior to January, 1981.

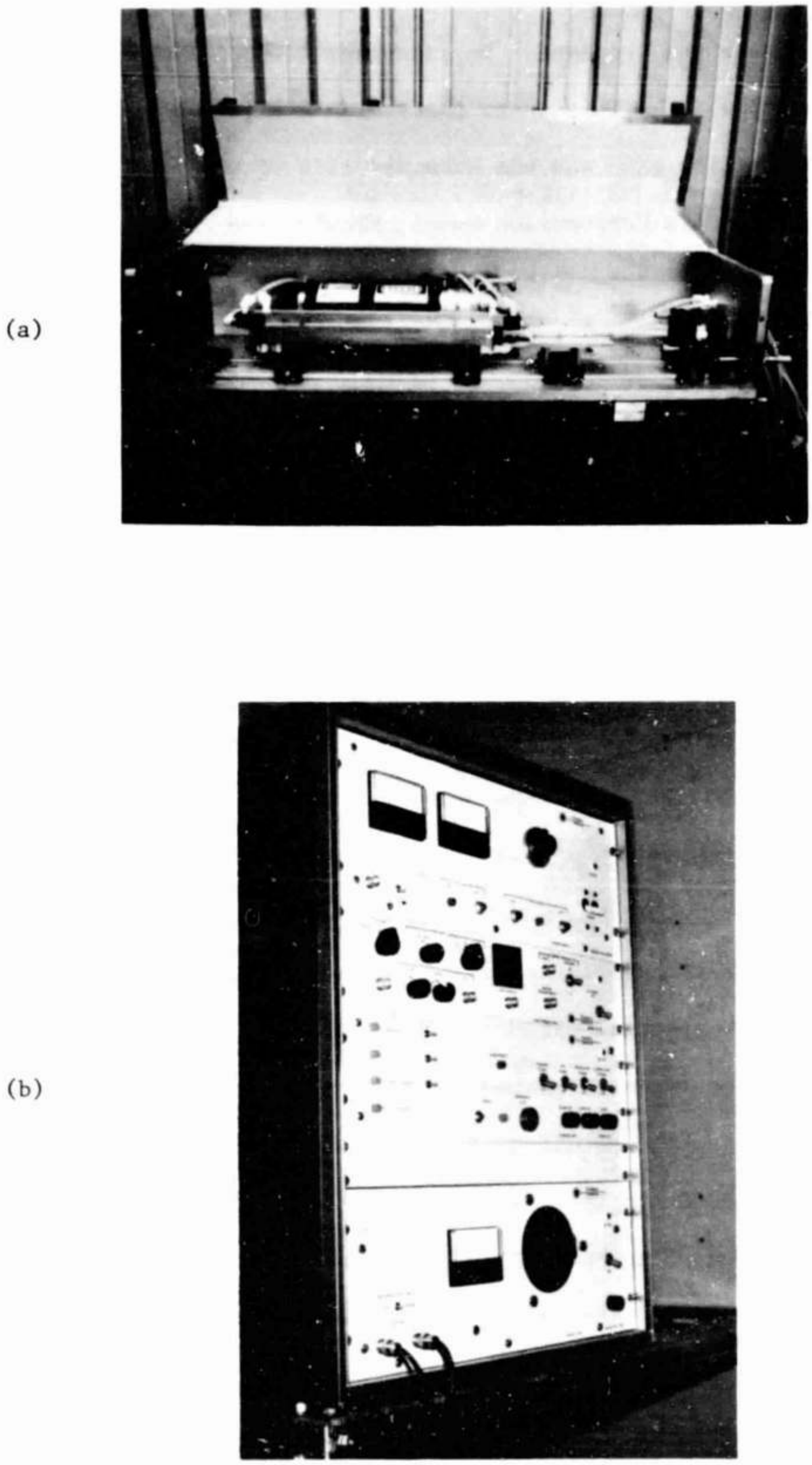

Figure 2.6 Photograph of the Candela dye laser. Photograph (a) shows the laser head. The power supply and triggering unit is shown in photograph (b).

When this laser was replaced in January, 1981, the quality of data improved dramatically. This was partially a result of an increase in the laser pulse repetition rate and the extended life of the new flashlamps. The new laser is a Candela Corporation Model LFDL-5 laser which has been modified to meet a special narrow linewidth requirement. The narrow linewidth modification has not been used in data collection activities. It is anticipated that this feature will be used in the future to attempt temperature measurements of the sodium. Table 2.2 contains parameters describing both the old and new lasers.

TABLE 2.2 LASER PARAMETERS

	Old Laser	Candela Laser	
		Broadband	Narrowband
Energy per pulse	100 mj	50 mj	20 mj
Pulse repetition rate	0.5 Hz	10 Hz	10 Hz
Wavelength	589.0 nm	589.0 nm	589.0 nm
Linewidth	6 pm	1 pm	0.2 pm
Pulsewidth (FWHM)	4 μs	2 μs	2 μs
Beam divergence	1 mrad	1 mrad	1 mrad

The operation and characteristics of the Candela laser as well as a means of measuring the spectral linewidth of the laser output are described by Nilssen [1981]. The improved system performance is explained by the increased pulse repetition rate, extended flashlamp lifetime, and increased spectral energy density at 5890 Å. The spectral energy density of the old laser was approximately 100 mj/6 pm or 16.7 mj/pm whereas the Candela laser can produce 50 mj/pm in the broadband configuration. In addition, the spatial resolution is improved somewhat by the shorter output pulse width (2 microseconds as opposed to 4 microseconds). The increased pulse repetition rate available with the Candela laser (10 Hz) makes greater temporal resolution possible by decreasing the amount of time required to acquire a spatial photocount profile. Actually, the effective laser pulse repetition rate is limited to approximately 4 hertz by the Z-80 system. This system requires roughly 250 milliseconds to collect a laser shot of data and update the video presentation summarizing the status of the spatial profile.

One of the consequences of the extended flashlamp lifetime is that long data sets may be collected without dismantling the laser to replace the flashlamps (as was the case with the old laser). The current system has consistently run from sunset to sunrise with no major tuning or equipment problems. These long data sets, which contain as many as 128 spatial profiles, make temporal filtering an attractive addition to the signal processing techniques which are applied to the photocount data. These processing techniques are described in Chapter 3.

2.5 DESCRIPTION OF THE PHOTOCOUNT DATA

The lidar equation relates the received photocounts due to laser induced fluorescence of the sodium layer to the sodium concentration profile. The contributions of the various lidar system parameters as well as atmospheric effects are included. The lidar equation derived by Measures [1977] has been modified to include temporal variations in sodium density.

$$\lambda(z,t) = \frac{\eta A_R}{h\nu} \int_0^\infty d\sigma \int_{-\infty}^{z} d\tau\, \ell(z - \tau)\, p(\tau - \sigma)\, \gamma(\sigma,t) \qquad (2.1)$$

$$\gamma(z,t) = \frac{\beta(z,t)}{z^2} \exp\left[-2 \int_0^z ds\, \alpha(s)\right] \qquad (2.2)$$

where λ = photoelectron counting rate (s^{-1})

γ = scattering profile (m^{-3})

$\ell = T_\ell^{-1}\exp(-2z/cT_\ell)$, $z \geq 0$ (s^{-1})

T_ℓ = radiative lifetime of the scatterer (s)

p = laser pulse shape ($J \cdot m^{-1}$)

η = overall system efficiency

A_R = receiver aperture area (m^2)

h = Planck's constant ($J \cdot s$)

ν = optical frequency (s^{-1})

α = volume extinction coefficient (m^{-1})

β = volume backscatter coefficient (m^{-1})

The backscatter coefficient is proportional to the concentration of sodium and is therefore the parameter of interest. Note that this parameter is dependent upon both altitude and time. The altitude dependence is a consequence of the vertical structure of the sodium layer and layer dynamics account for the temporal dependence. The volume extinction coefficient is negligable for heights greater than 30 km. Hence, we have

$$\gamma(z,t) \propto \frac{\beta(z,t)}{z^2} \qquad (2.3)$$

for the region of the sodium layer. If $\ell(z)$ and $\gamma(z,t)$ are assumed to be zero for $z>0$, the range of integration for both integrals in equation (2.1) may be extended to infinity. This results in an expression for $\lambda(z,t)$ which is a double convolution.

$$\lambda(z,t) = \frac{\eta A_R}{h\nu}\, \ell(z) * p(z) * \gamma(z,t) \qquad (2.4)$$

In this case, $\ell(z)$ and $p(z)$ have the effect of convolutionally smearing $\gamma(z,t)$.

The above results apply to the returns from a single laser pulse. However, the returns from 50 to 500 pulses are integrated to yield a single spatial profile of data. Also, the lidar system does not measure the instantaneous photon rate. Instead, it integrates the rate over the spatial variable, z, by counting the detected photons in each range bin to yield a photocount, x. The relation between the rate parameter of the counter interface (which is the counter sampling period, T) and the range, Δh, over which the photons are integrated is $\Delta h = cT/2$ where c is the speed of light.

If the counting rate is deterministic, then x is Poisson and the expected value of the photocounts obtained from one laser pulse occuring at time t is

$$<x(z,t)> = \int_{z}^{z+\Delta h} ds\lambda(s,t) + <b> \tag{2.5}$$

or

$$<x(z,t)> = <x_{\gamma}(z,t)> + <b> \tag{2.6}$$

where $<b>$ is the expected photocount due to additive noise and $<x_{\gamma}(z,t)>$ is the expected signal photocount. The integration in equation (2.5) may be expressed as the convolution of $\lambda(z,t)$ with a gate function, $g(z)$, where the gate function is defined as:

$$g(z) = \begin{cases} \frac{1}{\Delta h} ; & 0 \leq z \leq \Delta h \\ \\ 0 ; & \text{elsewhere} \end{cases} \tag{2.7}$$

When combined with equation (2.4), the expression for the expected signal photocounts is seen to contain a threefold convolution.

$$<x_\gamma(z,t)> = \frac{\eta A_R}{h\nu}\, \ell(z) * p(z) * g(z) * \gamma(z,t) \tag{2.8}$$

or

$$<x_\gamma(z,t)> = f(z) * \gamma(z,t) \tag{2.9}$$

where $f(z) = (\frac{\eta A_R}{h\nu})\, \ell(z)*p(z)*g(z)$. In the spatial Fourier domain, this may be written as

$$<X_\gamma(\omega_s,t)> = F(\omega_s)<\Gamma(\omega_s,t)> \tag{2.10}$$

where $<X_\gamma>$, $<\Gamma>$ and F are the spatial Fourier transforms of x_γ, γ and f, respectively. ω_s is the spatial frequency. In practice, the returns from a number of laser pulses are summed to yield a spatial photocount profile. These sums are also Poisson. The loss of temporal resolution resulting from this integration is discussed in Chapter 3. The photocounts available from the counter interface are the samples of $x(z,t)$ at the points $z=k\Delta h$. Thus, the photocounts for the k^{th} range bin and the m^{th} spatial profile may be expressed as $x(k\Delta h,m\Delta T)$ where ΔT is the time interval separating spatial profiles. Since $x(k\Delta h,m\Delta T)$ is Poisson, the expected value and variance are equal:

$$<x(k\Delta h,m\Delta T)> = \mathrm{Var}[x(k\Delta h,m\Delta T)] \tag{2.11}$$

The noise photocount contained in equation (2.5) is primarily due to background sky illumination and PMT dark counts. The expected value of this photocount is equal to $\lambda_n T$ where λ_n is the noise rate and T is the counter sampling period. Generally, the noise counts due to background sky illumination make the most significant contribution to the total noise count. The noise source may be reduced by using a narrower bandpass interference filter in the receiving telescope. Because a Fresnel lens is used in the telescope, it is not practical to reduce the bandpass of the filter much below its current value. Since the telescope is not diffraction limited, collimation errors begin to introduce significant losses and alignment becomes extremely difficult. Noise counts due to PMT dark noise are minimized by cooling the PMT to -20° C.

Estimates of sodium concentration are obtained by filtering the photocount data in such a manner that the convolutional effects described by equation (2.9) are minimized. The filtering process is described in Chapter 3. Calibration of the filtered data yields estimates of absolute sodium density. This process entails normalizing the data by photocounts arising from Rayleigh scattering and scaling the result to account for the effective scattering cross section of sodium and the backscattering coefficient of the atmosphere at the altitude of the Rayleigh scattering. The received photocounts are related to sodium density through the following equation [Cerny and Sechrist, 1980].

$$\rho_k \simeq \frac{\left(z_k + \frac{\Delta h}{2}\right)^2}{z_R^2} \frac{N_k}{N_R} \frac{\sigma_R(\pi)}{\sigma_{\mathrm{eff}}} \rho_R \tag{2.12}$$

where ρ_k = sodium density in the k^{th} range bin (m^{-3})

ρ_R = atmospheric density at range z (m^{-3})

z_k = height of the k^{th} range bin (m)

N_k = signal photocounts from the k^{th} range bin

N_R = signal photocounts from the range z

$\sigma_R(\pi)$ = Rayleigh backscatter coefficient (m^2)

σ_{eff} = effective sodium cross section (m^2)

Calibrating the data in this manner results in sodium density estimates which are independent of system variables such as laser pulse energy variations and overall system efficiency.

3. SIGNAL PROCESSING

3.1 INTRODUCTION

Theoretically, laser pulse length, receiver range gate width, data integration time and sampling interval place the fundamental limits on the spatial and temporal resolution of lidar profiles. However, in practice the resolution of sodium lidar data is usually limited by shot noise. Spatial filtering has been shown to be an effective technique for enhancing the spatial resolution of sodium lidar profiles by reducing shot noise in the photocount data [Rowlett and Gardner, 1979]. Estimates of sodium density are obtained by spatially filtering the photocount data to remove shot noise and to deconvolve the effects of receiver range gate and laser pulse shape. The appropriate spatial filter cutoff frequencies are determined by computing the average spatial periodogram (power spectrum) of the profiles collected during the nights operation.

Temporal filtering of the photocount data is a logical extension of this processing technique. Until recently, however, the Urbana lidar system was not capable of collecting a sufficient number of profiles in one night to permit temporal processing. In June, 1979 a new receiving telescope was installed and in January, 1981 a new laser was integrated into the lidar system. A description of these items is included in Chapter 2. System performance has improved dramatically and, because of the lengthy data sets now being collected, temporal filtering has become a viable addition to the data processing techniques used to filter sodium lidar photocount data.

As in the spatial filtering techniques developed by Rowlett and Gardner, one of the most critical aspects of the temporal filtering process is the determination of an appropriate cutoff frequency. Actually, since the photocount data is now being two-dimensionally filtered, the spatial and temporal filter cutoffs should be jointly determined. The two-dimensional filter described in this chapter is a separable filter so that the temporal and spatial filter cutoffs may be selected and implemented independently. However, because of the deleterious effects of shot noise, tradeoffs must be made in determining these parameters, i. e., the spatial cutoff may be extended by sacrificing temporal resolution and vice versa. These cutoffs are selected by examining temporal and spatial periodograms of the photocount data. The periodogram, which is used as an estimate of the power spectrum of the data, is computed using the Discrete Fourier Transform (DFT).

3.2 TEMPORAL PERIODOGRAM OF PHOTOCOUNT DATA

The temporal periodogram is used as an estimate of the temporal power spectrum of photocount data. From this estimate, the cutoff frequency for a temporal filter will be determined. However, there are several difficulties encountered in computing and analyzing this periodogram. The temporal variations in the sodium layer density at a fixed altitude are usually a small percentage of the average background sodium density. This is illustrated in Figure 3.1 where the signal photocounts in the 80, 85 and 90 kilometer range bins are plotted as a function of time for data collected on October 28-29, 1979. At 85 and 90 km the average level is very high with rapid shot noise fluctuations superimposed on top of small amplitude, long term variations. In addition, there are sharp discontinuities in the temporal data at the beginning and end of the observation period. The sharp discontinuities along with the high average level dominate the temporal periodogram and overshadow

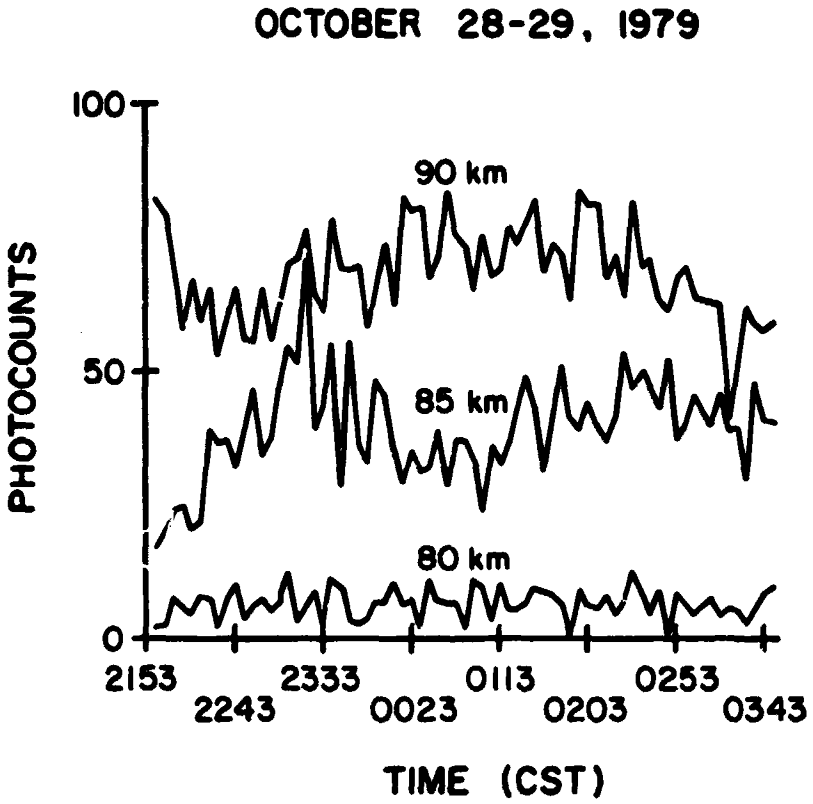

Figure 3.1 Temporal variations of the raw photocount data in the 80, 85, and 90 km range bins [Gardner and Shelton, 1981].

spectral components due to actual temporal variations in the sodium layer. This problem can be ameliorated by subtracting the average sodium background level from each range bin and then multiplying the resulting temporal data by a window function to eliminate the discontinuities at the beginning and end of the observation period. A Hamming window is typically used. The nature of the Hamming window is discussed in section 3.6.1. The temporal periodogram can then be computed by taking the Fast Fourier Transform (FFT) of the windowed data and computing the square of its magnitude.

However, it should be noted that windowing does introduce some spectral distortion. To see this let $x(k\Delta h,m\Delta T)$ denote the photocount in the k^{th} range bin corresponding to the m^{th} profile. Δh is the altitude separating successive range bins and ΔT is the time increment between successive spatial profiles. The average photocount level in the k^{th} range bin due to sodium and background noise is

$$\frac{N(k\Delta h)}{K} = \frac{1}{K}\sum_{m=0}^{K-1} x(k\Delta h,m\Delta T) \tag{3.1}$$

where K is the total number of spatial profiles collected and $N(k\Delta h)$ is the sum over all spatial profiles of the photocounts in the k^{th} range bin. If the window function is denoted by $w(m\Delta T)$ then the temporal periodogram for the k^{th} range bin is

$$|\Phi(k\Delta h,\omega)|^2 = \left|\sum_{m=0}^{K-1} w(m\Delta T)\{x(k\Delta h,m\Delta T) - \frac{N(k\Delta h)}{K}\}\ e^{-i\omega m\Delta T}\right|^2 \tag{3.2}$$

To simplify notation, Δh and ΔT will be dropped and w, x and N will be expressed as functions of k and m.

The expected value of the temporal periodogram may be evaluated by noting that x and N are Poisson. This implies that

$$<x(k,m)\ x(k,n)> = <x(k,m)>\ <x(k,n)> \quad m \neq n \tag{3.3}$$

$$<x(k,m)\ x(k,n)> = <x(k,m)>^2 + <x(k,m)> \quad m = n \tag{3.4}$$

$$<N^2(k)> = <N(k)>^2 + <N(k)> \tag{3.5}$$

$$<N(k)\ x(k,m)> = <x(k,m)> + <x(k,m)>\ <N(k)> \tag{3.6}$$

Taking the expected value of equation (3.2) yields the result;

$$<|\Phi(k,\omega)|^2> = \sum_{m=0}^{K-1} w^2(m)\ <x(k,m)>$$

$$+ \sum_{m=0}^{K-1} \sum_{n=0}^{K-1} w(m)\ w(n)\left[<x(k,m)> - \frac{<N(k)>}{K}\right]\left[<x(k,n)> - \frac{<N(k)>}{K}\right] e^{i\omega(m-n)} \tag{3.7}$$

$$+ \sum_{m=0}^{K-1} \sum_{n=0}^{K-1} \frac{1}{K}\, w(m)\ w(n)\left[\frac{<N(k)>}{K} - <x(k,m)> - <x(k,n)>\right] e^{i\omega(m-n)}$$

Ultimately, this reduces to

$$<|\Phi(k,\omega)|^2> = \left|<\Gamma(k,\omega)> * W(\omega) - \frac{W(\omega)}{K}\right|^2 - \frac{[<N(k)> + 1]}{K^2}\,|W(\omega)|^2$$

$$+ \sum_{m=0}^{K-1} w^2(m)\ <x(k,m)>$$

where

$$<\Gamma(k,\omega)> = \sum_{m=0}^{K-1}\left[<x(k,m)> - \frac{<N(k)>}{K}\right]e^{-i\omega m} \tag{3.8}$$

$$W(\omega) = \sum_{m=0}^{K-1} w(m)\ e^{-i\omega m}$$

$<\Gamma(k,\omega)>$ is just the DFT of the expected photocount variation in the kth range bin. $|<\Gamma(k,\omega)>|^2$ is the function we are attempting to estimate by computing $|\Phi(k,\omega)|^2$.

As can be seen from equation (3.8), $|\Phi|^2$ will provide a slightly distorted estimate of $|<\Gamma>|^2$. The first term in equation (3.8) is approximately equal to $|<\Gamma>|^2$. However, the convolution of $<\Gamma>$ with W reduces spectral resolution and the W/K term introduces some distortion for $\omega<1/(K\Delta T)$. The last term in equation (3.8) is due to shot noise and is approximately equal to $<N(k)>$. At

high temporal frequencies this shot noise term is the most significant in equation (3.8). To reliably observe temporal variations in the lidar data, $|\langle\Gamma\rangle|^2$ (i.e., the first term in equation (3.7)) must be large compared to the shot noise level. The second term involving $|W|^2$ is a distortion term which is significant only at low frequencies where $\omega<(1/K\Delta T)$. Note also that the periodogram is a biased estimate of $|\langle\Gamma\rangle|^2$. The bias is a constant level which depends upon the total number of photons counted in the temporal profile and upon the temporal window, $w(m)$. At $\omega=0$, the expectation obtained from equation (3.7) is

$$\langle|\Phi(k,0)|^2\rangle = \sum_{m=0}^{K-1} w^2(m)\,\langle x(k,m)\rangle - \left[\frac{2}{K}\left(\sum_{m=0}^{K-1} w(m)\right)\right]\left[\sum_{m=0}^{K-1} w(m)\,\langle x(k,m)\rangle\right]$$

$$+\frac{\langle N(k)\rangle}{K^2}\left[\sum_{m=0}^{K-1} w(m)\right]^2 + \left[\sum_{m=0}^{K-1} w(m)\left(\langle x(k,m)\rangle - \frac{N(k)}{K}\right)\right]^2 \qquad (3.9)$$

If no window is applied, i.e. if $w(m) = 1$ for all m, then equation (3.9) becomes zero. $(x(k,m) - N(k)/K)$ is by definition zero mean. However, in the presence of temporal windowing, $w(m)(x(k,m) - N(k)/K)$ is no longer zero mean.

If no temporal window is applied, the expected value of the periodogram becomes

$$\langle|\Phi(k,\omega)|^2\rangle = |\langle\Gamma(k,\omega)\rangle|^2 + \langle N(k)\rangle$$

$$+\frac{\sin(\frac{K\omega}{2})}{\sin(\frac{\omega}{2})}\left[\frac{\sin(\frac{K\omega}{2})}{\sin(\frac{\omega}{2})}\,\frac{\langle N(k)\rangle}{K^2} - \frac{2}{K}\,Re\{e^{-i\omega(\frac{M-1}{2})}\langle X(k,\omega)\rangle\}\right] \qquad (3.10)$$

where $X(k,\omega)$ is the DFT of $x(k,m)$. It was assumed that K temporal samples were collected at intervals of ΔT. Except for $\omega = 0$, at frequencies which are integer multiples of $(2\pi)/(K\Delta T)$ the third term in the above expression is zero. Since the FFT computes the values of the DFT only at these points, if the FFT is used to compute the periodogram, this last term will contribute only for $\omega = 0$. At this point, its value will be $-\langle N(k)\rangle$. This effectively cancels the constant shot noise term permitting the anticipated result that (in the absence of temporal windowing) $<|\Phi(k,0)|^2> = 0$.

Unfortunately, the periodogram provides a very noisy estimate of the power spectrum [Oppenheim and Schafer, 1977]. In addition, it is often difficult to obtain a simple expression for the covariance of a periodogram. Such is the case for the covariance of $|\Phi(k,\omega)|^2$ unless it is assumed that the expected value of photocounts in the temporal profile, $<N>$, is known. This assumption, of course, also yields a slightly different expression for the expected value of the periodogram since $<N>/K$ is now subtracted from $x(k,m)$ rather than N/K. The new periodogram is

$$|\Phi_2(k,\omega)|^2 = \left|\sum_{m=0}^{K-1} w(m)\ [x(k,m) - \frac{<N(k)>}{K}]\ e^{-i\omega m}\right|^2 \tag{3.11}$$

and the expected value of this periodogram becomes

$$<|\Phi_2(k,\omega)|^2> = |<\Gamma(k,\omega)> * W(\omega)|^2 + \sum_{m=0}^{K-1} w^2(m)\ <x(k,m)> \tag{3.12}$$

As before, the signal spectrum falls into a constant shot noise level given by the second term in the above equation. The distortion at low frequencies is no longer present. The convolutional smearing of the desired power spectrum by $W(\omega)$ remains present, however.

To obtain the variance of $|\Phi_2(k,\omega)|^2$, the covariance is first evaluated. For a photocount periodogram, the covariance is given by

$$\begin{aligned}\mathrm{cov}[|\Phi_2(k,\omega_1)|^2, |\Phi_2(k,\omega_2)|^2] = \sum_{j=0}^{K-1}\sum_{l=0}^{K-1}\sum_{m=0}^{K-1}\sum_{n=0}^{K-1} [&<\gamma(k,j)\gamma(k,l)\gamma(k,m)\gamma(k,n)> \\ &- <\gamma(k,j)\gamma(k,l)><\gamma(k,m)\gamma(k,n)>]\ e^{i\omega_1(j-l)}\ e^{i\omega_2(m-n)}\end{aligned} \tag{3.13}$$

where $\gamma(k,j) = w(j)[x(k,j) - \frac{<N(k)>}{K}]$

The summation is broken into special cases: $k=l=m=n$, $k=l=m\neq n$, etc. These cases are then evaluated by using the property of independent increments and the required moments of a Poisson process [Saleh, 1978]. The final result for the covariance is

$$\mathrm{cov}[|\Phi_2(k,\omega_1)|^2, |\Phi_2(k,\omega_2)|^2]$$

$$= \sum_{m=0}^{K-1} w^4(m) <x(k,m)> + |W_2(\omega_1 - \omega_2) * <X(k,\omega_1 - \omega_2)>|^2$$

$$+ |W_2(\omega_1 + \omega_2) * <X(k,\omega_1 + \omega_2)>|^2$$

$$+ 2Re\{[W(\omega_1) * <\Gamma(k,\omega_1)>][W_3(\omega_1) * <X(k,\omega_1)>]^*\}$$

$$+ 2Re\{[W(\omega_2) * <\Gamma(k,\omega_2)>][W_3(\omega_2) * <X(k,\omega_2)>]^*\}$$

$$+ 2Re\{[W_2(\omega_1 + \omega_2) * <X(k,\omega_1 + \omega_2)>][W(\omega_1) * <\Gamma(k,\omega_1)>]^*$$

$$[W(\omega_2) * <\Gamma(k,\omega_2)>]^*\} + 2Re\ [W_2(\omega_1 - \omega_2) * <X(k,\omega_1 - \omega_2)>]$$

$$[W(\omega_1) * <\Gamma(k,\omega_1)>]^*\ [W(\omega_2) * <\Gamma(k,\omega_2)>]\} \qquad (3.14).$$

where $<X(k,\omega)> = \sum_{m=0}^{K-1} <x(k,m)>\ e^{-i\omega m}$

$$W_2(\omega) = \sum_{m=0}^{K-1} w^2(m) e^{-i\omega m}$$

$$W_3(\omega) = \sum_{m=0}^{K-1} w^3(m) e^{-i\omega m}$$

The variance is found by setting $\omega_1 = \omega_2 = \omega$ in equation (3.14):

$$\mathrm{Var}[|\Phi_2(k,\omega)|^2] = \sum_{m=0}^{K-1} w^4(m) <x(k,m)> + [\sum_{m=0}^{K-1} w^2(m) <x(k,m)>]^2$$

$$+ |W_2(2\omega) * <X(k,2\omega)>|^2 + 4Re\{[W(\omega) * <\Gamma(k,\omega)>][W_3(\omega) * <X(k,\omega)>]^*\}$$

$$+ 2Re\{[W_2(2\omega) * <X(k,2\omega)>][W(\omega) * <\Gamma(k,\omega)>]^{*2}\}$$

$$+ 2[\sum_{m=0}^{K-1} w^2(m) <x(k,m)>]\ |W(\omega) * <\Gamma(k,\omega)>|^2 \qquad (3.15)$$

As ω becomes large, the variance approaches $\left(\sum_{m=0}^{K-1} w^2(m)\langle x(k,m)\rangle\right)^2$. Thus, in this region the variance is equal to the square of the expected value. One method of reducing the variance of the periodogram is to average the periodograms of a number of temporal profiles. This technique (Bartlett's procedure) [Oppenheim and Schafer, 1977] has been used to reduce the variance in spatial periodograms [Rowlett and Gardner, 1979]. If the true power spectrum which we are attempting to estimate does not change from temporal profile to temporal profile, the resulting average periodogram will have the same expected value, but the variance will be reduced by a factor of J, where J is the number of profiles averaged together. Actually, spectral features will vary with altitude as a result of the nature of the layer response to wave activity. However, the temporal periodogram is being computed for the purpose of choosing an appropriate temporal filter cutoff frequency. Thus, the slight distortion at low frequencies induced by the temporal window and the effects of averaging a number of periodograms are not significant.

3.3 TEMPORAL PERIODOGRAM OF SPATIALLY FILTERED PHOTOCOUNT DATA

It is instructive to determine the effect spatial filtering has on the temporal resolution of the lidar photocount data. It is anticipated that the achievable temporal resolution should be increased in data which have previously been spatially filtered. The expected value and variance of the temporal periodogram of spatially filtered data may be found by noting the fact that, rather than raw photocount data, an estimate of the power spectrum of data given by

$$y(k,m) = \sum_{l=\frac{-(N-1)}{2}}^{(N-1)/2} h(k-l)[x(l,m) - b(m)] \tag{3.16}$$

is being sought. N is the number of points in the spatial profile. $h(k)$ is the spatial filter impulse response which is convolved with the photocount data, $x(k,m)$. $b(m)$ represents the constant background noise present in the m^{th} spatial profile due to sources such as PMT dark counts and background sky illumination. This is assumed to be a deterministic quantity. In practice, an accurate estimate of $b(m)$ can be computed from the lidar returns obtained from above the sodium layer. Thus, $y(k,m)$ represents the spatially filtered data for the k^{th} range bin and the m^{th} time bin. It is a simple matter to determine the expected value and the first four moments of $y(k,m)$ which are required to evaluate the covariance of the periodogram.

$$<y(k,m)> = \sum_{l=-(N-1)/2}^{(N-1)/2} h(k-l)\,[<x(l,m)> - b(m)] \tag{3.17}$$

$$<y^2(k,m)> = <y(k,m)>^2 + \sum_{l=-(N-1)/2}^{(N-1)/2} h^2(k-l)\ <x(l,m)> \tag{3.18}$$

$$\begin{aligned} <y^3(k,m)> = {} & <y(k,m)>^3 + 3\sum_{l=-(N-1)/2}^{(N-1)/2} h^2(k-l)\ <x_\gamma(l,m)><x(l,m)> \\ & + \sum_{l=-(N-1)/2}^{(N-1)/2} h^3(k-l)\ <x(l,m)> \end{aligned} \tag{3.19}$$

$$\begin{aligned} <y^4(k,m)> = {} & <y(k,m)>^4 + 6\sum_{l=-(N-1)/2}^{(N-1)/2} h^2(k-l)\ <x_\gamma(l,m)><x(l,m)> \\ & + 4\sum_{l=-(N-1)/2}^{(N-1)/2} h^3(k-l)\ <x_\gamma(l,m)><x(l,m)> \\ & + 3\sum_{l=-(N-1)/2}^{(N-1)/2} h^4(k-l)\ <x(l,m)>^2 \\ & + \sum_{l=-(N-1)/2}^{(N-1)/2} h^4(k-l)\ <x(l,m)> \end{aligned} \tag{3.20}$$

where $<x_\gamma(l,m)> = <x(l,m)> - b(m)$

The temporal periodogram of the spatially filtered data for the k^{th} range bin is given by:

$$|\Phi_s(k,\omega)|^2 = \left|\sum_{m=0}^{K-1} w(m)\left[y(k,m) - \frac{N'(k)}{K}\right] e^{-i\omega m}\right|^2 \tag{3.21}$$

The expected value of the periodogram can now be calculated by evaluating the following expression:

$$<|\Phi_s(k,\omega)|^2> = \sum_{m=0}^{K-1} \sum_{n=0}^{K-1} w(m)\, w(n)\, <\left[y(k,m) - \frac{N'(k)}{K}\right]>$$

$$<\left[y(k,n) - \frac{N'(k)}{K}\right]>\, e^{i\omega(m - n)} \tag{3.22}$$

As before, $w(m)$ is the temporal window and $N'(k)/K$ is the average number of signal photocounts in the spatially filtered temporal profile. After some manipulation, an expression which is similar to equation (3.8) is obtained.

$$<|\Phi_s(k,\omega)|^2> = \sum_{m=0}^{K-1} \sum_{r=-(N-1)/2}^{(N-1)/2} w^2(m)\, h^2(k - r)\, <x(r,m)>$$

$$+ \left|<\Gamma_s(k,\omega)> * W(\omega) - \frac{W(\omega)}{K}\right|^2 - \frac{<N'(k)> + 1}{K^2}|W(\omega)|^2$$

$$\text{where} \quad <\Gamma_s(k,\omega)> = \sum_{m=0}^{K-1} \left[<y(k,m)> - \frac{<N'(k)>}{K}\right] e^{-i\omega m} \tag{3.23}$$

$$<N'(k)> = \sum_{m=0}^{K-1} \sum_{r=-(N-1)/2}^{(N-1)/2} h(k - r)\left[<x(r,m)> - b(m)\right]$$

Once again, distortion at low frequencies is encountered and a constant shot noise level is present. Assuming that spatial filtering does not alter the dominant spectral features in the temporal periodogram (as should be the case if the spatial filter is selected properly), the main difference between the temporal periodograms of raw and spatially filtered data is in the constant shot noise level. The decrease in shot noise level will be by a factor of G where G is given by:

$$G = \frac{\sum_{m=0}^{K-1} \sum_{r=-(N-1)/2}^{(N-1)/2} w^2(m)\ h^2(k - r)\ \langle x(k,m) \rangle}{\sum_{m=0}^{K-1} w^2(m)\ \langle x(k,m) \rangle} \tag{3.24}$$

The numerator of the fraction in this expression is simply the spatially filtered version of the denominator. The impulse response of this filter is the square of the impulse response of the spatial filter. Therefore, as the cutoff frequency of the spatial filter becomes lower (i.e., the filtering is more severe), features with longer vertical wavelengths are removed from the filtered data. However, the effect of the filter in equation (3.24) also becomes more severe and the decrease in shot noise level apparent in the temporal periodogram becomes more significant. Since the level is lower, features which were previously masked may now become apparent. As a result, the cutoff for the temporal filter (which is selected by examining the temporal periodogram) can be extended yielding better temporal resolution in the filtered data.

Just as the expected value of the temporal periodogram is affected by spatial filtering, so is the variance. As before, it is extremely difficult to obtain an expression for the periodogram variance when the expected value of the sum of the spatially filtered photocounts in the k^{th} range bin, $\langle N(k) \rangle$, is not known. As a result, it is assumed that this quantity is know a priori and the covariance and variance expressions are evaluated. Rather than repeat much of the development presented in section 3.2, only the resulting variance expression is presented here. The development closely parallels the previous work. The variance expression is

$$
\begin{aligned}
\mathrm{var}[|\Phi_{2s}(k,\omega)|^2] = & \sum_{m=0}^{K-1} \sum_{r=-(N-1)/2}^{(N-1)/2} w^4(m)\, h^4(k-r)\, \langle x(r,m) \rangle \\
& + |H_2(2\omega)[W_2(2\omega) * \langle X(k,2\omega) \rangle]|^2 \\
& + [\sum_{m=0}^{K-1} \sum_{r=-(N-1)/2}^{(N-1)/2} w^2(m)\, h^2(k-r)\, \langle x(r,m) \rangle]^2 \\
& + 4Re\{[W(\omega) * \langle \Gamma_s(k,\omega) \rangle][H_3(\omega)(W_3(\omega) * \langle X(k,\omega) \rangle)]^*\} \\
& + 2Re\{[H_2(2\omega)(W_2(2\omega) * \langle X(k,2\omega) \rangle)][W(\omega) * \langle \Gamma_s(k,\omega) \rangle]^{*2}\} \\
& + 2[\sum_{m=0}^{K-1} \sum_{r=-(N-1)/2}^{(N-1)/2} h^2(k-r)\, w^2(m)\, \langle x(r,m) \rangle]\, |W(\omega) * \langle \Gamma_s(k,\omega) \rangle|^2 \qquad (3.25)
\end{aligned}
$$

At high frequencies, the dominant term is $(\sum_{m=0}^{K-1} \sum_{r=-(N-1)/2}^{(N-1)/2} w^2(m)h^2(k-r)\langle x(r,m)\rangle)^2$ Thus, as in section 3.2, the variance is the square of the expected value for large ω. As in this previous section, the variance of this estimate is reduced by averaging the temporal periodograms from altitudes between 80 and 100 km.

Figure 3.2 shows the average temporal periodogram computed from data collected on October 28-29, 1979. This data set consisted of 71 spatial profiles collected at 5 minute intervals. The 3 dB decrease in shot noise level after spatial filtering is apparent. In this case, the spatial filter was a deconvolution filter of the type used by Rowlett and Gardner with a spatial cutoff at a frequency of 0.44 km^{-1}.

3.4 SPATIAL PERIODOGRAM OF PHOTOCOUNT DATA

Just as an average temporal periodogram is used to determine the appropriate temporal filter cutoff, the spatial periodogram is used to select a spatial filter cutoff. The nature of the spatial filter is discussed in

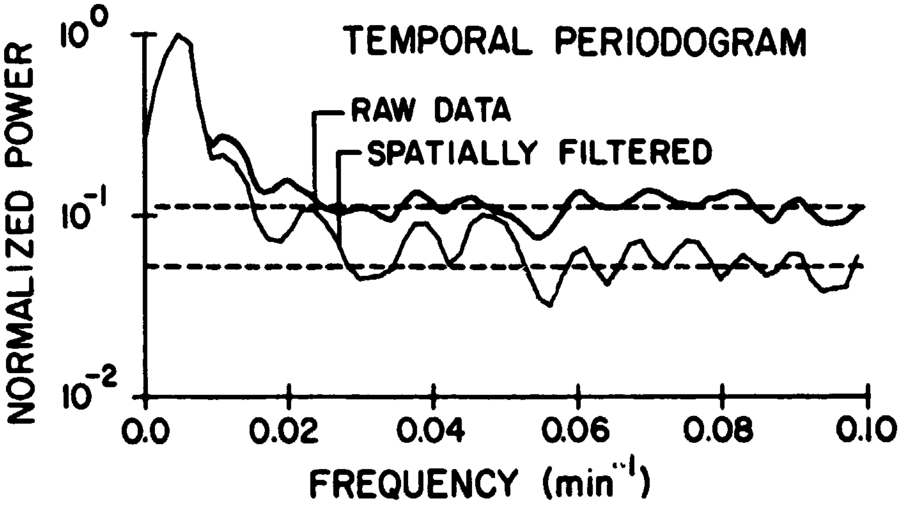

Figure 3.2 Temporal periodogram of the sodium lidar photocount data collected during the night of October 28-29, 1979. The cutoff frequency for the spatially filtered data is 0.44 km^{-1}. [Gardner and Shelton, 1981].

section 3.7. The spatial periodogram of photocount data has been analyzed in detail by Rowlett and Gardner, [1979]. Their results are presented here for comparison with the spatial periodogram of temporally filtered data.

The spatial periodogram of photocount data for the m^{th} spatial profile is given by

$$|\theta(\omega,m)|^2 = \left|\sum_{k=0}^{N-1} x_\gamma(k,m)e^{-i\omega k}\right|^2 = \left|\sum_{k=0}^{N-1} [x(k,m) - b(m)]e^{-i\omega k}\right|^2 \qquad (3.26)$$

Notice that the background counts are subtracted from the raw photocounts. It is assumed that this background count is known a priori. Using the fact that $x(k,m)$ is Poisson, the expected value of $|\theta(\omega,m)|^2$ is readily found.

$$\langle|\theta(\omega,m)|^2\rangle = \sum_{k=0}^{N-1} \langle x(k,m)\rangle + |\langle\theta(\omega,m)\rangle|^2 \qquad (3.27)$$

The first term is a constant shot noise level and is equal to the expected total number of photons counted in the spatial profile. The second term is the power spectrum of the expected signal photocounts. This latter term is the quantity we are attempting to estimate by computing the periodogram. At $\omega = 0$, the expectation is $\langle P(m)\rangle + \langle P_\gamma(m)\rangle^2$, where $P(m)$ is the total number of photocounts and $P_\gamma(m)$ is the total number of signal photocounts in the m^{th} spatial profile. As ω grows large, the constant shot noise term dominates the periodogram. The shot noise level is down from the value of the periodogram at $\omega = 0$ by a factor of

$$\left[1 + \frac{\langle P_\gamma(m)\rangle^2}{\langle P(m)\rangle}\right]^{-1} = \left[1 + \frac{\left[\sum_{k=0}^{N-1} (\langle x(k,m)\rangle - b(m))\right]^2}{\left[\sum_{k=0}^{N-1} \langle x(k,m)\rangle\right]}\right]^{-1} \qquad (3.28)$$

As mentioned in previous sections, if this shot noise level is too high, it will obscure features in the power spectrum. From equation (3.28) it is clear that increasing the number of signal photons will decrease the shot noise level.

The variance of the spatial periodogram has also been derived by Rowlett and Gardner.

$$\mathrm{var}[|\theta(\omega,m)|^2] = 2\langle P(m)\rangle\ |\langle\theta(\omega,k)\rangle|^2 + 2\mathit{Re}\{\langle X(2\omega,m)\rangle\langle\theta^*(\omega,m)\rangle^2\}$$
$$+ 4\mathit{Re}\{\langle X(\omega,m)\rangle\langle\theta^*(\omega,m)\rangle^2\} + |\langle X(2\omega,m)\rangle|^2 + \langle P(m)\rangle^2 + \langle P(m)\rangle \tag{3.29}$$

where $\langle X(\omega,m)\rangle = \sum_{k=0}^{N-1} \langle x(k,m)\rangle e^{-i\omega k}$

At $\omega = 0$, the first two terms dominate yielding a variance of $4\langle P(m)\rangle\langle P_\gamma(m)\rangle^2$. For large ω, the variance is approximately $\langle P(m)\rangle^2$. As in previous cases, it is seen that for large ω, the variance of the periodogram is the square of its expected value. Periodogram averaging is used to reduce the variance of this estimate of the power spectrum by averaging the periodograms of individual spatial profiles together. This procedure was discussed in earlier sections on temporal periodograms.

3.5 SPATIAL PERIODOGRAM OF TEMPORALLY FILTERED DATA

Just as spatially filtering the data prior to computing the temporal periodogram lowers the shot noise floor, temporal filtering can be used to lower the shot noise floor in the spatial periodogram. This permits the spatial cutoff frequency to be extended by extending the frequency at which the true power spectrum becomes obscured by the shot noise level. The temporally filtered data is given by:

$$y_t(k,m) = \sum_{i=-(M-1)/2}^{(M-1)/2} g(m-i)\ x(k,i) \tag{3.30}$$

The periodogram of the m^{th} temporally filtered spatial profile is

$$|\theta_T(\omega,m)|^2 = \left|\sum_{k=0}^{N-1} [y_t(k,m) - b'(m)]e^{-i\omega k}\right|^2 \qquad (3.31)$$

$b'(m)$ is the background noise count present in the m^{th} spatial profile of the temporally filtered data. N is the length of the temporal filter impulse response. The characteristics of the filter are discussed in section 3.6.1.

The expected value and variance of $|\theta_T(\omega,m)|^2$ may be found in a manner similar to that presented in section 3.3 where the temporal periodogram of spatially filtered data was examined. This problem is analogous to the present problem of evaluating the expected value and variance of the spatial periodogram of temporally filtered data. In the present problem, however, no window is applied to the data before the periodogram is computed. The expected value is

$$<|\theta_T(\omega,m)|^2 = \sum_{k=0}^{N-1} \sum_{i=-(M-1)/2}^{(M-1)/2} g^2(m-i) <x(k,i)> + |<\theta_T(\omega,m)>|^2 \qquad (3.32)$$

where $|<\theta_T(\omega,m)>|^2$ is the true power spectrum we are attempting to find. The constant shot noise floor is due to the presence of the first term. At $\omega = 0$ the expected value of the periodogram is

$$<|\theta_T(0,m)|^2> = \sum_{k=0}^{N-1} \sum_{i=-(M-1)/2}^{(M-1)/2} g^2(m-i) <x(k,i)> +$$
$$+ \left[\sum_{k=0}^{N-1} \sum_{i=-(M-1)/2}^{(M-1)/2} g(m-i) <x(k,i)> - b'(m)\right]^2 \qquad (3.33)$$

The shot noise floor is below this value by a factor of

$$R = \left[1 + \frac{\left[\sum_{k=0}^{N-1} \sum_{i=-(M-1)/2}^{(M-1)/2} g(m-i) <x(k,i)> - b'(m)\right]^2}{\left[\sum_{k=0}^{N-1} \sum_{i=-(M-1)/2}^{(M-1)/2} g^2(m-i) <x(k,i)>\right]}\right]^{-1} \qquad (3.34)$$

The value of temporal filtering in decreasing the shot noise level is also illustrated by this equation. As the temporal filter cutoff is extended, the value of equation (3.34) generally becomes smaller until it becomes equivalent to equation (3.28) when no temporal filter is used. As the temporal filter cutoff becomes low (i.e. severe filtering), the value of this expression becomes small. This principle may be demonstrated by assuming that the temporal filter impulse response is a rectangular function. In order to insure that the magnitude of the filter frequency response is unity at $\omega = 0$, the value of $g(m)$ must be $1/M$, where M is the length of the FIR impulse response. As the filter cutoff becomes smaller, the length of the filter impulse response becomes larger. It is also assumed that $x(k,m) = x(k)$ does not vary with m. This, of course, is an unrealistic assumption. However, it simplifies equation (3.34) and serves to clarify the effect that varying the temporal filter cutoff has on this equation. Under these conditions, equation (3.34) simplifies to

$$R = \left(1 + \sum_{k=0}^{N-1} M\langle x(k)\rangle\right)^{-1} \qquad (3.35)$$

As the filter cutoff is reduced, M grows larger and R decreases. This indicates that the separation between the spectral peak at $\omega = 0$ and the shot noise floor is increased. Figure 3.3 contains plots of average spatial periodograms for raw and temporally filtered data. The separation between the spectral peak and the shot noise level is 11 dB greater after a temporal filter was applied. In this case the temporal filter cutoff is 0.03 min^{-1}. In addition, the spatial periodograms were averaged for the entire data set to reduce the variance.

As in previous cases, the periodogram is a noisy estimate of the power spectrum. Using the same methodology reported in earlier sections, the

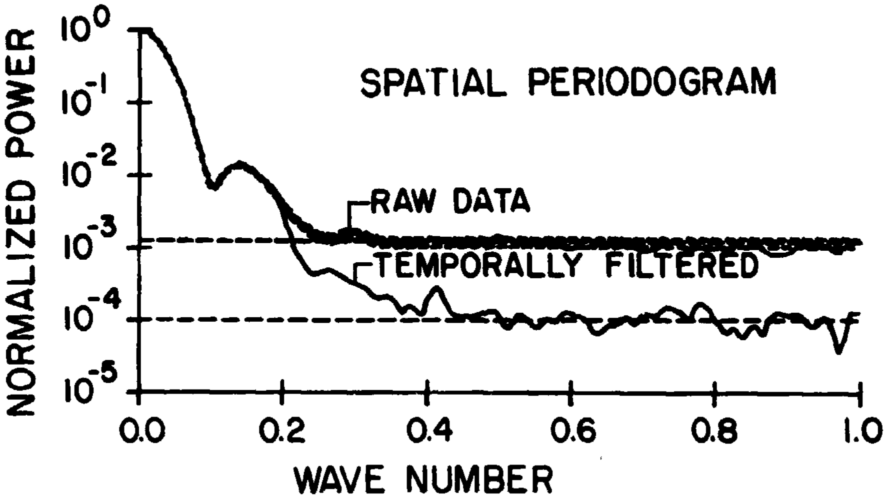

Figure 3.3 Spatial periodogram of the sodium lidar photocount data collected during the night of October 28-29, 1979. The cutoff frequency for the temporally filtered data is 0.033 min^{-1}. The dashed lines are one standard deviation away from the periodogram of raw data. [Gardner and Shelton, 1981].

variance expression was found to be

$$\mathrm{Var}[|\theta_T(\omega,m)|^2] = \sum_{k=0}^{N-1} \sum_{i=-(M-1)/2}^{(M-1)/2} g^4(m-i) <x(k,i)> + |<R_2(2\omega,m)>|^2$$

$$+ \left[\sum_{k=0}^{N-1} \sum_{i=-(M-1)/2}^{(M-1)/2} g^2(m-i) <x(k,i)>\right]^2 + 4Re\{<\theta_T(\omega,m)><R_3^*(\omega,m)>\}$$

$$+ 2Re\{<R_2(2\omega,m)><\theta_T^*(\omega,m)>^2\}$$

$$+ 2\left[\sum_{k=0}^{N-1} \sum_{i=(M-1)/2}^{(M-1)/2} g^2(m-i) <x(k,i)>\right] |<\theta_T(\omega,m)>|^2 \qquad (3.36)$$

where $$<R_n(\omega,m)> = \sum_{k=0}^{N-1} \sum_{i=-(M-1)/2}^{(M-1)/2} g^n(m-i) <x(k,i)>$$

The form of this expression is quite similar to the variance expression for the spatial periodogram of raw photocount data (equation (3.29)). As before, at high frequencies the variance is the square of the mean. To reduce the variance, the temporally filtered spatial periodograms are averaged.

3.6 TWO-DIMENSIONAL FILTERING

3.6.1 TEMPORAL FILTER

The periodograms discussed in previous sections are used to determine the cutoff frequencies for temporal and spatial filters. First the average temporal periodogram is computed and examined. A temporal filter with the desired cutoff frequency is designed and applied to the data. At this point, the spatial filtering technique developed by Rowlett and Gardner is used to complete the two-dimensional filtering process. The implementation of the temporal and spatial filters are quite different. Aspects of the temporal filter are discussed in this part of the section and the spatial filtering technique is reviewed at the end of this section.

technique is reviewed at the end of this section.

Because the sodium layer has infinite temporal extent, as opposed to the limited spatial extent of the layer, temporal windowing was utilized in computing the temporal periodogram. The limited temporal extent of the data set presents problems in the filter implementation as well. To avoid distortion induced by the sharp discontinuities at the beginning and end of the observation period, a Finite Impulse Response (FIR) filter is used. This has an added advantage in that it is a simple matter to insure that the filter has a linear phase response.

Since the returns from a number of pulses are integrated to yield a spatial profile of data, it is possible to apply a temporal deconvolution filter to reduce the distortion introduced by this effect. This distortion is much the same as the distortion introduced by the range bin width in the altitude profile. If the returns are integrated for T_p minutes (by summing the returns from all the laser pulses in this interval), the returns are effectively smeared in the temporal domain. This may be illustrated by noting that the photocounts for each laser pulse, $x_p(k,n)$, are actually summed over a period T_p to obtain the integrated photocount $x(k,m)$.

$$x(k\Delta h, m\Delta T) = \sum_{n=0}^{M_p-1} x_p(k\Delta h, m\Delta T + n\Delta\tau) \tag{3.37}$$

where M_p is the number of laser pulses per spatial profile. More precisely $T = M_p\Delta\tau$ where $\Delta\tau$ is the period separating laser pulses. This is actually the convolution of $x(k,n)$ with a rectangular filter impulse response. The convolution is equivalent to a multiplication in the temporal frequency domain by $\sin(\pi f T_p)/(\pi f T_p)$ where f is the temporal frequency. The first zero occurs in this function at $f = 1/T_p$, where T_p is usually on the order of 2 minutes.

Examination of temporal periodograms indicates that there is no discernible structure which can be attributed to temporal variations in sodium density with periods less than 20 to 40 minutes. Thus, the distortion introduced by this convolution is negligible in current data and there is little need for a temporal deconvolution filter.

A linear phase low pass filter will be utilized to reduce the shot noise contributions in the temporal data. A filter with short impulse response is desirable in order to insure that the length of the temporally filtered data set is comparable to the length of the raw data set. The number of points in the temporally filtered data set (K_T) is less than the number of points in the original data set (K). The relation between K_T and K is

$$K_T = K - M + 1 \tag{3.38}$$

where M is the duration of the filter impulse response. To maintain linear phase, the impulse response must satisfy the relation

$$g(m) = g(M - 1 - m) \tag{3.39}$$

This amounts to a requirement that the impulse response be symmetric about its midpoint. If this condition is satisfied, the filter is linear phase and the various spectral components in the temporal response of the layer will all suffer equal delays. This can be an important consideration when trying to interpret filtered data in terms of a layer density response to wave activity.

In addition to the requirement for a short impulse response, we desire to have small sidelobes and a sharp transition from the passband to the stopband in the filter frequency response. Unfortunately, these requirements are at odds with each other since a short impulse response usually means large sidelobes or a gradual passband to stopband transition. A compromise is made by selecting a Hamming function as the impulse response. The Hamming function, which is a member of the family of raised cosine curves, is defined as

$$g(m) = \begin{cases} 0.54 - 0.46\cos\left(\frac{2\pi m}{M-1}\right); & 0 \leq m \leq M-1 \\ 0 & ; \text{ elsewhere} \end{cases} \qquad (3.40)$$

The magnitude squared of the DFT of this impulse response, $|G(\omega)|^2$, has a stopband which is in excess of 40 dB below the passband. The width of the passband is $2/(M\Delta T)$, where ΔT is the interval between spatial profiles. The passband is defined as the range of frequencies between $\omega = 0$ and the first null in the DFT of the filter frequency response. Figure 3.4 contains a plot of the magnitude of the filter frequency response for a 13 point Hamming impulse response when $\Delta T = 5$ minutes. In this case, the cutoff frequency is 0.0308 min^{-1} (corresponding to a period of 32.5 minutes). It is evident that the response in the passband is not flat. Thus, the higher frequency components in the passband will suffer substantial attenuation as the cutoff frequency is approached. By selecting cutoff frequencies which are somewhat greater than the frequency at which the shot noise level dominates the signal portion of the temporal periodogram, this problem is circumvented to some extent. Unfortunately, the requirements for a flat passband, linear phase and short impulse response cannot all be meet simultaneously. The Hamming impulse response filter is a reasonable compromise.

The effect of temporal filtering on the expected value and variance of the photocount data is easily determined. Since $x(k,m)$ is Poisson, the photocounts collected in non-overlapping time or range intervals are statistically independent. The expected value and variance of filtered data corresponding to the k^{th} range bin and the m^{th} spatial profile, $y(k,m)$, are

$$\langle y_T(k,m)\rangle = \sum_{i=-(M-1)/2}^{(M-1)/2} g(m - i)\ \langle x(k,i)\rangle \tag{3.41}$$

$$\mathrm{Var}[y(k,m)] = \sum_{i=-(M-1)/2}^{(M-1)/2} g^2(m - i)\ \langle x(k,i)\rangle \tag{3.42}$$

The signal to noise ratio (SNR) at the filter output, defined as

$$\mathrm{SNR} = \frac{\langle y_T(k,m)\rangle^2}{\mathrm{Var}[y_T(k,m)]} \tag{3.43}$$

is seen to be

$$\mathrm{SNR} = \frac{\left[\sum_{i=-(M-1)/2}^{(M-1)/2} g(m - i)\ \langle x(k,i)\rangle\right]^2}{\sum_{i=-(M-1)/2}^{(M-1)/2} g^2(m - i)\ \langle x(k,i)\rangle} \tag{3.44}$$

The next step in the processing technique is spatial filtering.

3.6.2 SPATIAL FILTER

The spatial deconvolution filter which is applied after temporal filtering was developed by Rowlett and Gardner [1979]. In equation (2.7) the lidar equation was used to express a spatial profile of data as the three-fold convolution of the radiative lifetime of the sodium, $l(z)$, the receiver range gate, $g(z)$, the laser pulse shape, $p(z)$, and the sodium scattering profile, $\gamma(z)$. The application of temporal filtering does not affect the nature of the spatial deconvolution filter. It can be seen by examining equation (2.8) that the proper deconvolution filter is simply

$$H(\omega) = \begin{cases} F^{-1}(\omega); & |\omega| \le \omega_c \\ 0 & |\omega| > \omega_c \end{cases} \tag{3.45}$$

where ω_c is the cutoff frequency determined by examination of the spatial periodogram of temporally filtered data and $H(\omega)$ is the DFT of the spatial filter impulse response, $h(k)$. The background count is subtracted from each spatial profile and the resulting profile is transformed via FFT techniques. At this point, the spatial deconvolution filter, $H(\omega)$, is applied to the temporally filtered data by multiplication in the spatial frequency domain. After an inverse Fast Fourier Transform, the spatially and temporally filtered data are range squared corrected (i.e., the filtered data are multiplied by the square of their range). By applying the calibration technique discussed in Chapter 2, the final estimates of sodium density can now be calculated.

The expected value and variance of the two-dimensionally filtered data are easily found.

$$<z(k,m)> = \sum_{j=-(N-1)/2}^{(N-1)/2} h(k-j)\left[<y_t(j,m)> - b(m)\right] \tag{3.46}$$

$$\mathrm{Var}[z(k,m)] = \sum_{j=-(N-1)/2}^{(N-1)/2} \sum_{i=-(M-1)/2}^{(M-1)/2} h^2(k-j)\, g^2(m-i)(<x(j,i)>-b(m)) \tag{3.47}$$

where $b(m)$ is the background count present in the m^{th} spatial profile and $z(k,m)$ is the two-dimensionally filtered data. It is assumed that $b(m)$ is known a priori. The signal to noise ratio may be expressed, as in equation (3.43),

$$\mathrm{SNR} = \frac{\left[\sum_{j=-(N-1)/2}^{(N-1)/2} \sum_{i=-(M-1)/2}^{(M-1)/2} h(k-j)g(m-i)<x(j,i)> - \sum_{j=-(N-1)/2}^{(N-1)/2} h(k-j)b(m)\right]^2}{\sum_{j=-(N-1)/2}^{(N-1)/2} \sum_{i=-(M-1)/2}^{(M-1)/2} h^2(k-j)\, g^2(m-i)\, <x(j,i)>} \tag{3.48}$$

As mentioned previously, this procedure ultimately yields a two-dimensionally filtered data set for which the two-dimensional filter is separable. The frequency response of this filter is given by $G(\omega_T)H(\omega_S)$, where

ω_T is the temporal frequency and ω_S is the spatial frequency. The parameters and implementation of each filter are independent. The order in which the filters are applied has no effect on the filtered data. Temporal filtering has been applied first simply because a more dramatic decrease in shot noise level is apparent in the spatial periodogram than is evident in the temporal periodogram after spatial filtering. The temporal and spatial cutoff frequencies may also be chosen by examining the two-dimensional periodogram of the photocount data. The characteristics of this periodogram are discussed in the next section.

3.7 TWO-DIMENSIONAL PERIODOGRAM

The two-dimensional periodogram discussed in this section can be used to choose the optimal set of cutoff frequencies for the spatial and temporal filters discussed previously. The constant background count, b, is subtracted from each spatial photocount profile. It is assumed that this quantity is known and, to simplify the following analysis, is constant from spatial profile to spatial profile. Once again, the nature of the temporal variations in sodium density present a problem. These variations are a small percentage of the background sodium density. Unlike the temporal periodogram, however, the average photocounts at each altitude cannot be subtracted since the spatial variations in the data set are also of interest. A temporal window is applied to prevent the large discontinuities at beginning and end of the data set from contributing significantly to the periodogram. The periodogram is expressed as:

$$|T(\omega_S,\omega_T)|^2$$

$$= \sum_{k=0}^{N-1} \sum_{l=0}^{N-1} \sum_{m=0}^{K-1} \sum_{n=0}^{K-1} w(m)\ w(n)\ x_\gamma(k,m)\ x_\gamma(l,n) e^{i\omega_S(k-l)}\ e^{i\omega_T(m-n)} \tag{3.49}$$

ω_S and ω_T are spatial and temporal frequencies, respectively, and $x_\gamma(m,n) = x(m,n) - b$. $w(m)$ is the temporal window. The expected value of this expression is evaluated yielding the result:

$$<|T(\omega_S,\omega_T)|^2> = \sum_{k=0}^{N-1} \sum_{m=0}^{K-1} w^2(m)\ <x(k,m)> + |W(\omega_T)\ *\ <\Gamma(\omega_S,\omega_T)>|^2 \tag{3.50}$$

where $W(\omega_T)$ is the DFT of $w(m)$ and $|<\Gamma(\omega_S,\omega_T)>|^2$ is the two-dimensional power spectrum we are attempting to estimate. As in previous periodograms, a constant shot noise level is present.

The variance expression for the periodogram is now evaluated. This is accomplished by evaluating the covariance, $\mathrm{cov}[|T(\omega_{S1},\omega_{T1})|^2,\ |T(\omega_{S2},\omega_{T2})|^2]$, for $\omega_{S1} = \omega_{S1}$ and $\omega_{T1} = \omega_{T2}$. The covariance expression for a two-dimensional photocount periodogram is given by:

$$\mathrm{cov}[|T(\omega_{S1},\omega_{T1})|^2,\ T(\omega_{S2},\omega_{T2})|^2] = \sum_{k=0}^{N-1} \sum_{l=0}^{N-1} \sum_{p=0}^{N-1} \sum_{r=0}^{N-1} \sum_{m=0}^{K-1} \sum_{n=0}^{K-1} \sum_{s=0}^{K-1} \sum_{t=0}^{K-1} w(m)\, w(n)\, w(s)\, w(t)$$

$$\cdot\ [<x_\gamma(k,m)\ x_\gamma(l,n)\ x_\gamma(p,s)\ x_\gamma(r,t)> - <x_\gamma(k,m)\ x_\gamma(l,n)><x_\gamma(p,s)\, x_\gamma(r,t)>]$$

$$e^{i\omega_{S1}(k-l)}\ e^{i\omega_{S2}(p-r)}\ e^{i\omega_{T1}(m-n)}\ e^{i\omega_{T2}(s-t)} \tag{3.51}$$

The eightfold summation is broken into special cases: $k=l=m=n=p=r=s=t$, $k=l=m=n=p=r=s\neq t$, etc. in order to apply the property of independent increments and the first four moments of a Poisson process.

$$<x_\gamma(k,m)\ x_\gamma(l,n)> = <x_\gamma(k,m)><x_\gamma(l,n)> \quad k \neq l \quad m \neq n \tag{3.52}$$

$$<x_\gamma^{\,2}(k,m)> = <x_\gamma(k,m)>^2 + <x_\gamma(k,m)> \tag{3.53}$$

$$<x_\gamma^{\,3}(k,m)> = <x_\gamma(k,m)>^3 + 3<x_\gamma(k,m)><x(k,m)> + <x(k,m)> \tag{3.54}$$

$$\begin{aligned}\langle x_\gamma{}^4(k,m)\rangle = \langle x_\gamma(k,m)\rangle^4 + 6\langle x_\gamma(k,m)\rangle^2\langle x(k,m)\rangle + 4\langle x_\gamma(k,m)\rangle\langle x(k,m)\rangle \\ + 3\langle x(k,m)\rangle^2 + \langle x(k,m)\rangle\end{aligned} \tag{3.55}$$

After tedious algebraic manipulations the covariance expression is found to be

$$\begin{aligned}\mathrm{cov}[|T(\omega_{S1},\omega_{T1})|^2,\ |T(\omega_{S2},\omega_{T2})|^2] = \sum_{k=0}^{N-1}\sum_{m=0}^{K-1} w^4(m)\ \langle x(k,m)\rangle \\ + |\langle S(\omega_{S1}+\omega_{S2},\ \omega_{T1}+\omega_{T2})\rangle * W_2(\omega_{T1}+\omega_{T2})|^2 \\ + |\langle S(\omega_{S1}-\omega_{S2},\ \omega_{T1}-\omega_{T2})\rangle * W_2(\omega_{T1}-\omega_{T2})|^2 \\ + 2Re\{[\langle T(\omega_{S1},\ \omega_{T1})\rangle * W(\omega_{T1})][\langle S(\omega_{S1},\ \omega_{T1})\rangle * W_3(\omega_{T1})]^*\} \\ + 2Re\{[\langle T(\omega_{S2},\ \omega_{T2})\rangle * W(\omega_{T2})][\langle S(\omega_{S2},\ \omega_{T2})\rangle * W_3(\omega_{T2})]^*\} \\ + 2Re\{[\langle T(\omega_{S1},\ \omega_{T1})\rangle * W(\omega_{T1})][\langle T(\omega_{S2},\ \omega_{T2})\rangle * W(\omega_{T2})] \\ [\langle S(\omega_{S1}+\omega_{S2},\ \omega_{T1}+\omega_{T2})\rangle * W_2(\omega_{T1}+\omega_{T2})]^*\} + 2Re\{[\langle T(\omega_{S1},\ \omega_{T1})\rangle * W(\omega_{T1})] \\ [\langle T(\omega_{S2},\ \omega_{T2})\rangle * W(\omega_{T2})][\langle S(\omega_{S1}-\omega_{S2},\ \omega_{T1}-\omega_{T2})\rangle * W_2(\omega_{T1}-\omega_{T2})]^*\}\end{aligned} \tag{3.56}$$

where $$\langle S(\omega_S,\omega_T)\rangle = \sum_{k=0}^{N-1}\sum_{m=0}^{K-1} w(m)\ \langle x(k,m)\rangle e^{-i\omega_S k}\ e^{-i\omega_T m}$$

$$W(\omega_T) = \sum_{m=0}^{K-1} w(m)e^{-i\omega_T m}$$

$$W_n(\omega_T) = \sum_{m=0}^{K-1} w^n(m)e^{-i\omega_T m}$$

Setting $\omega_{S1} = \omega_{S2} = \omega_S$ and $\omega_{T1} = \omega_{T2} = \omega_T$ yields the variance expression:

$$\mathrm{Var}[|T(\omega_S,\omega_T)|^2] = 2\left[\sum_{k=0}^{N-1}\sum_{m=0}^{K-1} w^2(m)\ \langle x(k,m)\rangle\right]|\langle T(\omega_S,\omega_T)\rangle * W(\omega_T)|^2$$

$$+\ 2Re\{[\langle T(\omega_S,\omega_T)\rangle * W(\omega_T)]^2\,[\langle S(2\omega_S\ 2\omega_T)\rangle * W_2(2\omega_T)]^*\}$$

$$+\ 4Re\{[\langle T(\omega_S,\omega_T)\rangle * W(\omega_T)][\langle S(\omega_S,\omega_T)\rangle * W_3(\omega_T)]^*\}$$

$$+\ |\langle T(2\omega_S,2\omega_T)\rangle * W_2(2\omega_T)|^2 + \sum_{k=0}^{N-1}\sum_{m=0}^{K-1} w^4(m)\ \langle x(k,m)\rangle$$

$$+\left[\sum_{k=0}^{N-1}\sum_{m=0}^{K-1} w^2(m)\ \langle x(k,m)\rangle\right]^2 \tag{3.57}$$

When ω_S and ω_T equal zero, the first two terms dominate and the variance is approximately:

$$\mathrm{Var}[|T(0,0)|^2]$$

$$\approx 4\left[\sum_{k=0}^{N-1}\sum_{m=0}^{K-1} w^2(m)\ \langle x(k,m)\rangle\right]\left[\sum_{k=0}^{N-1}\sum_{m=0}^{K-1} w(m)(\langle x(k,m)\rangle - b)\right]^2 \tag{3.58}$$

As ω_S and ω_T increase, the second term falls off rapidly because of its $2\omega_S$, $2\omega_T$ dependence. For large ω, the last term dominates. Since the variance does not approach zero as ω_S and ω_T grow large, this is not a consistent estimate of the two-dimensional power spectrum. As was typical of the periodograms analyzed previously, the variance is the square of the expected value for large frequencies. Following Oppenheim and Schafer [1977], a possible method of reducing the variance of the periodogram is to apply a spatial window, $u(k)$, before computing the periodogram. This has the effect of smoothing the periodogram and thus reducing its variance. Note that the same effect was observed when the temporally windowed temporal periodogram was analyzed. Applying the spatial window has the effect of convolving the frequency response of the window, $U(\omega_S)$, with the spectral content of the signal. The variance expression becomes modified by this windowing so that the term which dominates at large frequencies is

$$\left[\sum_{k=0}^{N-1}\sum_{m=0}^{K-1} w^2(m)\, u^2(k)\, \langle x(k,m)\rangle\right]^2 \qquad (3.59)$$

and at ω_S and $\omega_T \approx 0$, the variance is

$$\mathrm{Var}[|T(0,0)|^2]$$

$$\approx 4\left[\sum_{k=0}^{N-1}\sum_{m=0}^{K-1} w^2(m)\, u^2(k)\, \langle x(k,m)\rangle\right]\left[\sum_{k=0}^{N-1}\sum_{m=0}^{K-1} w(m)\, u(k)(\langle x(k,m)\rangle - b)\right]^2 \qquad (3.60)$$

The expected value of the periodogram becomes

$$\langle|T(\omega_S,\omega_T)|^2\rangle = \sum_{k=0}^{N-1}\sum_{m=0}^{K-1} w^2(m)\, u^2(k)\, \langle x(k,m)\rangle + |\langle\Gamma(\omega_S,\omega_T) ** U(\omega_S)\, W(\omega_T)|^2 \qquad (3.61)$$

where the second term is the two-dimensional convolution of the spectrum of signal photocounts and the two-dimensional frequency response of the window, $U(\omega_S)\, W(\omega_T)$.

We see that when ω_S and $\omega_T \approx 0$ the ratio of the variance to the expected value is

$$\frac{\mathrm{Var}}{\langle\ \rangle} \approx \frac{4\left[\sum_{k=0}^{N-1}\sum_{m=0}^{K-1} w^2(m)\, u^2(k)\, \langle x(k,m)\rangle\right]\left[\sum_{k=0}^{N-1}\sum_{m=0}^{K-1} w(m)\, u(k)(\langle x(k,m)\rangle - b)\right]^2}{\sum_{k=0}^{N-1}\sum_{m=0}^{K-1} w^2(m)\, u^2(k)\, \langle x(k,m)\rangle + \left[\sum_{k=0}^{N-1}\sum_{m=0}^{K-1} w(m)\, u(k)(\langle x(k,m)\rangle - b)\right]^2} \qquad (3.62)$$

and for large frequencies this ratio is

$$\frac{\mathrm{Var}}{\langle\ \rangle} \approx \left[\sum_{k=0}^{N-1}\sum_{m=0}^{K-1} w^2(m)\, u^2(k)\, \langle x(k,m)\rangle\right] \qquad (3.63)$$

Oppenheim and Schafer [1977] have estimated the variance reduction ratio, which is the ratio of the variance after windowing to the variance before windowing. For raised cosine curves which are expressed as

$$u(k) = \beta - \alpha\cos\left(\frac{2\pi k}{N-1}\right) \qquad (3.64)$$

they estimate the reduction in variance to be a factor of

$$R \approx 2\alpha^2 + \beta^2 \qquad (3.65)$$

where N = length of the window and $\beta = 0.54$ and $\alpha = 0.46$ for a Hamming window. Under these conditions, $R \approx 0.3974$. However, it is clear from the variance expression derived here that the variance at high frequencies is still the square of the expected value. Unfortunately, this is the region where the power spectrum is obscured by the shot noise level. Further, the reduction in variance is fairly meager and is obtained by sacrificing spectral resolution. As a result, spatial windowing does not seem to offer much improvement.

The two-dimensional power spectra should yield more insight into the nature of sodium layer dynamics as well as provide a more precise means of determining appropriate filter cutoffs. Unfortunately the variance of the periodogram cannot be reduced substantially without sacrificing the spectral resolution of the periodogram. Further, the temporal variations in photocounts become masked by the large average levels upon which they are superimposed. This problem was solved by subtracting the average counts from each altitude in the case of the temporal periodogram. This technique cannot be applied here without destroying the spatial variations in photocounts which are also of interest. Thus, little can be done to correct these shortcomings. The dramatic decreases in variance possible by averaging the periodograms is not possible because we have only one sample of the two-dimensional periodogram.

4. THE LAYER RESPONSE TO GRAVITY WAVES

4.1 INTRODUCTION

Lidar measurements of the nighttime sodium layer often reveal wavelike density perturbations moving through the layer. It appears that the motion of these features is associated with the propagation of internal gravity waves [Rowlett et al., 1978; Clemesha et al., 1978; Megie and Blamont, 1977]. Thus, in order to interpret sodium layer dynamics the response of an atmospheric layer to wave activity must be considered.

In this chapter two mechanisms by which atmospheric waves may perturb the atomic sodium density are considered. The first mechanism, the corkscrew mechanism, is considered only briefly because it is most effective only in the upper half of the sodium layer. Further, it is difficult to account for the large density variations observed in the sodium layer, particularly in the lower half of the layer, by this process alone. The layer density response to atmospheric waves, which is derived in section 4.4, appears to provide a more satisfactory explanation for the observed sodium layer dynamics. This mechanism is discussed in some detail. It is found that the layer response can be highly nonlinear in certain areas of the sodium layer.

Although it appears that gravity waves are responsible for many of the observed sodium layer dynamics, the results presented in this chapter are more general in nature and may be applied to other types of atmospheric waves. Gravity waves, however, are an important type of wave motion at mesospheric heights, probably dominating atmospheric motions [Houghton, 1977]. Since some of the results in this chapter are discussed in terms of gravity wave parameters, a brief review of internal gravity waves is included in the next section.

4.2 INTERNAL GRAVITY WAVES

Internal gravity waves are a type of atmospheric wave which can exist in a stably stratified fluid. Since the medium is stably stratified, a small fluid parcel which is displaced vertically from its equilibrium level will be subjected to a force which tends to return it to its equilibrium position. Once an atmospheric parcel is displaced and released, a wave may be generated. Internal gravity waves are a very important subset of the general class of gravity waves. Internal gravity waves exhibit phase variations with height while the remaining type of gravity wave, sometimes called an external gravity wave, does not. Thus, only internal gravity waves propagate vertically. Many of the gravity waves observed in the region of the sodium layer are probably generated much lower in the atmosphere and propagate upward to mesospheric heights.

The linear theory of gravity waves is well developed and has been considered in detail by Hines [1960]. Rather than repeat the mathematical development describing these waves, results which are applied in following sections are summarized. The assumptions made in obtaining these results are as follows;

1. Perturbations are sufficiently small to permit nonlinear effects to be ignored.

2. The atmosphere is stationary in the absence of wave activity (no mean winds are considered).

3. Only forces due to pressure, gravity, and inertia are considered. It is assumed that the gravitational field is constant in magnitude and direction.

The linearized equations of motion (4.1), adiabatic state (4.2), and continuous mass conservation (4.3), as given below, are solved to obtain the perturbations in pressure and density and the horizontal and vertical velocities associated with the propagation of internal gravity waves.

$$\rho_0 \left(\frac{\partial \underline{V}}{\partial t} \right) = \rho \underline{g} - \nabla p \tag{4.1}$$

$$\frac{\partial \rho}{\partial t} + \underline{V} \cdot \nabla p_0 = c^2 \left[\frac{\partial \rho}{\partial t} + \underline{V} \cdot \nabla \rho_0 \right] \tag{4.2}$$

$$\frac{\partial \rho}{\partial t} + \underline{V} \cdot \nabla \rho_0 + \rho_0 \nabla \cdot \underline{V} = 0 \tag{4.3}$$

From the solution to these equations it is found that the wave numbers and wave frequency are related by the dispersion equation;

$$\omega^4 - \omega^2 c^2 (K_x^2 + K_z^2) + (\gamma - 1)\, g^2 K_x^2 + i \gamma g \omega^2 K_z = 0 \tag{4.4}$$

where ω = wave frequency (s^{-1})

c = speed of sound (m/s)

$K_x = k_x$ = horizontal wave number (m^{-1})

$K_z = k_z + i/2H$ = vertical wave number (m^{-1})

γ = ratio of specific heats

g = acceleration of gravity (m/s^2)

p = pressure (N/m^2)

ρ = density (g/m^3)

$\underline{V}$ = velocity (m/s)

H = atmospheric scale height (m)

The solution has the form;

$$\left(\frac{p - p_0}{p_0 P}\right) = \left(\frac{\rho - \rho_0}{\rho_0 R}\right) = \frac{V_x}{X} = \frac{V_z}{Z} = A\exp[i(\omega t - K_x x - K_z z)] \tag{4.5}$$

The unperturbed density and pressure are given by ρ_o and p_o, respectively. Because of the complex nature of K_z, the amplitudes of the density and pressure perturbations and the vertical and horizontal winds are seen to grow exponentially with altitude. The polarization factors, R, P, X, and Z, determine the relative magnitudes and phases of these quantities. It may be shown that they have the form

$$P = \gamma\omega^2 K_z - i\gamma g\omega^2/C^2 \tag{4.6}$$

$$R = \omega^2 K_z + i(\gamma - 1)gK_x^{\,2} - i\gamma g\omega^2/C^2 \tag{4.7}$$

$$X = \omega K_x K_z C^2 - ig\omega K_x \tag{4.8}$$

$$Z = \omega^3 - \omega K_x^{\,2} C^2 \tag{4.9}$$

An examination of equation (4.4) reveals that for any pair of real wave numbers (k_x and k_z), two distinct, real values of ω exist. One of these values must be greater than $\omega_a = \gamma g/2C$ (the natural frequency) and the other must be smaller than $\omega_b = (\gamma-1)^{1/2} g/C$ (the Brunt-Vaisala frequency). ω_a is always greater than ω_b. If $\omega > \omega_a$, the wave is an acoustic wave. Likewise, if $\omega < \omega_b$, the wave is an internal gravity wave. No internal waves will propagate in the frequency gap $\omega_b < \omega < \omega_a$.

In this chapter, only internal gravity waves are considered. These atmospheric oscillations will always have a period greater than the Brunt-Vaisala period, τ_b. At 90 km, τ_b is approximately 4 minutes. In addition, the processes of reflection and dissipation serve to restrict the possible values of k_x, k_z, and ω. Because of the structure of the atmosphere below 90 km, regions where $\tau_b > 4$ minutes exist. Specifically, near 54 km the Brunt-Vaisalla period is probably closer to 8 minutes. This will have the effect of preventing some of the higher frequency waves from reaching the sodium layer. In contrast to this effect is viscous dissipation which becomes stronger with increasing altitude. This effectively places an upper limit on the propagation of these waves which is a function of the frequency and wave number of the wave. Figure 4.1 [Hines, 1960] shows the allowed propagation modes at meteor radar heights.

Although this figure indicates that waves with periods less than 10 minutes can be present, only longer period perturbations in sodium density have been observed. If a low frequency approximation is made, the polarization relations become much simpler. On the basis of experimental data, this simplification appears to be justified. If $\omega << \omega_b$, the relation between the horizontal and vertical winds and the density perturbations become;

$$V_x = \frac{X}{R}\left(\frac{\rho - \rho_0}{\rho_0}\right) \simeq \frac{ik_x g}{\omega}\left[\frac{\omega^2\gamma H - g(\gamma - 1)}{i\omega^2 + g(\gamma - 1)K_z}\right]\left(\frac{\rho - \rho_0}{\rho_0}\right) \tag{4.10}$$

$$V_z = \frac{Z}{R}\left(\frac{\rho - \rho_0}{\rho_0}\right) \simeq \left[\frac{-g\omega(1 - i\gamma HK_z)}{i\omega^2 + g(\gamma - 1)K_z}\right]\left(\frac{\rho - \rho_0}{\rho_0}\right) \tag{4.11}$$

The winds are expressed in terms of density perturbations to simplify the formulation of the layer density response to these waves in a subsequent section.

It is interesting to note that under the conditions

$$k_z^2 >> \omega_a^2/c^2 \tag{4.12}$$

and

$$\omega^2 << \omega_b^2 \tag{4.13}$$

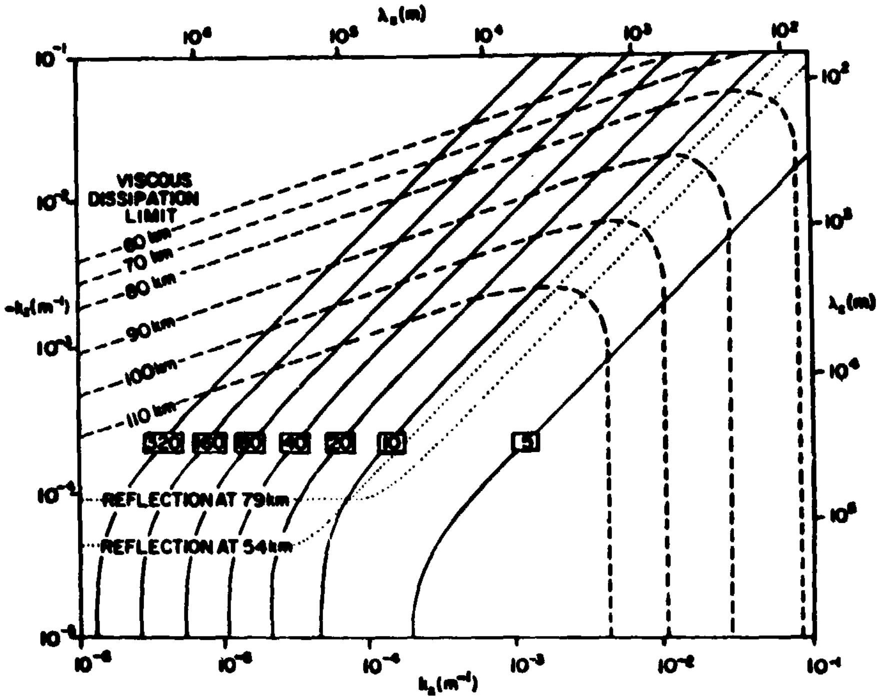

Figure 4.1 Gravity wave propagation modes at mesospheric heights. Gravity wave periods, measured in minutes, are shown in boxes on the corresponding constant period contours (solid lines). The limits of the permitted spectrum as determined by viscous damping are shown for heights of 60, 70, 80, 90, 100, and 110 km (dashed lines). Modes lying above and to the right of these curves are excluded. The modes subject to reflection at heights of 54 and 79 km are also shown (dotted lines). Modes lying below these curves cannot proceed from the lower atmosphere to the upper [Hines, 1960].

the dispersion relation simplifies to

$$\omega^2 k_z^2 \simeq \omega_b^2 k_x^2 \qquad (4.14)$$

and the polarization relations can be reduced to

$$\frac{Z}{X} \simeq \frac{-k_x}{k_z} \qquad (4.15)$$

$$\frac{R}{X} \simeq \frac{i(\gamma - 1)^{1/2}}{c} \qquad (4.16)$$

In this case, energy flow is almost horizontal while the phase progression is nearly vertical. As in all internal gravity waves, the vertical component of phase progression will be opposite to the vertical component of energy flow. Thus, an upward transfer of energy accompanies a downward phase progression. Since many of the gravity waves at mesospheric heights probably originate lower in the atmosphere and transfer energy upward, they should be associated with a downward phase progression.

4.3 CONVERGENCE OF IONIZATION

The motion of long-lived ions, such as Na^+ in the nighttime mesosphere, can be very sensitive to neutral winds. A magnetoionic process exists through which horizontal winds blowing across the geomagnetic lines of force impart a vertical velocity to ionization. As ions are swept along by the neutral wind, a Lorentz force will be established due to interactions with the magnetic field. Ions will acquire a velocity perpendicular to their previous velocity and the direction of the magnetic field. Above 145 km, the ion-neutral collision frequency is quite low (much less than the ion-gyrofrequency). In this case, the ions are effectively trapped on a line of magnetic force and will exhibit little vertical motion due to horizontal neutral winds. At lower heights, below 90 km, the ion-neutral collision frequency is much greater than the ion-gyrofrequency. In this case, the ions will be swept along by the neutral wind. However, in the region between approximately 90 and 145 km, a net vertical motion will be imparted to the ionization due to the Lorentz force.

A wind blowing towards the east across the geomagnetic field will produce an upward welling of positive ionization in this region. Similarly, a wind blowing towards the west will cause a downward movement of ionizaton. If the winds are produced by a gravity wave, for example, a region where the wind blows towards the east will be bounded above and below by winds blowing towards the west. At the interface where westward winds are above eastward winds, ionization will tend to converge. Where an eastward wind is above a westward wind, ionization will be depleted.

This mechanism has been used to explain sporadic E [Chimonas and Axford, 1968; Macleod, 1966; Axford, 1963]. Gravity waves which propagate upward will exhibit a downward phase progression. Thus, layers of ionization trapped at the wind nodes will move downward and be dumped around 90 km where this mechanism becomes ineffective. Figure 4.2 [Chimonas, 1969] contains the result of a computer simulation indicating how ionization can be collected and transported downward by a gravity wave. Richter and Sechrist [1978] have calculated the Na^+ ion drift velocity (Figure 4.3). Below 90 km these drift velocities are quite small. However, this mechanism can cause layers of sodium ions to be swept downwards and dumped in this region. When these ions are converted to atomic sodium, corresponding enhancements in Na density would be apparent in lidar observations of the sodium layer. Since the $[Na]/[Na^+]$ ratio is high (probably 30 to 90 [Richter and Sechrist, 1978]), it

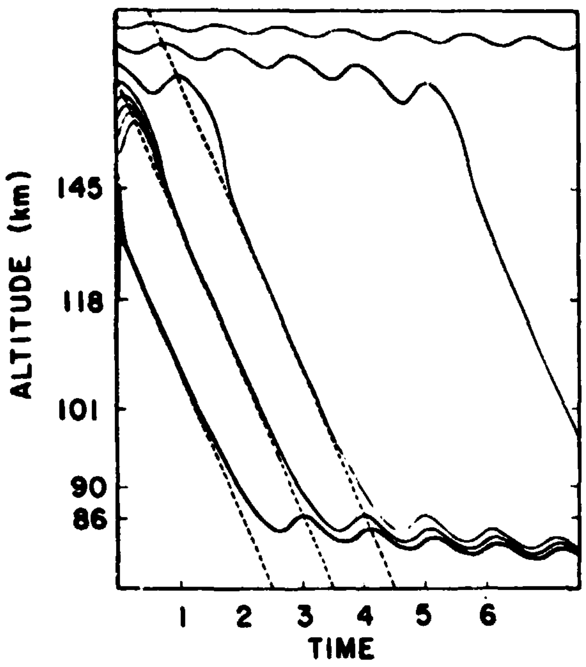

Figure 4.2 Computer simulation of the downward motion of ionization under the influence of gravity wave motions. Initially the ions were equally spaced in altitude (at T = 0). The downward motion and accumulation of the ions is indicated by the solid lines. Dashed lines indicate the motion of the wind nodes. A maximum horizontal wind of 50 m/s and a vertical phase velocity of 1 m/s were assumed. [Chimonas, 1979].

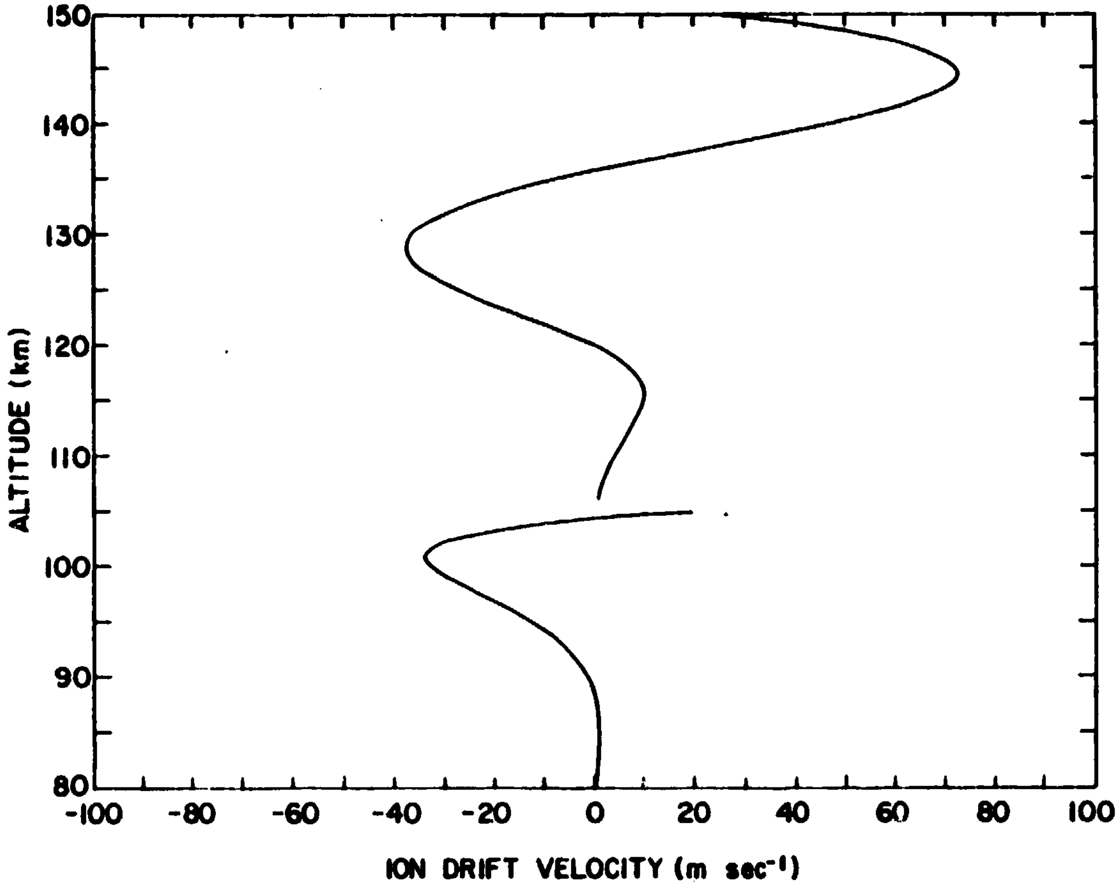

Figure 4.3 Theoretical values for Na^+ drift velocity. The neutral winds are assumed to be zero at 120 km. Drift velocities below 105 km are multiplied by 100 [Richter and Sechrist, 1978].

appears that this mechanism is not responsible for the large sodium density variations observed in the nighttime layer. The mechanism is not very effective below 90 km where the largest fluctuations in density are found. These large density variations are more readily explained in terms of perturbations in the neutral layer associated with the passage of atmospheric waves.

4.4 LAYER DENSITY RESPONSE

4.4.1 RESPONSE TO PERTURBATIONS; THE CONTINUITY EQUATION

Although we are primarily concerned with the mesospheric sodium layer, the following development is less restricted in nature and applies, in general, to atmospheric layers composed of a neutral minor constituent. The density response of a neutral atmospheric layer to wave activity may be found by examining the equation of continuity;

$$\frac{\partial n}{\partial t} + \nabla \cdot (n\underline{V}) = P - Q \qquad (4.17)$$

where n = density of the minor constituent

$\underline{V}$ = velocity of the minor constituent

P = source terms

Q = loss terms

The velocity field, $\underline{V}$, associated with an atmospheric wave can, in general, be written as follows;

$$\underline{V} = A\underline{\beta} \exp(i(\omega t - K \cdot \underline{r})) \qquad (4.18)$$

where A = wave amplitude

$\underline{\beta} = \beta_x \hat{x} + \beta_z \hat{z}$

ω = wave frequency

$\underline{K} = K_x\hat{x} + K_z\hat{z}$ = wave vector

$\underline{r} = x\hat{x} + z\hat{z}$ = position vector

$\underline{V}$ is expressed as a complex exponential in order to simplify the problem. Because equation (4.17) is nonlinear, only the real part of $\underline{V}$ should be used. However, for the first order approximation made in section 4.4.2 little error is introduced. In the perturbation series solution presented in section 4.4.3 the back-coupling of high frequency perturbations to lower frequency perturbations is neglected because of this approximation. The oscillatory density variations associated with the second order terms are accurately represented. Higher order terms suffer larger errors. However, the contributions of the higher order terms to the total layer response are not significant for low amplitude waves.

In general, β_x and β_z are expressed in terms of other quantities perturbed by wave activity. These relationships may be deduced by utilizing the polarization relations of the type of wave activity being considered. We desire to express the layer density response in terms of the wave induced atmospheric density perturbations. Letting $A\exp(i\omega t - i\underline{K}\cdot\underline{r})$ represent the atmospheric density perturbations, the polarization relations are used to find the appropriate $\underline{\beta}$. In this case, β_x relates the magnitude and phase of the atmospheric density perturbations to the horizontal wind, V_x, and β_z relates the magnitude and phase of the density perturbations to the vertical wind, V_z.

Several other assumptions are made in obtaining the solutions presented in this section. It is assumed that the diffusion time of the minor constituent forming the atmospheric layer is much greater than the period of the atmospheric waves inducing the observed density perturbations. This implies that the velocity field of the minor constituent equals the atmospheric velocity field. Only wave induced dynamics are considered; no chemical effects associated with atomic sodium or sources of new atomic sodium are included in these solutions. This has the effect of reducing the source and loss terms, P and Q in equation (4.17), to zero. Finally, it is assumed that the sodium layer has a density profile, $n_s(\underline{r})$, in the absence of wave activity that is a function of position vector only. Time variations in this background or steady state profile are not considered. Under these conditions, two expressions for the solution of the continuity equation are found.

4.4.2 THE EXACT SOLUTION

It is assumed that the solution of equation (4.17) has the form

$$n(\underline{r},t) = e^{\phi} n_s(\underline{r} + \underline{\theta}) \qquad (4.19)$$

The factor, e^{ϕ}, represents an "amplification" term which will induce perturbations in the magnitude of n_s. In addition, the argument of n_s is perturbed by the factor, $\underline{\theta}$. $\underline{\theta}$ has a horizontal component, θ_x, as well as a vertical component, θ_z, since n_s is a function of both horizontal and vertical variables. This term accounts for vertical and horizontal displacements in the layer as it is swept along by the atmospheric waves. When equation (4.19) is substituted into (4.17), three differential equations describing ϕ, θ_x, and θ_z are obtained.

$$\frac{\partial\phi}{\partial t} = -(-i\underline{K}\cdot\underline{\beta} + \underline{\beta}\cdot\nabla\phi)\ A\exp(i(\omega t - \underline{K}\cdot\underline{r})) \qquad (4.20)$$

$$\frac{\partial\theta_x}{\partial t} = -(\beta_x + \underline{\beta}\cdot\nabla\theta_x)\ A\exp(i(\omega t - \underline{K}\cdot\underline{r})) \qquad (4.21)$$

$$\frac{\partial\theta_z}{\partial t} = -(\beta_z + \underline{\beta}\cdot\nabla\theta_z)\ A\exp(i(\omega t - \underline{K}\cdot\underline{r})) \qquad (4.22)$$

In each case, as A approaches zero, ϕ, θ_x, and θ_z must also approach zero.

The solutions to these equations are not immediately obvious. However, power series techniques may be used to solve them. Note that all three equations have the general form

$$\frac{\partial\gamma}{\partial t} = -(\alpha + \underline{\lambda}\cdot\nabla\gamma)\ \Delta N \tag{4.23}$$

α and $\underline{\lambda}$ are complex constants. ΔN is the source function. In this case, it is seen that $\Delta N = A\exp(i\omega t - i\underline{K}\cdot\underline{r})$. The solution of equation (4.23) is expressed in power series form;

$$\gamma = \sum_{\ell=1}^{\infty} \gamma_\ell = \sum_{\ell=1}^{\infty} C_\ell (\Delta N)^\ell \tag{4.24}$$

By substituting (4.24) into (4.23) and collecting terms which contain similar powers of ΔN, the coefficients, C_ℓ, may be determined. It is seen that

$$\frac{\partial\gamma_\ell}{\partial t} = \ell i\omega C_\ell (\Delta N)^\ell \tag{4.25}$$

and

$$\underline{\lambda}\cdot\nabla\gamma_\ell = -\ell i(\underline{\lambda}\cdot\underline{K})\ C_\ell(\Delta N)^\ell \tag{4.26}$$

Combining these results, it is concluded that

$$C_\ell = \frac{-\alpha(\ \underline{\lambda}\cdot\underline{K})^{\ell-1}}{\ell(i\omega)^\ell} \tag{4.27}$$

and

$$\gamma = \sum_{\ell=1}^{\infty} -\frac{\alpha(i\lambda\cdot\ K\ )^{\ell-1}}{\ell(i\omega)^\ell}(\Delta N)^\ell \tag{4.28}$$

This result may be simplified somewhat by utilizing the following relationship;

$$\ln(1 - z) = -\sum_{n=1}^{\infty}\left(\frac{z^n}{n}\right) \tag{4.29}$$

As a result, it is seen that

$$\gamma = \frac{i\alpha}{\underline{\lambda}\cdot\underline{K}}\ \ln\left[1 - \frac{\underline{\lambda}\cdot\underline{K}}{\omega}\ \Delta N\right] \tag{4.30}$$

is a solution of equation (4.23).

This result is now used to find the solutions for ϕ, θ_x, and θ_z. To obtain the solution of equation (4.20), we let $\underline{\lambda}=\underline{\beta}$ and $\underline{\alpha}=\underline{K}\cdot\underline{\beta}$. To solve equations (4.21) and (4.22), we let $\underline{\lambda} = \underline{\beta}$ and $\alpha = \beta_x$ and $\alpha = \beta_z$, respectively. The results of these manipulations are

$$\phi = -\ln\left(1 - \frac{\underline{K}\cdot\underline{V}}{\omega}\right) \tag{4.31}$$

$$\underline{\theta} = \frac{-i\underline{V}}{\underline{K}\cdot\underline{V}} \ln\left(1 - \frac{\underline{K}\cdot\underline{V}}{\omega}\right) \tag{4.32}$$

Thus, the exact solution for the layer density response is given by;

$$n(\underline{r},t) = \frac{n_s\left[\underline{r} - \dfrac{i\,\underline{V}}{\underline{K}\cdot\underline{V}} \ln\left(1 - \dfrac{\underline{K}\cdot\underline{V}}{\omega}\right)\right]}{\left(1 - \dfrac{\underline{K}\cdot\underline{V}}{\omega}\right)} \tag{4.33}$$

At this point, the gravity wave polarization relations have not been utilized so that the solution is valid for a variety of atmospheric waves. The numerator of the solution is simply a nonlinear mapping of the steady state layer profile, n_s. The shape of the layer is distorted further by the amplification factor;

$$\frac{1}{\left(1 - \dfrac{\underline{K}\cdot\underline{V}}{\omega}\right)}$$

If wave induced perturbations are small, equation (4.33) may be simplified. Specifically, if $|\underline{K}\cdot\underline{V}/\omega| << 1$, the layer density response may be approximated by

$$n(\underline{r},t) \simeq \left(1 + \frac{\underline{K}\cdot\underline{V}}{\omega}\right) n_s\left(\underline{r} + \frac{i\underline{V}}{\omega}\right) \tag{4.34}$$

The argument of n_s is perturbed by a sinusoid with the same temporal and spatial dependence as the atmospheric wave responsible for the density perturbations. If the steady state density profile is a function of altitude only, the argument is perturbed only by the vertical component of the wave induced wind. Under this condition, a wave with a period of 180 minutes and a maximum vertical velocity of 1 meter/second (such as some low frequency gravity waves) would perturb the argument of n_s by as much as 1.72 km. Since the sodium layer is typically 15 to 20 km wide and contains large gradients, such a shift in the layer's features would be quite obvious. Lower frequency waves and larger vertical velocities would create larger displacements in the layer's features. It should also be noted that the maximum upward displacement in features occurs one quarter of a wave period after the maximum vertical wind. This is a reasonable result. Features are swept upward by the vertical wind, attaining their maximum height when the upward wind becomes zero. As soon as the vertical wind changes direction (1/4 of a period after the maximum upward wind) the layer features will begin to be swept downward. The undulatory behavior of the sodium layer's topside, bottomside and peaks are consistent with the layer behavior indicated by these arguments. Such periodic oscillation in the structure of the sodium layer has been observed in many lidar data sets collected at the University of Illinois [Richter et al., 1981].

In addition to the perturbation in the argument of n_s, equation (4.34) indicates that the layer density is influenced by the amplification factor, $(1 + \underline{K}\cdot\underline{V}/\omega)$. For low frequency gravity waves, the phase of this amplification factor with respect to the vertical perturbations in layer features gives rise to an interesting effect. It is still assumed that the steady state density profile is a function of altitude only. Using the polarization relations for low frequency gravity waves, the amplification factor may be related to atmospheric density perturbations by noting that

$$\frac{\underline{K}\cdot\underline{V}}{\omega} \simeq \frac{-1}{\gamma - 1} A\exp[i(\omega t - \underline{K}\cdot\underline{r})] \qquad (4.35)$$

where γ is the ratio of specific heats. Further, the atmospheric density perturbations will lag the vertical wind by 1/4 period for low frequency gravity waves. Thus, the amplification factor will lead the vertical wind by 1/4 of a period, i.e., the amplification factor is at a maximum 1/4 of a period after the vertical wind is at a minimum and at a minimum 1/4 of a period after the vertical wind is at a maximum. One quarter of a period after the maximum vertical wind, the largest upward displacement of layer features occurs as does the smallest amplification factor. Conversely, when the layer features are perturbed to their lowest height, the amplification factor reaches a maximum. Obviously, the magnitude of the resultant layer density perturbations at a fixed altitude are very dependent on the local density gradients of the layer. However, the density perturbations below the layer peak will generally be larger than those above the peak as a result of the relative phases of the amplification factor and the perturbation in the argument of n_s.

In addition to the imbalance in the size of density perturbations above and below the layer peak, the layer density perturbations below the peak are 180 degrees out of phase with atmospheric density perturbations. Above the steady state layer peak, these perturbations are in phase. Of course, these are general observations and the specific layer response can only be determined when an exact description of the layer is known. The phase reversal in the layer density response mentioned above is easily explained if a steady state density profile which is symmetric about a single peak is assumed. The atmospheric density perturbation is at a maximum 1/4 of a period after the maximum vertical wind. At the same time, the layer peak reaches its maximum upward displacement. Above the steady state location of the layer peak, this has the effect of enhancing the density of the minor constituent. Below the layer peak, the layer density is depleted as the low density portions of the layer are swept upward by the wind. The net effect is that when the atmospheric density perturbation is at a maximum, the minor constituent density reaches a maximum above and a minimum below the layer peak. A similar argument may be used to show that when the atmospheric density perturbation is at a minimum, the layer density perturbation will be at a minimum above the layer peak and at a maximum below the layer peak. As a result, the density perturbations of the minor constituent are generally 180 degrees out of phase with atmospheric density perturbations below the layer peak and in phase above the layer peak.

Although equation (4.33) is a concise expression for the exact solution of the continuity equation and yields insight into the layer response, it is not necessarily the simplest formulation of the solution to work with. Another form of this solution may be obtained which separates the linear and nonlinear portions of the layer response. This is accomplished by expanding the solution given in equation (4.33) in a Maclaurin series. It comes as no surprise that the results obtained in this manner are identical to the complete perturbation series solution presented in the next section.

4.4.3 THE PERTURBATION SERIES SOLUTION

In order to separate the linear and nonlinear portions of the layer response, a series solution of equation (4.17) is sought which has the following form;

$$n(\underline{r},t) = \sum_{\ell=0}^{\infty} n_\ell = \sum_{\ell=0}^{\infty} P_\ell (\Delta N)^\ell \tag{4.36}$$

As in section 4.4.2, $\Delta N = A\exp(i\omega t - iK\cdot\underline{r})$. This solution is, in fact, the perturbation series solution of equation (4.17). It is apparent that n_1 will be the linear response and n_2 will represent the nonlinear portion of the response associated with a double frequency oscillation in density. In general, the i^{th} term will describe the portion of the layer response associated with density oscillations whose frequency is the i^{th} harmonic of the atmospheric wave.

To determine P_ℓ, equation (4.36) is substituted into (4.17) and terms of equal power in ΔN are collected. This is the same technique used in obtaining the power series solution for the exact layer response (section 4.4.2). Unlike this example, however, the coefficients, P_ℓ, are functions of the position vector, $\underline{r}$. By applying the boundary condition

$$\lim_{\Delta N\to 0} n(\underline{r},t) = n_s(\underline{r}) \tag{4.37}$$

it is determined that $P_0 = n_s(\underline{r})$. The coefficients of higher order terms must satisfy the recursion relation;

$$P_\ell = \left(\frac{\underline{K}\cdot\underline{\beta}}{\omega}\right)\left[P_{\ell-1} + \frac{i}{\ell\underline{K}\cdot\underline{\beta}}\left(\beta_x\frac{\partial P_{\ell-1}}{\partial x} + \beta_z\frac{\partial P_{\ell-1}}{\partial z}\right)\right] \qquad \text{for } \ell \geq 1 \tag{4.38}$$

and the series solution is given by;

$$n(\underline{r},t) = n_s(\underline{r}) + \left(\frac{\underline{K}\cdot\underline{\beta}}{\omega}\right)\sum_{\ell=1}^{\infty}\left[P_{\ell-1} + \frac{i}{\ell\underline{K}\cdot\underline{\beta}}\left(\beta_x\frac{\partial P_{\ell-1}}{\partial x} + \beta_z\frac{\partial P_{\ell-1}}{\partial z}\right)\right](\Delta N)^\ell \tag{4.39}$$

In order to simplify the result, it is assumed that $n_s(\underline{r}) = n_s(z)$; the density profile in the absence of wave activity is a function of altitude only. This is not an unreasonable restriction. Without this restriction on the horizontal variability of n_s, the expression for the series solution becomes quite cumbersome. The simplified result is;

$$n(\underline{r},t) = \sum_{m=0}^{\infty}\sum_{\ell=0}^{m}\left(A\,\frac{\underline{K}\cdot\underline{\beta}}{\omega}\right)^m\left(\frac{i\beta_z}{\underline{K}\cdot\underline{\beta}}\right)^\ell \alpha_{m,\ell}\,\frac{d^\ell n_s(z)}{dz^\ell}\exp[im(\omega t - \underline{K}\cdot\underline{r})] \tag{4.40}$$

where $$\alpha_{m,0} = 1$$

$$\alpha_{m,\ell} = \frac{1}{m!}\,[m\alpha_{m-1,\ell} + \alpha_{m-1,\ell-1}] \qquad \ell \le m$$

$$\alpha_{m,\ell} = 0 \qquad \ell > m$$

Therefore, the first three terms in the series are;

$$n_0(\underline{r},t) = n_s(z) \tag{4.41}$$

$$n_1(\underline{r},t) = \left(A\frac{\underline{K}\cdot\underline{\beta}}{\omega}\right)\left[n_0 + \left(\frac{i\beta_z}{\underline{K}\cdot\underline{\beta}}\right)\frac{dn_s}{dz}\right]\exp[i(\omega t - \underline{K}\cdot\underline{r})] \tag{4.42}$$

$$n_2(\underline{r},t) = \left(A\frac{\underline{K}\cdot\underline{\beta}}{\omega}\right)^2\left[n_0 + \frac{3}{2}\left(\frac{i\beta_z}{\underline{K}\cdot\underline{\beta}}\right)\frac{dn_s}{dz} + \frac{1}{2}\left(\frac{i\beta_z}{\underline{K}\cdot\underline{\beta}}\right)^2\frac{d^2n_s}{dz^2}\right]$$

$$\exp[2i(\omega t - \underline{K}\cdot\underline{r})] \tag{4.43}$$

Note that derivatives of $n_s(z)$ up to the i^{th} order are contained in the i^{th} term.

The polarization relations for gravity waves may now be used to determine the nature of the layer density response to gravity waves. Since low frequency gravity waves are apparently responsible for many of the dynamic features observed in the sodium layer, the polarization relations for low frequency gravity waves [Hines, 1960] are used to relate β_x and β_z to wave induced perturbations in atmospheric density. Using these relations, which are expressed in equations (4.10) and (4.11), it can be shown that;

$$\left(\frac{\underline{K}\cdot\underline{\beta}}{\omega}\right) \simeq \frac{-1}{\gamma - 1} \tag{4.44}$$

$$\left(\frac{i\beta_z}{\underline{K}\cdot\underline{\beta}}\right) \simeq \left(\gamma H + \frac{i}{K_z}\right) \tag{4.45}$$

The linear layer response obtained by utilizing these relation is identical to the linear layer response reported in previous results [Chiu and Ching, 1978; Weinstock, 1978].

$$\frac{n_1}{n_0} \simeq \frac{-A}{\gamma - 1} \left(1 + \frac{\gamma H}{n_s} \frac{dn_s}{dz} \right) \exp[i(\omega t - \underline{K} \cdot \underline{r})] \qquad (4.46)$$

Experimental evidence indicating such a response in atmospheric layers has been reported for the mesospheric sodium layer [Shelton et al., 1980], in $O_2({}'\Sigma)$ airglow measurements [Weinstock, 1978], and in nightglow emissions of the hydroxyl radical [Frederick, 1979].

Several of the characteristic features of the linear layer response are summarized below. The density perturbations in the atmospheric layer associated with the linear response can be substantially larger than the atmospheric density perturbations associated with the gravity wave. This is a result of the advection of density gradients. In general, large density gradients will give rise to large "amplification" factors, i.e., large perturbations in the density of the minor constituent. As a result of the sum in the righthand side of equation (4.46), density perturbations below the layer peak (where dn_s/dz is generally positive) will typically be larger than those above the peak (where dn_s/dz is negative). In addition, a phase reversal in the layer response occurs at the point where $\frac{\gamma H}{n_s} \frac{dn_s}{dz} = -1$. Below this point, atmospheric and sodium density perturbations are 180 degrees out of phase while above this point these density perturbations are in phase. Recall that this type of behavior was deduced by examining the exact solution. Since the nonlinear part of the layer response does not generally approach zero at the point of phase reversal, the layer response will usually be dominated by the nonlinear terms in this region. Evidence of such nonlinearities in the sodium layer response has been reported [Shelton et al., 1980].

4.4.4 SPATIAL POWER SPECTRUM OF THE LINEAR LAYER RESPONSE

The vertical structure associated with the linear layer response complicates the interpretation of lidar data. One of the consequences of the phase reversal in this response is that peaks in the sodium layer will not necessarily be separated by distances equal to the gravity wave's vertical wavelength. The spatial power spectrum will reflect this fact. If it is to be used as an interpretive aid, the effects of the vertical structure of the layer response on the power spectrum must be understood. If only the linear portion of the layer response to gravity waves is included, the sodium layer density may be expressed as;

$$n(\underline{r},t) \simeq n_s(z) - \left(\frac{A}{\gamma - 1}\right)\left[n_s(z) + \gamma H \frac{dn_s(z)}{dz}\right]\cdot\exp[i(\omega t - K_x x - K_z z)] \qquad (4.47)$$

The spatial Fourier transform of this equation is readily found. The power spectrum due to the linear layer response is simply the square of the magnitude of this transform. The transform will be expressed as a function of the vertical spatial frequency, f_z, where $K_z = 2\pi f_z$. The following equations are written as functions of spatial frequency rather than wave number because estimates of the power spectrum calculated from experimental data are traditionally plotted as functions of spatial frequency. The Fourier transform relating the spatial variable, z, to f_z is evaluated yielding the result;

$$N(x,f_z,t) \simeq N_s(f_z) - \left(\frac{A}{\gamma - 1}\right) \exp[i(\omega t - K_x x)]$$

$$\cdot[(1 + i2\pi f_z \gamma H)\, N_s(f_z)] * \delta(f'_z - f_z) \qquad (4.48)$$

or

$$N(x,f_z,t) \simeq N_s(f_z) - \left(\frac{A}{\gamma - 1}\right) \exp[i(\omega t - K_x x)]$$

$$\cdot [1 + i2\pi(f'_z - f_z)\ \gamma H]\ N_s(f'_z - f_z) \qquad (4.49)$$

N and N_s are the Fourier transforms of n and n_s respectively and $f'_z = 1/\lambda_z$ where λ_z is the vertical wavelength of the gravity wave. The transform of the linear portion of the layer response is in the righthand side of each of these equations. The linear response, as expressed in equation (4.46), is the product of a complex exponential, $\exp(i\omega t - iK\cdot\underline{r})$, which describes the time and space dependence of the sinusoidal variations in density and an envelope, $(\frac{-1}{\gamma - 1}(n_s + \gamma H\frac{dn_s}{dz}))$, which determines the vertical structure of the magnitude of the density oscillations. The transform of the linear response is the convolution of the transform of this envelope and the transform of the complex exponential.

The power spectrum is easily found.

$$|N(x,f_z,t)|^2 \simeq |N_s(f_z)|^2 + \left(\frac{A}{\gamma - 1}\right)^2 |(1 + i2\pi(f'_z - f_z)\ \gamma H)\ N_s(f'_z - f_z)|^2$$

$$- \left(\frac{2A}{\gamma - 1}\right) \mathrm{Re}\{\exp[i(\omega t - K_x x)](1 + i2\pi(f'_z - f_z)\ \gamma H)\ N_s^*(f_z)\ N_s(f'_z - f_z)\} \qquad (4.50)$$

In practice, the average spatial periodogram of experimental data is evaluated. In order to make direct comparisons convenient, the average spatial power spectrum (ASPS) is found by averaging equation (4.50) over one period of the gravity wave. The resulting equation is;

$$\mathrm{ASPS} \simeq |N_s(f_z)|^2 + \left(\frac{A}{\gamma - 1}\right)^2 |(1 + i2\pi(f'_z - f_z)\ \gamma H)\ N_s(f'_z - f_z)|^2 \qquad (4.51)$$

This expression is very dependent upon the transform of the steady state layer profile, $N_s(f_z)$. The nature of this dependence may be examined by evaluating a special case.

The steady state sodium layer density profile may often be approximated by a gaussian shape. Thus, it is assumed that

$$n_s(z) = P\exp\left[\frac{-(z - z_0)^2}{2\sigma^2}\right] \tag{4.52}$$

where P is the peak density, z_0 is the altitude of the layer peak and σ is related to the layer width. The ASPS for such a layer becomes;

$$\begin{aligned}\text{ASPS} \simeq 2\pi\sigma^2P^2\Big[&\exp(-4\pi^2\sigma^2f_z^2) + \left(\frac{A}{\gamma - 1}\right)^2 (1 + 4\pi^2(f_z' - f_z)^2\,\gamma^2H^2) \\ &\cdot\exp[-4\pi^2\sigma^2(f_z' - f_z)^2]\Big]\end{aligned} \tag{4.53}$$

The second term in the above equation peaks at

$$f_z = f_z' \pm \frac{1}{2\pi}\sqrt{\frac{1}{\sigma^2} - \frac{1}{\gamma^2H^2}} = f_z' \pm \Delta f_z \tag{4.54}$$

This behavior may be understood by examining equation (4.48). For a gaussian layer, the peaks of $(1 + i2\pi f_z\gamma H)N(f_z)$ occur at $f_z' = \pm\Delta f_z$. These peaks are shifted by the convolution in equation (4.48). A plot of the calculated ASPSs for several values of A and several vertical wavelengths are shown in Figure 4.4. Aside from the lack of a constant noise level, these ASPSs are very similar to the periodograms used to estimate the power spectra of experimental data. One of the unusual consequences of the vertical structure of the layer response is that a local minimum occurs in the ASPS at the spatial frequency corresponding to the vertical wavelength of the gravity wave. At this frequency, the contribution to the ASPS from the linear layer response is approximately $(A/(\gamma - 1))^2$.

(a)

(b)

(c)

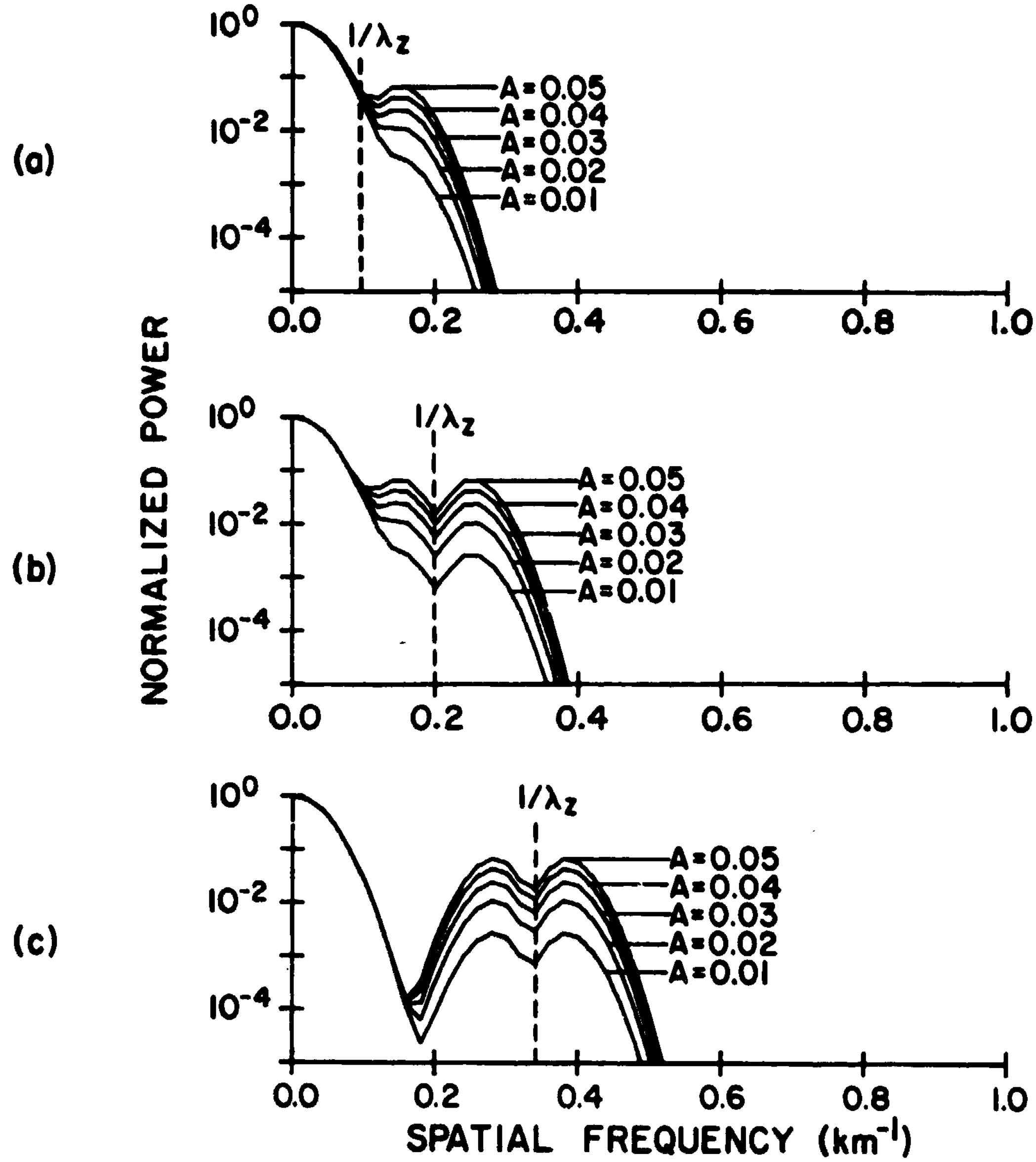

Figure 4.4 Plots of the simulated average spatial power spectra resulting from the linear layer density response to gravity wave perturbations. The wave amplitude is given by *A*. The vertical wavelength of the gravity wave is (a) 10 km, (b) 5 km, and (c) 3 km.

4.4.5 COLUMN ABUNDANCE VARIATIONS

The Fourier transform of the layer response as given in equation (4.49) has another interesting use. By evaluating this expression at $f_z = 0$, the column abundance of the layer may be found. However, high order terms (i.e. nonlinear effects) also contribute to column abundance variations. If the perturbation series solution (equation 4.40) is integrated over the spatial variable, z, an expression for the total column abundance is found.

$$C(x,t) = \mathrm{Re}\left\{\int_0^\infty dz\, n(\underline{r},t)\right\} = \mathrm{Re}\left\{\int_0^\infty dz \sum_{i=0}^{\infty} n_i(\underline{r},t)\right\} \tag{4.55}$$

Because $n(\underline{r},t)$ is zero for $z < 0$, the lower limit of integration may be extended to $-\infty$. The resulting expression for column abundance is;

$$C(x,t) = \mathrm{Re}\left\{\sum_{m=0}^{\infty} C_m(x,t)\right\} = \mathrm{Re}\left\{\sum_{m=0}^{\infty} \sum_{\ell=0}^{m} \left(A\frac{\underline{K}\cdot\underline{\beta}}{\omega}\right)^m \right.$$

$$\left. \cdot\left(\frac{-\beta_z K_z}{\underline{K}\cdot\underline{\beta}}\right)^{\ell} \alpha_{m,\ell}\, N_s(mK_z)\, \exp[im(\omega t - K_x x)] \right\} \tag{4.56}$$

The m^{th} order term is responsible for variations in column abundance with a temporal frequency of $m\omega$. The linear term ($m = 1$) dominates the variations in column abundance. This becomes obvious when the magnitudes of the first several terms in this series are examined. Recall that $K_z = 2\pi f_z$.

$$C_0 = N_s(f_z = 0) \tag{4.57}$$

$$C_1 = -\left(\frac{A}{\gamma - 1}\right)(1 + i2\pi f_z'\gamma H)\, N_s(f_z = f_z') \tag{4.58}$$

$$C_2 = \left(\frac{A}{\gamma - 1}\right)^2 (1 - 2\pi^2 f_z'^2\gamma^2 H^2 + i3\pi f_z'\gamma H)\, N_s(f_z = 2f_z') \tag{4.59}$$

The gravity wave polarization relations have been used to obtain the above expressions. The factors responsible for the rapid decrease in the magnitude of C_m with increasing m are the dependence of C_m on $(A/(\gamma - 1))^m$ and the value of N_s at $f_z = mf_z'$. The magnitude of the gravity wave, A, is quite small so that A^m rapidly decreases with increasing m. Typically, N_s falls off rapidly with increasing f_z. For example, if n_s is gaussian (as given in equation (4.52)), then

$$N_s(f_z) = \sqrt{2\pi}\ \sigma P \exp[-2\pi^2\sigma^2 f_z^2] \exp[-i2\pi f_z z_0] \qquad (4.60)$$

As a result, the magnitude of C_m decreases with increasing m at the approximate rate of

$$\left(\frac{A}{\gamma - 1}\right)^m \exp[-2\pi^2\sigma^2(mf_z')^2] \qquad (4.61)$$

due to these factors. This decrease is opposed, to some extent, by an increase in the size of the coefficient of $N_s(f_z = mf_z')$ in the expression for C_m (equation 4.56)).

Because the magnitude of the m^{th} term, C_m, decreases rapidly as m increases, the column abundance is usually described adequately by the first few terms in equation (4.56). As a result, the approximate column abundance is obtained by utilizing only the first three terms from this equation.

$$C(x,t) \doteq \mathrm{Re}\{C_0 + C_1 + C_2\} \qquad (4.62)$$

It is evident that $C(x,t)$ varies sinusoidally about $\mathrm{Re}\{N_s(0)\}$. For a gaussian layer given by equation (4.52) the column abundance becomes;

$$\begin{aligned} C(x,t) \doteq \sqrt{2\pi}\ \sigma P\Bigg[1 - &\left(\frac{A}{\gamma - 1}\right) \exp[-2\pi^2\sigma^2 f_z'^2] \\ &\cdot(1 + 4\pi^2 f_z'^2\gamma^2 H^2)^{1/2} \cos(\omega t - K_x x + \tan^{-1}(2\pi f_z'\gamma H) - 2\pi f_z' z_0) \\ &+ \left(\frac{A}{\gamma - 1}\right)^2 \exp[-8\pi^2\sigma^2 f_z'^2][(1 - 2\pi^2 f_z'^2\gamma^2 H^2)^2 + 9\pi^2 f_z'^2\gamma^2 H^2]^{1/2} \\ &\cos\left(2\omega t - 2K_x x + \tan^{-1}\left(\frac{3\pi f_z'\gamma H}{1 - 2\pi^2 f_z'^2\gamma^2 H^2}\right) - 4\pi f_z' z_0\right)\Bigg] \end{aligned} \qquad (4.63)$$

This expression contains the sum of three terms; a constant (the zero order term), a term with a temporal frequency of ω (the first order term), and a term with a temporal frequency of 2ω (the second order term). Variations in column abundance due to the linear layer response are associated with the first order term. The magnitude of the linear variation in column abundance normalized by the average column abundance is given by;

$$\Delta C_1 = \frac{A}{\gamma - 1} \exp[-2\pi^2\sigma^2 f_z'^2](1 + 4\pi^2 f_z'^2 \gamma^2 H^2)^{1/2} \qquad (4.64)$$

ΔC_1 is the magnitude of the normalized variation in $C(x,t)$ due to the linear layer response about its mean value. Figure 4.5 shows how the ratio of ΔC_1 to A varies with λ_z and σ. For a gaussian layer, the largest column abundance variations occur when $f_z' = \frac{1}{2\pi}\left(\frac{1}{\sigma^2} - \frac{1}{\gamma^2 H^2}\right)^{\frac{1}{2}}$. At this point, the ratio of ΔC to A is approximately $0.6065 \cdot \gamma H/(\sigma(\gamma - 1))$. If $\sigma = 3$, this corresponds to a gravity wave with a vertical wavelength of 19.8 km and column abundance variations whose magnitude is roughly 5.2 times the magnitude of the atmospheric density variations. It is clear from Figure 4.5 that large variations in column abundance will be evident when the layer is narrow (i.e. σ is small).

The magnitude of the column abundance variations associated with the second order term in the layer response (equation 4.59) for a gaussian layer are

$$\Delta C_2 = \left(\frac{A}{\gamma - 1}\right)^2 \exp[-8\pi^2\sigma^2 f_z'^2][(1 - 2\pi^2 f_z'^2 \gamma^2 H^2)^2 + 9\pi^2 f_z'^2 \gamma^2 H^2]^{1/2} \qquad (4.65)$$

Figure 4.6 shows how the ratio of ΔC_2 to A^2 varies with σ and λ_z. Although ΔC_2 is usually much smaller than ΔC_1, for large wave amplitudes and vertical wavelengths, nonlinearities become more important. Figure 4.7 shows the maximum wave amplitude, A, as a function of λ_z and σ for which $\Delta C_1 = \Delta C_2$. It is

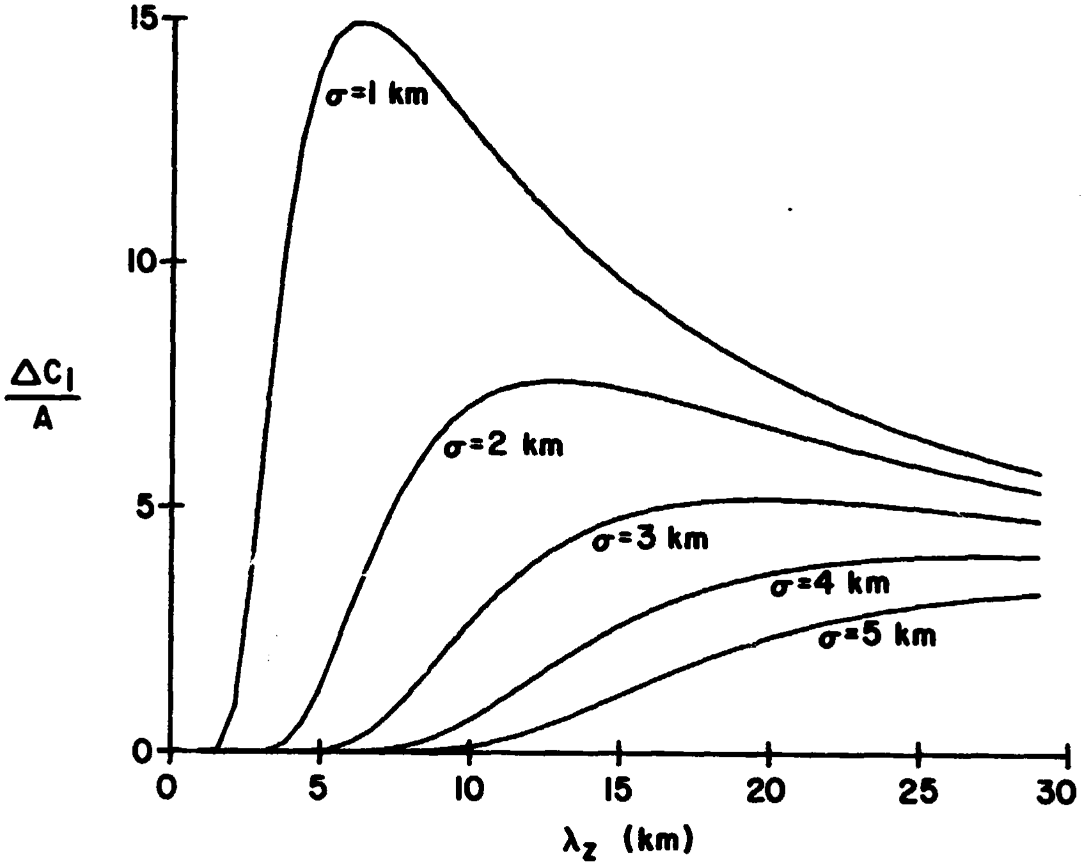

Figure 4.5 Plots of the ratio of the normalized perturbation in column abundance due to the linear layer response (ΔC_1) to the wave amplitude (A). A gaussian layer with width σ has been assumed.

C-2

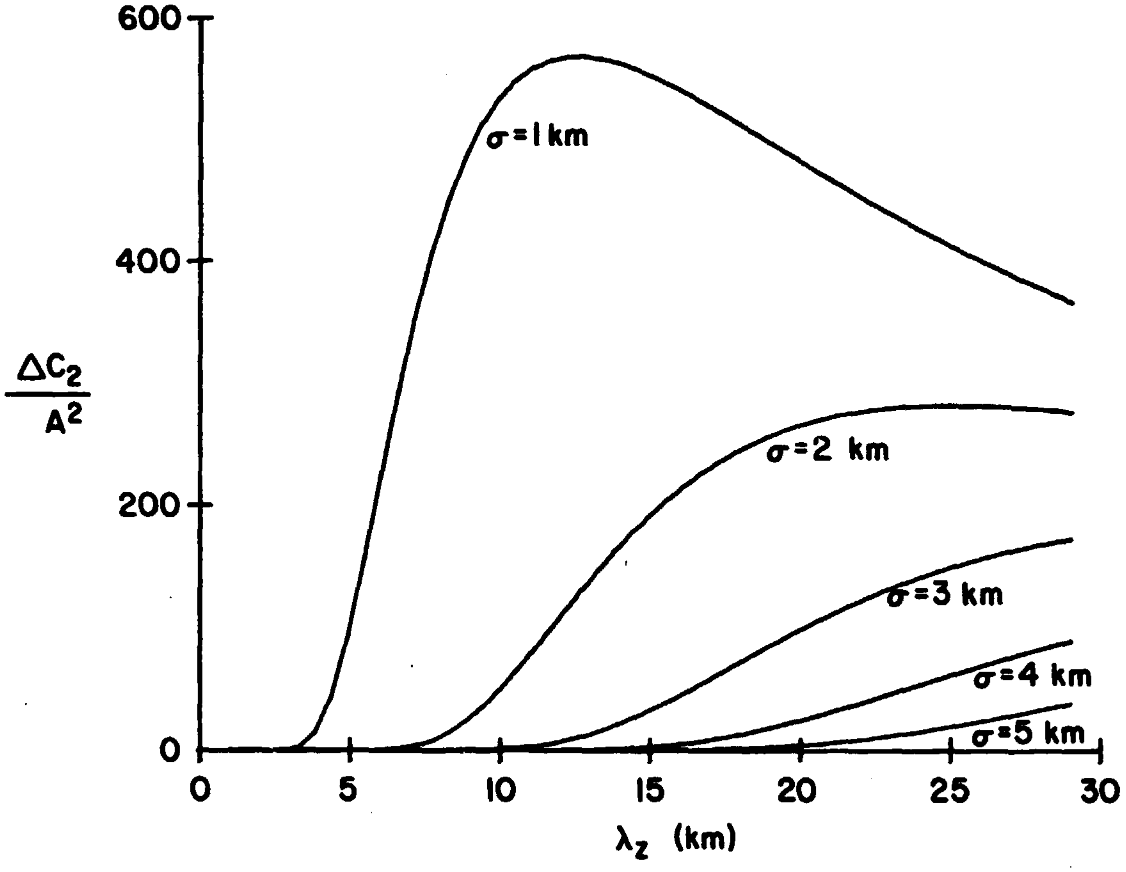

Figure 4.6 Plots of the ratio of the normalized perturbation in column abundance due to the second order layer response (ΔC_2) to the wave amplitude squared (A^2). A gaussian layer with width σ has been assumed.

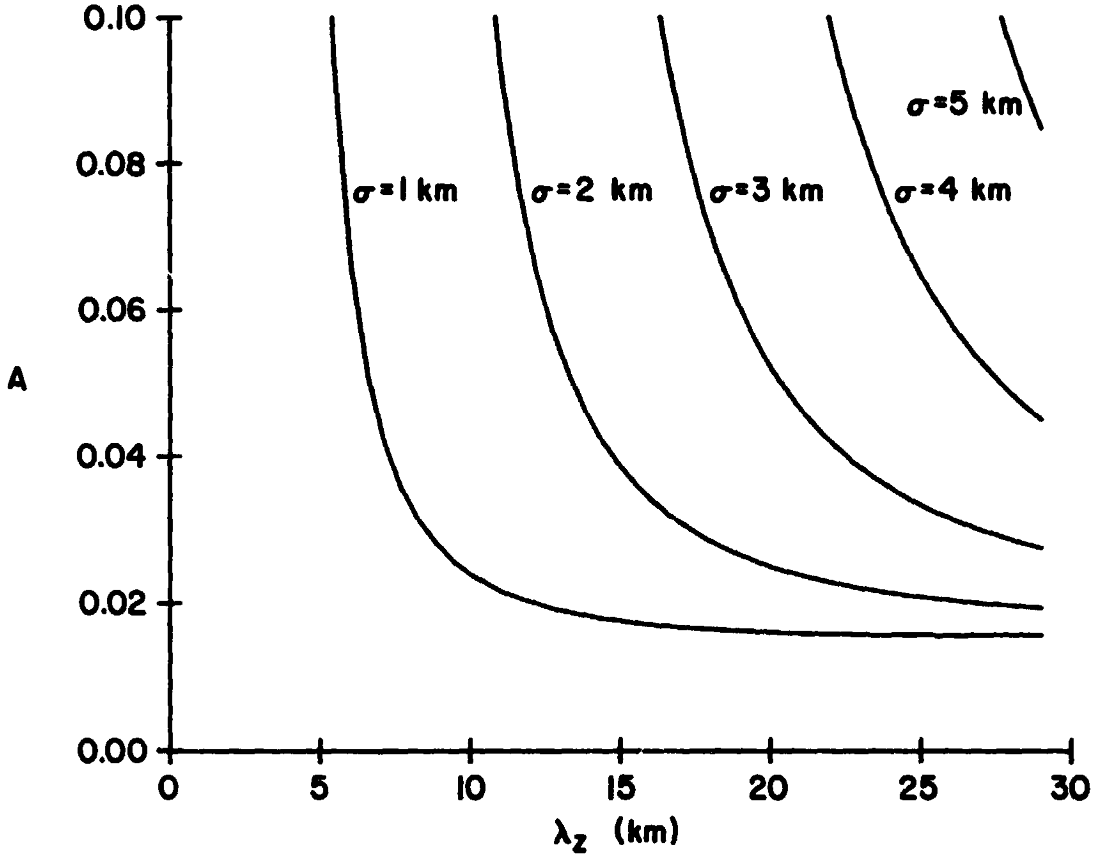

Figure 4.7 The wave amplitude (A) for which the linear and second order perturbations in column abundance are equal. A gaussian layer with width σ has been assumed.

clear that ΔC_2 can safely be neglected for $\sigma \geq 3$ km and $\lambda_z \leq 15$ km.

Because of the presence of high order terms in equation (4.56), column abundance variations with temporal periods less than the period of the gravity wave may add significantly to $C(z,t)$. As is apparent from equation (4.63), the relative magnitudes and phases of these nonlinear terms are very dependent on the layer shape and the vertical wavelength and amplitude of the gravity wave. To illustrate, the percent column abundance variations due to C_1 and C_2 for a gaussian layer are plotted in Figure 4.8. As the layer becomes narrow and as the wave amplitude increases, the relative contribution of the first nonlinear term, C_2, increases.

4.4.6 NONLINEAR NATURE OF THE LAYER RESPONSE

The degree to which the sodium layer response is nonlinear depends upon several factors. Since the layer density response is highly dependent on the density gradients occuring in the layer, the steady state layer density profile becomes very important. Large density gradients encourage nonlinearities in the layer response. Two other important factors are the amplitude and the vertical wavelength of the gravity wave inducing the density perturbations. The degree to which these two factors influence the nonlinear nature of the layer response has been investigated. Recall that the polarization relations for low frequency gravity waves are being used. Since the sodium layer shape can often be approximated by a gaussian function, this shape was used as the steady state sodium density profile for simulations in which the gravity wave amplitude and vertical wavelength were varied. In each case, a gaussian density profile centered at 90 km with $\sigma = 3$ km was assumed. The dependence of the total RMS error on vertical wavelength and wave

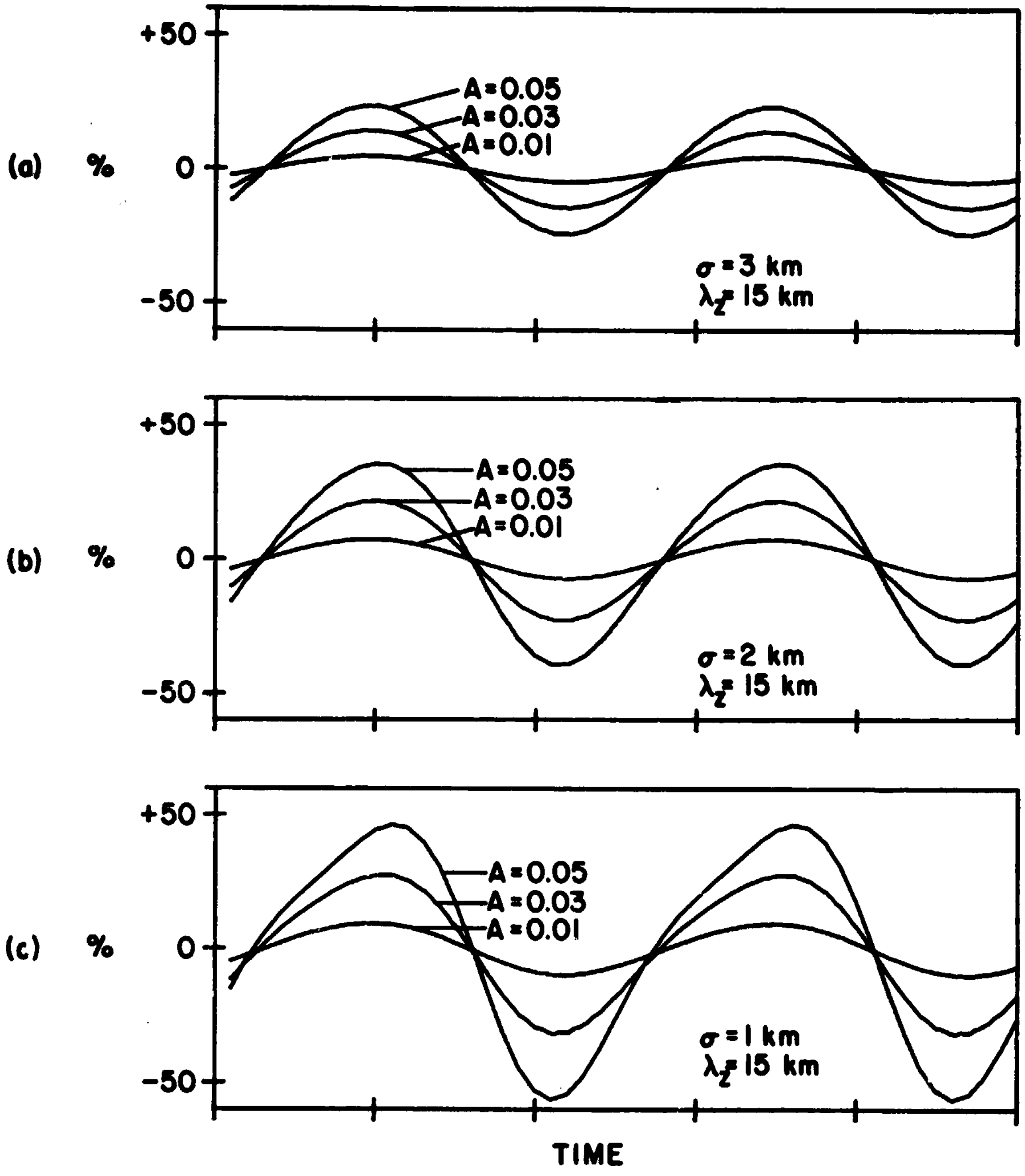

Figure 4.8 The percent variations in sodium column abundance due to linear and second order density perturbations. The variations are plotted for 2 periods of the gravity wave. A gaussian layer with width σ has been assumed. The dependence of $\Delta C_1 + \Delta C_2$ on *A* and σ is illustrated.

amplitude is given in Figure 4.9. Wave amplitudes are given by the peak percent atmospheric density variations associated with the wave propagation. The total RMS error was calculated by taking the square root of the ratio of the integrated, squared nonlinear layer density response and the integrated, squared total layer density response as indicated in the Figure. Equation (4.33) was utilized to compute the total layer response and the nonlinear layer response was obtained by subtracting the linear response from this. The time integrals were performed over one period of the gravity wave, and the limits of the spatial integral were 70 and 110 km. Outside of this altitude range the density perturbations are negligibly small. If the layer response were completely linear, the total RMS error would be 0%. Similarly, if the layer response were completely nonlinear, the total RMS error would be 100%. Figure 4.4 indicates that the degree of nonlinearity is only slightly sensitive to vertical wavelength, but very sensitive to wave amplitude for gaussian steady state layers. Even for gravity waves which create only 5% peak atmospheric density variations, at least 27% total RMS error will be incurred by assuming a strictly linear response.

As shown before, the nonlinear portion of the layer response will tend to dominate in restricted regions of the layer. Figure 4.10 shows an RMS error analogous to that of Figure 4.9. In this case the altitude integral is not performed and the resulting error expression is a function of altitude, wave amplitude, and vertical wavelength. Since the errors are relatively insensitive to changes in vertical wavelength, a vertical wavelength of 10 km is assumed and the simulation results are displayed as a function of altitude and wave amplitude only.

$$\text{TOTAL RMS ERROR} = \left[\frac{\iint dz\, dt \left(\sum_{i=2}^{\infty} n_i \right)^2}{\iint dz\, dt \left(\sum_{i=1}^{\infty} n_i \right)^2} \right]^{\frac{1}{2}}$$

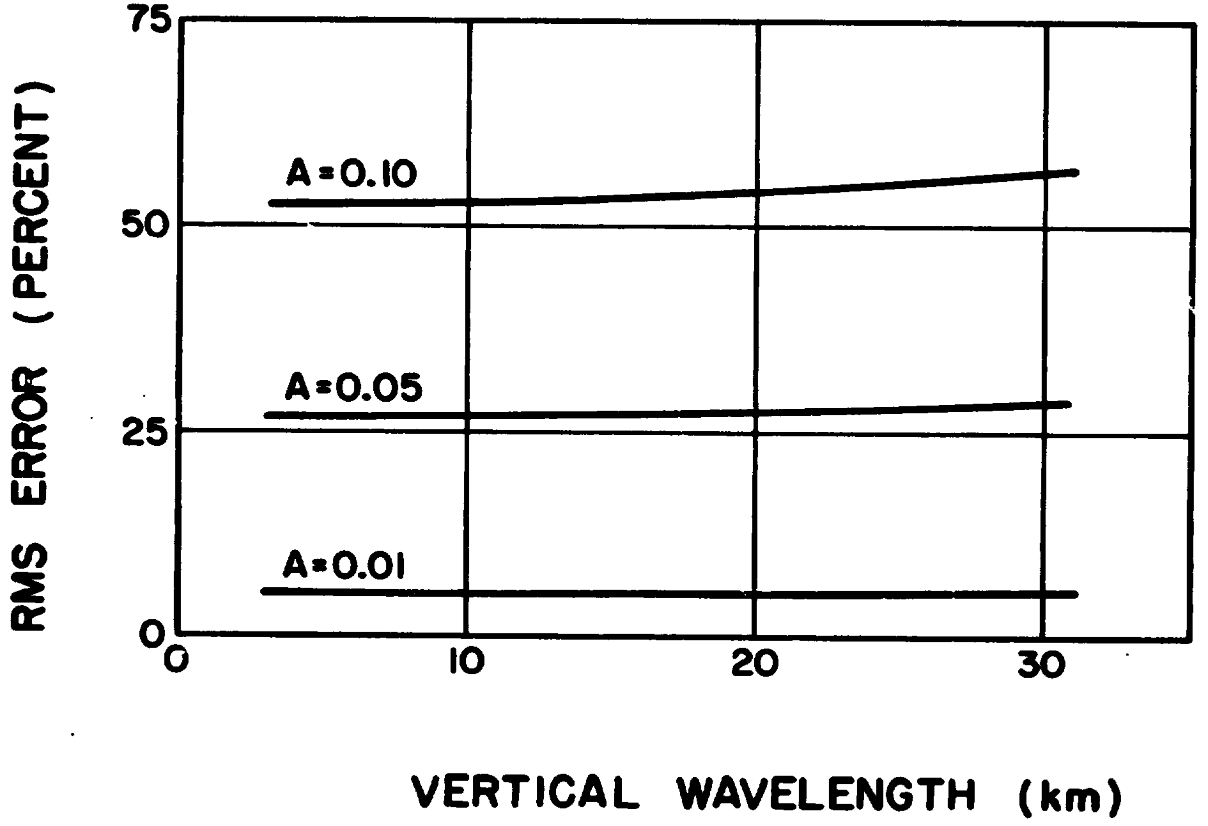

Figure 4.9 Total RMS error as a function of vertical wavelength, (λ_z), and wave amplitude, (A). A gaussian layer with $\sigma = 3$ km has been assumed.

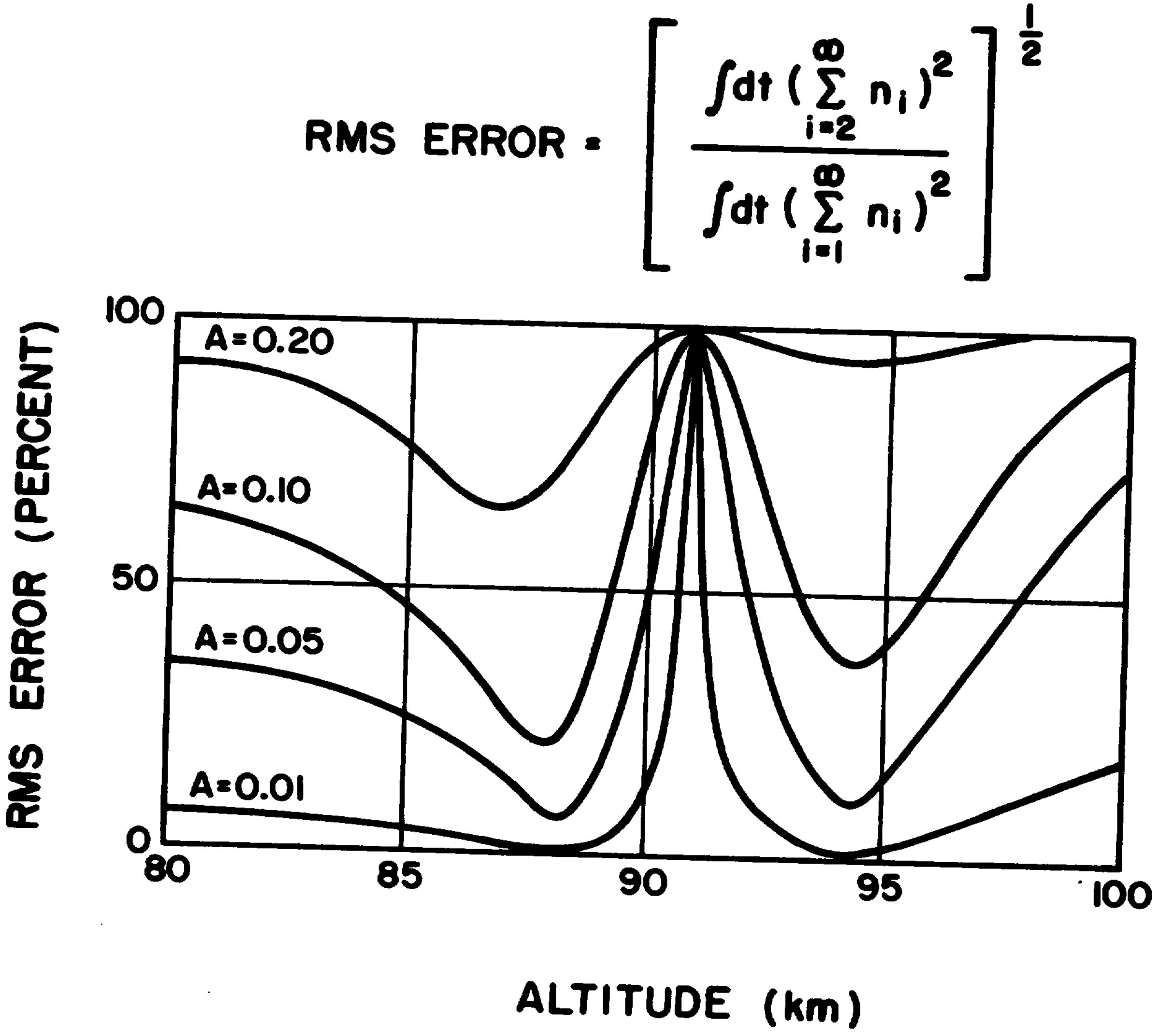

Figure 4.10 RMS error as a function of altitude and wave amplitude, (*A*), for a vertical wavelength of 10 km.

Figure 4.10 shows that the RMS error peaks to 100% at 90.92 km. This corresponds to the point of phase reversal in the linear layer response, i.e. the point where the linear layer response is zero. In general, the RMS error is smaller below than above the layer peak (which occurs at 90 km) because the linear response is larger below the layer peak. The RMS error approaches 100% as the distance from the layer peak increases. The nonlinear terms in the perturbation series solution dominate the linear term in these regions. Note, however, that the sodium density perturbations become very small at these extremes where the layer is quite tenuous. Figure 4.11 illustrates the size of density perturbations associated with n_1, n_2 and n_3. The envelope of perturbations for each term has been plotted. The gravity wave amplitude was chosen to be consistent with 5% peak to peak variations in atmospheric density. It is quite evident that the second order term, n_2, dominates the layer response in the 90.3 to 91.2 km region. Note, however, that the third order term, n_3, is larger than the second order term at times.

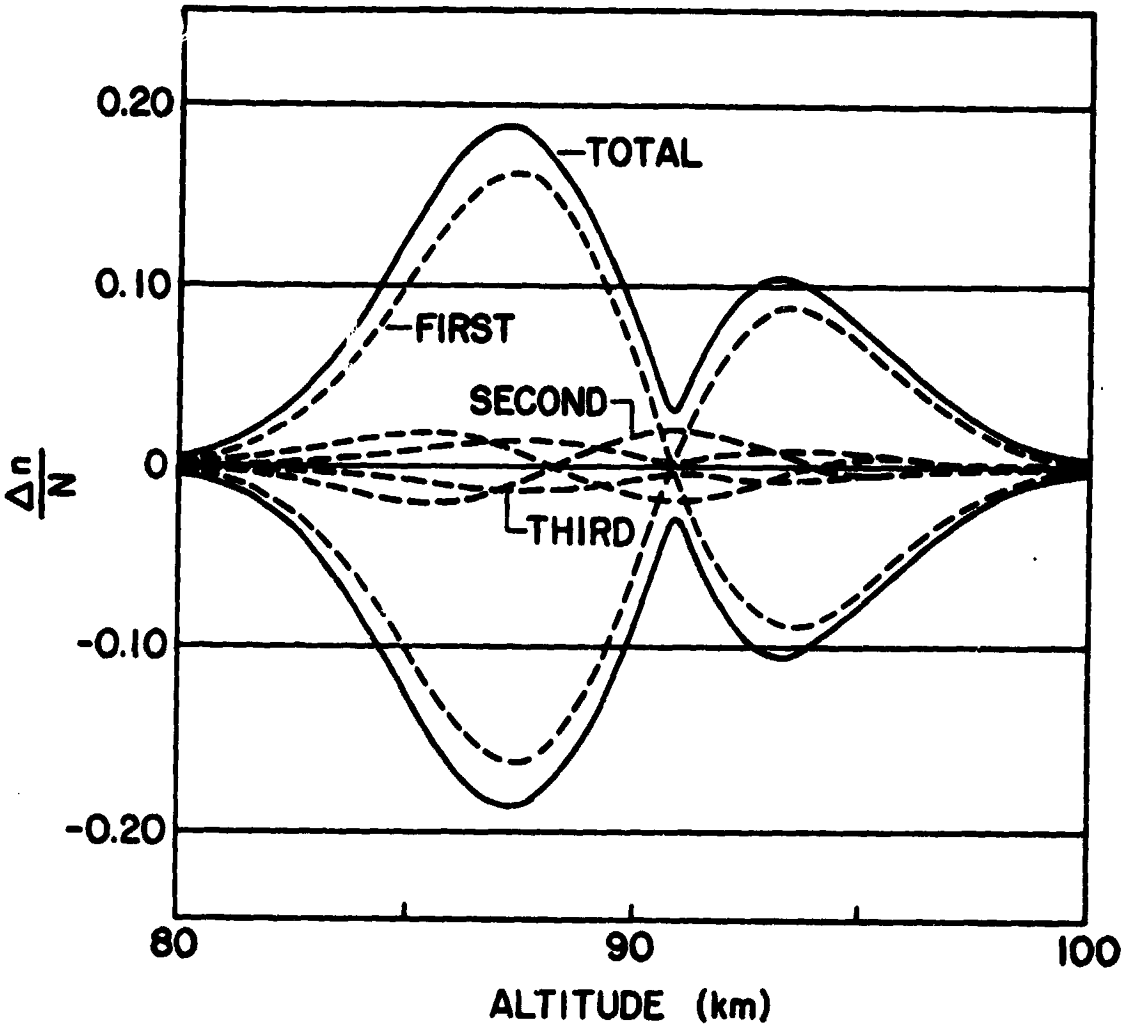

Figure 4.11 Predicted envelope of normalized density perturbations due to the first three terms of the perturbation series solution. A gaussian layer centered at 90 km with $\sigma = 3$ km and a wave amplitude of 3% ($A = 0.03$) have been assumed.

5. SODIUM LIDAR OBSERVATIONS AT URBANA, ILLINOIS

5.1 BACKGROUND INFORMATION

Evidence of wave activity is often found in lidar observations of the sodium layer made at Urbana, Illinois. These observations are made with the lidar system pointing at zenith. Because low frequency atmospheric waves may be responsible for many of the observed layer dynamics, data sets spanning long observation periods are essential. In some data, density oscillations with periods as long as 8 and 12 hours are present. Extended observation periods are necessary to detect these low frequency oscillations. The length of the observation periods varied with each data set. The period of observation as well as other pertinent parameters are summarized in Table 5.1. The *'s indicate that data was collected with the original laser. If no * is present, the Candela laser was utilized. Not all data were calibrated. In some cases, overloading distorted all Rayleigh scattering making calibration impossible. In each case where calibration could be achieved, the time variations in column abundance are presented. After March 11-12, 1981 the overloading problem was permanently solved by gating the PMT. This was accomplished by electronically switching the first PMT dynode voltage as discussed in Chapter 2. As a result, all data collected after March 11-12, 1981 have been calibrated.

5.2 DATA COLLECTED WITH THE ORIGINAL LASER

5.2.1 OCTOBER 13-14, 1979

On the evening of October 13-14, 1979 the lidar system operated for almost 3 hours collecting 49 spatial profiles at 3 minute intervals. During this

TABLE 5.1 SUMMARY OF OBSERVATIONS

Date	Time	Number of Spatial Profiles	Shots per Profile	Laser Pulse Rep Rate (s^{-1})	Calibrated
Oct 13-14, 1979*	2255-0138 CDST	49	50	0.5	No
Oct 28-29, 1979*	2153-0343 CST	71	50	0.5	No
Dec 13-14, 1979*	2011-0106 CST	58	50	0.5	No
Feb 24-25, 1981	2155-0552 CST	97	500	4.0	Yes
Mar 11-12, 1981	2357-0530 CST	68	500	4.0	Yes
Mar 12-13, 1981	2115-0532 CST	103	500	4.0	Yes
Mar 13-14, 1981	1955-0529 CST	118	500	4.0	Yes
Mar 16-17, 1981	1855-0525 CST	128	500	4.0	Yes

period 5 profiles were lost due to equipment failure. These profiles were replaced with estimates obtained by applying a linear interpolation procedure to the remaining profiles. The Average Temporal Periodogram (ATP) is shown in Figure 5.1. It was discovered that the ATP was only slightly affected by leaving the 5 interpolated profiles out entirely. This indicated that no significant error was introduced by using interpolated data to replace the missing profiles.

The shot noise floor in the ATP is 10 dB below the peak at 0.0083 min^{-1}. This peak corresponds to a temporal period of roughly 120 minutes. Recall that the low frequency portion of the ATP is distorted somewhat by the effects of windowing. It is clear, however, that the dominant temporal variations in sodium density have long periods. Because this data set is fairly short, the spectral resolution of the ATP is not very great. The first null in the DFT of the window occurs at 0.012 min^{-1}. As a result, there is significant distortion at frequencies lower than this. The nature of the distortion is described by equation (3.8). In addition, the convolutional smearing of the ATP, as described by equation (3.8), is fairly severe. Although fine detail is obscured by this smearing, a cutoff for the temporal filter may still be chosen from the ATP. In this case the shot noise level dominates the ATP at frequencies greater than 0.024 min^{-1}. Because the passband of the temporal filter is not flat, a cutoff at 0.0444 min^{-1} was chosen. This insured that the gradual rolloff of the filter passband did not significantly alter the signal spectrum below 0.024 min^{-1}.

The Average Spatial Periodogram (ASP) of the temporally filtered data is shown in Figure 5.2. There is a significant amount of energy at the spatial frequencies 0.166 and 0.255 km^{-1}. At these points, the value of the ASP is

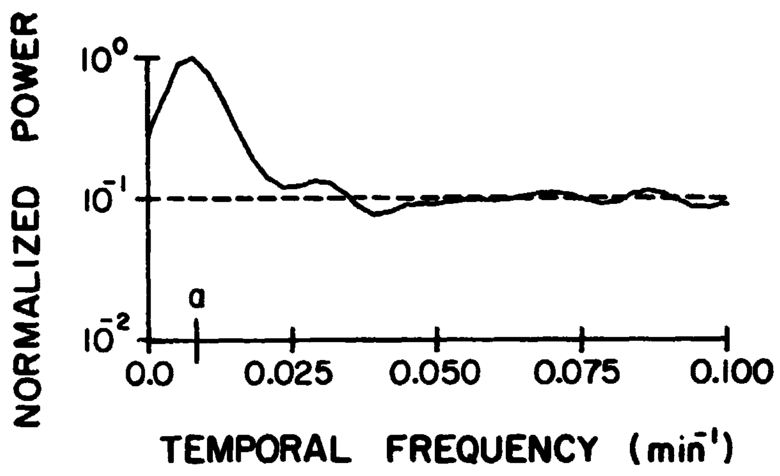

Figure 5.1 Plot of the normalized average temporal periodogram of data collected on October 13-14, 1979. The temporal frequency associated with the gravity wave (0.0083 min^{-1}) is indicated at a.

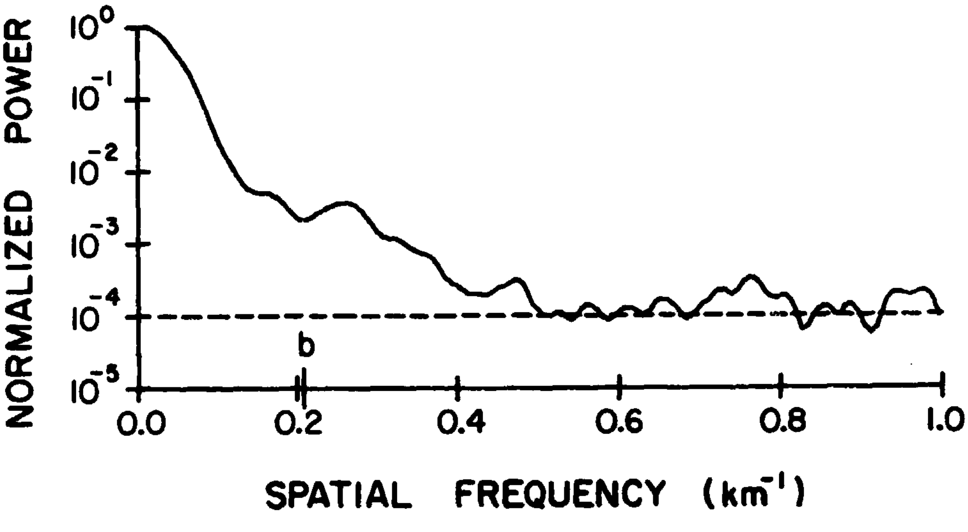

Figure 5.2 Plot of the normalized average spatial periodogram of temporally filtered data collected on October 13-14, 1979. The spatial frequency associated with the gravity wave (0.21 km^{-1}) is indicated at b.

about 22 dB less than the peak value. It is clear, therefore, that features with vertical wavelengths of 3.9 and 6.0 km are present. This ASP is quite similar to the simulated power spectrum plotted in Figure 4.4(b). Taking into account the nature of the linear layer response as developed in Chapter 4, it appears that a gravity wave with a vertical wavelength of λ_z is responsible for these spectral peaks, where $1/\lambda_z = .5(0.255+0.166)$ km^{-1}. The amplitude of this wave may be estimated by noting that the magnitude of the periodogram at $f_z = 1/\lambda_z$ is roughly 3.1×10^{-3} and, therefore, the amplitude of the gravity wave is approximately $(\gamma-1)\sqrt{3.1 \times 10^{-3}}$. Thus, a gravity wave with a vertical wavelength of roughly 4.7 km associated with 4% peak to peak variations in atmospheric density may be present. Since the shot noise level dominates the ASP for frequencies greater than 0.5 km^{-1}, a spatial filter cutoff at this frequency was chosen. This filter was applied to the temporally filtered data to yield the final two-dimensionally filtered data.

A plot of the spatial variations in estimates of the sodium density is contained in Figure 5.3. The layer is fairly narrow; it does not extend below 83 km nor above 102 km. Further, the main layer peak gradually moves from 90 km at 2330 to 88 km at 0112 CST. The peak initially located at 87 km moves steadily downward with a velocity of 0.64 m/s. Although the relative amplitudes of the layer features above 90 km change, it is more difficult to discern the same consistent motions above the layer peak. The diagonal lines drawn in this figure indicate the apparent phase progression of the wavelike features. These lines are separated vertically by the previously deduced value of 4.7 km. Below 90 km peaks in sodium density lie on the lines. Above 90 km, these peaks become valleys. The valleys appear to share the peaks' downward velocity of 0.64 m/s. Note that the peaks below 90 km are more

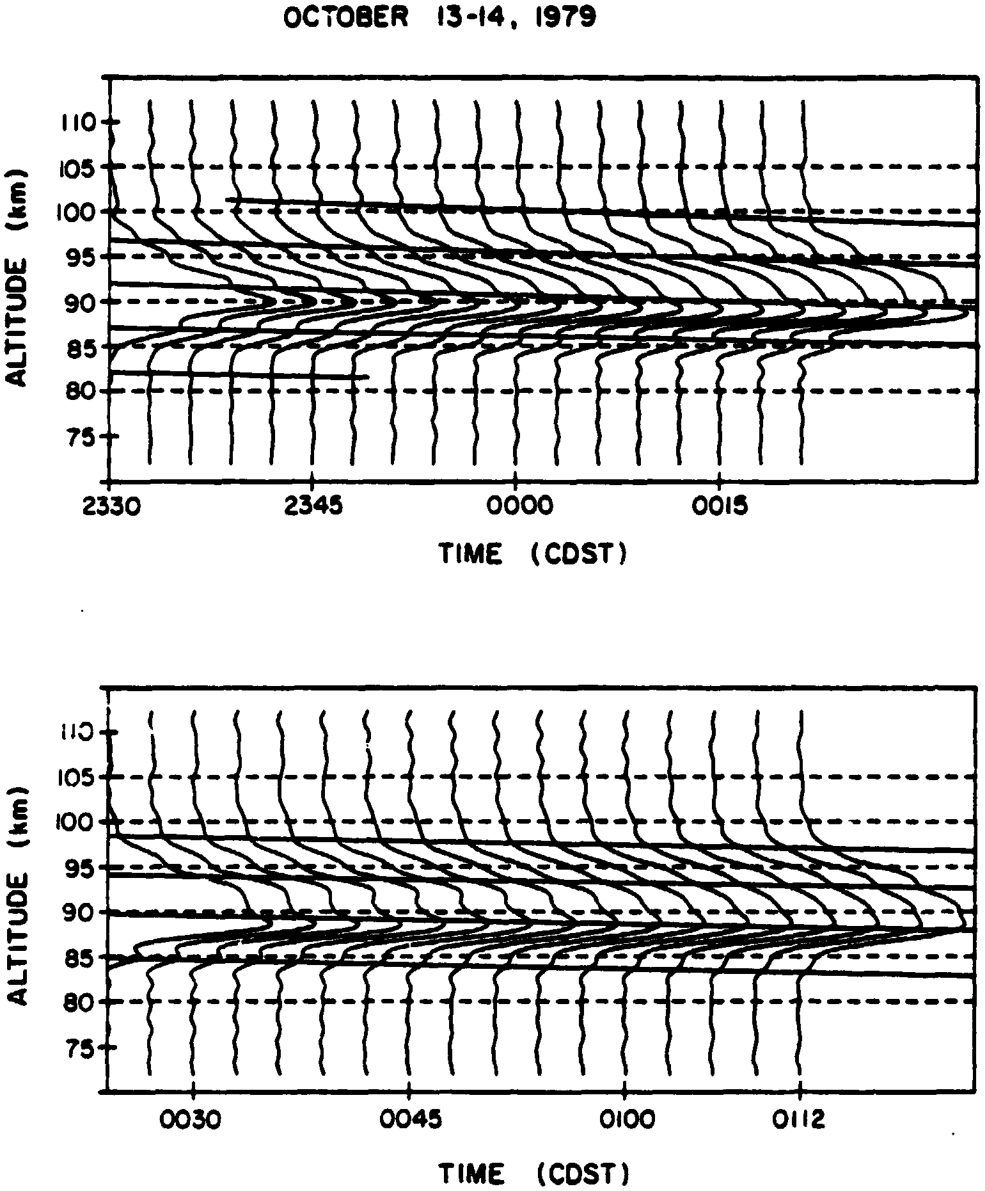

Figure 5.3 Time history of the estimated altitude profiles of sodium density observed on October 13-14, 1979. The spatial and temporal filter cutoffs were 0.5 km^{-1} and 0.044 min^{-1}, respectively. The diagonal lines indicate the apparent phase progression.

pronounced than the valleys above 90 km. It appears that density perturbations below the layer peak are greater than those above the peak. This change in the magnitude of wavelike features and the observed phase reversal near the layer peak are characteristic of a layer response to gravity waves.

Another way of displaying sodium density variations is shown in Figure 5.4. The temporal variations in sodium density about their means at specific altitudes have been plotted. Each of these temporal profiles is then normalized so that the peak to peak variations are equal at each altitude. A downward phase progression in the density variations below 90 km is evident. Associated with this wave motion is a 120 minute period and a 4.8 km vertical wavelength. The wavelength is consistent with the ASP and the downward phase velocity matches the velocity of the layer features observed in the spatial profiles of sodium density. A gravity wave with this temporal period and vertical wavelength would have a horizontal wavelength of approximately 120 km. At an altitude of 89.1 km, a double frequency oscillation with a period of 60 minutes is noticeable. This is consistent with the prediction that nonlinearities should be present in the layer response, particularly near the layer peak. Above 90 km, these periodic fluctuations in sodium density are no longer as apparent. Instead, a gradual decrease in density is observed. This may be caused by temporal changes in the steady state sodium profile or it may be a layer response to atmospheric waves of much lower frequencies than can be observed in this short data set.

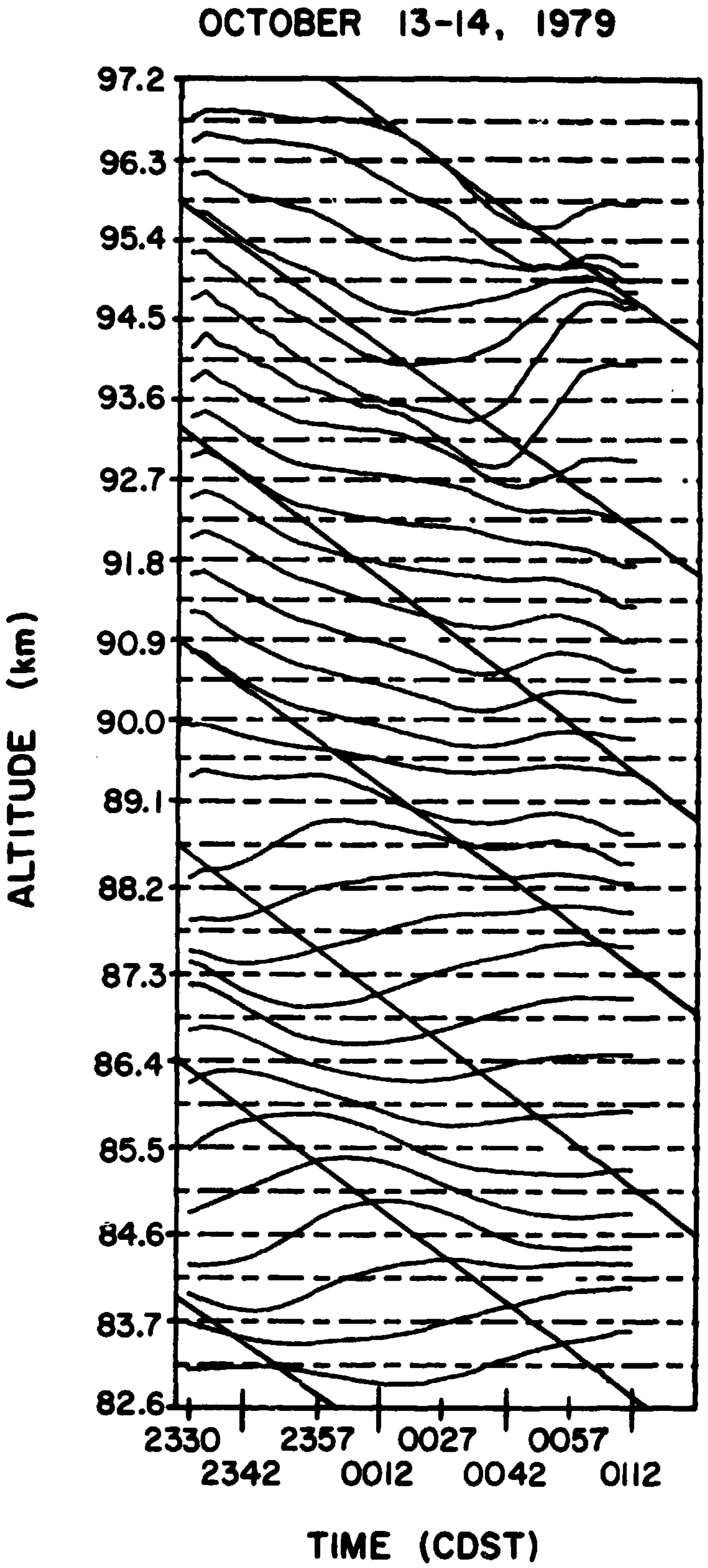

Figure 5.4 Plot of the temporal variations in sodium density observed on October 13-14, 1979. The spatial and temporal filter cutoffs were 0.5 km^{-1} and 0.044 min^{-1}, respectively. The diagonal lines indicate the apparent phase progression.

5.2.2 OCTOBER 28-29, 1979

The lidar system operated for approximately 6 hours on the evening of October 28-29, 1979. 71 spatial profiles were collected at intervals of 5 minutes. The ATP for these data is shown in Figure 5.5. The effects of the temporal window on this ATP have been discussed in Chapter 3. Two distinct peaks near 0.0059 min^{-1} and 0.0118 min^{-1} are obvious. These frequencies correspond to temporal periods of 170 and 85 minutes, respectively. The fact that the second frequency is twice the first suggests that nonlinearities in the layer response to wave activity may be observable. A temporal filter with cutoff at 0.033 min^{-1} was applied to the photocount data. The ASP of the temporally filtered data is shown in Figure 5.6. A single large sidelobe is present. If this sidelobe is attributed to the layer response to a gravity wave, it would appear that the vertical wavelength of this wave is greater than or equal to the wavelength associated with the local minimum in the ASP at 0.102 km^{-1}. Thus, it is probable that the vertical wavelength of the wave is greater than 9.8 km. The portion of the ASP due to the steady state layer profile dominates the portion of the ASP resulting from the layer response to waves since the latter is confined to small spatial frequencies. As a result, the exact vertical wavelength cannot be determined from an examination of the ASP. This is apparent in the simulated power spectrum shown in Figure 4.4(a). However, the ASP is used to select a spatial filter cutoff at 0.44 km^{-1}.

Two-dimensionally filtered spatial profiles are presented in Figure 5.7. In order to conserve space, estimates of the spatial variations in sodium density are plotted at 15 minute intervals. In addition, a three dimensional plot of these data is presented in Figure 5.8. Below the layer peak, which occurs near 90 km, a great deal of activity is present. The peak, which is initially located near 88 km, moves down to 84 km over a period of 4.25 hours.

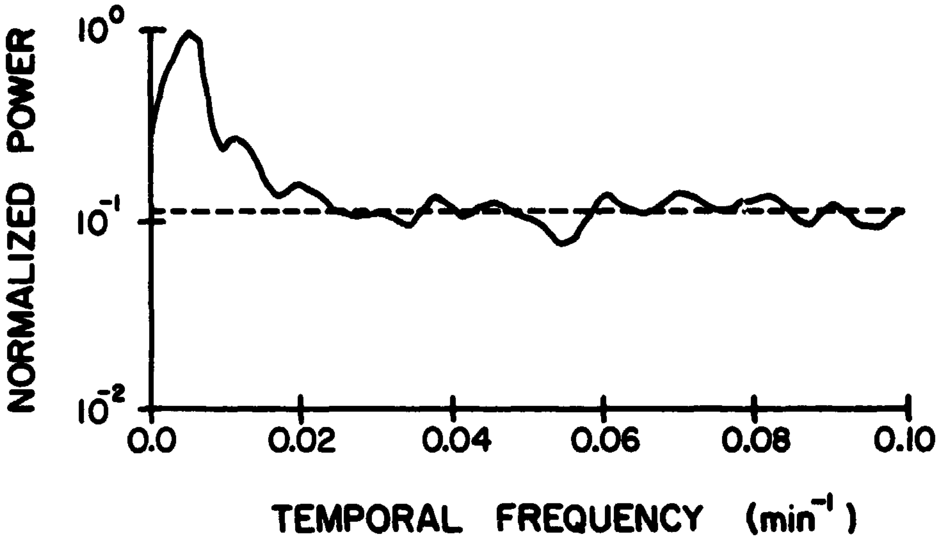

Figure 5.5 Plot of the normalized average temporal periodogram of data collected on October 28-29, 1979.

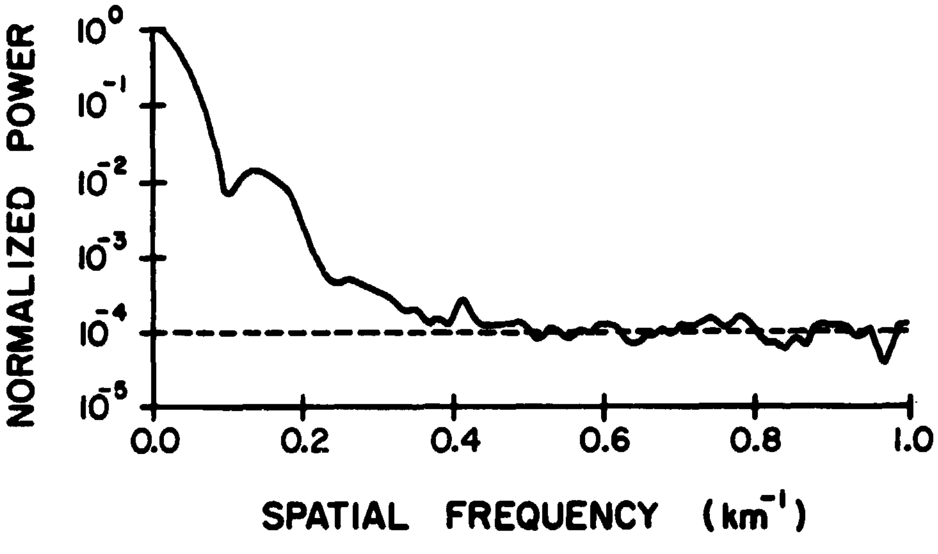

Figure 5.6 Plot of the normalized average spatial periodogram of temporally filtered data collected on October 28-29, 1979.

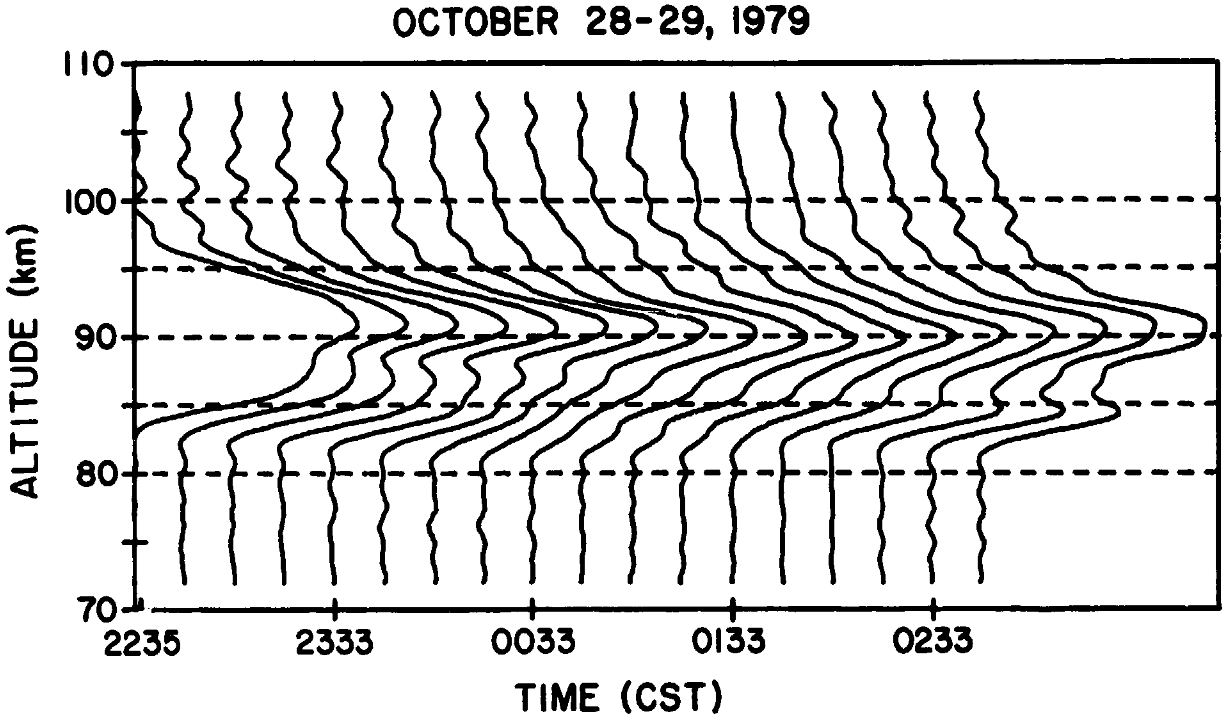

Figure 5.7 Time history of the estimated altitude profiles of sodium density observed on October 28-29, 1979. The spatial and temporal filter cutoffs were 0.44 km^{-1} and 0.033 min^{-1}, respectively. Profiles are plotted at 15 minute intervals.

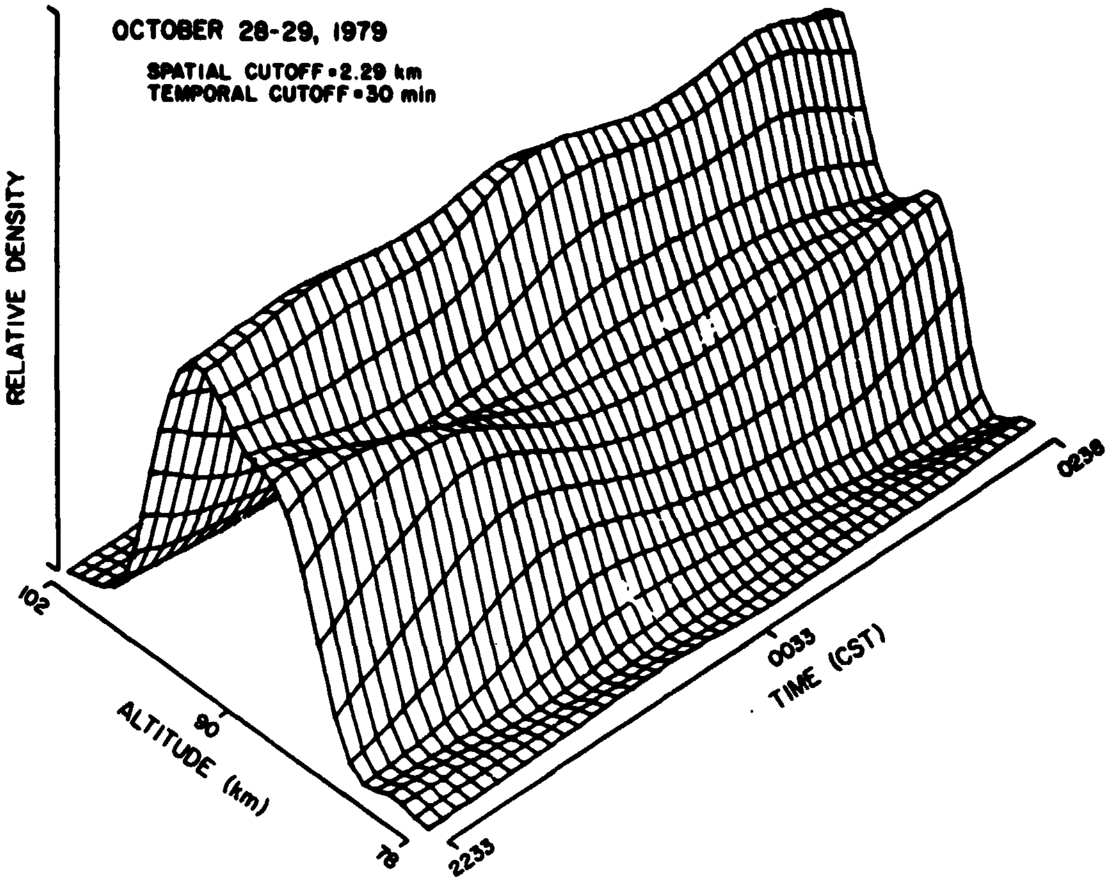

Figure 5.8 Three-dimensional view of the estimated profiles of sodium density observed on October 28-29, 1979.

Near 0100 CST, this secondary peak has almost disappeared. As a result, the layer becomes narrower and then broadens as the secondary peak reappears. Temporal variations in the two-dimensionally filtered data are shown in Figure 5.9. A downward phase progression of wavelike features is apparent. Associated with this phase progression is a vertical wavelength of 12 km and a temporal period of 170 minutes. Both the temporal and spatial periodograms are consistent with these parameters. Near 91 km density oscillations with a period of 85 minutes appear. These are probably associated with the second order (double frequency) portion of the layer response and are related to the peak in the ATP at 0.0118 min^{-1}. They appear at this altitude because the linear response becomes small just above the layer peak near the point of phase reversal. At the point of phase reversal, the linear layer response vanishes. This phase reversal, as discussed in Chapter 4, is apparent in Figure 5.9.

Figure 5.10(a) contains a plot of the maximum and minimum sodium densities observed during the evening's data collection (dashed lines). The average altitude profile of sodium density is shown by the solid line and is seen to be roughly gaussian. A gaussian layer with $\sigma=3$ km centered at 90 km was utilized to predict the maximum and minimum densities associated with the linear layer response (Figure 5.10(b)). There is good correlation between Figures 5.10(a) and (b) in several respects. The amplitude of the density variations below the layer peak are greater than those above the peak. For the gaussian layer, the largest density perturbations occur at 87.6 km and are 9.1 times larger than the atmospheric density variations. The magnitude of the density variations in experimental data are approximately the same. This indicates that the amplitude of the atmospheric density variations associated

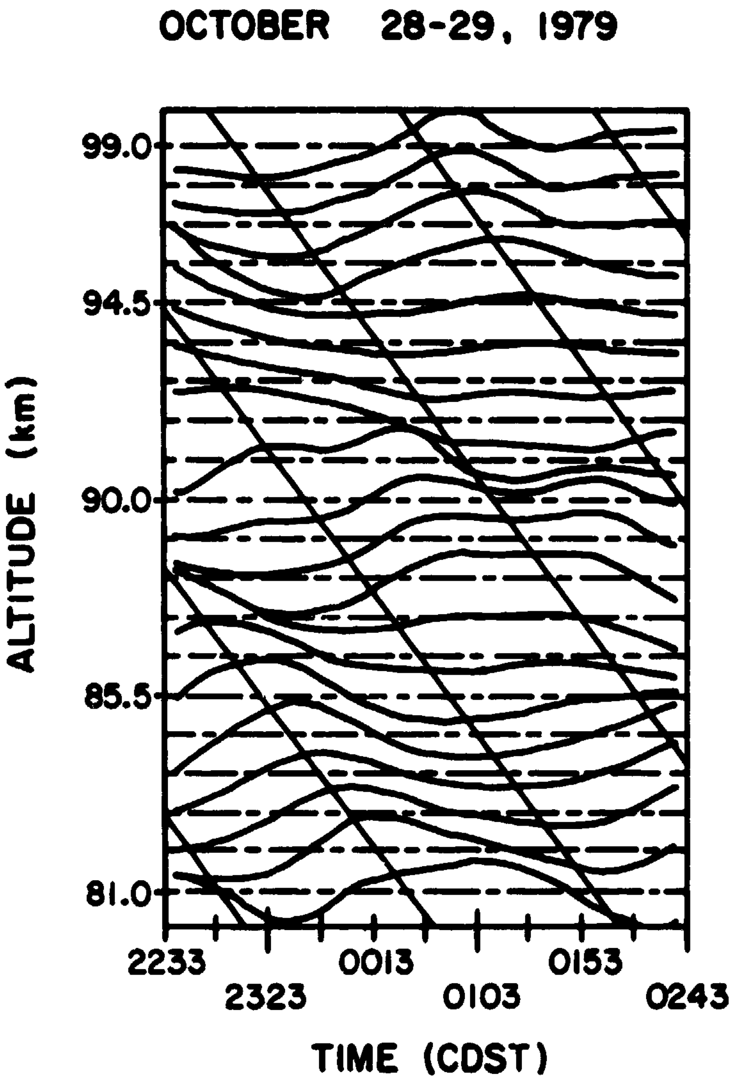

Figure 5.9 Plot of the temporal variations in sodium density observed on October 28-29, 1979. The spatial and temporal filter cutoffs were 0.44 km^{-1} and 0.033 min^{-1}, respectively. Diagonal lines indicate the apparent phase progression.

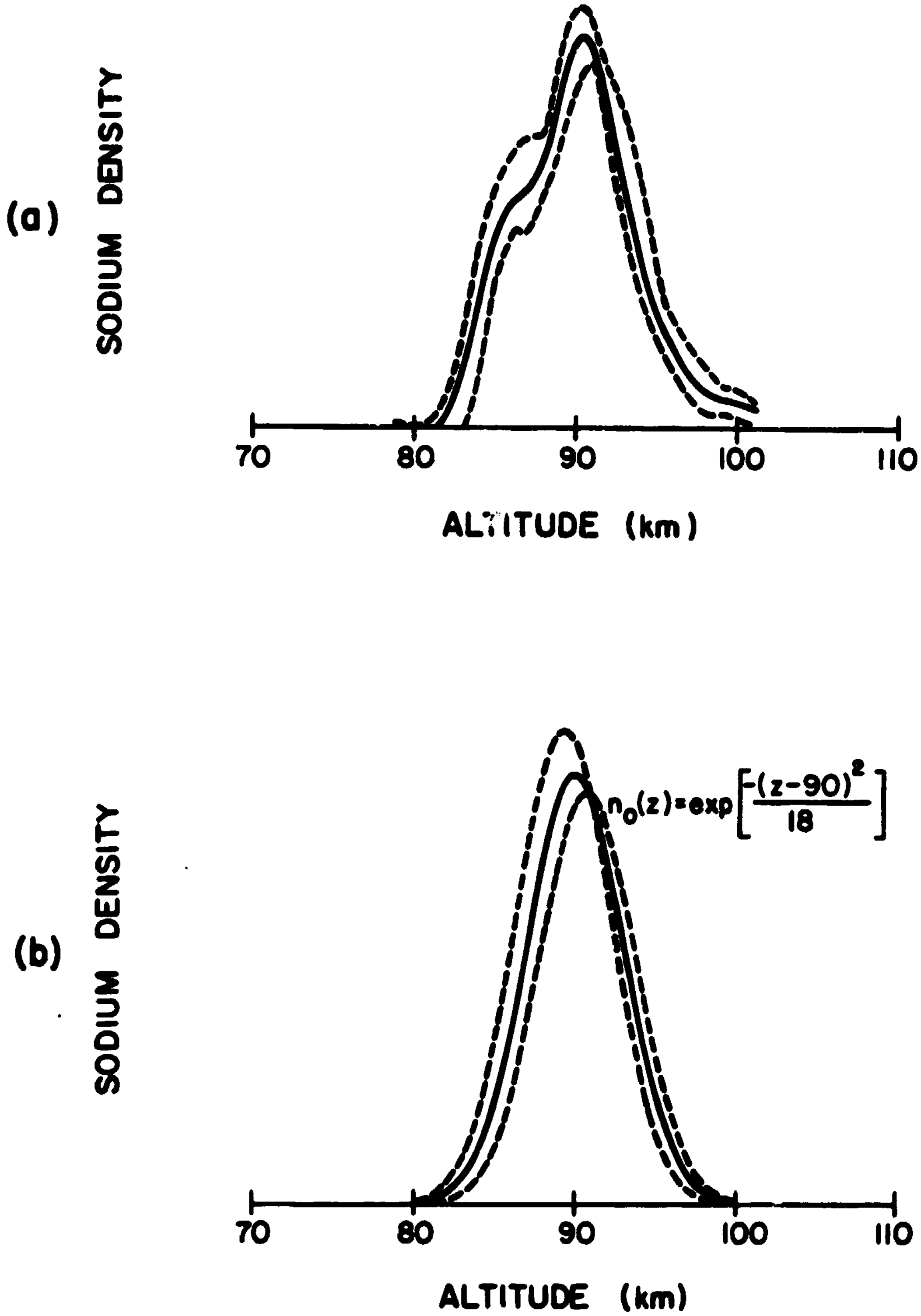

Figure 5.10 Plot of the envelope of sodium density variations (dashed lines) about the average density (solid line) observed on October 28-29, 1979 (a) and the simulated envelope of density perturbations (dashed lines) for a gaussian steady state layer (solid line) (b). A gravity wave amplitude consistent with 3% peak atmospheric density variations ($A = 0.03$) was assumed.

with the gravity wave are probably near 3% (i.e., $A \approx 0.03$). The closest approach of the curves describing maximum and minimum density profiles in Figure 5.10(a) occurs at 91.5 km (1 km above the layer peak at 90.5 km). This point probably corresponds to the point of phase reversal. The two curves do not meet at this point because higher order terms (especially the second order term) in the layer response are not zero at this altitude. The altitude of the point of phase reversal deduced above corresponds to the point of phase reversal observed in the plot of temporal variations in density (Figure 5.9). For the gaussian layer, the point of phase reversal occurs 0.92 km above the layer peak. This is approximately the same as the separation of the layer peak and the point of phase reversal deduced from experimental data.

5.2.3 DECEMBER 13-14, 1979

On December 13-14, 1979 a series of 58 spatial profiles were collected at time intervals of 5 minutes. The ATP of these data is shown in Figure 5.11. Because the data spanned less than 5 hours, the low frequency distortion introduced by windowing the ATP must be considered. The first null in the DFT of the window occurs at 0.0069 min^{-1}. The peak of the ATP, which occurs at 0.0031 min^{-1}, is well within this region. As a result, the temporal frequency of density oscillations cannot be precisely determined by examining the ATP. It is clear, however, that the oscillations have a very low frequency. The period of the oscillations is probably in excess of 300 minutes. There is significant energy at temporal frequencies below 0.022 min^{-1}. At higher frequencies, the shot noise floor dominates the ATP. In order to pass spectral components with frequencies less than 0.022 min^{-1} without significant distortion, a temporal filter cutoff at 0.033 min^{-1} was selected and applied to the photocount data.

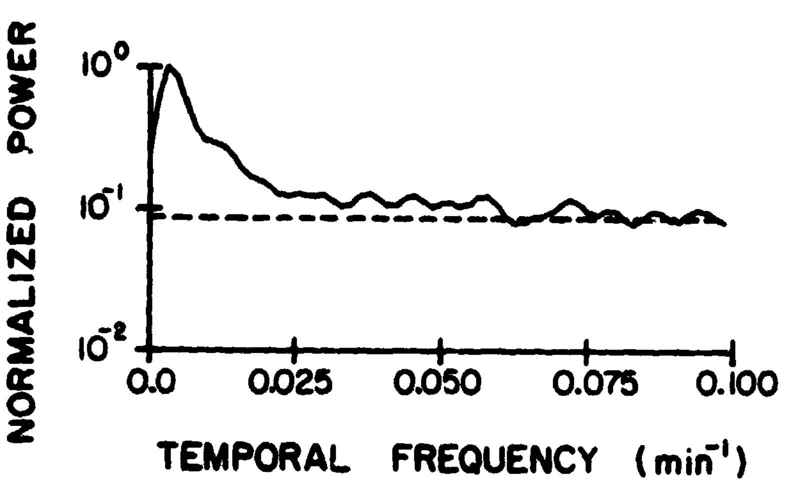

Figure 5.11 Plot of the normalized average temporal periodogram of data collected on December 13-14, 1979.

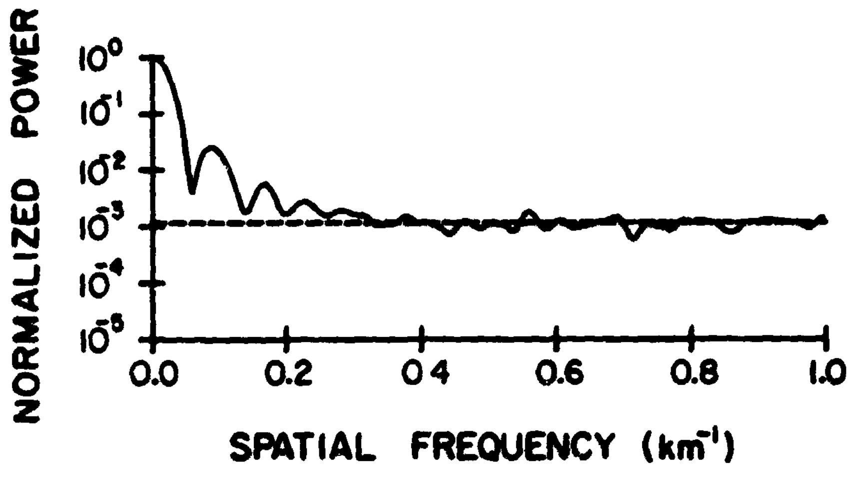

Figure 5.12 Plot of the normalized average spatial periodogram of temporally filtered data collected on December 13-14, 1979.

The ASP of the temporally filtered data is shown in Figure 5.12. This plot is interesting because it indicates that a series of peaks in the ASP exist which grow smaller with increasing spatial frequency. It is difficult to explain this in terms of a single gravity wave unless the magnitude of the nonlinearity in the layer response is large. The magnitude of the higher order components in the layer response are quite dependent upon both the wave amplitude and the steady state layer profile. As the wave amplitude and the density gradients in the steady state layer become large, so do the higher order components of the layer response. Other possibilities are that several waves are present or waves are "breaking" into structures with smaller scale due to nonlinearities in the propagation of the waves. These last possibilities have not been treated in this thesis. On the basis of the ASP, a spatial filter cutoff at 0.345 km^{-1} was selected and applied to the temporally filtered data.

Plots of two-dimensionally filtered spatial profiles are contained in Figure 5.13. Estimates of the profiles of sodium density are plotted every 10 minutes. The layer is observed to be fairly broad. It generally extends from 77 to 103 km. The initial bifurcated layer grows into a single peaked layer over a period of 2.5 hours. Near the end of the observation period, the layer is once again becoming broader as the wavelike features below the layer peak grow in amplitude. The changes in layer width can be explained in terms of the layer response to gravity waves. Because of the phase reversal in the layer response, waves with vertical wavelengths of the same order as the layer thickness can have the effect of causing the layer thickness to oscillate. The layer appears to become narrow when a minimum in atmospheric density occurs above the layer peak and a maximum occurs below. Conversely, when a

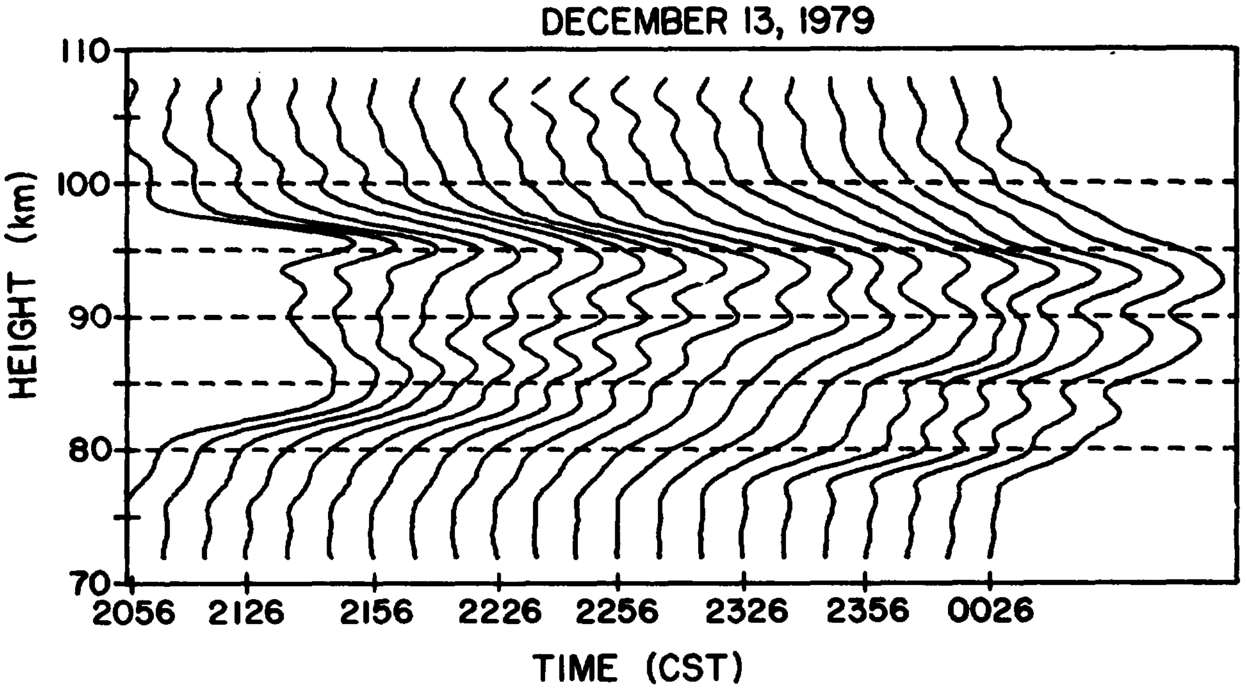

Figure 5.13 Time history of the estimated altitude profiles of sodium density observed on December 13-14, 1979. The spatial and temporal filter cutoffs were 0.345 km^{-1} and 0.033 min^{-1}, respectively. Estimated profiles are plotted at 10 minute intervals.

maximum occurs above the layer peak and a minumum occurs below the peak, the layer seems to broaden. This last effect may partially explain the bifurcations often seen in sodium lidar data. The highest peak may correspond to a peak in atmospheric density forced by a gravity wave. The sodium density maximum found below the layer midpoint may correspond to a minimum in atmospheric density. Since the sodium density perturbations due to the linear layer response and the atmospheric density perturbations are 180 out of phase at this point, a peak in sodium density would result.

Temporal variations in sodium density are shown in Figure 5.14. Most of the density variations observed are consistent with very low frequency oscillations. The observation period, in this case, was not long enough to cover one full period of the oscillation. The ATP was used to predict these low frequency oscillations. Near 92 and 97 km, higher frequency density oscillations are observed. These may be associated with higher order terms in the layer density response.

5.3 DATA COLLECTED WITH THE CANDELA LASER

5.3.1 FEBRUARY 24-25, 1981

A series of 97 spatial profiles were collected during this observation period. Five minutes separated the starting times of successive profiles. Because of the long observation period (roughly 8 hours), the severe low frequency distortion in the ATP is confined to temporal frequencies below 0.004 min^{-1}. An examination of the ATP shown in Figure 5.15 indicates that the main peak at 0.0033 min^{-1} is on the edge of the region of distortion. The shot noise floor is approximately 14 dB below the spectral peak and appears to dominate the signal spectrum at frequencies greater than 0.022 min^{-1}. As a

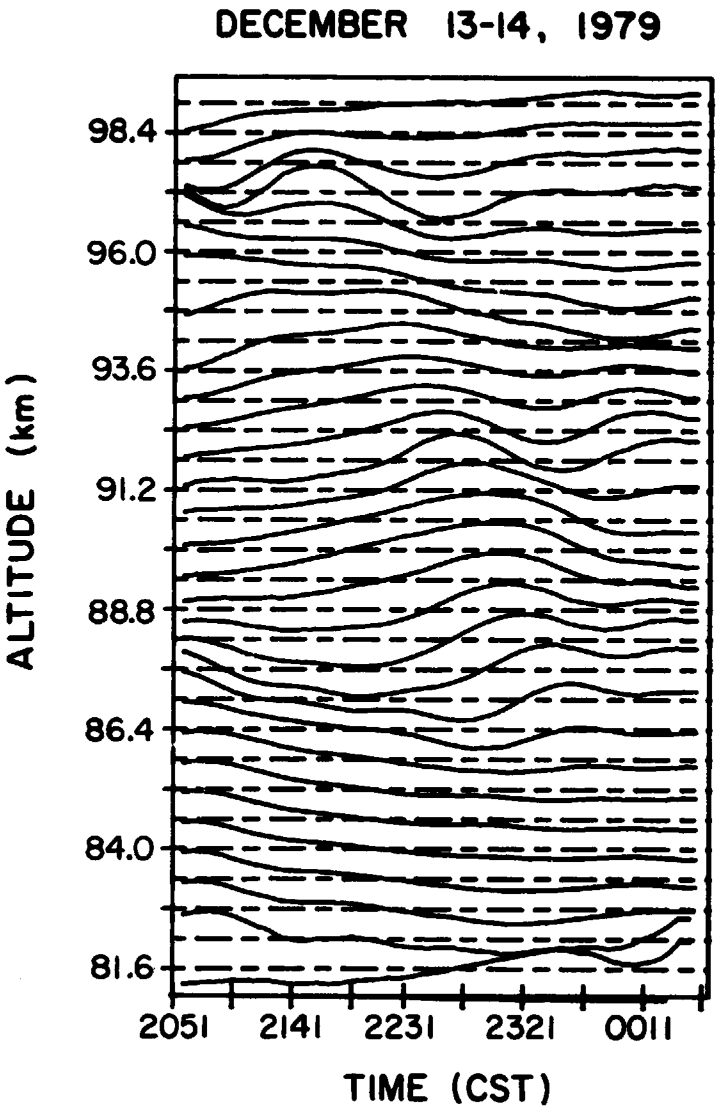

Figure 5.14 Plot of the temporal variations in sodium density observed on December 13-14, 1979. The spatial and temporal filter cutoffs were 0.345 km^{-1} and 0.033 min^{-1}, respectively.

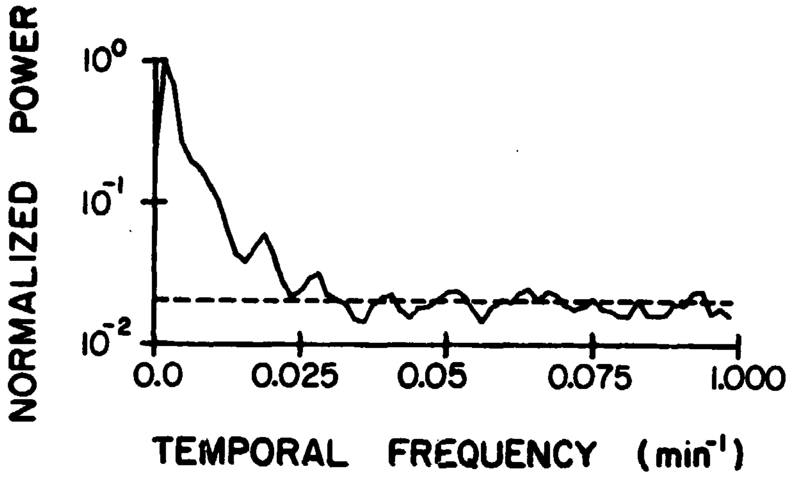

Figure 5.15 Plot of the normalized average temporal periodogram of data collected on February 24-25, 1981.

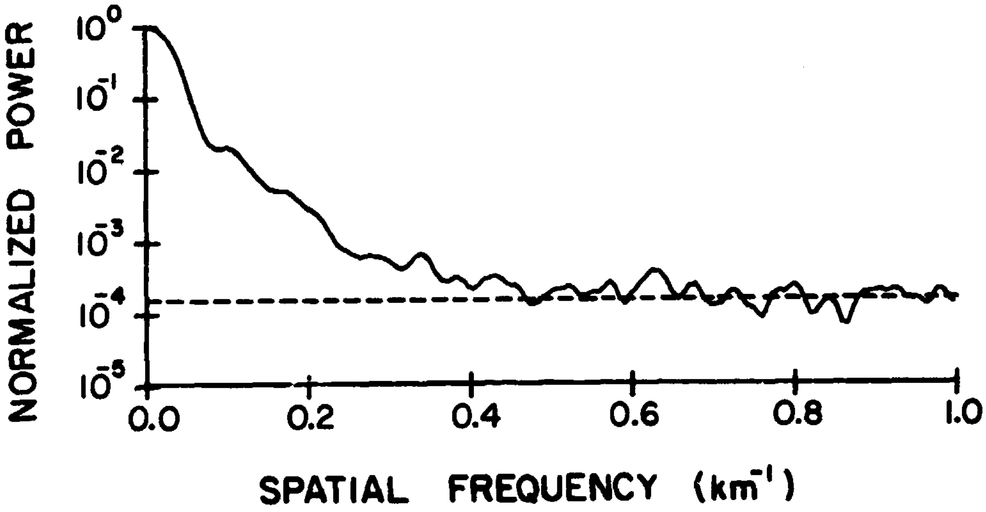

Figure 5.16 Plot of the normalized average spatial periodogram of temporally filtered data collected on February 24-15, 1981.

result, a temporal filter cutoff at 0.0267 min^{-1} was selected. The ASP of the temporally filtered data is shown in Figure 5.16. The shot noise floor is 38.3 dB below the spectral peak and appears to dominate the periodogram at spatial frequencies greater than 0.4 km^{-1}. The spatial filter cutoff was chosen to coincide with this frequency.

Two-dimensionally filtered spatial profiles are contained in Figure 5.17. There is much activity below the main layer peak. This peak is located near 94 km at 2230 CST and by the end of the observation period has moved down to 90 km. A ledge in the sodium density between 82 and 86 km is present at 2300. This ledge disappears by 0030 and reappears by 0130. After 0300 the ledge disappears permanently. One of the interesting features that later data also share is a high altitude increase in sodium density occuring in the pre-sunrise hours. Begining at 0200, the sodium density above 100 km appears to steadily increase.

The temporal variations in sodium density shown in Figure 5.18 make it clear that the increase is not confined to high altitudes. This plot was obtained by examining the temporal variations in calibrated data. An increase in column abundance appears as a general increase in sodium density at all altitudes above 82.2 km. Previous data could not be calibrated and, as a result, the temporal variations in sodium density were obtained by assuming the column abundance did not vary. In addition, these data did not typically span long periods and did not extend into the pre-sunrise hours when column abundance increases are observed. The enhanced sodium densities associated with the early morning hours tend to mask wavelike features in the temporal plots. To alleviate this problem, the temporal variations in sodium density have been plotted assuming no variations in column abundance occured (Figure

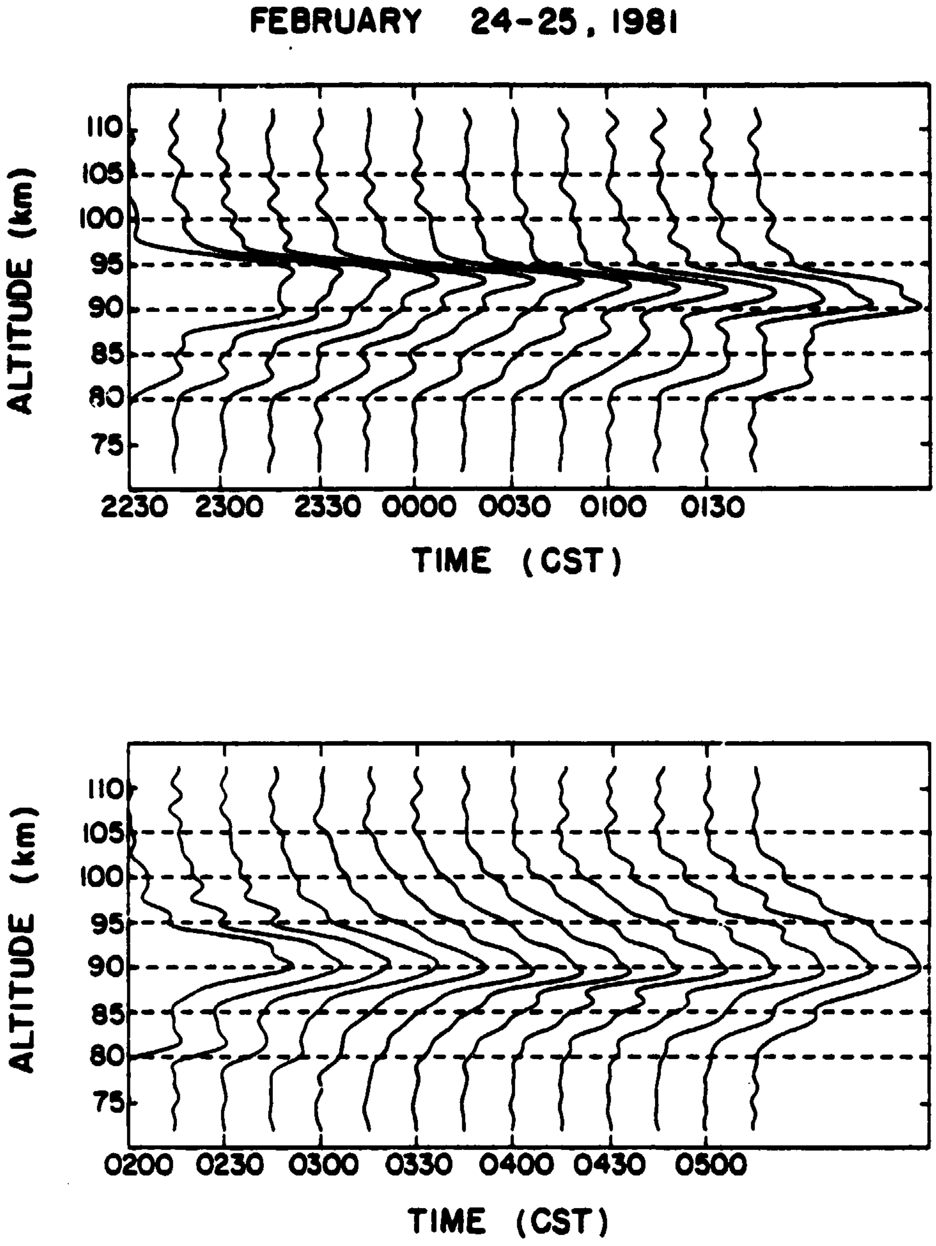

Figure 5.17 Time history of the estimated altitude profiles of sodium density observed on February 24-15, 1981. The spatial and temporal filter cutoffs were 0.4 km^{-1} and 0.0267 min^{-1}, respectively. Estimated profiles are plotted at 15 minute intervals.

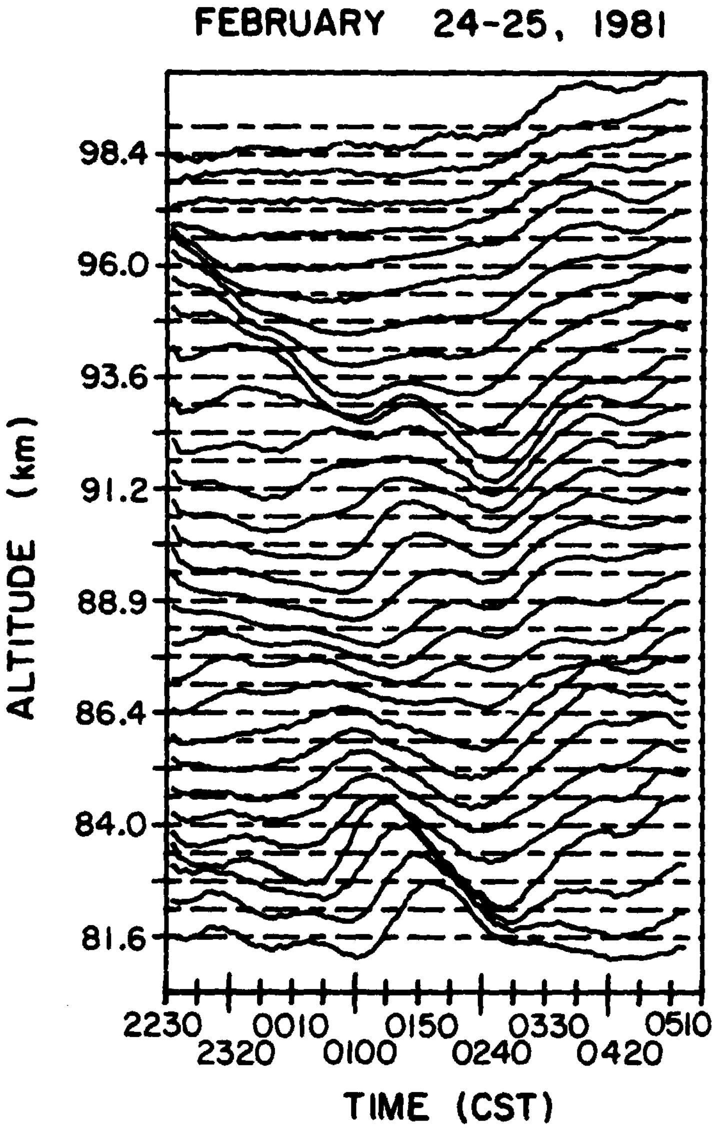

Figure 5.18 Plot of the temporal variations in sodium density observed on February 24-25, 1981. The spatial and temporal filter cutoffs were 0.4 km^{-1} and 0.0267 min^{-1}, respectively.

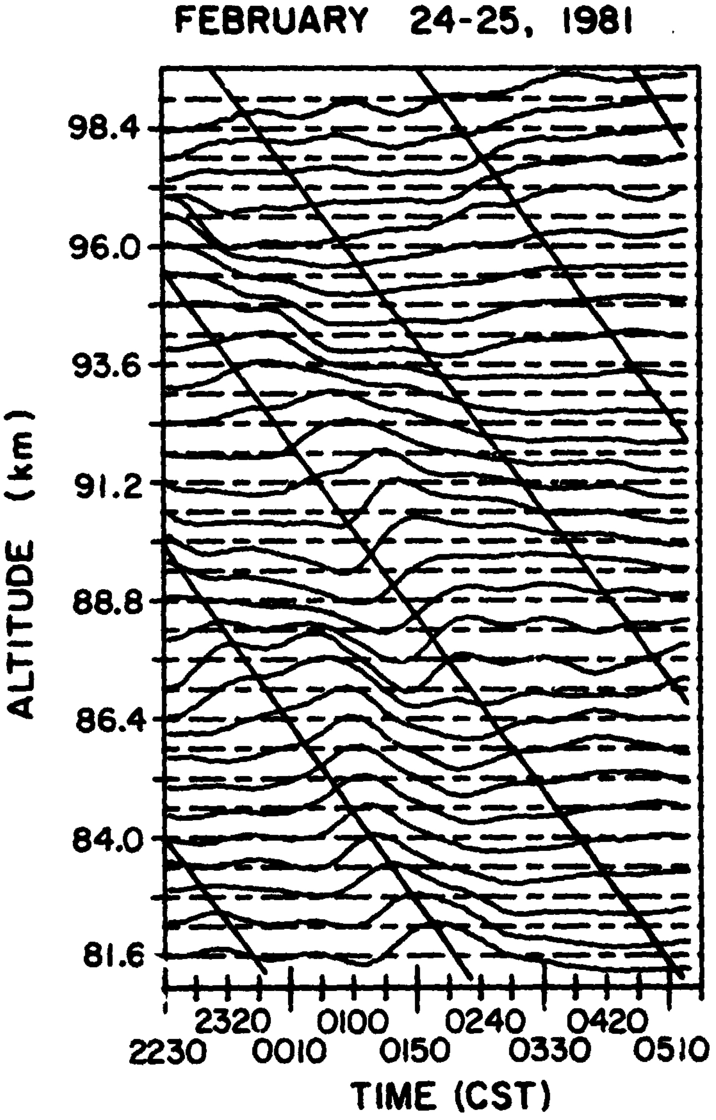

Figure 5.19 Plot of the temporal variations in sodium density observed on February 24-25, 1981. The spatial and temporal filters used in Figure 5.18 from used. These data have been normalized to remove the effects of large column abundance variation. The diagonal lines indicate the apparent phase progression.

5.19). This removes the effects of the dramatic increase in column abundance and makes wavelike features clearer. The dominant features are apparently related to a gravity wave with a vertical wavelength and temporal period of 11.5 km and 300 minutes, respectively. A horizontal wavelength of roughly 500 km would be associated with such a wave. Recall that the ATP contained a peak at 0.0033 min^{-1}. This corresponds to a period of 300 minutes. At a spatial frequency of 0.087 km^{-1}, corresponding to the wave's vertical wavelength, a valley occurs in the ASP contained in Figure 5.16. This is consistent with the predicted power spectrum presented in Chapter 4. Near 88 km a double frequency component with a temporal period of 150 minutes appears. In addition, a phase reversal in the features exhibiting a 300 minute period is evident near 88 to 90 km. This probably corresponds to the phase reversal associated with the linear layer response. The double frequency oscillations become evident in this region because of the small size of the linear term.

Figure 5.20(a) shows the average density profile (solid line) and the maximum and minimum densities observed during the evening (dashed lines). The layer peak at 92 km is evident. Additionally, it is seen that the density deviations below the layer peak are greater than those above the peak. Figure 5.20(b) contains curves representing the maximum and minimum densities (dashed lines) predicted by a linear simulation of the layer response assuming the average density profile of Figure 5.20(a) and gravity wave induced perturbation in atmospheric density of 6% peak to peak ($A = 0.03$). The point of phase reversal is observed at approximately 93 km. Figure 5.20(c) shows the result of a similar simulation in which the first nonlinear term, n_2 from equation (4.36), is included. This second order simulation agrees more closely with the experimental observations. It is clear that the second order

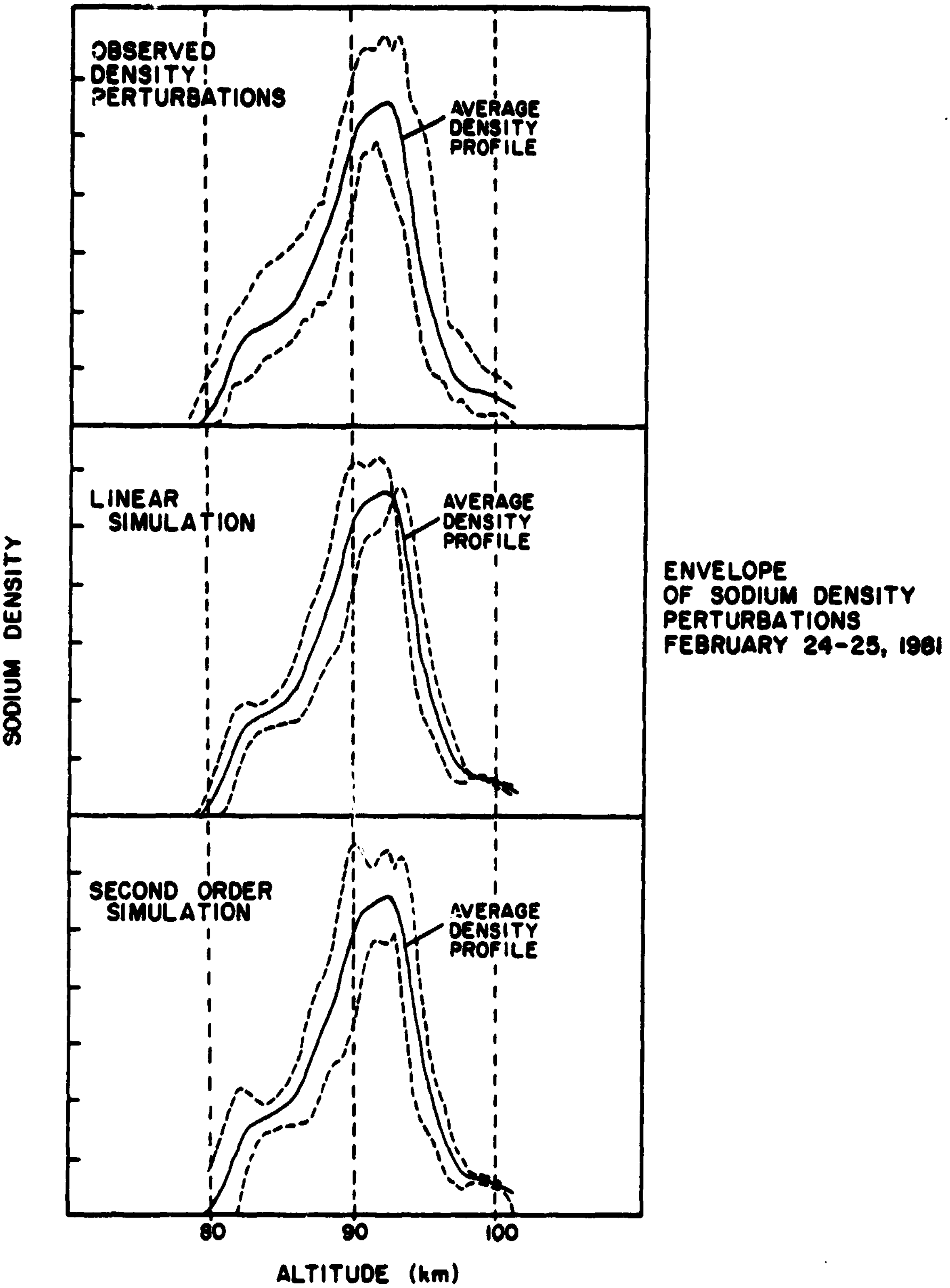

Figure 5.20 (a) Envelope of sodium density variations (dashed lines) about the average density (solid line) observed on February 24-25, 1981. Linear (b) and second order (c) simulations of the envelope of density perturbations assuming the same average density profile and a gravity wave amplitude consistent with 3% peak variations in atmospheric density ($A = 0.03$) are also plotted.

or double frequency term makes significant contributions near the layer peak and to a lessor extent near 82 km. These simulation results are consistent with the temporal profiles contained in Figure 5.19. The double frequency components observed in this figure appear at altitudes where the simulation indicates the second order term should make substantial contributions.

The time variations in column abundance are shown in Figure 5.21. Because of laser alignment problems, estimates of the absolute column abundance could not be made. The relative changes in abundance can be determined, however. It is clear that the column abundance more than doubled between 2230 and 0500 CST. The enhancement progresses rapidly after 0230. This was roughly 3.5 hours before ground sunrise. The regions in which the largest abundance increases occur are also described by Figure 5.19. Five kilometer slices of the layer were examined and the temporal variations in the column content for each slice are plotted. It is clear that the main increases in column content are due to enhanced sodium densities above 85 km. Temporal variations in column content due to the layer density response to wave activity should be apparent. However, these variations are obscured somewhat by the morning enhancement. Three peaks in the total column content are apparent at 2310, 0150 and 0355 CST. The peaks at 2310 and 0355 are separated by 285 minutes. The fact that this period is close to the 300 minute period estimated for the gravity wave indicates that these peaks may result from wave activity (see Chapter 4).

5.3.2 MARCH 11-12, 1981

Occasionally, lidar observations, such as those made on March 11-12, 1981, indicate a great deal of activity in the sodium layer that cannot clearly be

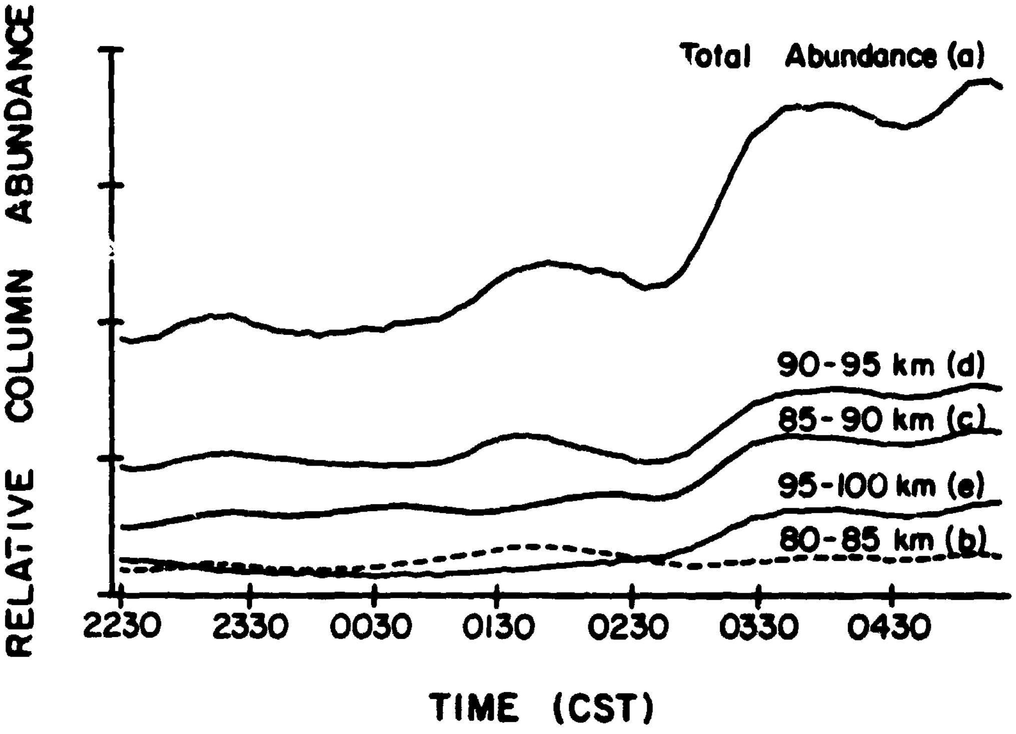

Figure 5.21 Temporal variations in the relative column abundance observed on February 24-25, 1981. Curves (a), (b), (c), (d) and (e) represent the total column abundance and the column content in the 80-85, 85-90, 90-95, and 95-100 km ranges, respectively.

attributed to the layer response to a single atmospheric wave. On this evening 68 spatial profiles were collected at 5 minute intervals. The ATP, shown in Figure 5.22, indicates a great deal of activity. Peaks occur at temporal frequencies of 0.00278, 0.011, 0.0175 and 0.0262 min^{-1}. Because of the length of the observation period and the effects of temporal windowing, features at frequencies below 0.0059 min^{-1} are distorted. A temporal filter with a cutoff at 0.031 min^{-1} was applied to the data. The ASP of the temporally filtered data is shown in Figure 5.23. Since the signal spectrum seems to disappear into the shot noise level near a spatial frequency of 0.358 km^{-1}, this frequency was selected as the cutoff of the spatial filter.

Two-dimensionally filtered spatial prifiles are contained in Figure 5.24. The layer peak occurs near 91.5 km. It is difficult to discern any sustained movement in the layer's features. In general, however, the layer appears to broaden as the evening progresses. This growth is not confined to the upper reaches of the layer, however. The bottomside of the layer moves from 83 km at 0025 to 79 km at 0505 CST. The large density gradient at 95 km becomes much smaller by the end of the observation period as a result of the upward expansion of the layer.

Temporal variations in sodium density are plotted in Figure 5.25. These curves have been normalized to remove the effects of increases in column abundance and make the wavelike variations in density clearer. There are many wavelike features present in these profiles that may result from the presence of several waves. As a result, it is very difficult to determine the parameters of any single wave. Temporal variations in column abundance are plotted in Figure 5.26. An increase in the column abundance by a factor of more than 2.5 is evident between 0025 and 0505 CST. This dramatic increase

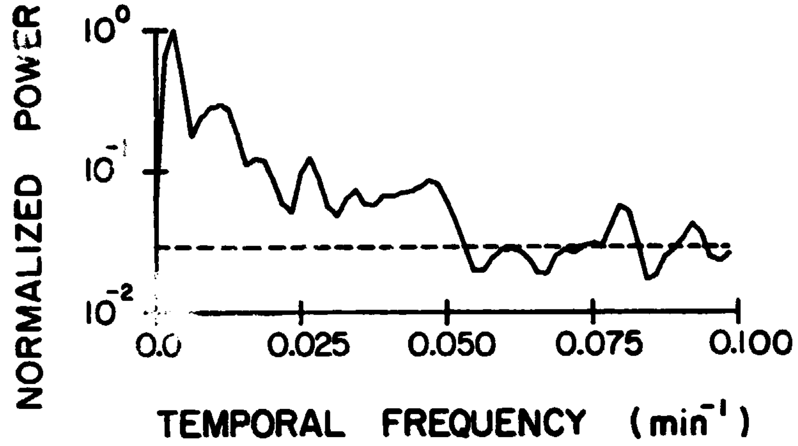

Figure 5.22 Plot of the normalized average temporal periodogram of data collected on March 11-12, 1981.

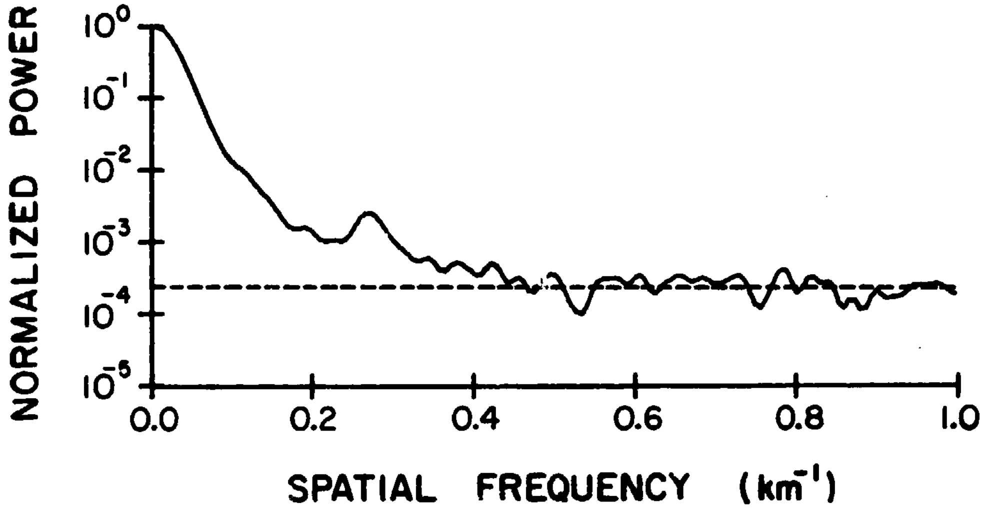

Figure 5.23 Plot of the normalized average spatial periodogram of temporally filtered data collected on March 11-12, 1981.

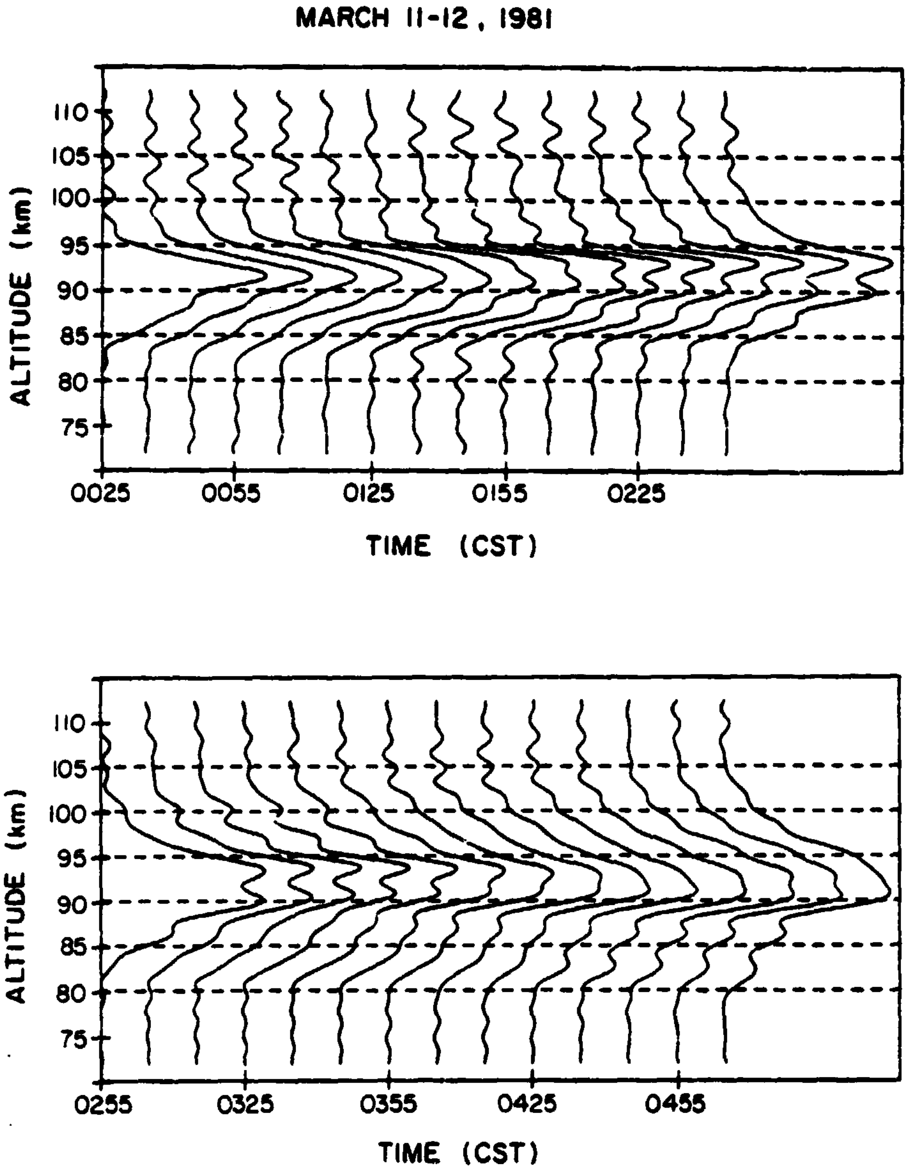

Figure 5.24 Time history of the estimated altitude profiles of sodium density observed on March 11-12, 1981. The spatial and temporal filter cutoffs were 0.358 km^{-1} and 0.031 min^{-1}, respectively. Estimated profiles are plotted at 10 minute intervals.

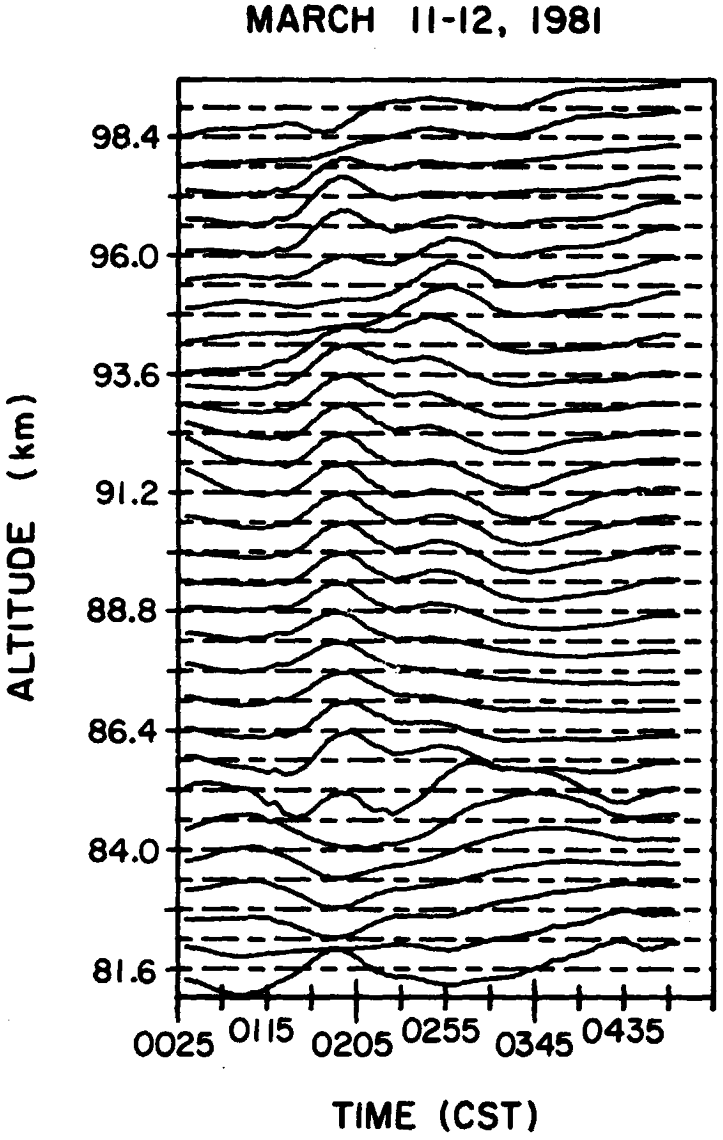

Figure 5.25 Plot of the temporal variations in sodium density observed on March 11-12, 1981. The spatial and temporal filter cutoffs were 0.358 km^{-1} and 0.031 min^{-1}, respectively. These data have been normalized to remove the effects of large variations in column abundance.

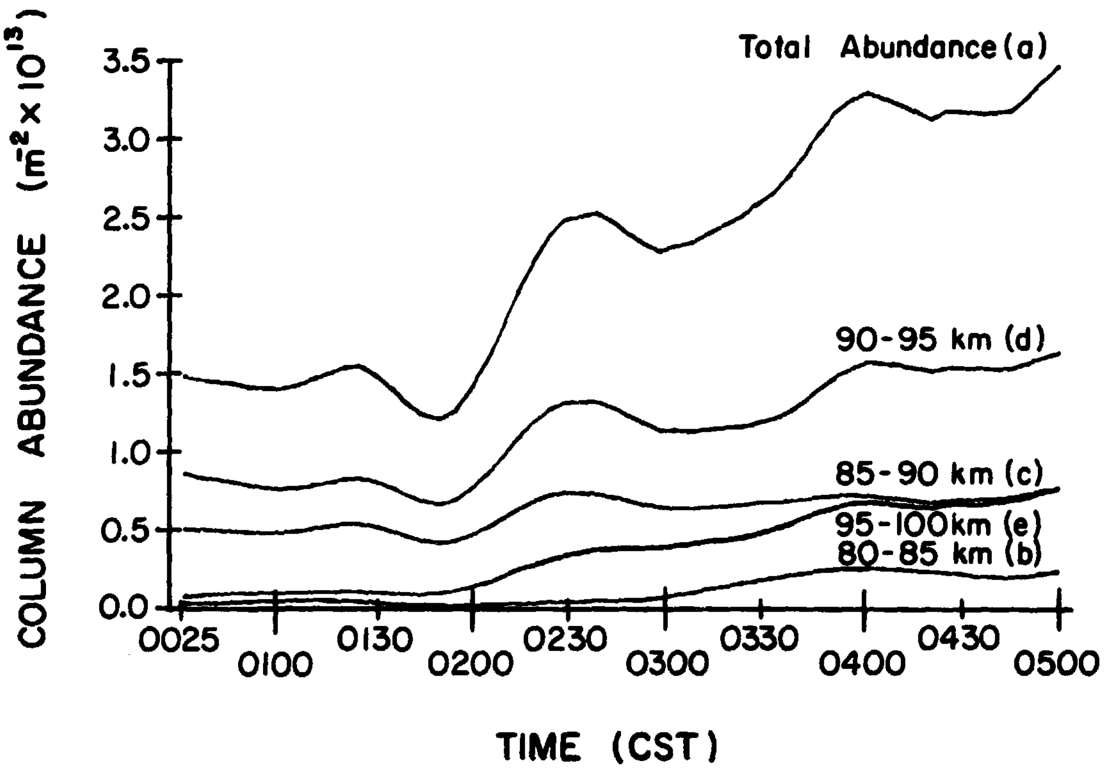

Figure 5.26 Plots of the temporal variations in column abundance observed on March 11-12, 1981. Curves (a), (b), (c), (d), and (e) represent the total column abundance and the column content in the 80-85, 85-90, 90-95, and 95-100 km ranges, respectively.

occurs primarily in the 90-100 km region. Approximately 75% of the total increase is accounted for by the increased column content in this altitude range. 42% of the increase occurs between 90 and 95 km and 33% occurs between 95 and 100 km.

5.3.3 MARCH 12-13, 1981

On the evening of March 12-13, 1981 103 spatial profiles spanning 8.58 hours were collected. The ATP for these data is presented in Figure 5.27. This ATP differs slightly from previous ATP's in that the spectral peak is broad and the shot noise floor is quite low (-22 dB). It appears that two overlapping spectral peaks are present. Even though the first spectral peak, at 0.0022 min^{-1}, is in the region of distortion, it is slightly larger than the peak at 0.0040 min^{-1}. Because of windowing, the spectral features below 0.0039 min^{-1} are distorted. This distortion, in general, decreases the magnitude of the periodogram below 0.0039 min^{-1}. These peaks indicate the presence of long period waves (450 and 250 minutes, respectively). Although the frequencies at which these two peaks appear suggest that the second peak may be associated with the second harmonic of the 0.0023 min^{-1} oscillations, an examination of the filtered data indicates the presence of a separate wave with a frequency of 0.0040 min^{-1}. A temporal filter with a cutoff at 0.0308 min^{-1} was applied to the data. The ASP of the temporally filtered data is shown in Figure 5.28. The low shot noise level (at -47.0 dB) results from the large number of signal photons in each spatial photocount profile and the effects of temporal filtering. No distinct peaks appear in the ASP and the magnitude of the ASP falls off gradually indicating a narrow sodium layer.

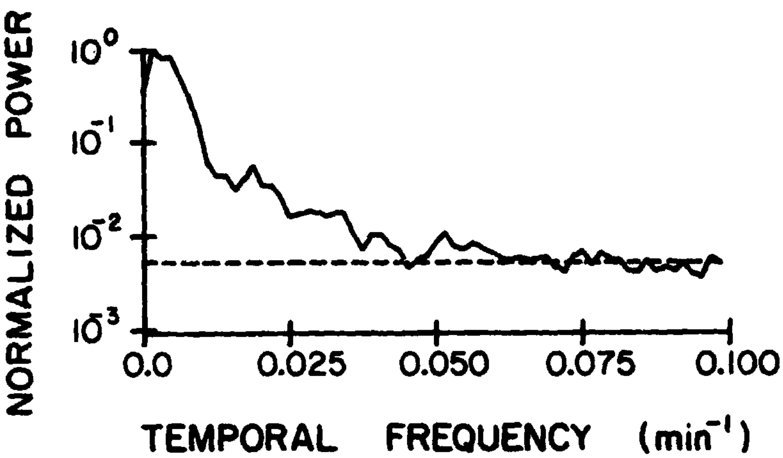

Figure 5.27 Plot of the normalized average temporal periodogram of data collected on March 12-13, 1981.

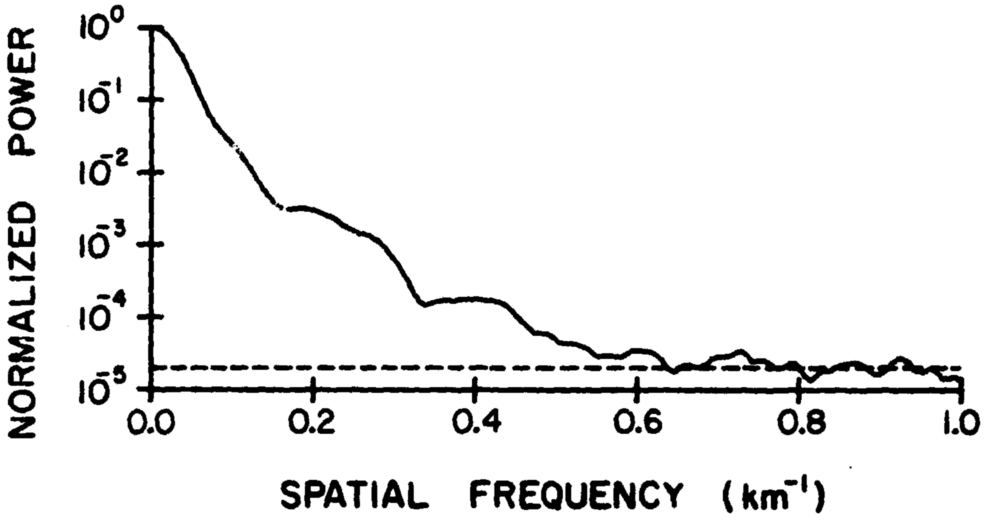

Figure 5.28 Plot of the normalized average spatial periodogram of temporally filtered data collected on March 12-13, 1981. The temporal filter cutoff was at 0.0308 min^{-1}.

A spatial filter with a cutoff at 0.476 km^{-1} was applied to the data. The resulting spatial profiles of sodium density are shown in Figure 5.29. As anticipated, the sodium layer remains narrow during most of the evening. Before 0300 CST its e^{-1} width varies between 7 and 8 kilometers. After 0300, the layer rapidly grows wider attaining a width of over 13 km after 0515. Peaks separated by 5.8 km are present below the layer peak. There is a striking and consistent downward movement of these features at 0.4 m/s. The temporal period associated with this motion (240 minutes) corresponds to the spectral peak at 0.004 min^{-1} in the ATP. The bottomside of the layer also appears to oscillate up and down as these peaks sweep downward. The 5.8 km spacing of the peaks is lost near the main layer peak. This probably results from the phase reversal in the layer response. The diagonal lines in Figure 5.29 indicate the apparent phase progression of the wave. The phase reversal appears to occur slightly above 90 km. Below this altitude, peaks in sodium density are aligned with the lines. Above this altitude, valleys in the sodium layer appear on the lines. These valleys are not as distinct as are the peaks below the point of phase reversal. This probably results from the fact that the density perturbations below the layer peak due to the linear layer response are, in general, larger than those above the layer peak.

Temporal variations in sodium density are plotted in Figure 5.30. The phase progression so evident in the plots of spatial profiles is not clear because of the confused jumble of wavelike features in this plot. This may result from the superposition of 2 dominant waves. A peak in the ATP also occured at a very low frequency (0.0022 min^{-1}). Low frequency density oscillations may be contributing to this confusion. In addition, the narrow nature of the layer serves to increase the magnitude of the nonlinearities in

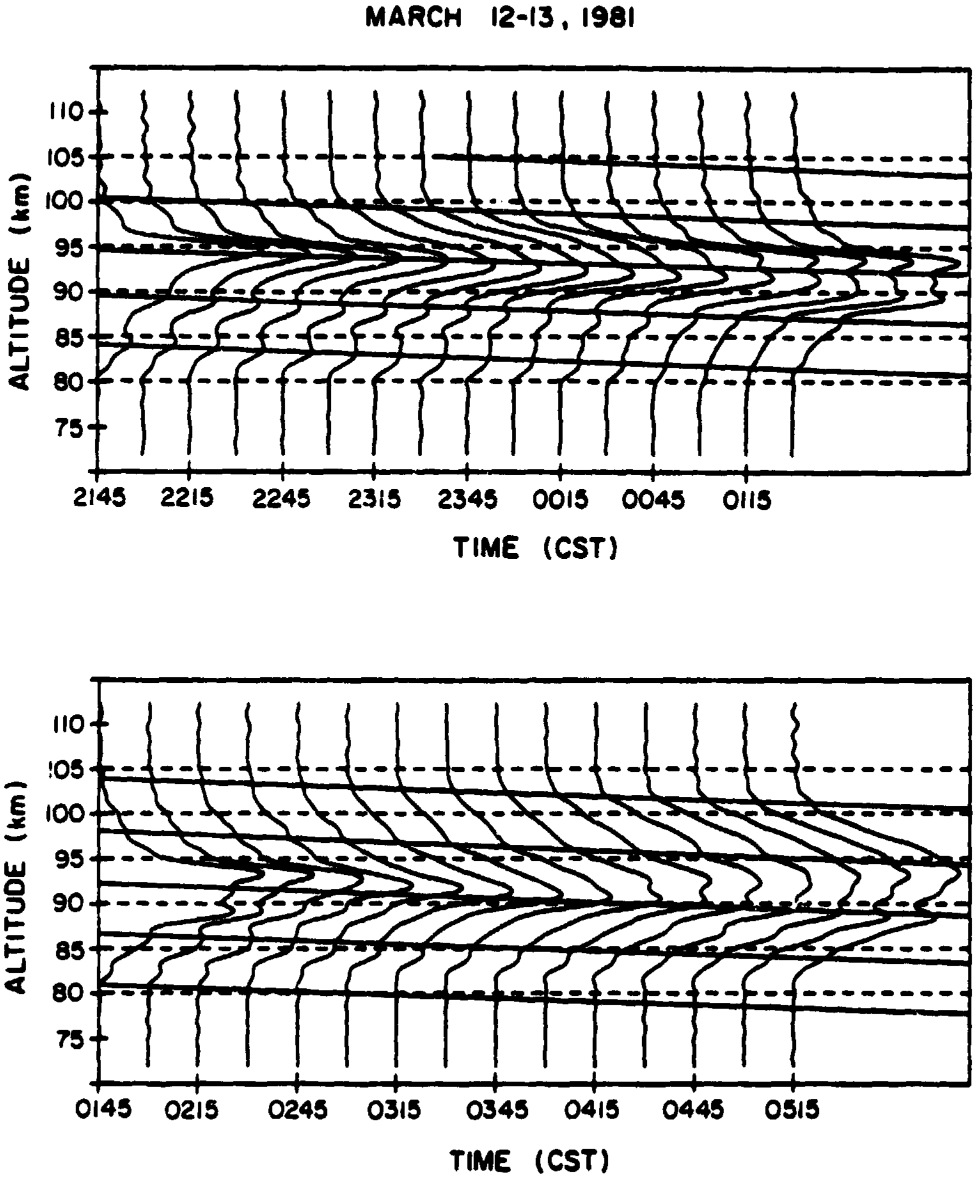

Figure 5.29 Time history of the estimated altitude profiles of sodium density observed on March 12-13, 1981. The spatial and temporal filter cutoffs were 0.476 km^{-1} and 0.0308 min^{-1}, respectively. Estimated profiles are plotted at 15 minute intervals. The diagonal lines indicate the apparent phase progression.

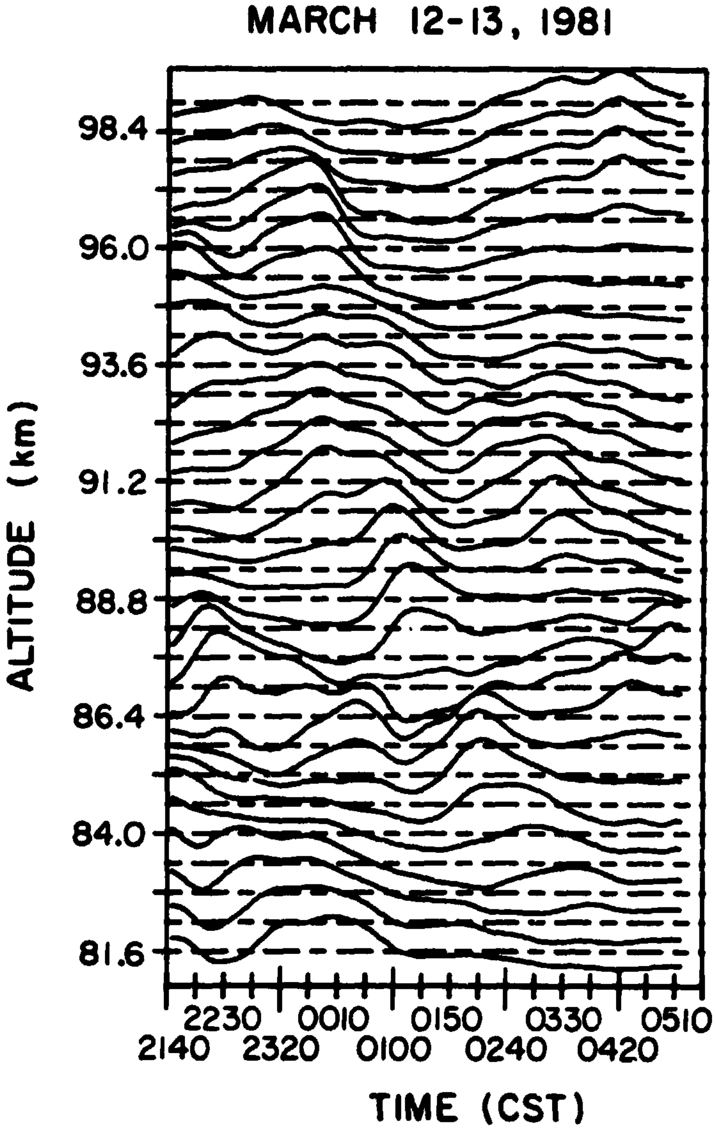

Figure 5.30 Plot of the temporal variations in sodium density observed on March 12-13, 1981. The spatial and temporal filter cutoffs were 0.476 km^{-1} and 0.0308 min^{-1}, respectively. These data have been normalized to remove the effects of large variations in column abundance.

the layer density response. A double frequency component with a temporal period of roughly 125 minutes is definitely present near 87 and 94 km. The combination of layer nonlinearities and the presence of two waves may explain the many wavelike features apparent in this figure.

Temporal variations in column abundance are shown in Figure 5.31. The peaks in abundance occuring at 2325 and 0345 CST may be induced by the 250 minute wave discussed previously. In addition to these peaks, a general increase in abundance is observed. The column abundance for the first 100 minutes of the observation period was roughly 1.85 X 10^{13} atoms/m^2. This increased by 43% to 2.65 X 10^{13} atoms/m^2 by the last 100 minutes of the observation period. As in previous evenings, most of this increase occured above 90 km.

5.3.4 MARCH 13-14, 1981

The ATP for data collected on this evening is shown in Figure 5.32. 113 spatial profiles collected at 5 minute intervals were collected during the 9.5 hours of this observation period. As a result of the length of this data set, the low frequency distortion in the ATP resulting from windowing is confined to temporal frequencies less than 0.0034 min^{-1}. A spectral peak near 0.002 min^{-1} is evident indicating the presence of long period oscillations in sodium density (with periods near 500 minutes). A temporal filter with a cutoff at 0.0308 min^{-1} was applied to the photocount data. The ASP of the temporally filtered data is shown in Figure 5.33. Because the shot noise level dominates the ASP at spatial frequencies greater than 0.4 km^{-1}, a spatial filter cutoff was selected at this point.

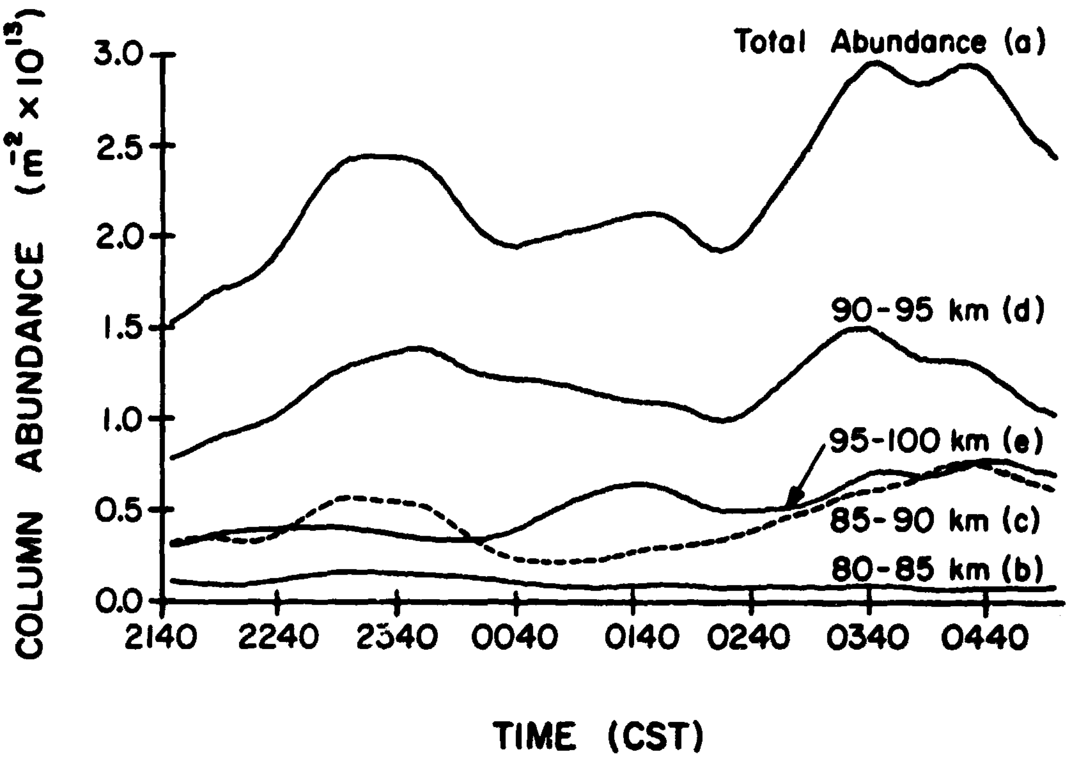

Figure 5.31 Plot of the temporal variations in column abundance observed on March 12-13, 1981. Curves (a), (b), (c), (d), and (e) represent the total column abundance and the column content in the 80-85, 85-90, 90-95, and 95-100 km ranges, respectively.

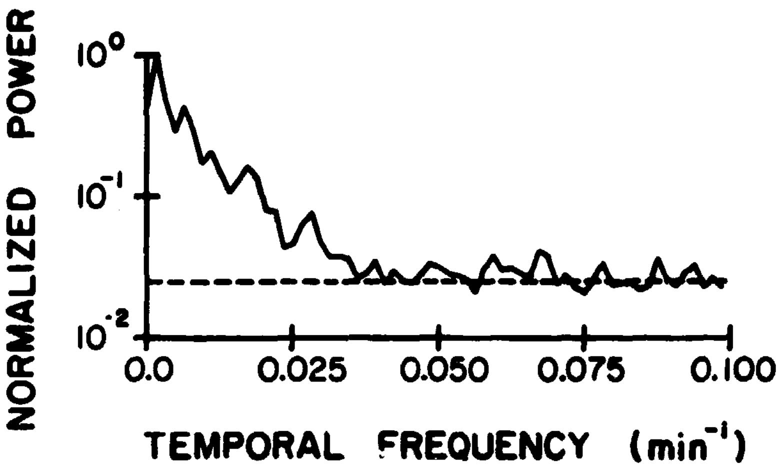

Figure 5.32 Plot of the normalized average temporal periodogram of data collected on March 13-14, 1981.

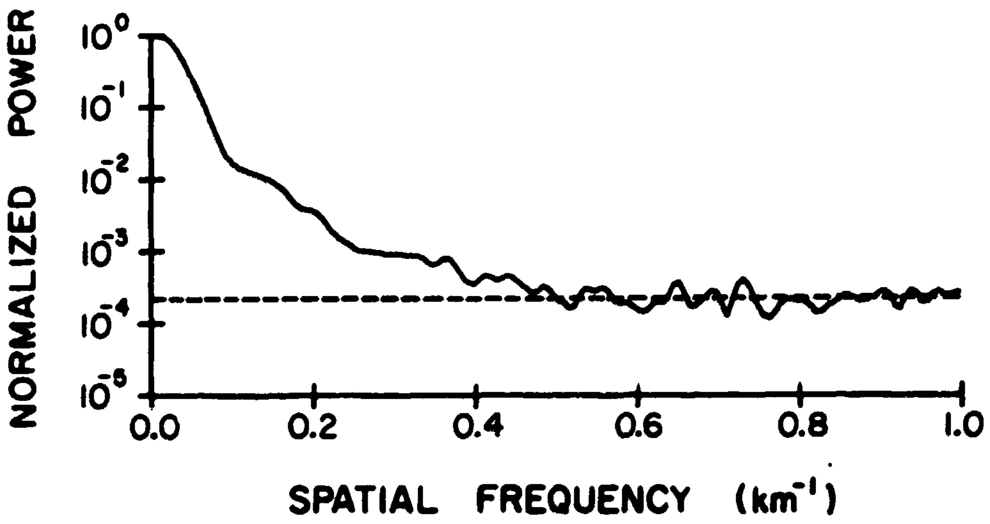

Figure 5.33 Plot of the normalized average spatial periodogram of temporally filtered data collected on March 13-14, 1981. The temporal filter cutoff was at 0.0308 min^{-1}.

The filtered spatial profiles are plotted in Figure 5.34. The layer is not generally as narrow as it was on the previous evening. At 2025 CST the e^{-1} width of the layer is 10 km. It narrows until attaining a width of 6 km at 0030. After 0100, it broadens, finally reaching a width of 11.5 km at 0540. A region in which the density gradient is large moves downward from its initial location near 95 km between 2200 and 0100 CST. However, the obvious downward movement of features apparent on March 12-13, 1981 is not present.

Plots of the temporal variations in density are shown in Figure 5.35. The diagonal lines indicate the apparent phase progression of a wave with a temporal period of approximately 490 minutes and a vertical wavelength of roughly 25 km. A phase reversal occurs near 95 km (above the layer peak at 92.5 km). In addition, higher frequency density oscillations are present near 89 and 95 km. The latter oscillations occur near the point of phase reversal. Large density gradients occur at both of these altitudes. Since large gradients promote nonlinearities, these high frequency oscillations appear to be evidence of the nonlinear layer response. The 490 minute period of the wave suggests atmospheric tidal wave activity.

The variations in column abundance are plotted in Figure 5.36. A 50% increase in column abundance begins to occur two hours before ground sunrise. As in previous observations, the large increases in column abundance are associated with a broadening of the sodium layer and an increase in column content at high altitudes in the pre-sunrise hours.

5.3.5 MARCH 16-17, 1981

On the evening of March 16-17, 1981, 128 spatial photocount profiles were collected over a period of 10.66 hours. The ATP of this data is shown in

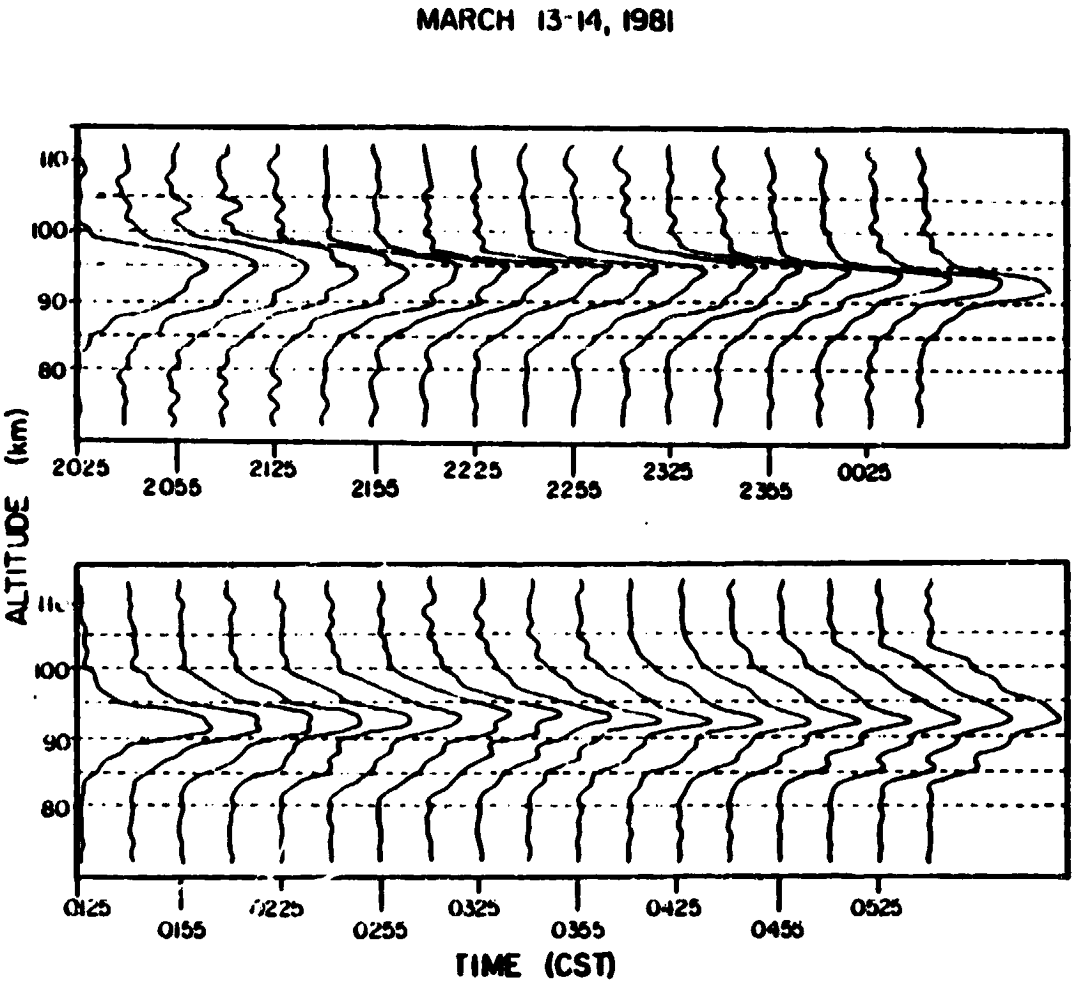

Figure 5.34 Time history of the estimated altitude profiles of sodium density observed on March 13-14, 1981. The spatial and temporal filter cutoffs were 0.40 km^{-1} and 0.0308 min^{-1}, respectively. Estimated profiles are plotted every 15 minutes.

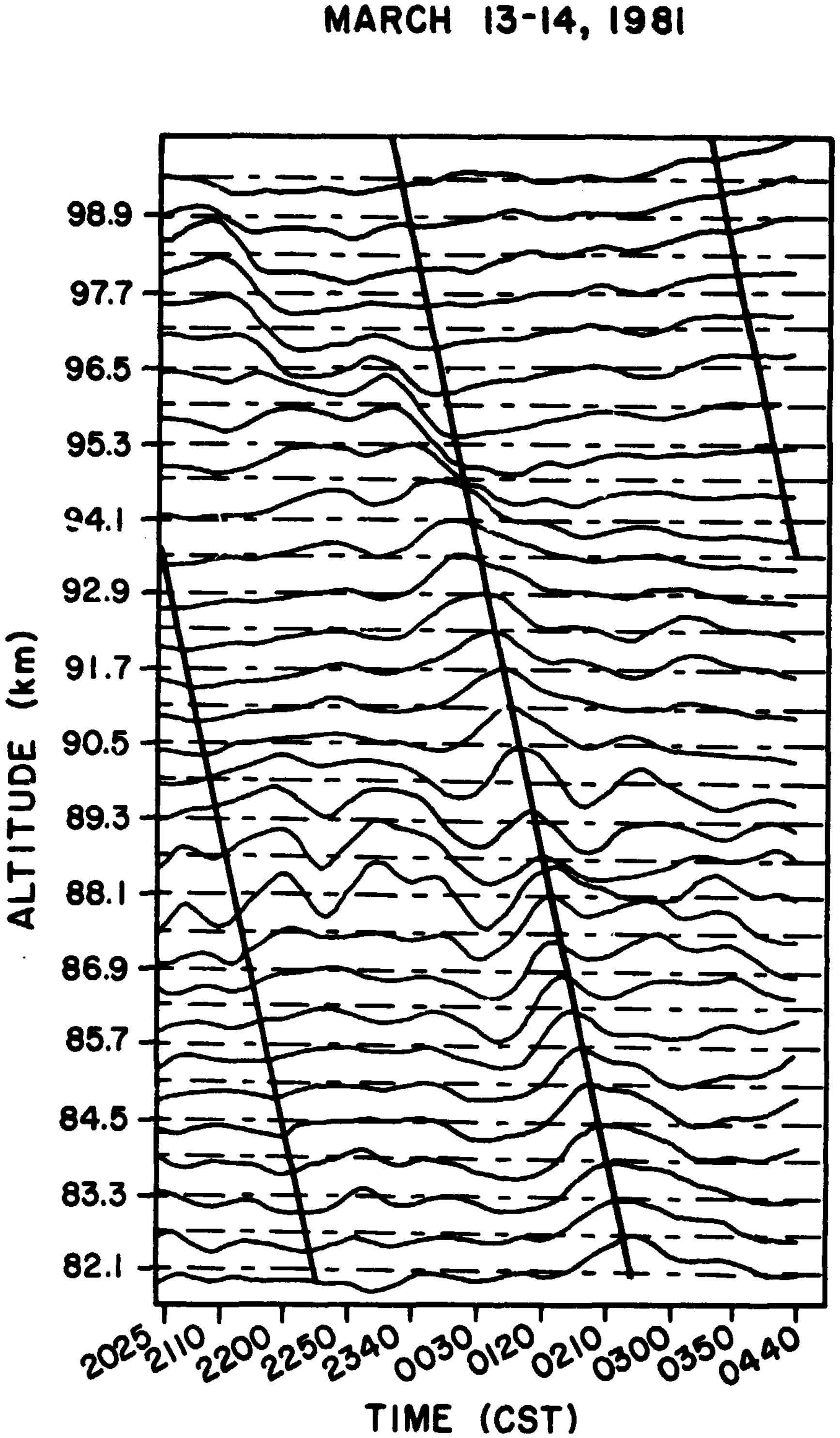

Figure 5.35 Plot of the temporal variations in sodium density observed on March 13-14, 1981. The spatial and temporal filter cutoffs were 0.40 km^{-1} and 0.0308 min^{-1}, respectively. The diagonal lines indicate the apparent phase progression. These data have been normalized to remove the effects of large variations in column abundance.

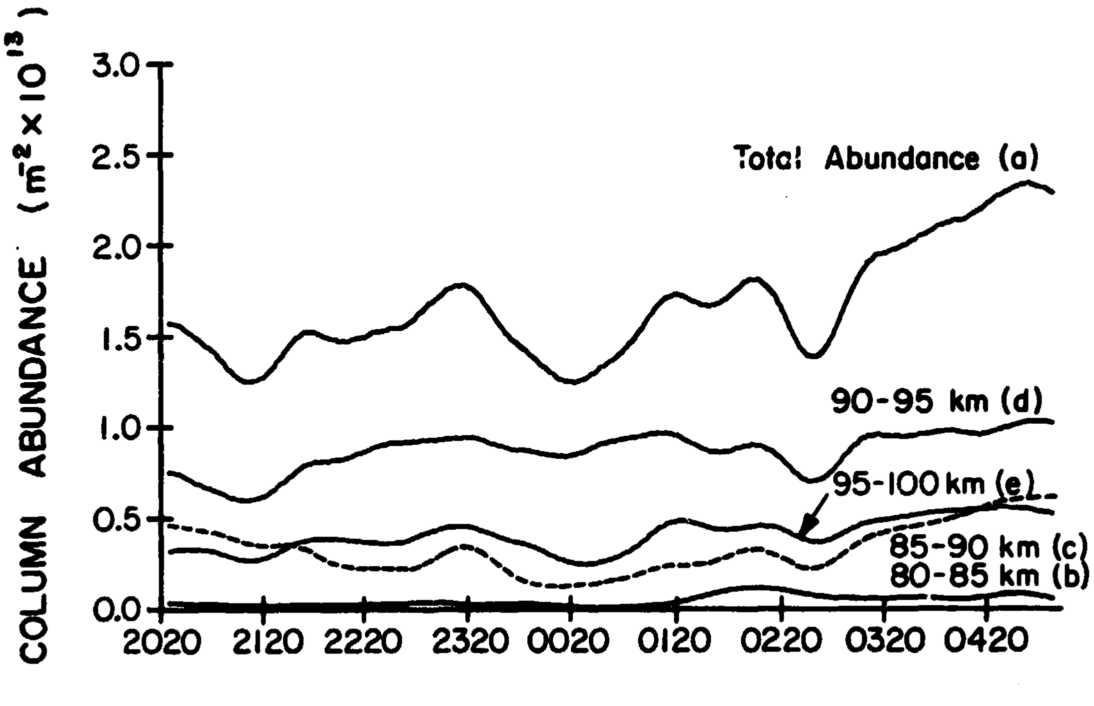

Figure 5.36 Plot of the temporal variations in column abundance observed on March 13-14, 1981. Curves (a), (b), (c), (d), and (e) represent the total column abundance and the column content in the 80-85, 85-90, 90-95, and 95-100 km ranges, respectively.

Figure 5.37. This ATP is unusual because the shot noise floor is so far below the spectral peak (-17.5 dB). This is a consequence of the large number of signal photons in each temporal profile and the size of the temporal variations in density. In addition, the ATP falls off into the shot noise level fairly rapidly. The temporal window used in computing the ATP results in distortion of spectral features below 0.003 min^{-1}. The spectral peak occurs below this point at a frequency of 0.002 min^{-1}. Because of the rapid fall off of the ATP with increasing frequency, a temporal filter cutoff at 0.025 min^{-1} was chosen. The ASP of temporally filtered data is shown in Figure 5.38. Since the signal spectrum falls into the shot noise floor near a spatial frequency of 0.476 km^{-1}, a spatial filter cutoff was selected at this frequency.

Spatial profiles of two-dimensionally filtered data are plotted in Figure 5.39. The layer is seen to evolve from a broad layer early in the evening into a narrow, sharply peaked layer at 0330 CST. By 0500, the layer is once more becoming broad. One of the major factors contributing to the formation of the narrow layer at 0330 is the decrease in amplitude of features below 90 km at this time. The undulatory behavior of atmospheric layers discussed in section 4.4 is evident in this figure. A peak in sodium density near 95.3 km is observed at 2005 CST. This peak steadily moves downward reaching a minimum altitude of 91.2 km at 0150. By 0450, the peak has moved upward to 93.5 km. The period of this oscillation is approximately 11.5 hours. The exact movement of the layer peak is plotted in Figure 5.40. In this figure, the peaks and valleys for each spatial profile of sodium density collected during the evening are plotted. The movement of the layer peak is clearly evident here. Since the period of this undulation is near 12 hours, this behavior is

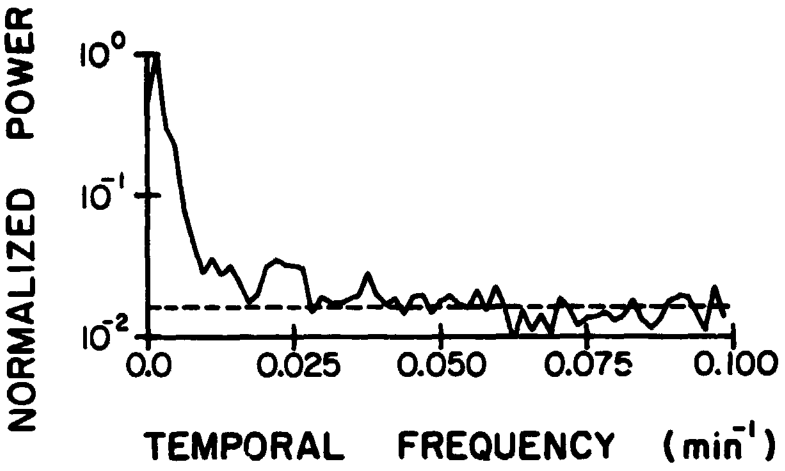

Figure 5.37 Plot of the normalized average temporal periodogram of data collected on March 16-17, 1981.

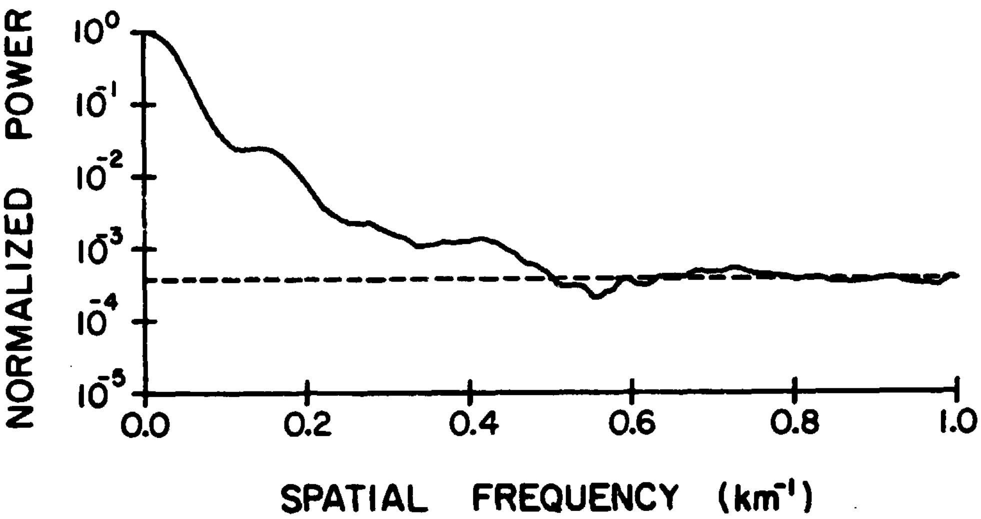

Figure 5.38 Plot of the normalized average spatial periodogram of temporally filtered data collected on March 16-17, 1981. The temporal filter cutoff was at 0.0308 min^{-1}.

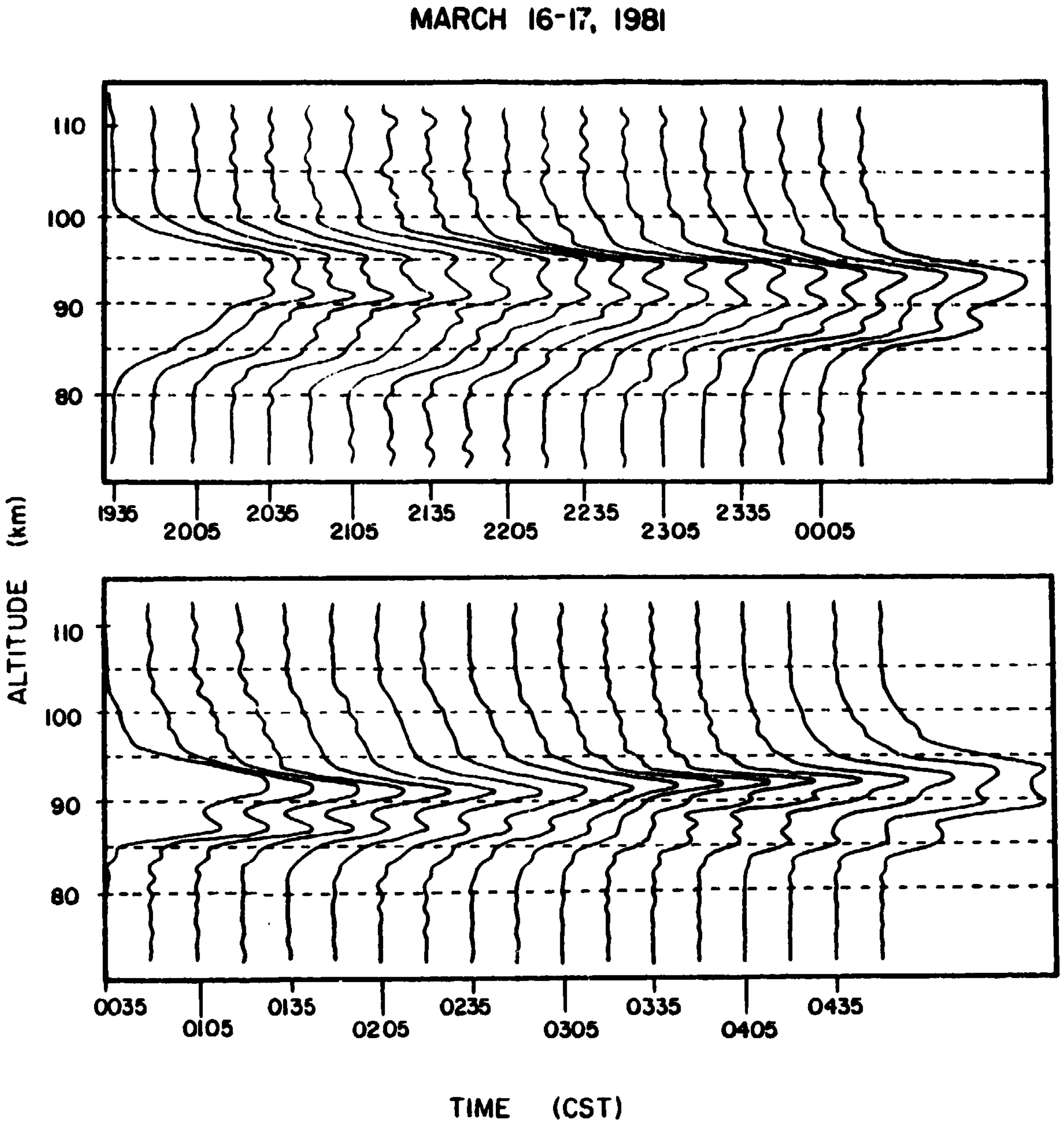

Figure 5.39 Time history of the estimated altitude profiles of sodium density observed on March 16-17, 1981. The spatial and temporal filter cutoffs were 0.476 km^{-1} and 0.0308 min^{-1}, respectively. Estimated profiles are plotted every 15 minutes.

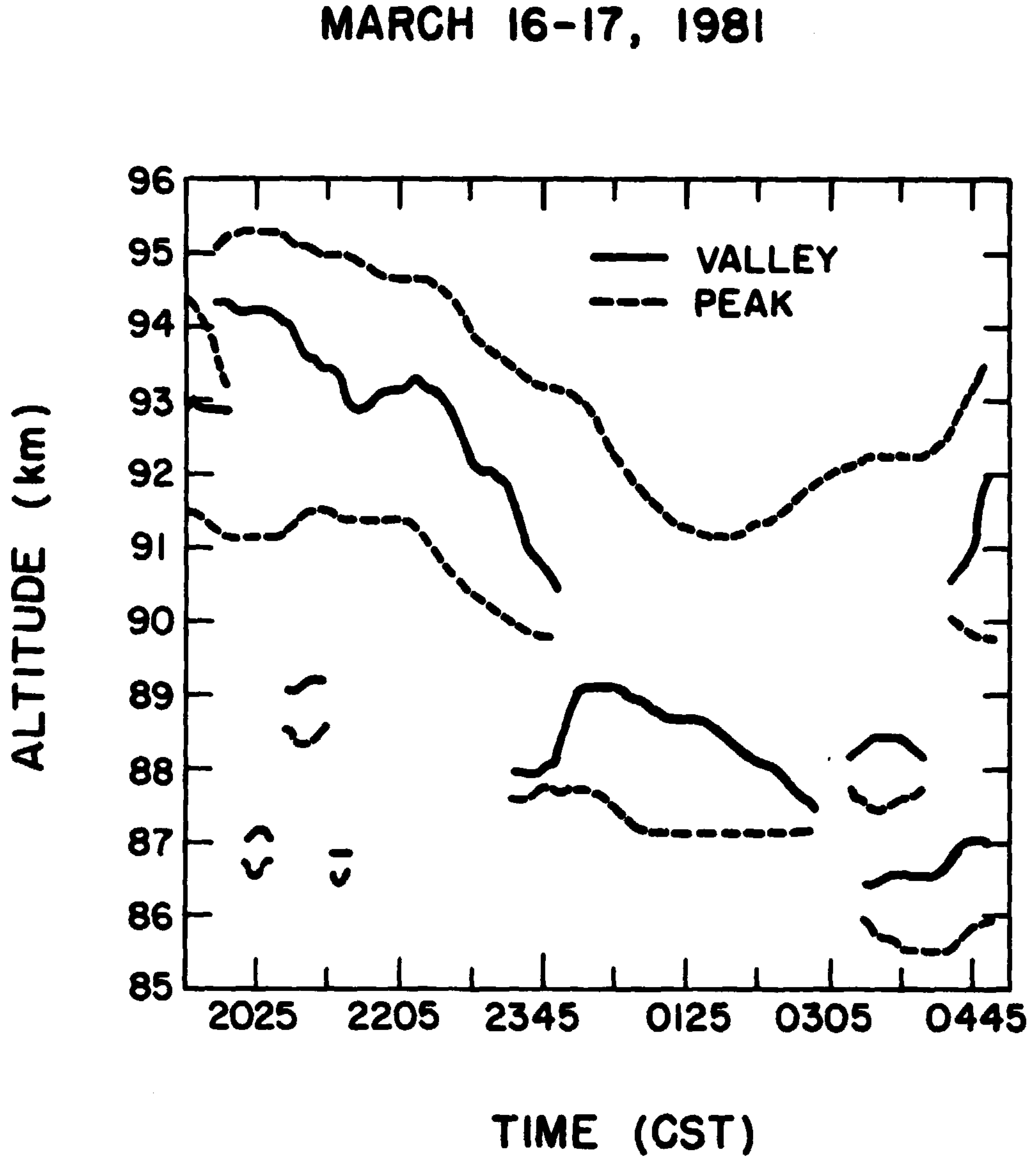

Figure 5.40 Plot of the locations of the peaks and valleys in two-dimensionally filtered estimates of sodium density observed on March 16-17, 1981. The same filter parameters used to produce Figure 5.39 were utilized.

suggestive of atmospheric tidal activity. If this is the case, the movement of the layer peak indicates a maximum upward wind occured near 1700 CST. The amplitude of this wind may be estimated by observing the maximum displacement of the layer peak. In this case, it is estimated that the maximum vertical wind was approximately 0.3 m/s. In addition to the undulatory motion of the layer peak, there are large density variations between 85 and 90 km. Many of the features in this region have peak to peak separations as small as 2 or 3 km. The period of oscillation of these features is much less than the 690 minute period associated with the movement of the main peak. This fine structure may be a layer response to gravity waves. Thus, the total layer response appears to be due to the presence of more than one atmospheric wave. Since the layer response is, in part, nonlinear, there can be an interaction between the responses to these various waves. This can cause density oscillations whose periods are not a harmonic of any of the atmospheric waves. Such nonlinear interactions have not been treated in this thesis.

Temporal variations in sodium density are plotted in Figure 5.41. Density oscillations with a temporal frequency of 290 minutes appear to be present. The vertical and horizontal wavelengths associated with the wave apparently responsible for these oscillations are 18 km and 800 km, respectively. These observations are tentative, however, because of the difficulty in clearly establishing the phase progression of the wave. It does appear that some form of wave activity is present in addition to the possible tidal motion discussed previously.

An increase in column abundance in the early morning hours was observed in these data as in previous observations. This is illustrated by Figure 5.42. The column abundance doubled from about 1.7 X 10^{13} atoms/m^2 to over

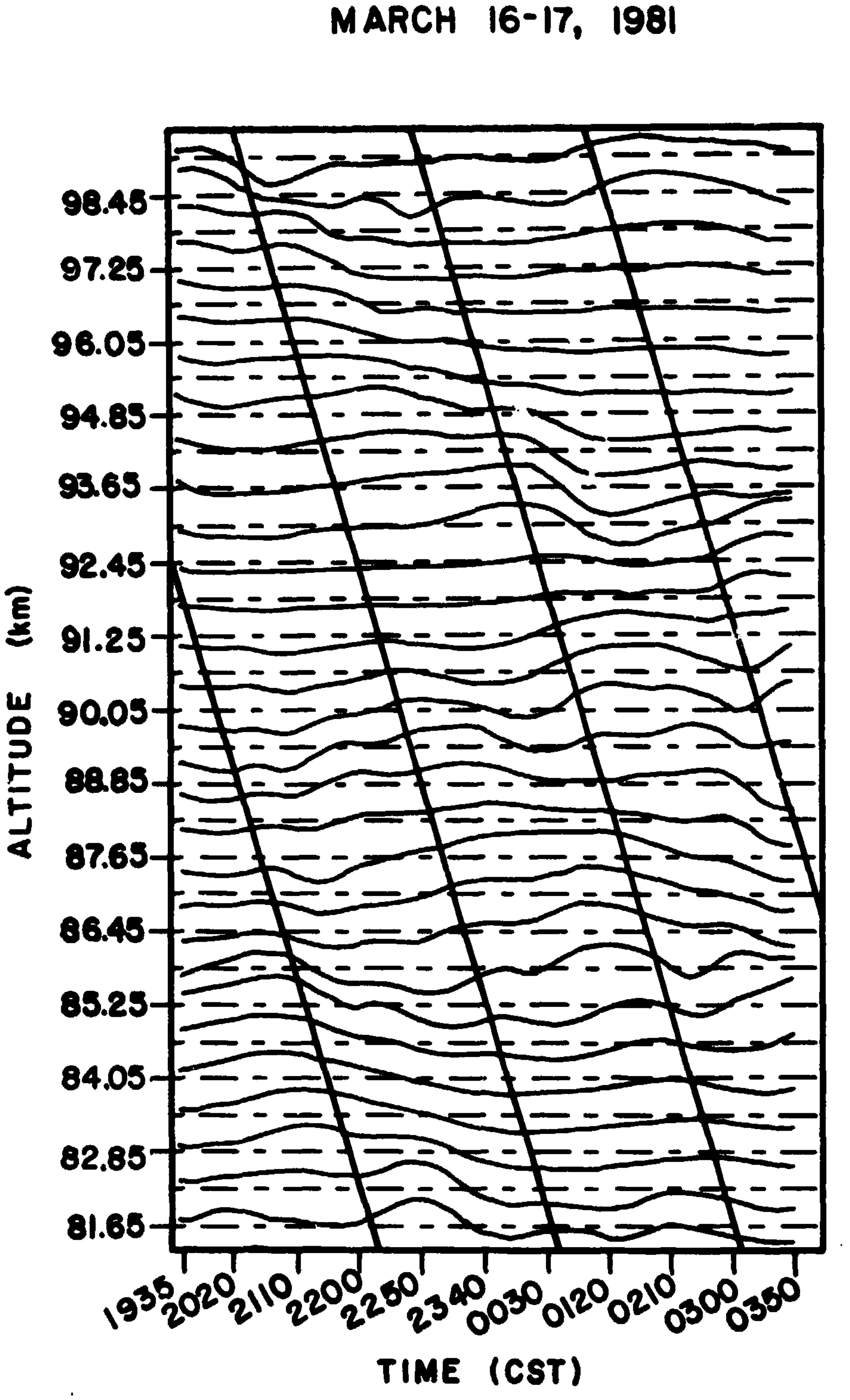

Figure 5.41 Plot of the temporal variations in sodium density observed on March 16-17, 1981. The spatial and temporal filter cutoffs were 0.476 km^{-1} and 0.0308 min^{-1}, respectively. These data have been normalized to remove the effects of large variations in column abundance.

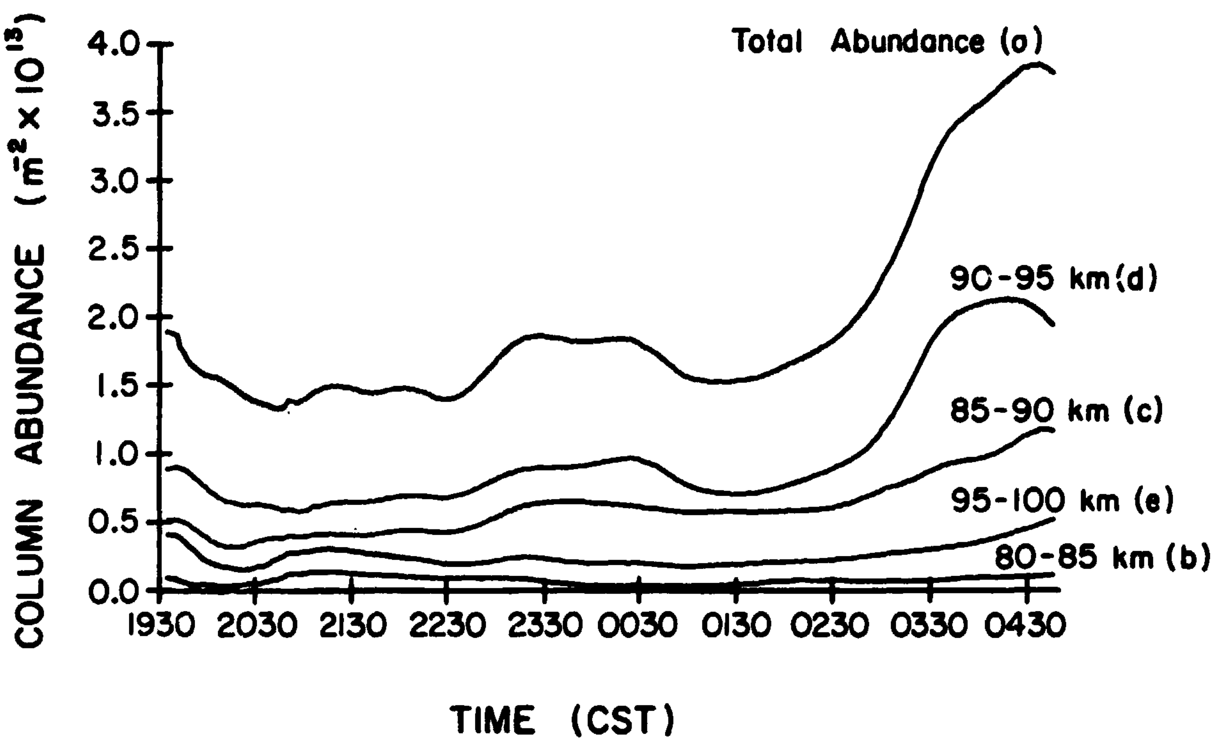

Figure 5.42 Temporal variations in column abundance observed on March 16-17, 1981. These data have been normalized to remove the effects of large variations in column abundance.

3.5×10^{13} atoms/m^2 during the 3 hours before ground sunrise. As in previous observations, most of this increase resulted from an increase in the column content above 90 km.

5.4 SUMMARY OF OBSERVATIONS

It has been demonstrated that many of the features in the sodium layer behave in a manner consistent with the layer density response to atmospheric waves. The features associated with the linear layer response are often observed. These include phase reversals in density fluctuations and larger density variations below the layer peak than above it. The periodic changes in thickness and the appearance and disappearance of bifurcations in the layer are probably associated with the layer response to atmospheric waves. In addition, the amplitude of atmospheric waves required to induce the observed sodium density perturbations are reasonable. Evidence of nonlinearities in the sodium layer response is evident and appears to cluster around the point of phase reversal in the linear response and around regions where large sodium density gradients are located. Spectral features in both temporal and spatial periodograms are consistent with a layer response to gravity waves.

An unexpected feature in these observations is the early morning sodium enhancement that was observed in every calibrated data set. This enhancement appears to be associated with the influx of atomic sodium in the upper half of the sodium layer. Yet, it is difficult to explain this enhancement with current theories of sodium layer chemistry. It may be the result of meteoric deposition of sodium. The morning enhancement which was also observed during our lidar measurements at the Goddard Optical Facility (Chapter 7) is discussed further in Chapter 8.

6. STEERABLE SODIUM LIDAR OBSERVATIONS

6.1 MEASUREMENT TECHNIQUE

Steerable lidar measurements have been used by some groups to study horizontal density variations in the sodium layer [Thomas et al., 1976; Clemesha et al., 1980]. These measurements are important for several reasons. The existence of significant horizontal structure in the steady state sodium layer (i.e. in the absence of atmospheric wave activity) will be reflected in the nature of the layer response to wave activity. As a result, the horizontal structure of the layer must be considered to accurately predict the layer response. If such horizontal structure exists, estimates of the magnitude and direction of the background wind may be made by observing the structure as it is carried along by the wind. Additionally, the horizontal wavelength of waves which are inducing density perturbations in the layer may be deduced from steerable observations. Without steerable measurements, this quantity must be inferred from estimates of the vertical wavelength and frequency of the gravity wave obtained by examining data collected at a fixed pointing angle.

In most cases, these measurements are made with a steerable lidar operating at a fixed elevation angle and pointed at several azimuth angles. Typically, three azimuth angles separated by 120° are chosen and spatial profiles of data are collected at each azimuth angle in a sequential manner. As a result, every third spatial profile is collected at the same azimuth angle. Large horizontal separations can be achieved by decreasing the elevation angle. Decreasing the elevation angle also introduces larger losses due to atmospheric scattering and absorption. Thus, more laser pulses are required to generate data profiles of equal quality as the elevation angle grows smaller. This effectively decreases the temporal resolution of the data since the rate at which profiles can be collected is reduced.

The reduction in signal strength as a function of elevation angle is shown in Figure 6.1. For mesospheric heights, the vertical atmospheric transmission factor, T, is approximately 0.6 [Bhattacharyya et al., 1978]. Thus, at an elevation angle of 60°, it is anticipated that only 64% of the energy received when the system is pointed at zenith will be available. At elevation angles below 40°, the effects of atmospheric attenuation become prohibitive. When three azimuth angles are scanned at an elevation angle of 60°, the temporal resolution is reduced to approximately 21% of the resolution which could be achieved with zenith measurements. This factor takes into account both atmospheric attenuation and the reduction in the profile collection rate resulting from the scanning of the lidar system. Therefore, insight into horizontal variations in sodium density can be obtained by sacrificing temporal resolution.

6.2 PAST OBSERVATIONS

The first steerable lidar measurements of the sodium layer were made between September, 1975 and January, 1976 at Winkfield, U. K. (51.4°N, 0.7°W) [Thomas et al., 1976]. Some of these observations indicated changes in the height distribution of sodium occuring over small horizontal separations (approximately 15 km) and short time periods (approximately 2 to 3 minutes). These density fluctuations were attributed to perturbations induced by gravity wave activity. The remaining observations, however, failed to indicate any significant differences over horizontal separations as great as 100 km.

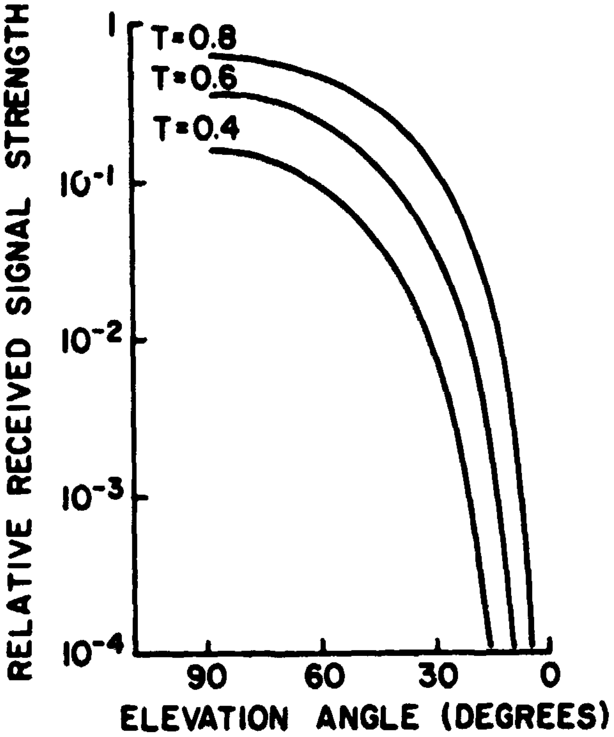

Figure 6.1 Variation in received signal strength as a function of the elevation angle (α) and the vertical atmospheric transmission (T) to the altitude of interest. For mesospheric heights and at a wavelength of 589.0 nm, $T \approx 0.6$ [Bhattacharyya et al., 1978].

Subsequent measurements by the same group (collected in August, 1976) led to the conclusion that the differences in density observed at three points separated by 80 km were due to horizontal variations in the steady state sodium layer rather than time variations in the density of a horizontally uniform layer [Thomas et al., 1977]. It should be noted, however, that in the majority of the data it was difficult to detect any systematic density variations and therefore no conclusions were reached. In addition, long term variations in sodium density could not be observed since the data sets did not span more than 2 hours.

More extended observations have been made in the southern hemisphere by Clemesha et al. [1981] at Sao Jose dos Campos, Brasil (23°S, 45°W). On the evening of July 21, 1979, ten hours of scanned data were collected at an elevation angle of 69.1° and at three azimuth angles. The horizontal separation of points achieved in this manner was roughly 60 km. A cross-correlation analysis was performed for data collected at heights between 82 and 99 km. Velocities were calculated from time-shifts derived in this manner. These velocities were found to vary in an oscillatory manner with amplitudes increasing with height. The east-west component of wind showed a vertical wavelength of approximately 10 km and the north-south component showed a vertical wavelength of 5 km. Wind velocities were estimated to vary between 6 and 146 m/s.

On August 25-26, 1979, using the same steerable system, this group observed a dramatic enhancement in sodium density [Clemesha et al., 1980]. This enhancement, associated with a tenfold increase in sodium density at 95 km, was restricted to a narrow time interval and a height interval of little more than 2 km. It was concluded that this enhancement was probably due to the influx of meteoric material. The time lags associated with the passage of this patch of enhanced sodium suggested a velocity of 205 m/s at a heading of 201°. In addition, it was estimated that the extent of the patch in the direction of motion was on the order of 100 km. The horizontal extent of the patch perpendicular to the direction of motion was considerably greater. Deducing the motion and shape of this patch illustrates one of the problems inherent in estimating velocities from this type of data. Both the shape and velocity of the patch affect the density variations observed at widely spaced points. A simple time lag approach is not sufficient to deduce wind velocities since the shape of the patch also determines the nature of the observed density variations.

6.3 EXPERIMENTAL RESULTS AT GSFC

In May and June, 1981, a 48 inch telescope located at the Goddard Space Flight Center Optical Test Site was used in conjunction with components of the University of Illinois sodium lidar system to make steerable lidar observations of the mesospheric sodium layer. The telescope facility, located at 39.1° N, 76.8° W, consists of a 48 inch Cassegrain astronomical telescope with Coudé focus and supporting equipment which enables this instrument to be used in a variety of laser ranging experiments. The telescope aperture area is approximately the same as the objective area of the receiving telescope used in Illinois. However, as well as making steerable measurements possible because of the sophisticated telescope mount, the high quality optics permit a small receiver field of view. This serves to reduce the noise counts due to background sky illumination. Photographs of the telescope are contained in Figures 6.2 and 6.3.

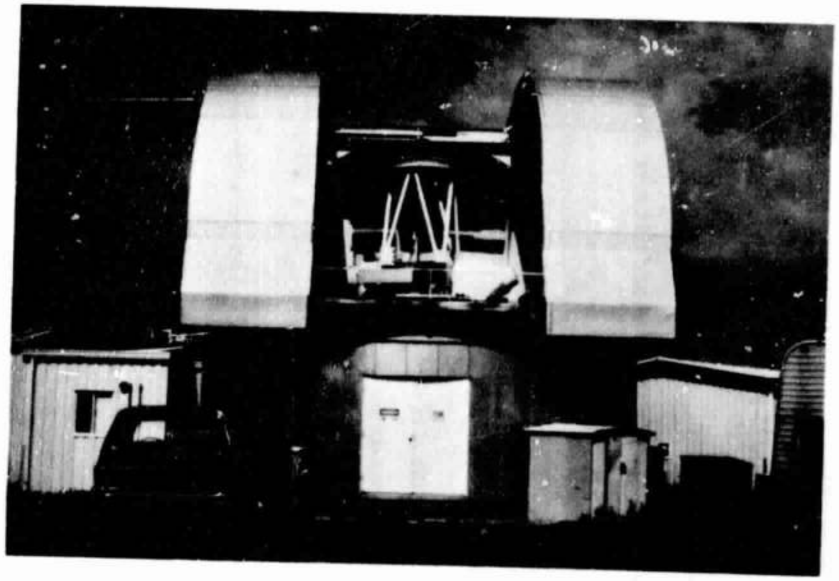

Figure 6.2 Photograph of the observatory housing the 48 inch telescope at the Goddard Space Flight Center Optical Test Site.

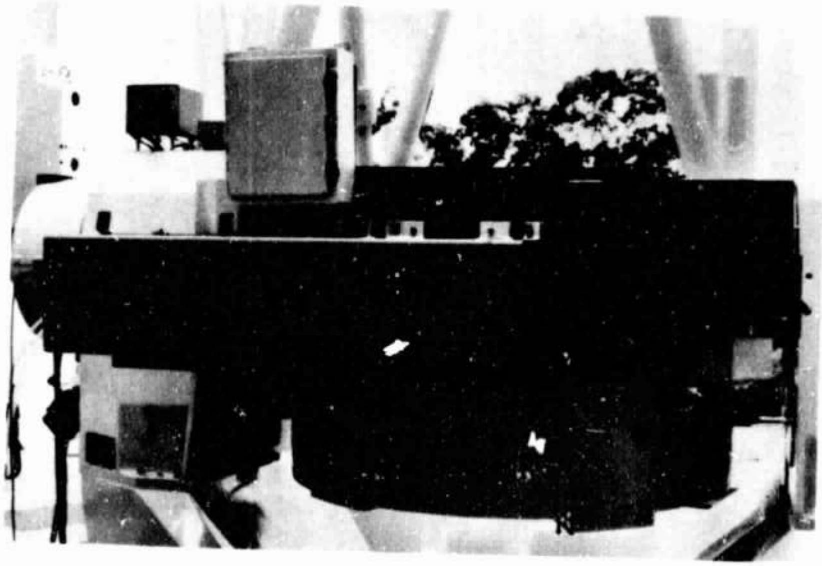

Figure 6.3 Photograph showing (from left to right) the location of the laser head, beam expander, and folding mirror on the base of the telescope.

A photograph of the telescope facility is shown in Figure 6.2. The telescope rests under the dome at the top of this photograph and access to the Coudé focus is on the ground floor. The inteference filter and PMT are positioned near the focal point of the telescope. No collimating lens is required due to the long focal length of the primary/secondary mirror combination in the telescope. The aperture of the focusing lens in the PMT cooled housing limits the telescope field of view to less than 1 mrad. This field of view can be reduced further by inserting a field stop iris in front of the PMT. Figure 6.3 contains a photograph of the telescope body showing the location of the laser head. The head was mounted on the telescope to insure that the laser beam tracked the telescope motions accurately. Coincidence of the transmitted laser beam and the telescope field of view was insured by adjusting the folding mirror (seen to the right of the laser head in Figure 6.3). Because the laser beam divergence angle was larger than the telescope field of view, a beam expander was inserted in the optical path between the laser and the folding mirror. This served to reduce the beam divergence to roughly 0.1 mrad. Laser tuning was monitored by examining the scattering of the laser output in a grating spectrometer (for rough tuning) and in a sodium cell (for fine tuning to the sodium D2 line). A fiber optic cable was used to couple the laser output to these instruments.

The position of the telescope was computer controlled and therefore the telescope was easily and rapidly positioned at the desired azimuth and elevation angles. The range of permissible angles was rather restricted, however, by mechanical considerations related to the laser head. The cables and hoses connecting the laser head to the dye reservoir and power supply were only 15 feet long. Since these last two items remained stationary, the azimuth angle could only be varied by 70° or 80°. In addition, the elevation angle could only be varied from 0° to 90° because of the telescope mount design. It was not possible to move the telescope past zenith. Steerable measurements were initially attempted on the evening of June 8-9, 1981. The telescope was scanned between three points; point A (azimuth=277°, elevation=90°), point B (azimuth=277°, elevation=70°), and point C (azimuth=307°, elevation=70°). A greater horizontal separation was achieved in later observations of the sodium layer. In order to examine 3 points which were equally spaced horizontally, the observations alternated between zenith measurements and measurements at an elevation angle of 60° while the azimuth angle was varied by 60°. Observations of sodium density at the increased horizontal spacing were made on June 17-18, 1981. The locations of the points at which sodium observations were made on both evenings are shown in Figure 6.4. Within the mechanical constraints mentioned above, an attempt was made to select points over sparsely populated regions in order to avoid areas where sodium vapor lights were used in large numbers. It should be noted that because data was gathered at depressed elevation angles, the horizontal separation of the observed points was a function of altitude. For the data collected on June 17-18, 1981, the observation points were separated by 50 km at an altitude of 100 km whereas at an altitude of 80 km the separation was only 40 km.

Nine spatial profiles of photocount data were collected on June 8-9, 1981. Each profile consisted of the integrated returns from 500 laser pulses. Because only three photocount profiles were collected at each pointing angle, it was not possible to temporally filter the data. Receiver range gate and delay times of 3 μs and 60 μs, respectively, were utilized at all three

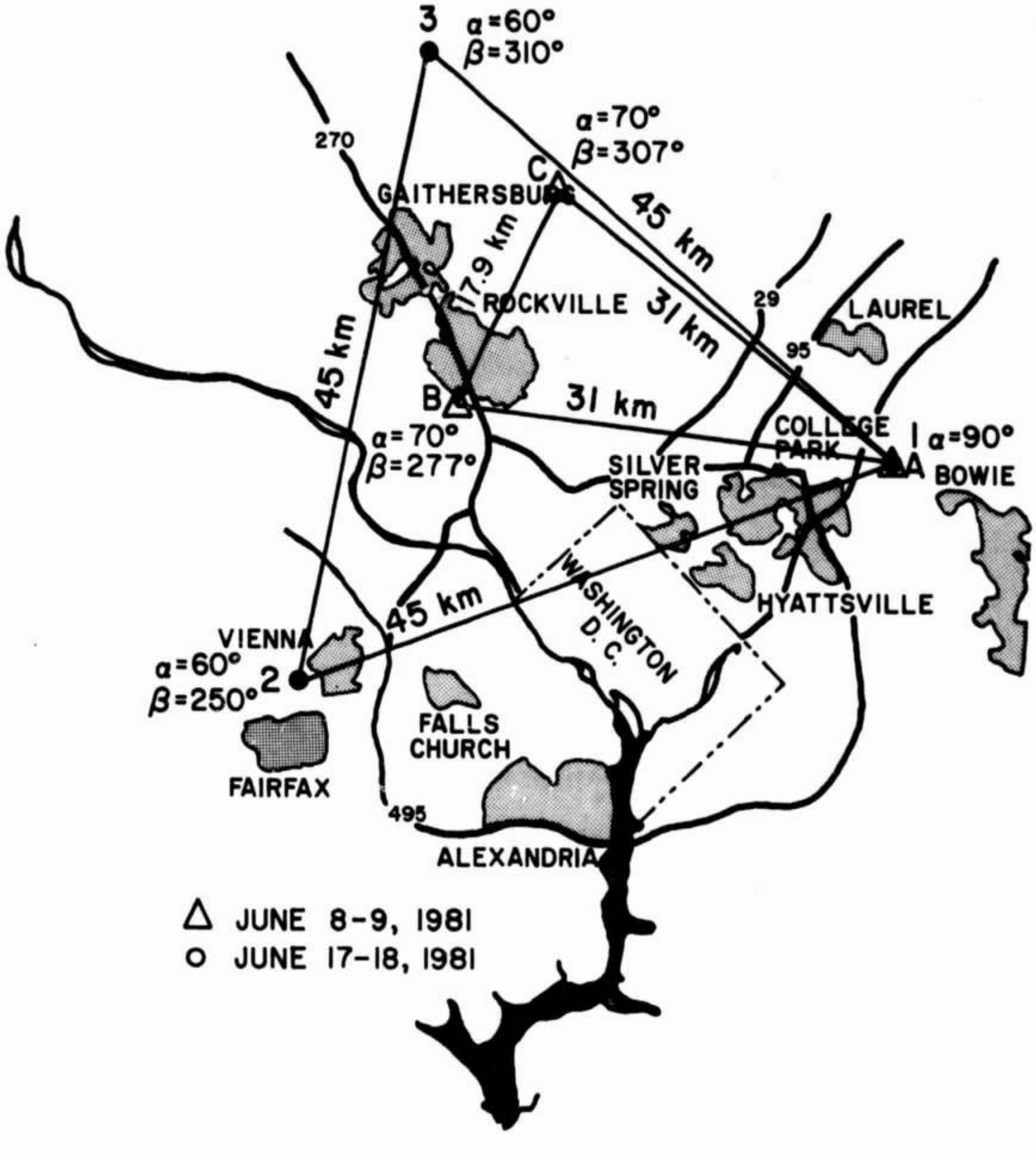

Figure 6.4 Horizontal spacing of observation points corresponding to an altitude of 90 km for measurements made on June 8-9, 1981 (points A, B, and C) and June 17-18, 1981 (points 1, 2, and 3). The elevation angle (α) and azimuth angle (β) are given for each point.

pointing angles. The ASP of the three profiles collected at zenith is plotted in Figure 6.5. The large peaks at 0.12 km^{-1}, 0.17 km^{-1}, and 0.28 km^{-1} indicate that wavelike features are present. These data were spatially processed in the manner described in Chapter 3. A spatial filter with a cutoff at 0.4 km^{-1} was applied to the zenith data. An effective cutoff of 0.4 km^{-1} for vertical variations in sodium density can be achieved for the remaining profiles by taking into account the elevation angle of off-zenith observations. As a result, a spatial filter with a cutoff at 0.376 km^{-1} was applied to the data collected at a zenith angle of 30^{o}.

Plots of the estimated sodium profiles for each pointing angle are shown in Figure 6.6, 6.7 and 6.8. A narrow, sharply defined peak in sodium density at 95 km is apparent in all three figures. This peak is approximately 2.5-3.0 km thick. The main layer peak appears near 90 km. Additionally, a peak in density near 102 km evolves during the 90 minutes covered by these observations. It is unusual to observe distinct features at such high altitudes. Above the main peak, layer features are consistent at each pointing angle. Below the layer peak, however, features are not so well behaved. Features below 90 km in the profiles collected at points B and C are similar whereas the profiles collected at point A differ more markedly from these. To illustrate, at 0346 EDST (point B) and 0356 EDST (point C), peaks in sodium density at 84 and 87 km and a valley at 87.5 km are observed. At 0406 EDST (point A), a peak at 84 km is apparent but no valley is observed at 87.5 km. The similarity in profiles at B and C is not surprising since B and C are closer to each other than to point A. The variability of the layer below 90 km indicates that variations in sodium density with small horizontal scales (perhaps as small as 30 km) are present. Layer features also appear to

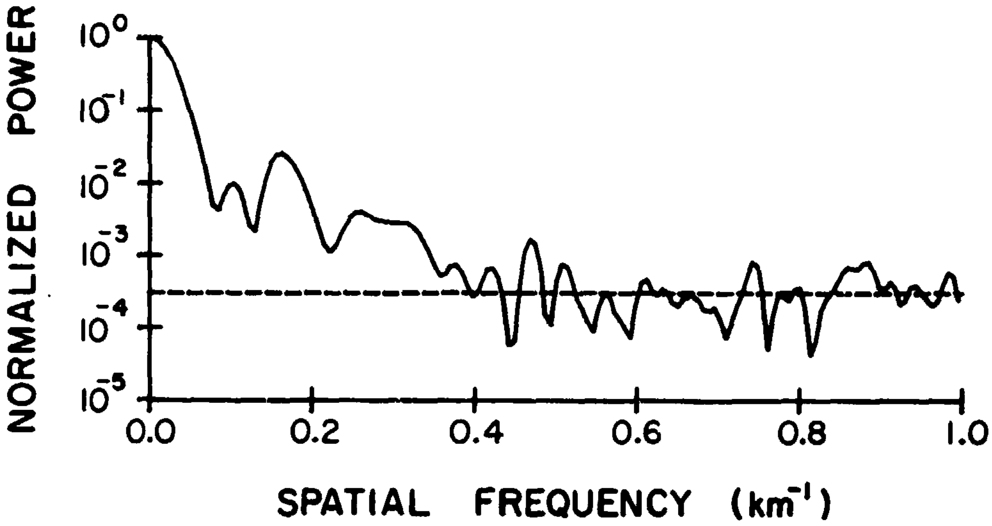

Figure 6.5 Normalized average spatial periodogram of zenith data collected on June 8-9, 1981.

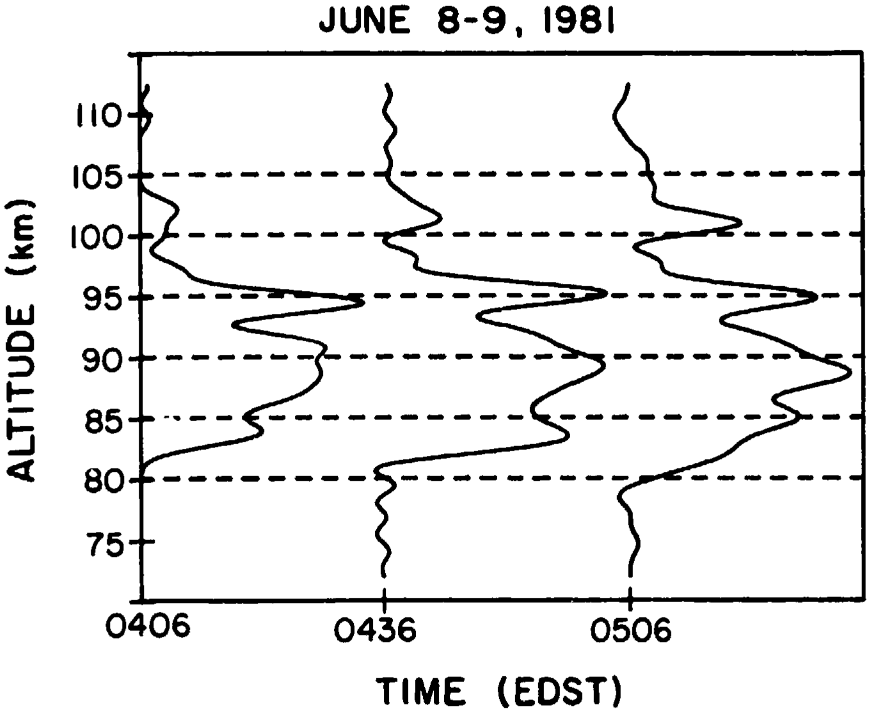

Figure 6.6 Altitude profiles of the estimated sodium density observed at point A ($\alpha = 90^{\circ}$) on June 8-9, 1981. The spatial filter cutoff was at 0.4 km^{-1}.

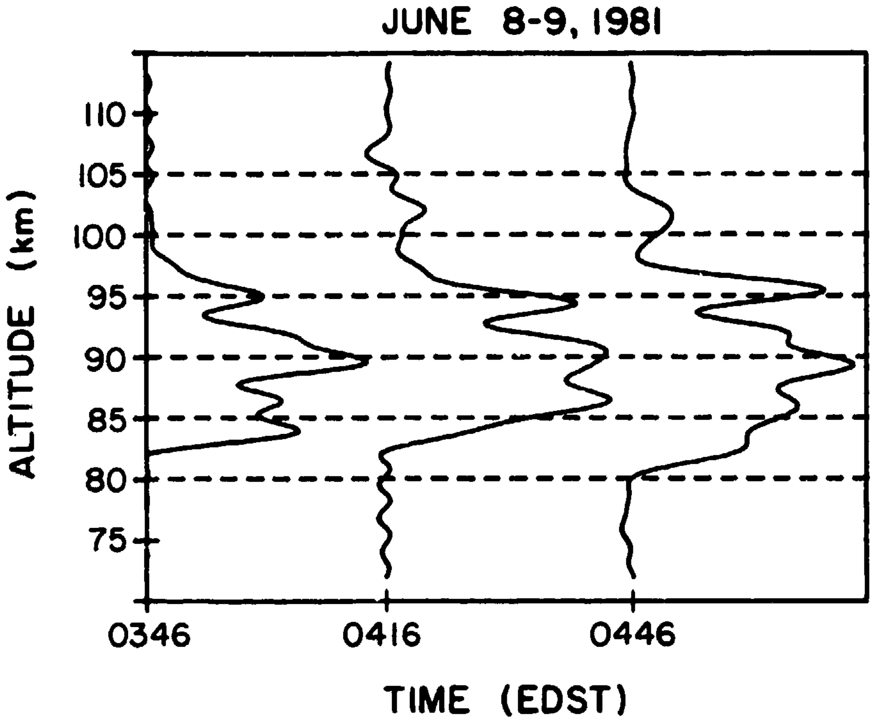

Figure 6.7 Altitude profiles of the estimated sodium density observed at point B ($\alpha = 70^{\circ}$, $\beta = 277^{\circ}$) on June 8-9, 1981. The spatial filter cutoff was chosen to give an effective vertical cutoff at 0.4 km^{-1}, as discussed in the text.

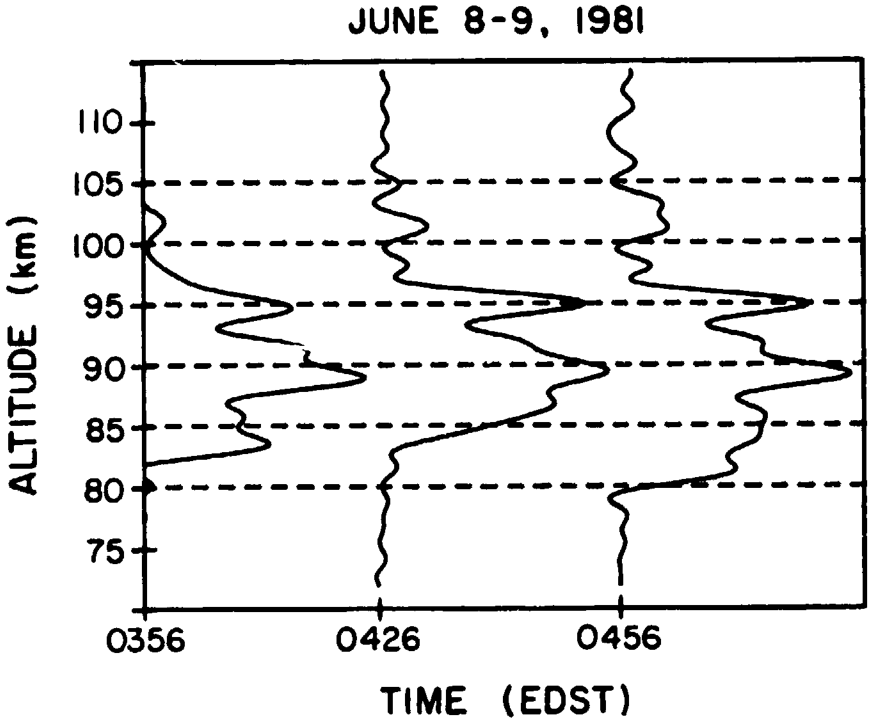

Figure 6.8 Altitude profiles of the estimated sodium density observed at point C (α = 70°, β = 307°) on June 8-9, 1981. The spatial filter cutoff was chosen to give an effective vertical cutoff at 0.4 km^{-1}, as discussed in the text.

change significantly within a 60 minute period. Unfortunately, these observations span only 1.5 hours and it is not possible to deduce details concerning the horizontal structure of the layer or the direction of propagation of atmospheric waves which may be present.

Because of poor weather, additional data could not be collected until June 17-18, 1981. On this evening, a series of 81 spatial profiles were collected. Recall that three points, separated horizontally by 45 km at an altitude of 90 km, were observed (Figure 6.4). Each spatial profile consisted of the integrated returns from 500 laser pulses. A 3 μs range gate and a 198 μs delay factor were used in obtaining this data. The delay factor was chosen to insure that Rayleigh scattering from 30 km as well as sodium returns could be received as the elevation angle was varied from 90° to 60°. The integration time for each profile was approximately 2 minutes and a new profile of data was started every 4 minutes. Thus, 12 minutes separated data profiles collected at the same pointing angle. Because of a laser malfunction, data was not collected between 0120 and 0200 EDST. For the purpose of temporal filtering, an interpolation procedure was utilized to provide estimates of the missing profiles. The temporal and spatial processing techniques described in Chapter 3 were adapted to process the off-zenith data.

The average temporal periodogram for zenith measurements is shown in Figure 6.9. To insure that no temporal variations in sodium density were inadvertantly removed, a temporal filter cutoff at 0.033 min^{-1} was chosen and applied to the data collected at all three pointing angles. The average spatial periodograms of the temporally filtered data are shown in Figures 6.10, 6.11 and 6.12. For off-zenith measurements, spatial frequencies have been scaled to reflect spatial photocount variations in the vertical rather

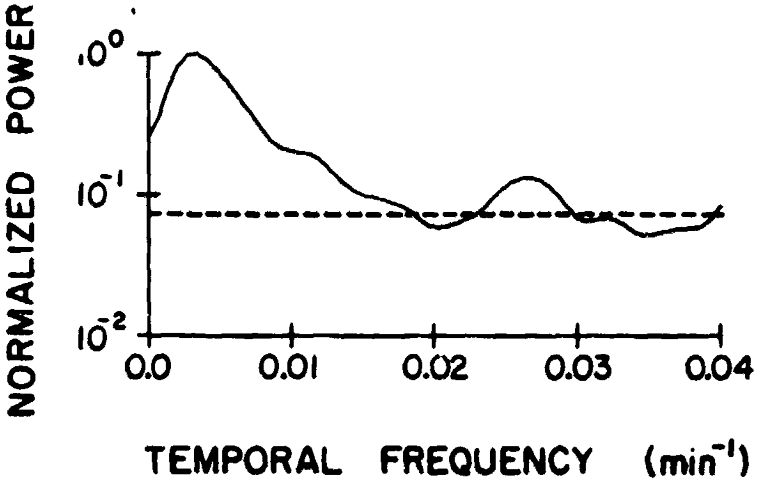

Figure 6.9 Plot of the normalized average temporal periodogram of zenith data collected on June 17-18, 1981.

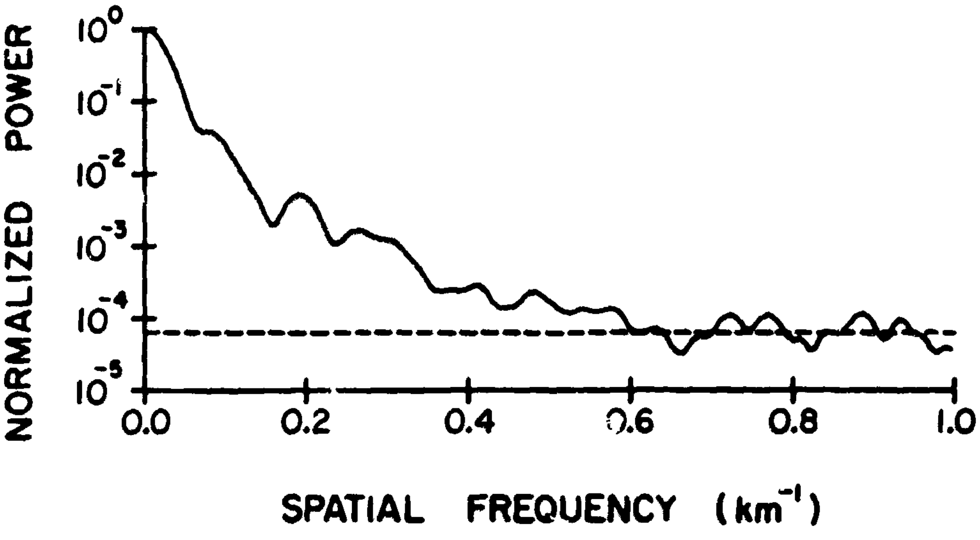

Figure 6.10 Plot of the normalized average spatial periodogram of temporally filtered data collected on June 17-18, 1981 at point 1. The temporal filter cutoff was at 0.033 min^{-1}.

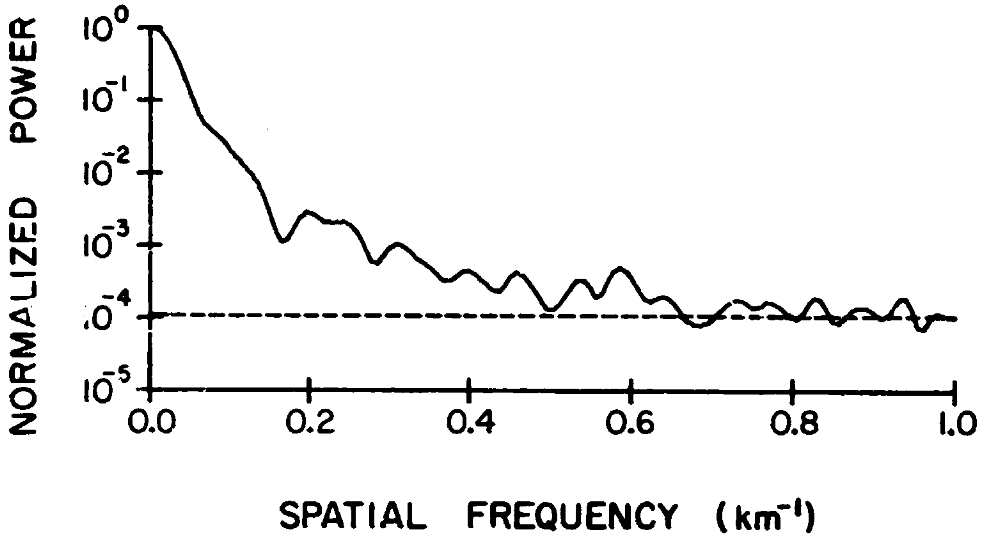

Figure 6.11 Plot of the normalized average spatial periodogram of temporally filtered data collected on June 17-18, 1981 at point 2. The temporal filter cutoff was at 0.033 min^{-1}.

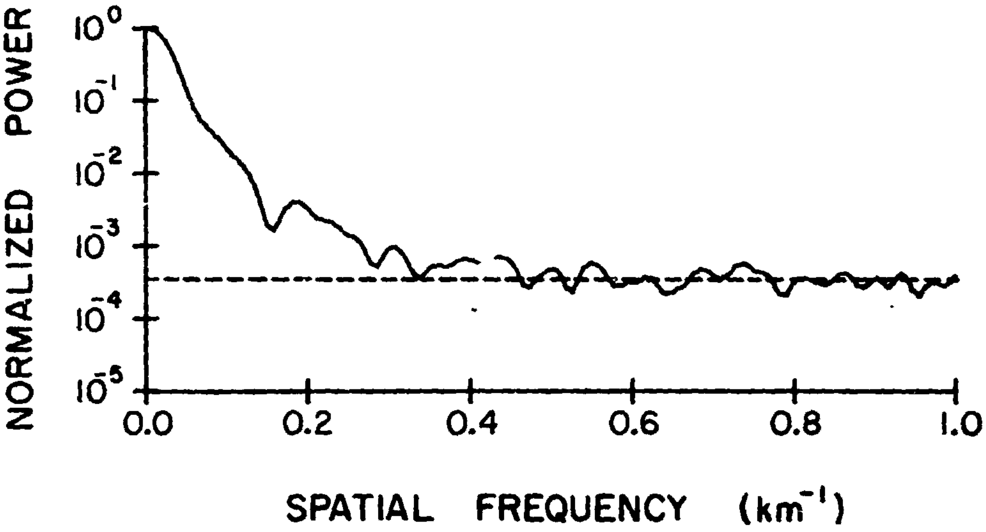

Figure 6.12 Plot of the normalized average spatial periodogram of temporally filtered data collected on June 17-18, 1981 at point 3. The temporal filter cutoff was at 0.033 min^{-1}.

than the slant range. As a result, the off-zenith periodograms may be compared directly with the periodogram of zenith photocount data. A spatial filter with a cutoff at 0.4 km^{-1} was applied to the temporally filtered zenith data and a spatial filter with a cutoff at 0.345 km^{-1} was applied to the off-zenith data. Taking into account the elevation angle of the off zenith data, this last filter gives an effective cutoff at 0.4 km^{-1} in the vertical direction. Thus, wavelike features with vertical wavelengths of 2.5 km or less will be removed from all three sets of data while features with longer wavelengths will be retained.

The two-dimensionally filtered data is presented in Figures 6.13, 6.14 and 6.15. It is evident that the data collected at each pointing angle are very similar. The most significant difference is the presence of a pronounced peak near 95 km at the start of the observation period in data sets 1 and 2 and its absence in data set 3. A great deal of activity is evident in all three data sets. In each case, the peak located near 98 km is observed to move downward, reaching 95 km by 0430. In addition, the sodium density associated with this peak approaches the density of the main peak at times. This behavior is observed in all three data sets. All three data sets also contain very large density gradients at the bottomside of the layer. In some cases, the sodium density increases from a very small to a very large value in 0.9 km. The spatial profile in Figure 6.16 contains such a feature. Sodium densities have been calculated from temporally filtered photocount data and two-dimensionally filtered data. In each case, the sodium density is observed to increase from 0.07 of its peak value at 82.35 km to 0.63 of its peak value at 83.25 km. As a result, the vertical sodium density gradient in this region is approximately 6.5×10^5 Na atoms/m^4.

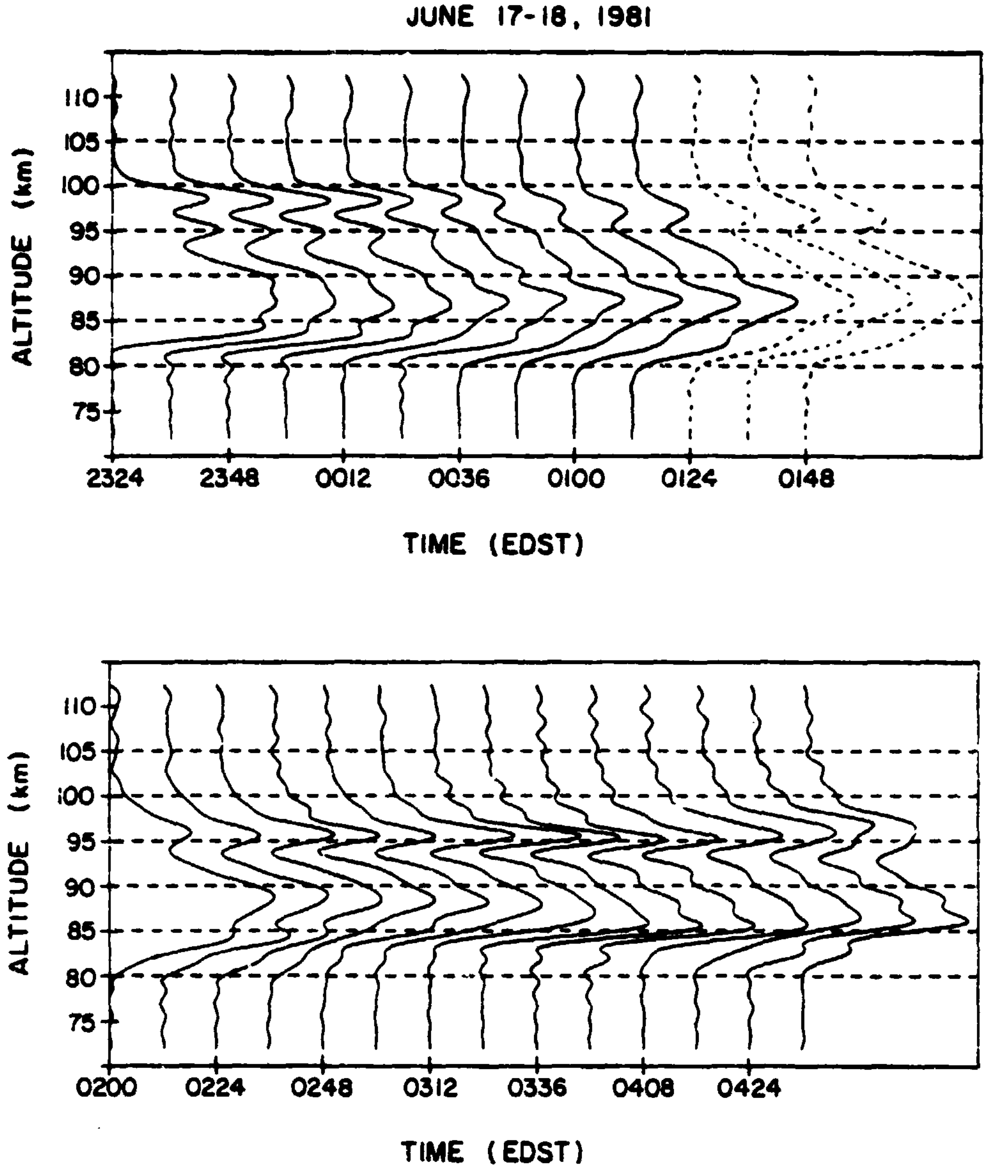

Figure 6.13 Altitude profiles of sodium density observed on June 17-18, 1981 at point 1 ($\alpha = 90^{\circ}$). The spatial and temporal filter cutoffs were 0.4 km^{-1} and 0.033 min^{-1}, respectively. Interpolated data are indicated by dashed lines.

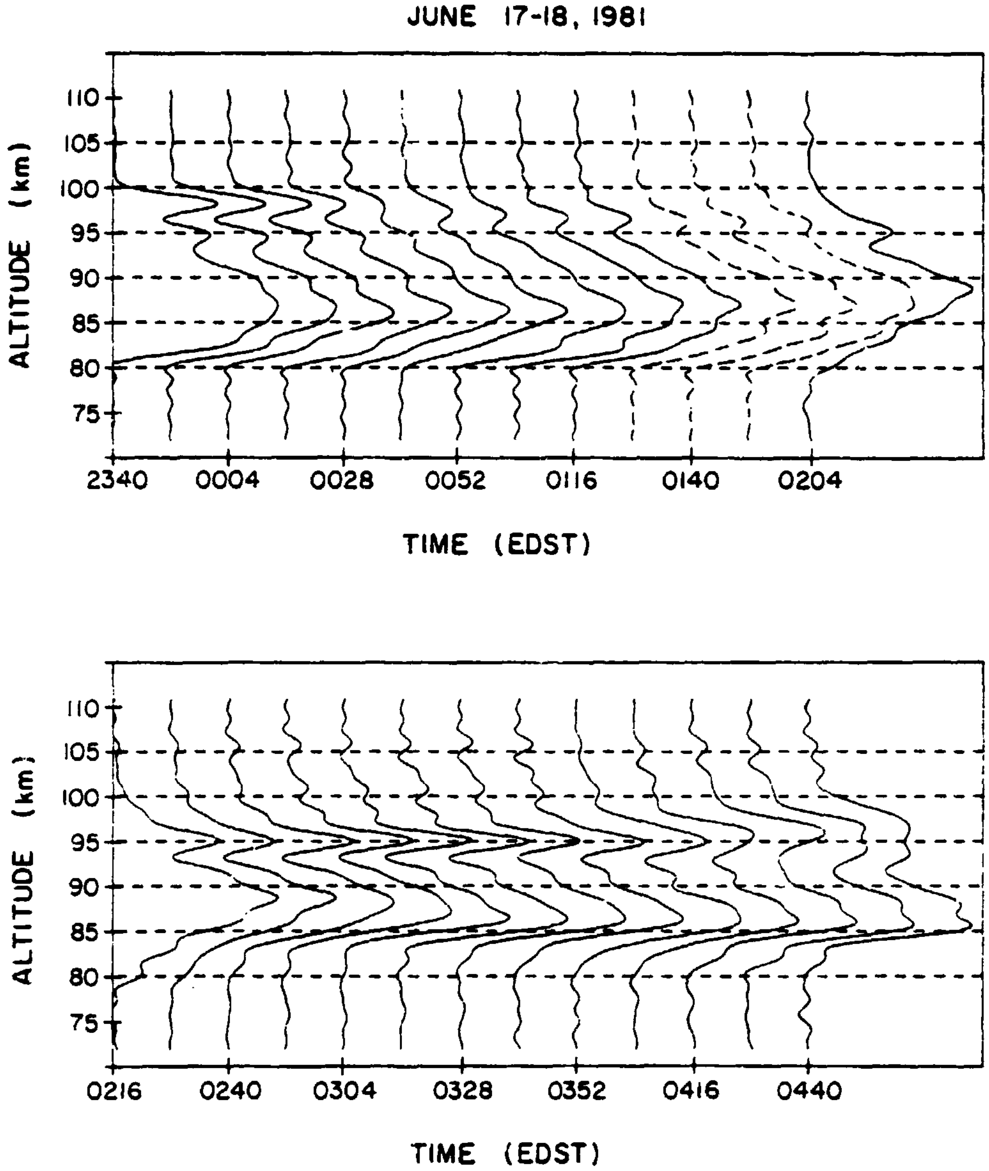

Figure 6.14 Altitude profiles of sodium density observed on June 17-18, 1981 at point 2 ($\alpha = 60^\circ$, $\beta = 250^\circ$). The filter parameters are given in the text. Interpolated profiles are indicated by dashed lines.

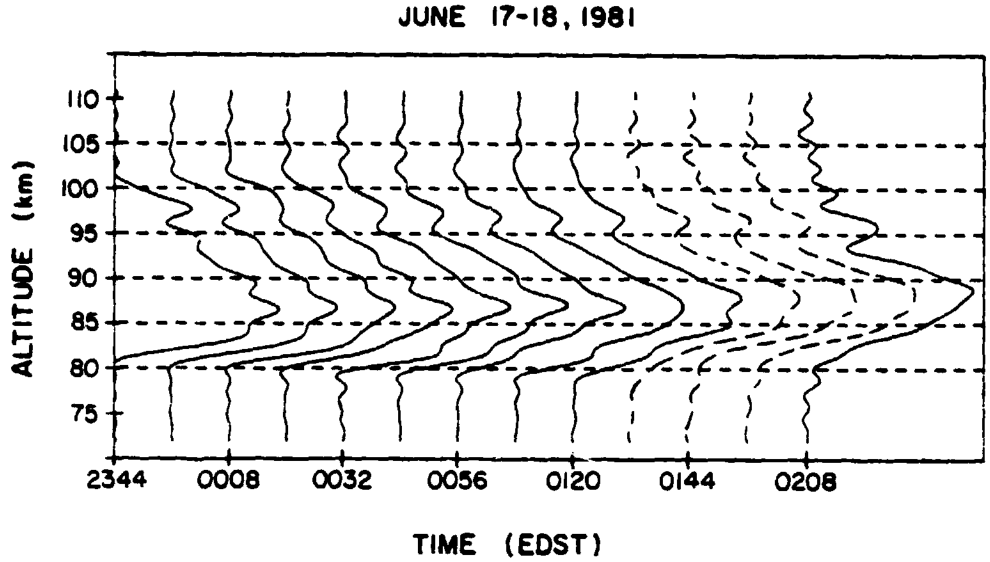

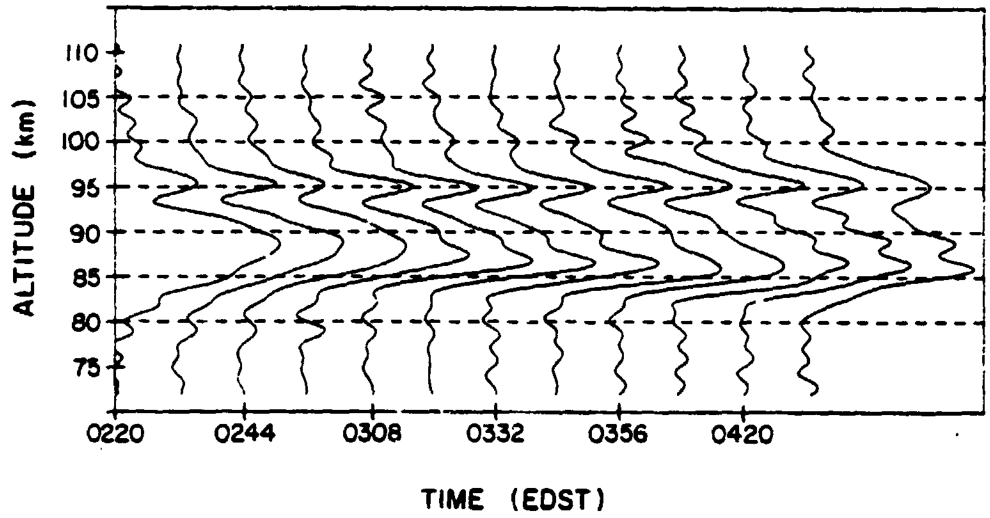

Figure 6.15 Altitude profiles of sodium density observed on June 17-18, 1981 at point 3 ($\alpha = 60^0$, $\beta = 310^0$). The filter parameters are given in the text. Interpolated profiles are indicated by dashed lines.

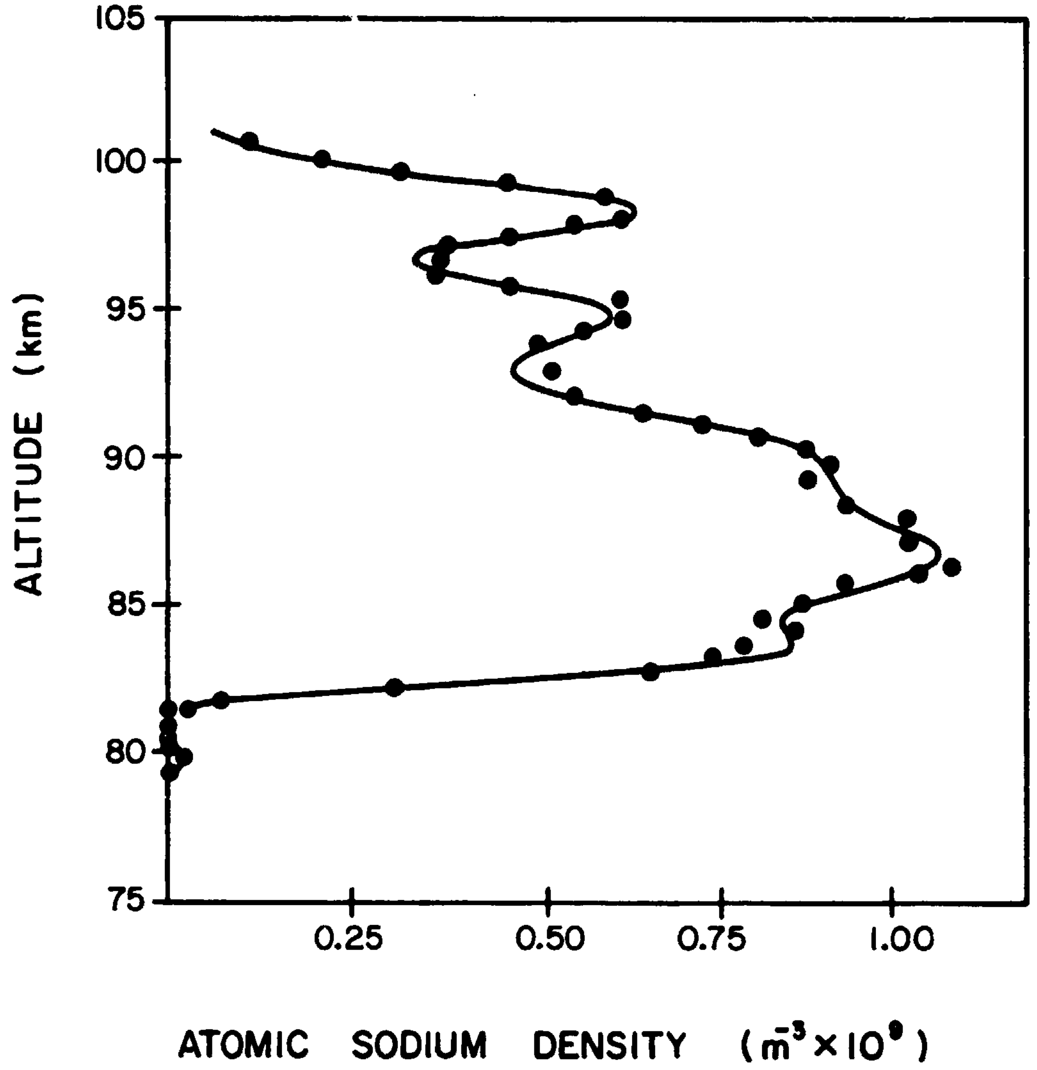

Figure 6.16 Plot of the spatial profile of density observed at 2348 EDST at position 1. The circles are range corrected photocount data and the smooth curve is two-dimensionally filtered photocount data.

Figure 6.17 shows the temporal variations in sodium density associated with data set 1 (the zenith measurement). These variations are plotted in the same fashion as the temporal profiles presented in Chapter 5. It is difficult to discern any evidence of a systematic movement of features. No phase progression is clearly evident and therefore it is difficult to conclude that wave activity is causing the density variations observed in these data sets. By plotting the locations of peaks and valleys in the layer, it should be possible to determine the direction of propagation and horizontal wavelength associated with waves inducing density perturbations in the layer. Figure 6.18 contains such a plot. Unfortunately, it is not clear that a single wave is responsible for the observed motions of the layer's peaks and valleys. If a single wave were responsible for these density variations (assuming there were no horizontal structure to the steady state sodium layer), the curves in this figure would differ from each other only by a phase delay. However, this is not the case. The observed activity could be the result of the interactions of several waves or it could indicate that a sodium layer with horizontal structure was being swept overhead by the mesospheric mean winds. The motion of the layer peak near 88 km is consistent with the motion of a patch of enhanced sodium density moving at approximately 90 m/s towards the southwest (at a heading of 220°). The extent of the patch in the direction of motion is approximately 300 km. It is not possible to accurately determine the extent of the patch in the direction perpendicular to the direction of motion. These deductions were made by examining the upward movement of the layer peak near 0230 EDST. The motion of the layer peak which, at 2330 EDST, is located at 98 km does not indicate the presence of a region of enhanced sodium density sharing the characteristics listed above. In fact, the peak

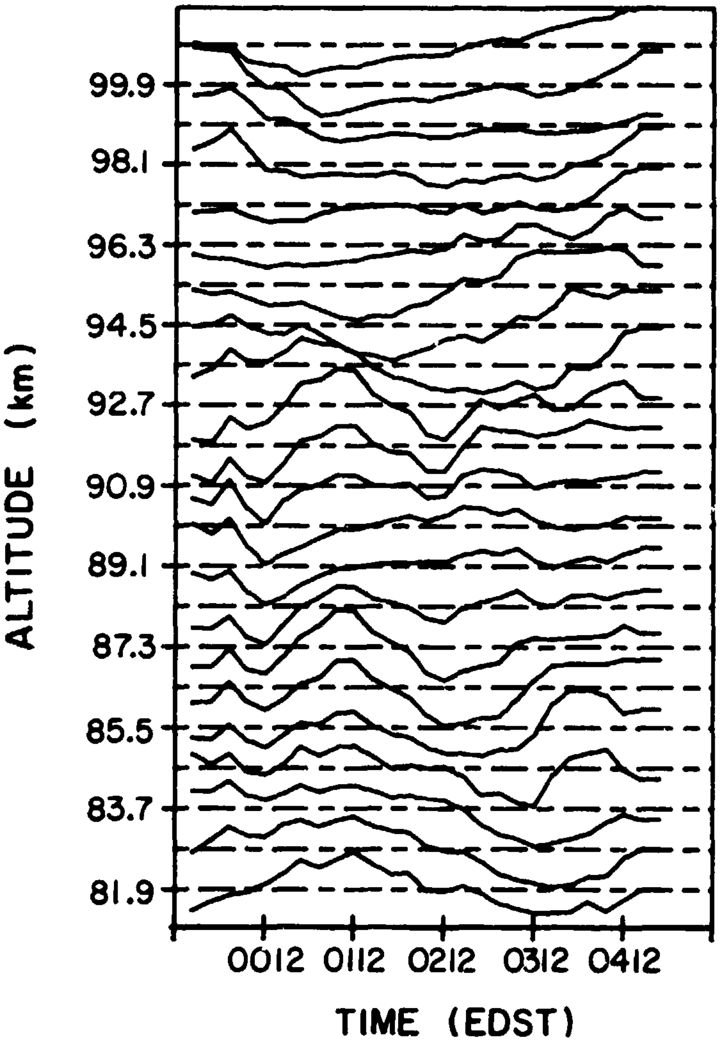

Figure 6.17 Temporal variations in sodium density observed at point 1 on June 17-18, 1981. The spatial and temporal cutoffs are at 0.4 km^{-1} and 0.033 min^{-1}, respectively.

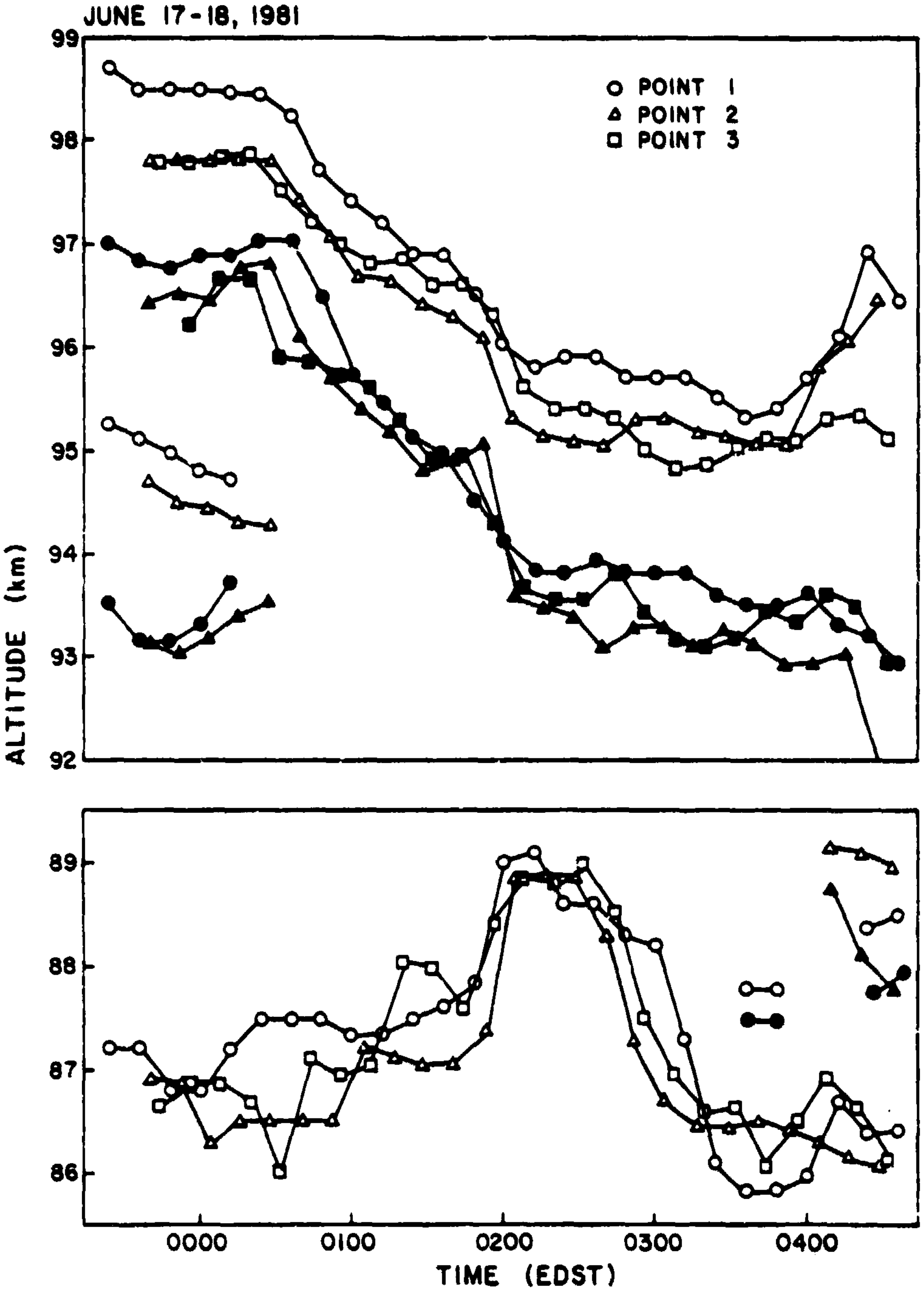

Figure 6.18 Movement of the peaks and valleys in two-dimensionally filtered data collected on June 17-18, 1981. Dark symbols represent valleys; light symbols represent peaks.

observed at position 1 is consistently above the peaks observed at positions 2 and 3. The conjectured region of enhanced sodium density responsible for the motion of the layer peak at 88 km does not appear to extend to 98 km. A more complete explanation of the observed density variations would include the effects of wave activity and the effects of a mean wind on a horizontally structured layer.

Figure 6.19 shows the time variations in column abundance for each pointing angle. The spatial profiles of sodium density used to calculate the column abundance have been spatially, but not temporally, filtered. The same spatial filter cutoffs used to obtain the profiles in Figures 6.13, 6.14 and 6.15 have been used. The laser malfunction which interrupted data collection at 0120 also rendered the laser tuning suspect. It is possible that the spectral output linewidth of the laser was increased as a result of optical misalignment in the laser cavity. This would have the effect of decreasing the effective sodium backscatter cross section. As a result, the estimates of column abundance for data collected after 0200 may be too low. Relative in these estimates after the interruption in data, however, will remain accurate. An examination of Figure 6.19 seems to confirm this suspicion. The calculated column abundances indicate a sudden drop between 0120 and 0200. After 0200, however, a steady rise in column abundance at all three pointing angles is apparent. This is consistent with data collected at Urbana, Illinois which is presented in Chapter 5 indicating a morning enhancement in sodium density. As indicated in these data sets, this enhancement begins near 0300 (about 3 hours before ground sunrise). The differences observed in the column abundance measurements after 0200 between each pointing angle may indicate that there was significant horizontal structure to the sodium layer.

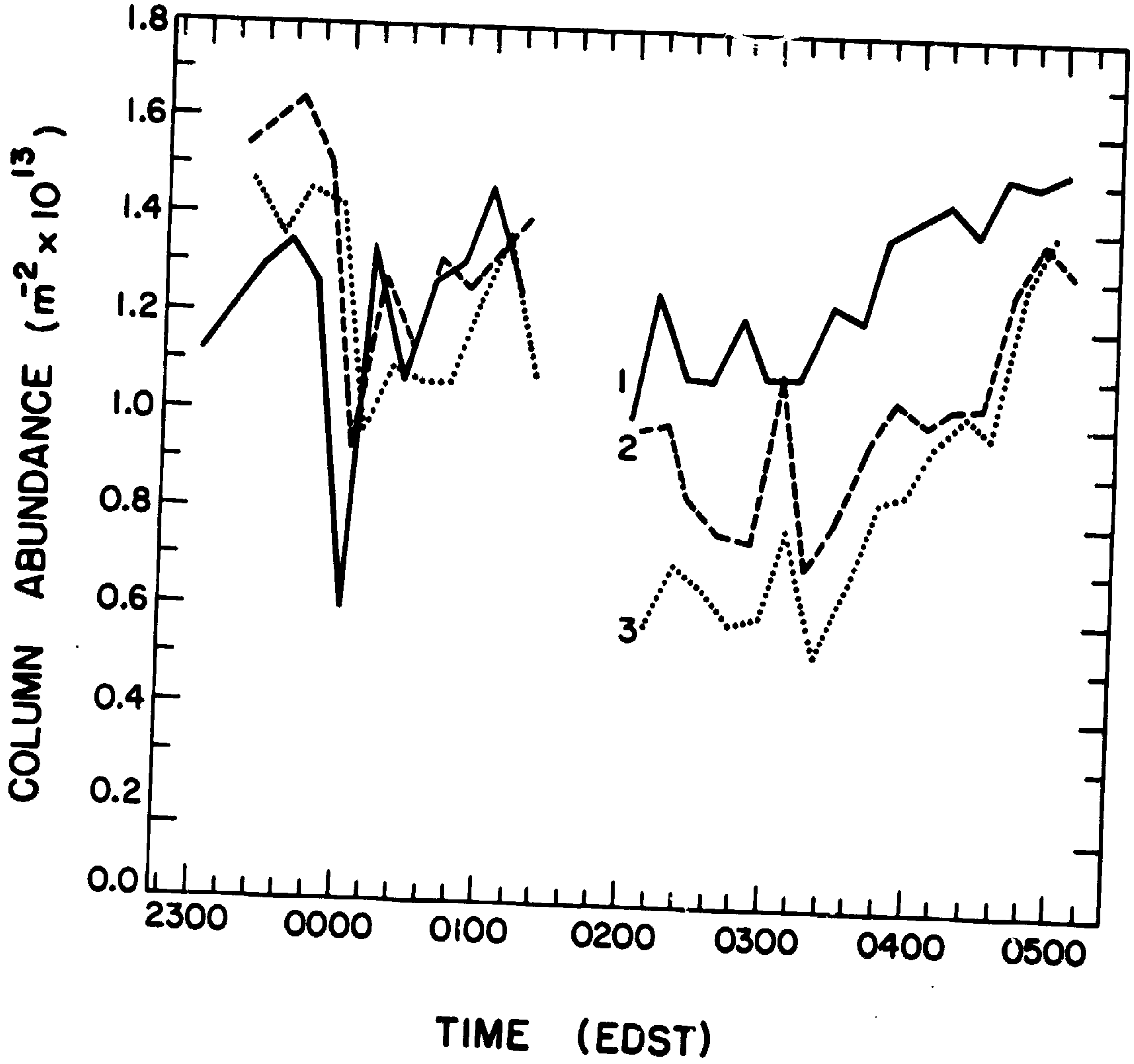

Figure 6.19 Column abundance variations observed on June 17-18, 1981. These data have been spatially but not temporally filtered. The spatial filter cutoffs were the same as used in Figures 6.13, 6.14, and 6.15. Observations at points 1, 2, and 3 are indicated by solid, dashed, and dotted lines, respectively.

A general eastward increase in column abundance is observed. The horizontal gradient in column abundance calculated at 0400 EDST indicates the maximum increase occurs at a heading of 110° (just south of due east). This is interesting since the region of highest meteor deposition occurs in this general direction at 0400. The region of maximum meteor deposition rate is inferred from meteor radar observations. These observations typically indicate a maximum meteor radar echo rate occurs near 0600 local time [McKinley, 1961]. The differences in column abundance at each pointing angle become smaller as the sodium density enhancement progresses and sunrise approaches.

Before 0130, the column abundances at each pointing angle were roughly equal. The sharp decrease in abundance near 0000, observed at all three points, is probably an artifact that arose as a consequence of a drift in laser tuning. Laser tuning was checked after each zenith photocount profile was collected to minimize problems of this type. After 0200, the abundance variations at points 2 and 3 closely track each other. A sudden increase in abundance at 0300 EDST is seen at these two points but not at point 1. No periodic variations in column abundance which could clearly be associated with atmospheric waves are evident.

7. LIDAR OBSERVATIONS OF STRATOSPHERIC AEROSOLS OVER URBANA, ILLINOIS

7.1 INTRODUCTION

A major eruption destroyed the summit of Mt. St. Helens in southern Washington (46.20 N, 122.18 W) and projected massive amounts of volcanic ash and dust into the stratosphere on May 18, 1980. Prevailing winds carried the dust clouds eastward over much of the United States. The vertical plume of dust and ash initially rose to more than 19 km above sea level (as measured by Portland airport's weather radar). The subsequent advance of clouds of dust at 3km, 9km, 16km and 18 km altitudes are shown in Figure 7.1 [SEAN Bulletin, 1980]. Some of these clouds reached central Illinois by noon on May 20. On May 25, the dust clouds reached Europe [Meixner et al., 1981; Hauchecorne et al., 1980; Ackerman et al., 1980]. Initially, layers of dust were located at low altitudes (near 13 km). Near July 10, however, stratospheric layers near 21 km were observed over France [Lefrere et al., 1981] and Italy [D'Altorio et al., 1981]. The initial dust clouds passed Japan on May 27 [Iwasaka and Hayashida, 1980] and were observed over Hawaii on July 7 [Deluisi et al., 1980].

In order to take advantage of this geophysical event, the Urbana lidar was reconfigured to observe scattering from stratospheric heights. Measurements of the height distribution of the volcanic dust began on May 20th. Receiver range gate and delay factors of 2 μs and 4 μs, respectively, were commonly utilized in collecting the data presented here. The laser output wavelength was 589.0 nm. The combined effects of receiver range gate and laser pulse shape limited the altitude resolution to approximately 750 meters. Receiver aperture and laser energy were reduced from the values listed in Tables 2.1

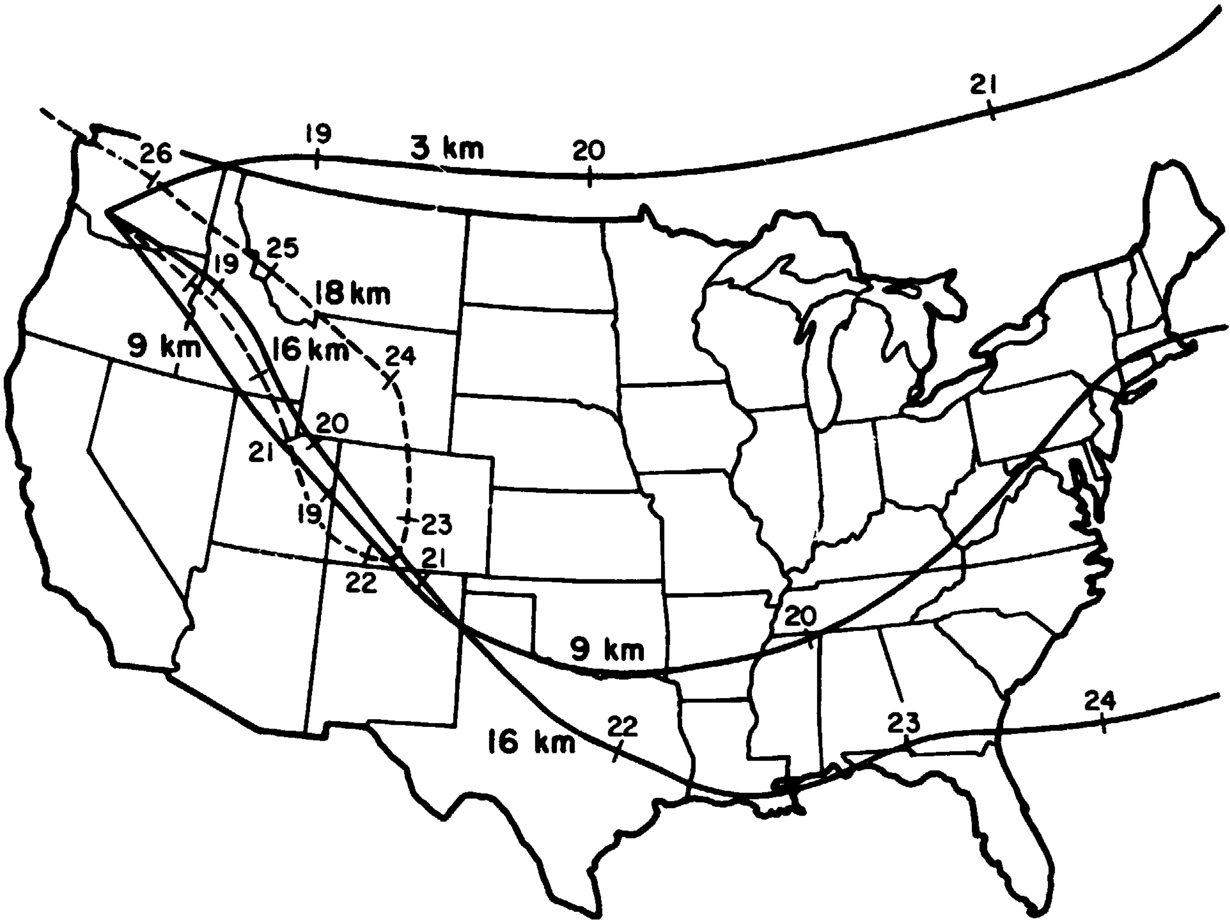

Figure 7.1 Paths traveled over North America by clouds of volcanic ash at 3 km, 9 km, 16 km, and 18 km altitude. Tick marks along each line show positions of ash cloud fronts at that altitude every 24 hours (at noon GMT). The date at each tick mark is indicated. [Sean Bulletin, 1980].

C-3

and 2.2 to prevent overloading of the PMT from the strong low altitude Rayleigh returns. Because the laser and receiving telescope were separated by 10 meters, their fields-of-view did not completely overlap for altitudes below 6 km. Individual profiles were obtained by firing the laser and accumulating the returns from each laser pulse over periods ranging from 2 to 10 minutes.

7.2 LIDAR MEASUREMENTS OF THE BACKSCATTER RATIO

Lidar aerosol measurements are usually made by utilizing elastic backscattering in which the received signal is at the same wavelength as the transmitted laser pulse. The lidar equation (equation 2.1) may be used to express the relationship between the expected photocount and the volume backscatter coefficient.

$$\langle x(z)\rangle = \frac{\eta A_R}{h\nu}\left(\frac{Tc}{2}\right)P\frac{\beta(z)}{z^2}\exp\left[-2\int_0^z ds\,\alpha(s)\right] + \lambda_n T \qquad (7.1)$$

where $\langle x\rangle$ = expected photons detected in the interval $(t-T,\ t)$

η = overall system efficiency

A_R = receiver aperture area (m^2)

$h\nu$ = energy of one photon at frequency ν (J)

λ_n = photocount rate due to background and dark noise (s^{-1})

P = laser pulse energy (J)

β = volume backscatter coefficient (m^{-1})

α = atmospheric extinction coefficient (m^{-1})

c = speed of light (m/s)

T = receiver gate time (s)

Because elastic backscatter is considered rather than resonant scattering, the lifetime of the excited state included in equation (2.1) is no longer of concern. In addition, we have ignored the effects of laser pulse shape on the received photocounts.

Both the volume backscatter and atmospheric extinction coefficients are composed of molecular (Rayleigh) and aerosol (particulate) components.

$$\beta(z) = \beta_R(z) + \beta_A(z) \tag{7.2}$$

$$\alpha(z) = \alpha_R(z) + \alpha_A(z) \tag{7.3}$$

It is often convenient to analyze lidar aerosol data in terms of the backscatter ratio, $R(z)$. This is defined as the ratio of the total backscatter coefficient to the Rayleigh backscatter coefficient.

$$R(z) = \frac{\beta_R(z) + \beta_A(z)}{\beta_R(z)} = 1 + \frac{\beta_A(z)}{\beta_R(z)} \tag{7.4}$$

A common means of determining $R(z)$ exists which depends upon scattering from an altitude at which β and the losses due to atmospheric attenuation are known [McCormick, 1975; Russel et al., 1979]. This altitude is known as the normalization height, z^*. The losses due to atmospheric attenuation were accounted for in equation (7.1) by the factor

$$Q^2(z) = \exp\left[-2\int_0^z ds\,\alpha(s)\right] = \exp[-2\tau_z] \tag{7.5}$$

where $Q(z)$ is actually the atmospheric transmissivity and τ_z is the optical thickness of the atmosphere between 0 and z. Quite often, z^* is in excess of

20 km or 30 km. At these high altitudes most of the backscatter can be attributed to Rayleigh backscatter since few aerosols are present. $R(z)$ can be derived from the lidar measurement as follows;

$$R(z) = \frac{z^2}{z^{*2}} \frac{Q^2(z^*)}{Q^2(z)} \frac{\beta_R(z^*)}{\beta_R(z)} \frac{\langle x_\gamma(z)\rangle}{\langle x_\gamma(z^*)\rangle} \tag{7.6}$$

where $\langle x_\gamma(z)\rangle = \langle x(z)\rangle - \lambda_n T$. $Q(z)$ is usually provided by an atmospheric model which may be updated using lidar data. $\beta_R(z)$ is determined from radiosonde or satellite data or from an atmospheric model. A scattering ratio of 1 indicates that few aerosols are present and large scattering ratios generally indicate large aerosol densities. The aerosol backscatter coefficient, $\beta_A(z)$, can be determined from $R(z)$ and $\beta_R(z)$. If the scattering properties of the aerosol are also known, the aerosol density can be computed once $\beta_A(z)$ is determined.

If Rayleigh scattering is present from an altitude where there are few aerosols, computing $R(z)$ is straightforward. Since the atmospheric aerosol content is not known beforehand and $\beta=\beta_A+\beta_R$ must be known at z^*, an initial choice of the normalization altitude above regions where aerosols often reside is made. For this reason, 30 km is typically used. Using an atmospheric model, $Q(z)$ can be estimated. For these measurements, values for $Q(z)$ were assumed based upon direct measurements of aerosol concentrations and properties from 5 to 28 km by Rosen [1966] in a series of six balloon flights. β_R can be estimated if the backscatter cross section and the atmospheric density are known. Radiosonde measurements often supply atmospheric pressure and temperature as a function of altitude for heights less than 30-35 km. Using the ideal gas law and these data, the atmospheric density can be approximated.

$$\rho(z) = \frac{p(z)}{R'T(z)} \qquad (7.7)$$

where ρ = number density of the atmosphere ($\text{mole}\cdot\text{m}^{-3}$)

p = atmospheric pressure ($\text{N}\cdot\text{m}^{-2}$)

T = atmospheric temperature ($^{\circ}\text{K}$)

R' = gas constant ($8.3143\ \text{J}\cdot\text{mole}^{-1}\cdot\text{K}^{-1}$)

If radiosonde data are not available up to the desired height, an exponentially decreasing density is assumed which matches the density computed from the highest available radiosonde measurements. The atmospheric scale height is used to determine the rate of decrease of the assumed density profile. The volume backscatter coefficient, $\beta_R(z)$, is given by

$$\beta_R(z) = \sigma_\pi\ \rho(z) \qquad (7.8)$$

where σ_π is the backscatter cross section. Temperature effects on the cross section are ignored with little resulting error. Combining $Q(z)$, $\beta_R(z)$ and the photocount data, $R(z)$ can be computed according to equation (7.6).

The initial choice of z^* must sometimes be altered since the aerosol content of the atmosphere is not known a priori. β_R and β_A are non-negative so it is clear from equation (7.4) that R cannot be less than 1. At z^*, $R = 1$ because it was assumed that no aerosols were present at this altitude. As a result, an iterative procedure may be required to select z^*, compute $R(z)$, and insure that the computed values of $R(z)$ are not consistently less than one. In effect, a search for an aerosol-free altitude takes place. In most cases, scattering from 30 km is due almost entirely to molecular scattering and no iterations are necessary.

7.3 EXPERIMENTAL DATA

The first clouds of volcanic dust associated with the eruption of Mt. St. Helens passed over Urbana, Illinois at approximately noon on May 20, 1980. A preliminary report on lidar observations of these clouds is contained in Gardner et al., [1980]. Figure 7.2(a) shows the scattering ratio computed from the average of 5 photocount profiles collected between 0004 and 0034 CDST on May 21. Four distinct layers at 7.5 km, 9.9 km, 12 km and 13 km are apparent. The scattering ratios associated with these peaks are 2.5, 5.5, 33 and 36, respectively. The layers at 7.5 km and 9.9 km may be associated with particulate matter from a large forest fire which was burning in northwestern Ontario at this time. The two peaks near 12.5 km actually appear to be one bifurcated layer. Radiosonde measurements obtained over Salem, Illinois, approximately 185 km south of Urbana, at 1800 CDST on May 20 were used to compute atmospheric density and, thus, $\beta_R(z)$. Since measurements such as these are routinely taken at Salem and are readily available, radiosonde data is used to deduce β_R for each data set presented in this Chapter. Because the density associated with these dust clouds was much greater than the aerosol concentration included in the model provided by Rosen, $Q^2(z)$ was underestimated. This generally results in estimates of $R(z)$ which are too low. In addition, the dust clouds on the evening of May 20-21 were so thick and dense that the transmitted laser pulse failed to penetrate them. As a consequence, scattering ratios above 14 km cannot be estimated since no backscattered radiation was received from above this altitude. The scattering ratios may be seriously underestimated above the regions where losses due to scattering and absorbtion from the dust clouds was great. However, other lidar measurements of $R(z)$ made over Illinois on the same evening tend to

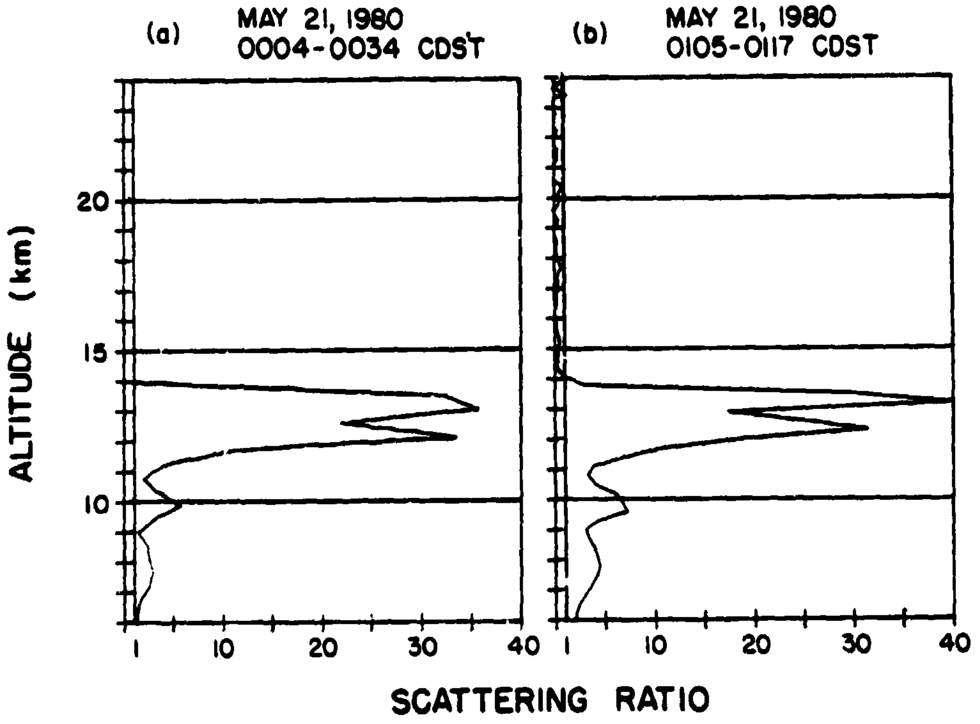

Figure 7.2 Scattering ratio profiles derived from Urbana lidar data collected on May 20-21, 1980.

confirm the scattering ratios plotted here. During the late evening of May 21 and early morning of May 22 an airborne aerosol lidar operated by NASA-Langley made measurements approximately 75 miles south of Urbana [McCormick et al., 1980]. At 2325 CDST, aerosol layers at 13.81 and 12.61 km associated with scattering ratios of 71 and 3.5 were observed (Figure 7.3). These data, collected with a ruby laser operating at a wavelength of 694.3 nm, compare favorably with the Urbana lidar measurements.

The scattering ratios observed later during the same evening, between 0105 and 0117 CDST, are plotted in Figure 7.2(b). The peaks below 11 km have not changed in the span of 30 minutes separating the plots in Figures 7.2(a) and (b). The peaks associated with the bifurcated layer near 12.5 km have changed in magnitude, however. The maximum scattering ratio, observed at an altitude of 13 km, is now 40. It appears that this large layer may have some horizontal structure associated with it.

Balloon measurements of temperature and wind speed and direction show an interesting correlation with $R(z)$. Figure 7.4 shows the wind speed and direction measured over Salem at 1800 CDST on May 20, 1980. Note the marked change in wind direction above 10.5 km, shifting from 270° at 10.8 km to 238° at 13 km. It appears that the main bifurcated layer between 11 and 14 km was associated with a southwesterly wind component over southern Illinois. The bifurcated layer also occurs at the same altitude as a wind speed minimum (20 knots at 13 km). Figures 7.5 and 7.6 show the temperature profiles measured over Salem on the evenings of May 20 and May 21, 1980, respectively. While a temperature minimum and a maximum are present near 11 km and 12.5 km, respectively, on May 20th, there is only an inflection present on May 21st. The bifurcated layer near 12.5 km is no longer present on May 21st. This is

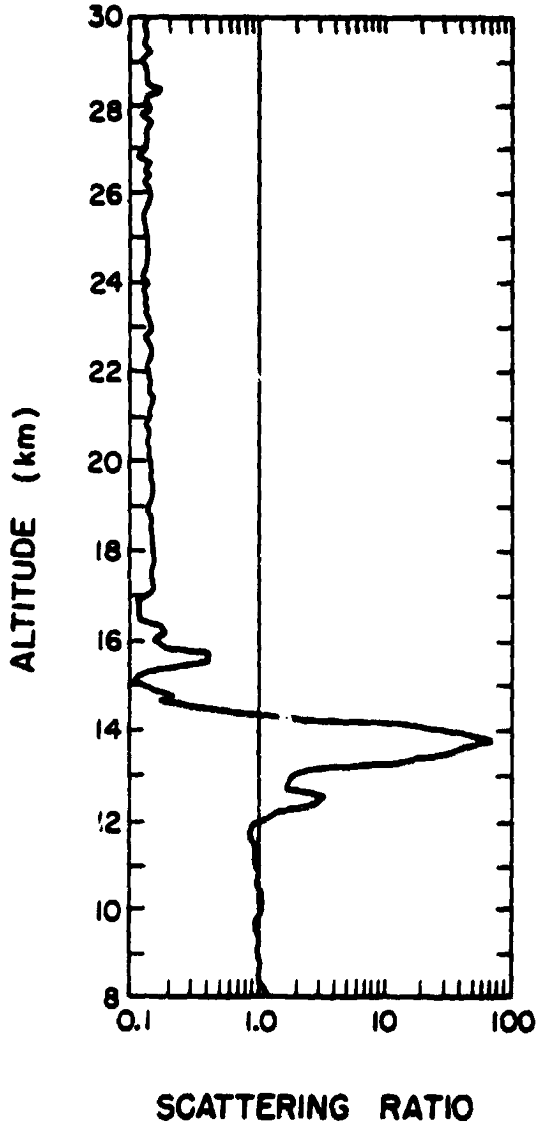

Figure 7.3 The profile of scattering ratio observed from an airborne lidar 75 miles south of Urbana. These data were collected at 2325 CDST on May 21, 1980 [McCormick et al., 1980].

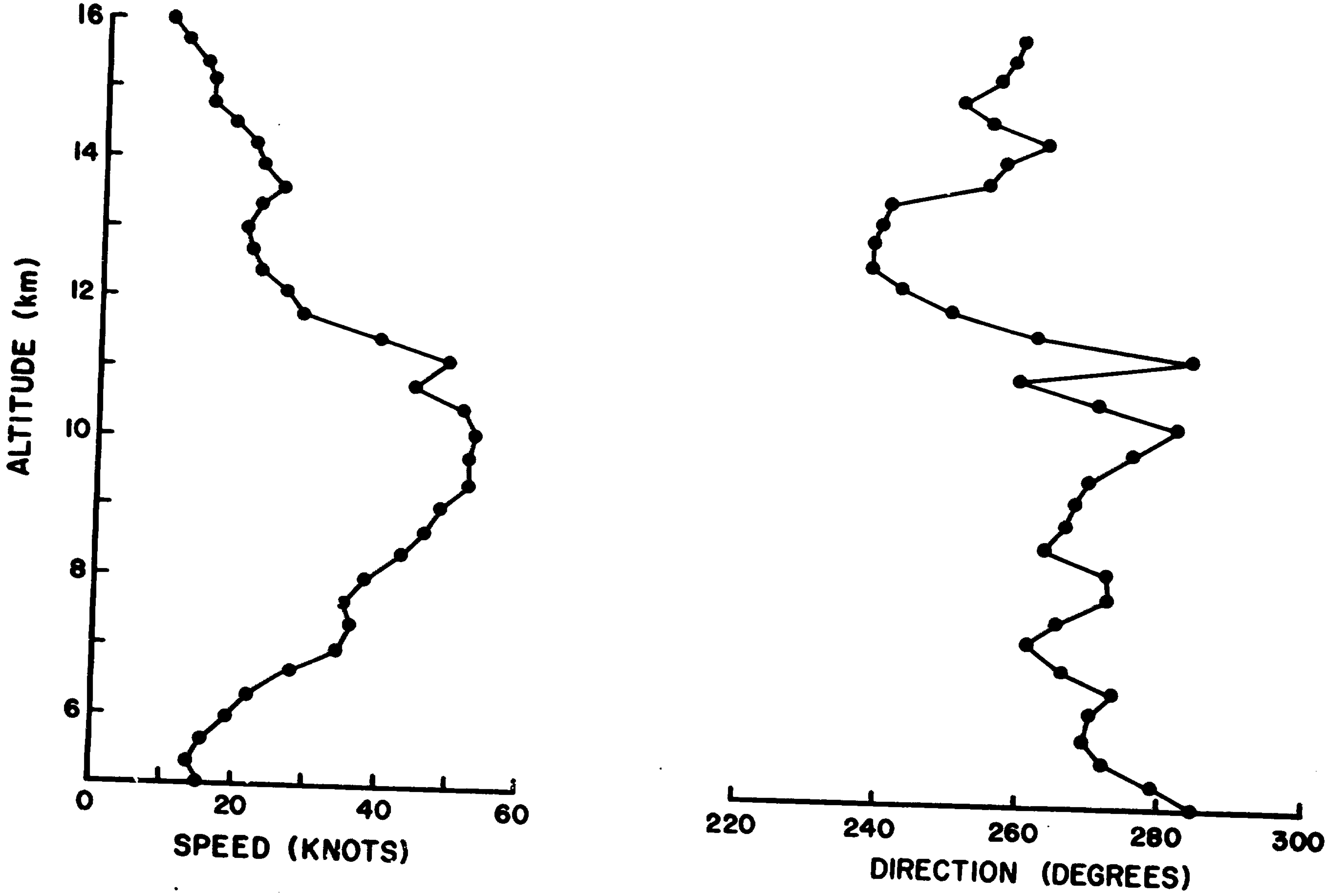

Figure 7.4 Wind speed and direction over Salem, Illinois, at 1800 CDST on May 20, 1980.

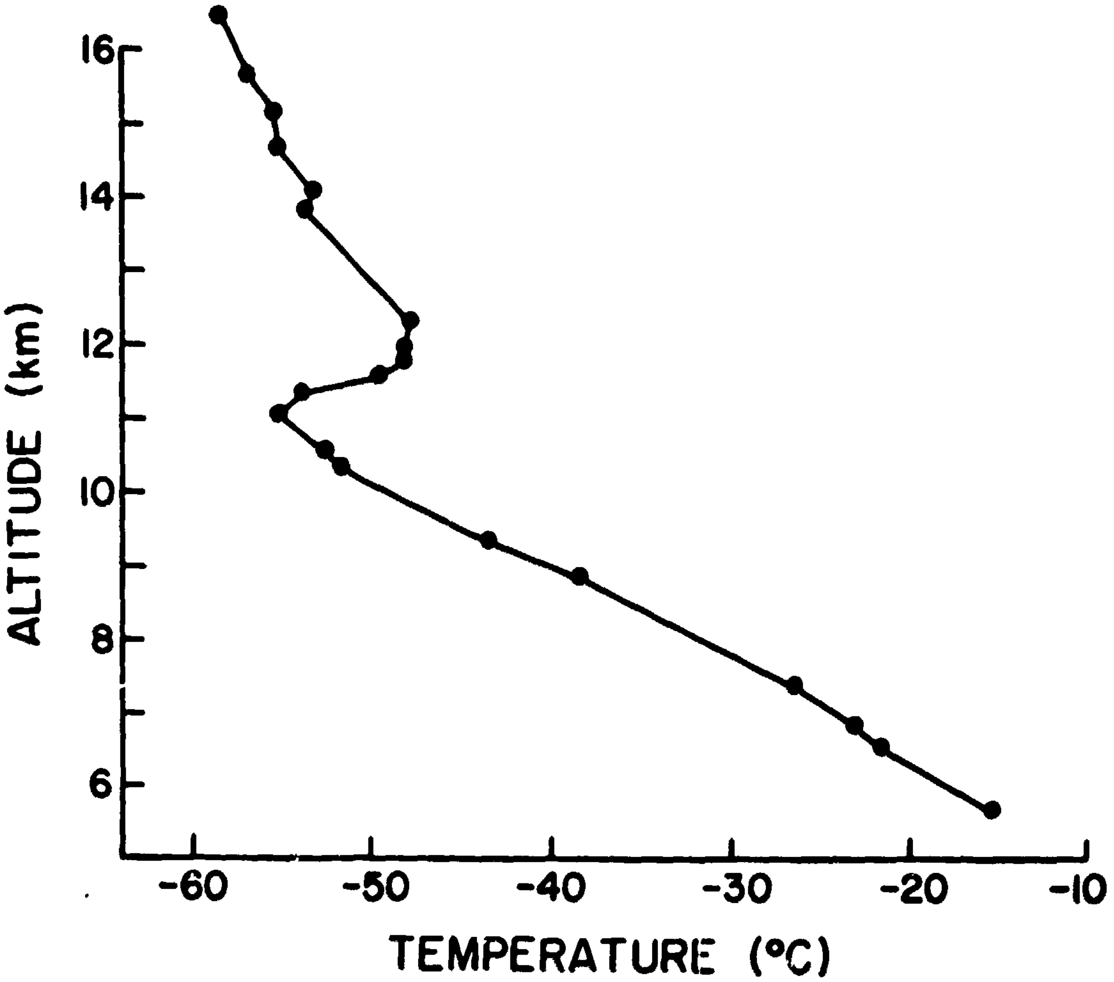

Figure 7.5 Temperature profile over Salem, Illinois at 1800 CDST on May 20, 1980.

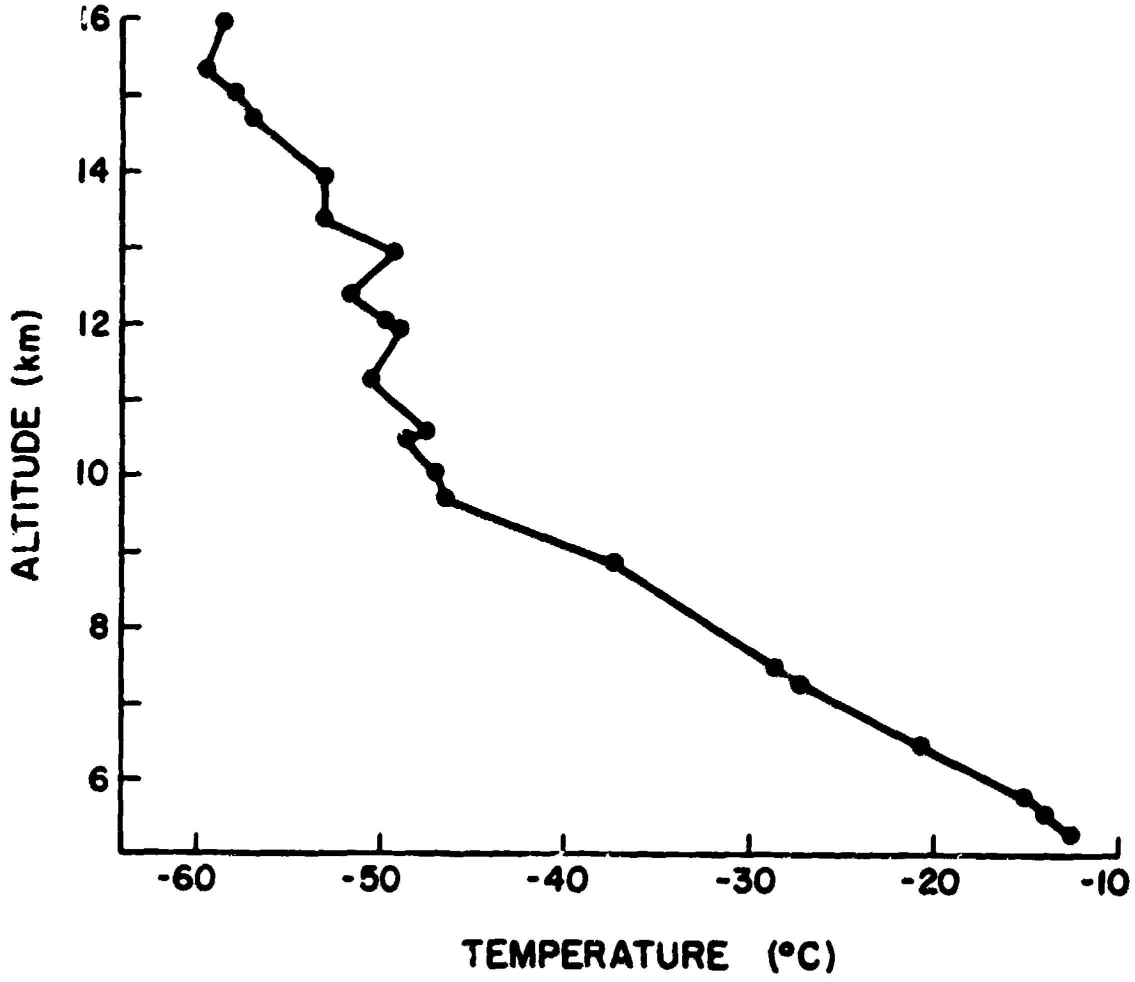

Figure 7.6 Temperature profile over Salem, Illinois at 1800 CDST on May 21, 1980.

illustrated in Figure 7.7(a). Seventeen profiles were collected during the evening and in each case the aerosol layers were penetrated by the laser pulse allowing the normalization height to be chosen above the layers of volcanic dust. A single distinct layer at 13.5 km is present associated with a maximum scattering ratio of 27. At times during the observation period this prominent layer did show evidence of a minor bifurcation. However, at no time was this bifurcation as pronounced as that observed on May 20th. By comparing the received signal strengths at 12 km and 15 km, the optical thickness of the layer at 13.5 km was calculated to be 0.82. The layers evident below 11 km on the previous evening are no longer distinct.

Poor weather prevented additional measurements until the evening of May 25-26, 1980. The scattering ratios observed on this evening are plotted in Figure 7.7(b). Once again, a bifurcated layer centered at 12.5 km is evident. However, the maximum scattering ratio has decreased by an order of magnitude over a period of 4 days to 2.9. The layer at 12.5 km seemed to persist for several weeks. In Figure 7.8(a) the profile of scattering ratio observed on June 17, 1980 is plotted. Once again, a layer at 13 km is present. The maximum scattering ratio has decreased to 2.0. It is not clear whether this layer resulted from a subsequent eruption on June 13, 1980 or was a residual from earlier volcanic eruptions.

A stratospheric layer of volcanic dust was observed at 21.5 km on July 25, 1980 (Figure 7.8(b)). The scattering ratio at 21.5 km was 3.0. The appearance of this high altitude layer was confirmed by other lidar groups at NOAA-Boulder [Deluisi et al., 1980], NASA-Langley [McCormick et al., 1980], and the University of Wisconsin [Eloranta, 1980]. This high altitude layer was also observed on the following evening (Figure 7.8(c)). The peak

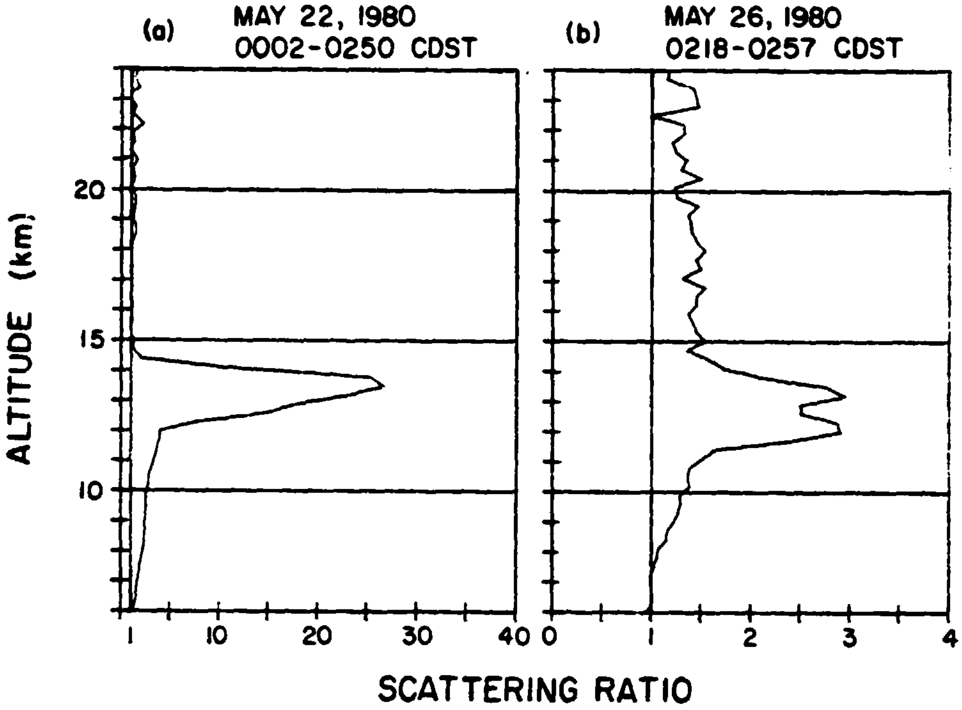

Figure 7.7 Scattering ratio profiles derived from Urbana lidar data collected on (a) May 21-22, 1980 and (b) May 25-26, 1980.

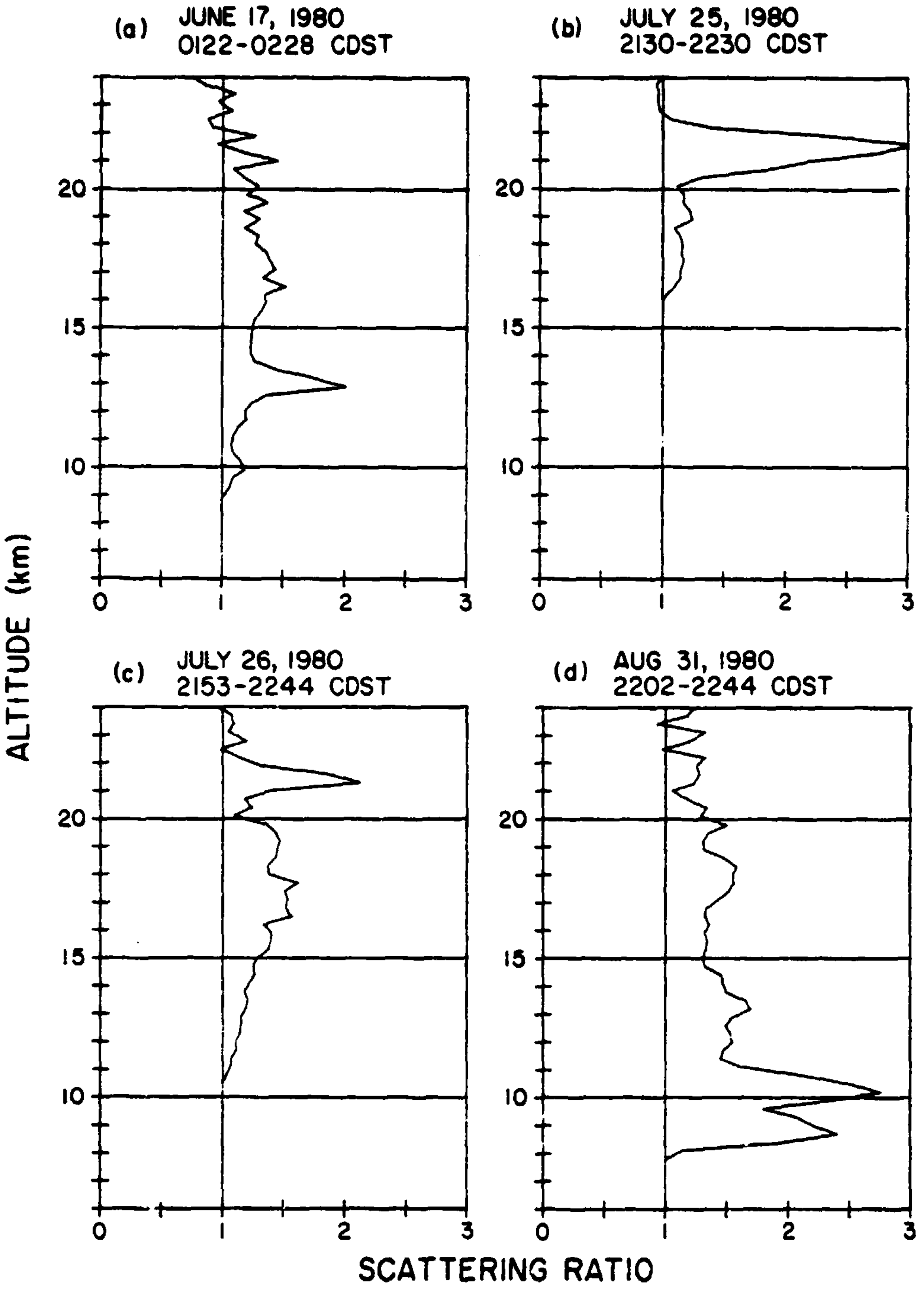

Figure 7.8 Scattering ratio profiles derived from Urbana lidar data collected on (a) June 17-18, 1980, (b) July 25-26, 1980, (c) July 26-27, 1980, and (d) the evening of August 31, 1980.

scattering ratio has decreased to 2.1 over the preceding 24 hours. This layer is probably associated with another eruption at Mt. St. Helens on July 22, 1980. By August 31, 1980, no distinct layers of aerosols are apparent. Figure 7.8(d) shows the scattering ratio profile computed from photocount data collected on this evening. The peaks near 10 km are apparently associated with sub-visible cirrus clouds. Subsequent observations have also failed to reveal evidence of distinct layers.

8. CONCLUSIONS AND RECOMMENDATIONS

8.1 Conclusion

Laser radar studies have revealed the dynamic nature of the mesospheric sodium layer. These data consist of photocount profiles which are used to estimate spatial and temporal profiles of sodium density. Because photocount data is subject to the degrading effects of shot noise, appropriate filtering techniques are required to increase the spatial and temporal resolution of the data. Rowlett and Gardner [1979] developed a spatial processing procedure that deconvolved the effects of laser pulse shape and receiver range gate as well as removing shot noise effects and improving spatial resolution. This technique has been extended to include a two-dimensional filtering technique which utilizes spatial and temporal filtering to further reduce shot noise and increase profile resolution. The most critical aspect of the two-dimensional filtering process is the determination of the appropriate spatial and temporal cutoff frequencies. This is accomplished by examining the spatial and temporal periodograms of the photocount data. Filter cutoffs are selected at the frequencies where the signal spectrum no longer dominates the periodogram and shot noise contributions are important. Expressions for the expected value and variance of the temporal and spatial periodograms before and after spatial and temporal filtering, respectively, are developed in Chapter 3. In addition to their use in determining filter cutoffs, the periodograms are useful in interpreting the photocount profiles.

An expression for the layer response to gravity waves has been developed that gives insight into the nature of the response and is required to correctly interpret the spatial periodogram. In addition to describing spatial and temporal variations in sodium density, variations in column abundance induced by gravity wave perturbations are explained. If the layer has no horizontal structure, the linear layer response is characterized by density oscillations with the same horizontal wavelength and temporal period as the gravity wave. The vertical variations in density, however, are very dependent on the vertical sodium density gradient. A phase reversal in the linear layer response occurs near the layer peak. Below this point oscillations in sodium density are 180 degrees out of phase with atmospheric density; above this point sodium and atmospheric density perturbations are in phase. Because of the vertical structure of the linear response, a local minimum may be observed in the spatial periodogram at the vertical wavenumber of the gravity wave. Consequently, the layer response must be understood before the spatial periodogram can be interpreted.

At points where the linear response is small or in regions where large sodium density gradients exist, nonlinearities in the layer response become important. It is convenient to use the perturbation series solution presented in Chapter 4 to determine the relative magnitudes of the nonlinear oscillations in density. The nonlinear terms are associated with sodium density oscillations with temporal frequencies which are harmonics of the temporal frequency of the gravity wave. Density perturbations consistent with nonlinearities in the layer response have been observed experimentally.

Lidar observations over Urbana, Illinois are presented which contain wavelike features that are apparently a layer response to gravity waves. In addition to nonlinearities in the layer response, which are most readily observed in temporal profiles of sodium density, many other layer features associated with a layer response to gravity waves are observed. These features include phase reversals in density perturbations which are apparent in both spatial and temporal plots of sodium density and larger density perturbations below than above the layer peak. Simulations of the layer response based upon theoretical and experimentally observed sodium profiles are consistent with observations. Steerable observations have been made at Goddard Space Flight Center in Maryland which may be used to deduce the horizontal structure of the layer. In addition to its influence on the layer response to atmospheric waves, the horizontal structure of the layer can be used to infer background winds at mesospheric heights.

Column abundance variations induced by gravity wave perturbations in sodium density have been observed. In addition, a systematic increase in sodium density above 90 km has been observed during the pre-sunrise hours. The resulting increase in column abundance is quite dramatic. In one case the column abundance almost tripled in a span of four hours prior to sunrise. The increase is apparently related to the influx of atomic sodium rather than the response of the sodium layer to atmospheric wave motions. Meteoric ablation is probably the major source of mesospheric sodium [Hunten, 1981]. It is interesting that the mean meteor rate and the column abundance both increase in the early morning hours. The meteor rate reaches a maximum at approximately 0600 local time [McKinley, 1961]. This is illustrated in Figure 8.1. Because the lidar measurements presented here did not extend beyond sunrise, the daytime behavior of the sodium column abundance and the time of maximum abundance are not known.

Early dayglow measurements indicated a marked diurnal variation with the column abundance increasing from sunrise and reaching a maximum at noon. The evening abundance declined to the same value as the morning abundance.

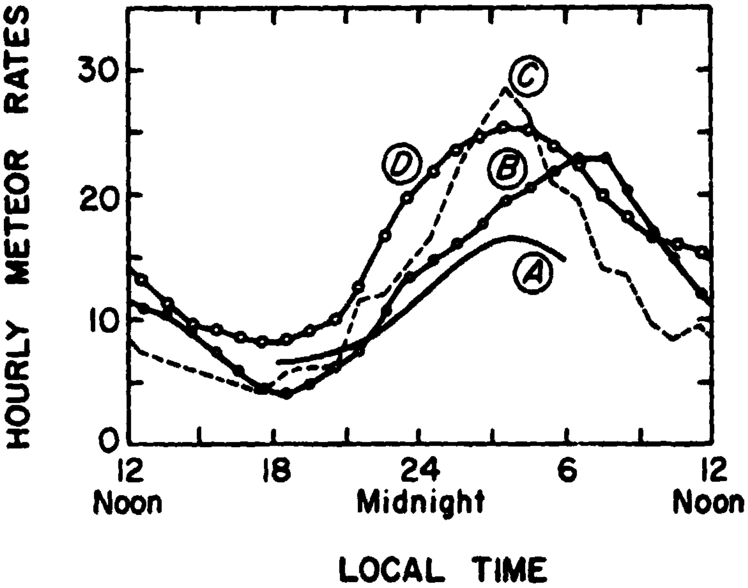

Figure 8.1 Diurnal variations in nonshower meteor rates obtained by (a) visual observations, (b and c) backscatter radar observations, and (d) forward scatter radar observations. [McKinley, 1961].

Daytime absorption measurements indicated much smaller diurnal variations than the dayglow observations. These observations are summarized in Brown [1973]. Daytime lidar observations [Gibson and Sandford, 1972] failed to reveal any substantial diurnal variation. In making dayglow measurements it is generally assumed that all the observed emission is due to a resonance line (i.e., sodium D1 or D2). This assumption may not be justified [Grainger and Ring, 1962; Noxon, 1968]. If the observed emission is contaminated by sources other than resonant emission, the abundance will be overestimated. This may explain some of the discrepancies in different experimental methods. Lidar observations at Urbana and Goddard Space Flight Center have also revealed an early morning increase in column abundance. It is clear that further observations are required to resolve the discrepancies.

8.2 SUGGESTIONS FOR FUTURE WORK

8.2.1 Experimental Efforts

In order to resolve questions concerning diurnal variations in sodium density, daytime measurements should be made. While the observations reported here indicate a pre-sunrise enhancement in sodium density, daytime lidar observations have failed to reveal any systematic variation [Gibson and Sandford, 1972]. Because of the narrow field-of-view possible with the telescope at Goddard Space Flight Center, the collection of high quality daytime data is feasible. By narrowing the telescope field-of-view and the bandpass of the interference filter in the receiver, the daytime background noise level may be reduced sufficiently to permit data collection. Observations spanning the period of morning increase in abundance and extending into the daylight hours should be made.

Additional steerable observations should be made. By scanning the telescope in azimuth while collecting data, a series of profiles is obtained which describes the vertical and horizontal variations in the sodium layer as well as temporal variations in density. If a sufficient number of horizontally spaced points are observed, data processing may be extended to include spatial filtering in the horizontal direction. This would yield three-dimensionally filtered data and would further reduce shot noise and increase profile resolution. Profiles of sodium density detailing the vertical and horizontal structure of the sodium layer as well as temporal variations in density at each observed point could be estimated. These estimates would be very useful in determining the horizontal structure of the layer thus permiting layer dynamics to be modeled more accurately. A horizontal gradient resulting from the morning enhancement in sodium density would be revealed in this type of observation. Because a large number of points would be scanned, these measurements would require rapid data collection and would have to take advantage of the 10 Hz pulse repetition rate of the Candela laser.

Correlative observations have been made in which the University of Illinois meteor radar and the sodium lidar made near simultaneous observations [Tetenbaum, 1981]. Mesospheric winds revealed by the meteor radar can be compared to lidar observations of sodium density to study the the effects of atmospheric motions on the sodium layer. In effect, two independant techniques can be utilized to estimate mesospheric winds. Radar methods, used to track the ionized trails left by meteors, and lidar observations of the sodium layer density response to atmospheric waves may both be utilized to deduce atmospheric motions at mesospheric heights. Because the lidar is adjacent to the meteor radar, interference prevents the lidar from operating when the meteor radar is transmitting. Thus, extended, uninterrupted lidar observations cannot be made when the meteor radar operates. Consequently, it is not practical to temporally filter the photocount data and, in general, the resulting resolution and short observation periods make it difficult to observe any periodic variations in sodium density. This makes comparisons of meteor radar winds and sodium density profiles difficult. The correlative observations made to date are promising but not conclusive. Comparisons of the two measurements can be made more readily if the lidar system can be shielded from the meteor radar sufficiently to permit simultaneous operation.

Sodium temperature measurements can be made. Because many of the chemical reactions responsible for the nature of the sodium layer are temperature dependent, further insights into sodium layer chemistry could be obtained from these measurements. Another means of monitoring atmospheric motions would be provided if the oscillations in temperature associated with the propagation of atmospheric waves could be observed. Sodium temperature may be inferred by obtaining estimates of the shape of the D2 emission line at 5890 Å. The temperature may be deduced from the doppler broadening of the line. The line shape is be observed by scanning the laser output frequency through the D2 line. In order to obtain the required spectral resolution, this method requires the laser to have a very narrow spectral output (much less than the width of the D2 line). Since the D2 line is approximately 1 pm wide, output linewidths near .1 or .2 pm are necessary. In addition, accurate measurements of the center frequency and output linewidth must be made. Because of laser instabilities, it may prove difficult to maintain laser tuning for the time necessary to make extended observations. An alternative approach is to scan the receiver tuning across the D2 line while the laser is aligned for a broad spectral output. In this case, the spectral width of the laser output should be at least as broad as the D2 line. Consequently, laser tuning is more easily maintained. The receiver efficiency may be reduced because of the very narrow bandpass and tunability requirements of this system. The receiver bandpass must be much less than the width of the sodium D2 line, so the required bandpass is roughly .1 or .2 pm.

8.2.2 Theoretical Development

Because the sodium layer response to gravity waves is in part nonlinear, the layer response to several gravity waves will include interactions between the layer responses to individual waves. The nonlinear interaction may make interpretation of experimental data difficult. For example, the data collected on March 11-12, 1981 (presented in Chapter 5) contains many wavelike features which cannot be attributed to the layer response to a single gravity wave. It is probable that a spectrum of gravity waves rather than a single wave is usually present. As a result, the layer response to several gravity waves should be developed. It is anticipated that a "beating" effect occurs in which density oscillations appear whose temporal frequencies are the sum and difference frequencies of the gravity waves. The effects of the wave interactions on spatial and temporal periodograms require investigation.

In Chapter 4, the effects of a background wind have been ignored. If the sodium layer has horizontal structure, the background wind will cause changes in sodium density as features are swept overhead. These density changes may be used to deduce the mean wind if the horizontal structure of the layer is known. This is one of the motivations for making steerable lidar observations. There will be interactions between density perturbations induced by atmospheric waves and density changes associated with the interaction of a background wind and a horizontally structured layer. Correct interpretation of lidar observations requires that the layer response to both background winds and atmospheric waves be known.

The morning enhancement observed in data presented in Chapters 5 and 6 is not understood. It appears to be associated with the influx of atomic sodium into the sodium layer. The mechanism for this influx must be explained. In addition, the influx affects the sodium layer response to atmospheric waves by changing the steady state layer profile. In developing the layer response, source and loss terms were ignored in order to simplify the development of the solution. It might be instructive to include a source term which reflects the observed increases in sodium density during the early morning hours.

The layer density response has been used to investigate sodium layer dynamics in terms of a layer density response to gravity waves. Atmospheric tides will also induce density perturbations. The motion of the layer peak on March 16-17, 1981 (with a period of 12 hours) was suggestive of tidal activity. The response of the layer to tidal oscillations should be developed. In addition, tidal-gravity wave interactions in the layer response should be investigated.

A complete study of sodium layer dynamics must include sodium layer chemistry as well as the corkscrew mechanism. The corkscrew mechanism may be important only in the upper half of the layer, but chemical effects could be quite important near the sink of atomic sodium at the layer bottomside. The layer chemistry and descriptions of the sink for atomic sodium are still not completely understood. Even though these effects are neglected, many of the dynamical features of the sodium layer are explained by the analysis in Chapter 4.

APPENDIX I

DESCRIPTION OF PMT BLANKING AND TIMING CONTROL CIRCUITS

Because the PMT is subject to overloading as a consequence of strong backscatter from below 30 km, a blanking circuit has been added to the receiving system. The PMT gain is reduced by decreasing the first dynode voltage to the cathode voltage. The circuit which performs this task is given in Figure I.1. When a low TTL level (0 volts) is present at the blanking input, the output of the opto-isolator (TIL 117) will be high (5 volts). As a result, transistors Q2 and Q3 will be turned off and the first dynode voltage will not be influenced by the gating circuitry. The current through the chain of bias resistors in the PMT housing is much greater than the leakage current from collector to emitter in Q3. When the blanking input is +5 volts, the opto-isolator output is near 0 volts and Q2 and Q3 are turned on. The first dynode voltage is pulled down to the cathode voltage and the PMT is blanked.

For safety reasons the PMT anode is maintained at approximately 0 volts and the cathode voltage is adjusted to -2000 volts. The opto-isolator protects the timing controller and operators from the high cathode voltage. The 5 volt supply which provides the bias voltage for the opto-isolator and Q2 is referenced to the cathode voltage (i.e. the bias voltages are +5 volts with respect to the PMT cathode).

The timing controller synchronizes laser firing and PMT blanking. Its schematic is given in Figure I.2. The LM555 operates as a free running oscillator and establishes the laser pulse repetition rate. The oscillator frequency and, therefore, the laser pulse repetition rate may be varied from roughly 0.3 to 30 Hz by adjusting R4. An external input has been supplied

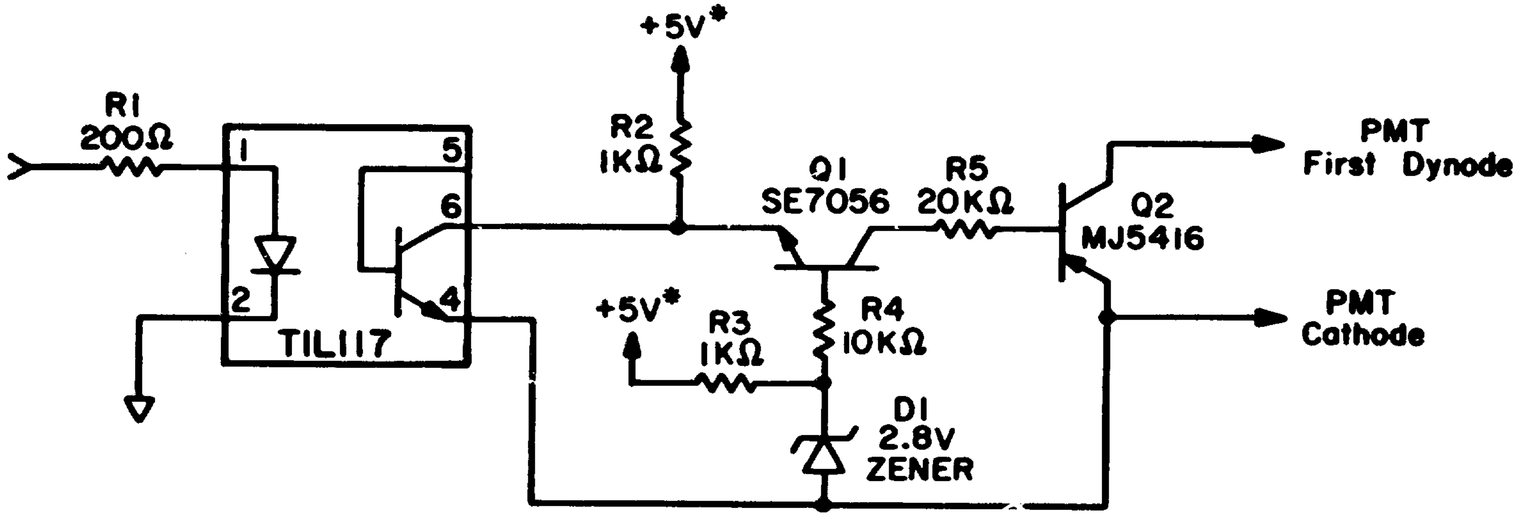

Figure I.1 Schematic diagram of the PMT blanking circuit. The * indicates that the +5 volt supply is referenced to the cathode supply voltage.

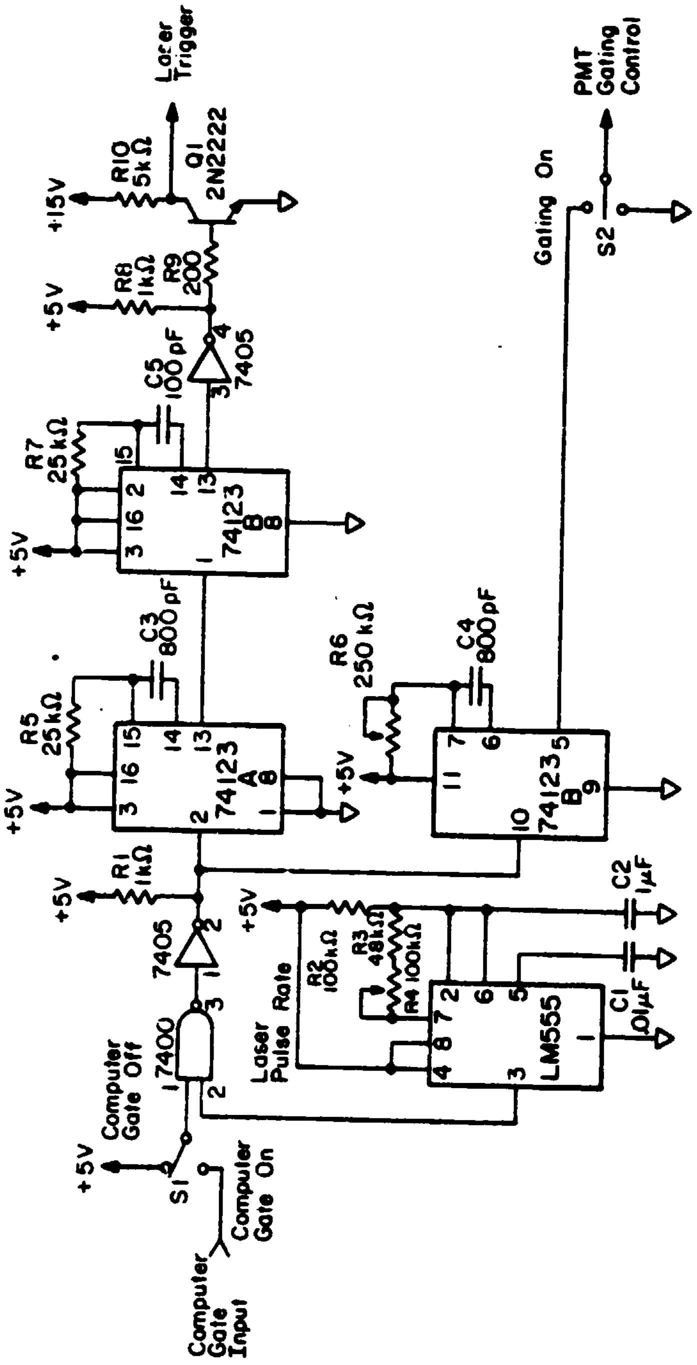

Figure I.2 Schematic diagram of the PMT timing controller which enables the lidar system computer to gate the oscillator output. When S1 is in the "Computer Gate On" position and 0 volts is placed on the computer gate input, the oscillator output is interupted and the laser will not be triggered. A +5 volt input will enable the oscillator and the laser will pulse at the rate established by the setting of R4. The oscillator is continuously enabled when S1 is in the "Computer Gate Off" position.

The PMT gating control output is normally at a 0 volt level. When an oscillator pulse triggers the monostable multivibrator (C) and S2 is in the "Gating On" position, a +5 volt pulse is sent to the blanking circuit. This blanks the PMT and prevents overloading. The duration of this pulse is nominally 205 μs, but may be adjusted with R6. If S2 is in the "Gating Off" position, the PMT is not blanked. However, the laser trigger continues to be generated.

The oscillator pulse which triggers the blanking pulse also triggers another monostable (A). The output of this monostable is a 5 μs positive pulse. The falling edge of this pulse triggers the remaining monostable (B). The output of (B) is delayed by 5 μs as a result. The duration of the pulse generated by (B) is nominally 6-10 μs. Q1 is used to increase the pulse voltage to approximately 12 volts. The resulting 12 volt, 10 μs pulse triggers the laser. The PMT gating control remains at +5 volts for another 200 μs (as determined by R6) insuring that the PMT is protected from overloading below 30 km.

REFERENCES

Ackerman, M., C. Lippens and M. Lechevallier [1980], Volcanic material from Mt. St. Helens in the stratosphere over Europe, Nature, 287, 614-615.

Axford, W. I. [1963], The formation and vertical movement of dense ionized layers in the ionosphere due to neutral wind shears, J. Geophys. Res., 68, 769-799.

Battaner, E. and A. Molina [1980], Turbopause internal gravity waves, 557.7 nm airglow, and eddy diffusion coefficient, J. Geophys. Res., 85, 6803-6810.

Bhattacharyya, S. K., A. J. Gibson, E. Hammond and M. C. W. Sandford [1978], A steerable laser radar system for atmospheric studies, Opt. Quant. Elect., 10, 243-252.

Blamont, J. E., M. L. Chanin and G. Megie [1972], Vertical distribution and temperature profile of the night time atmospheric sodium layer obtained by laser backscatter, Ann. Geophys., 28, 833-838.

Blamont, J. E. and T. M. Donahue [1961], The dayglow of the sodium D lines, J. Geophys. Res., 66, 1407-1423.

Bowman, M. R., A. J. Gibson and M. C. W. Sandford [1969], Atmospheric sodium measured by a tuned laser radar, Nature, 221, 456-457.

Brown, T. L. [1973], The chemistry of metallic elements in the ionosphere and mesosphere, Chem. Rev., 73, 645-667.

Cerny, T. and C. F. Sechrist, Jr. [1980], Calibration of the Urbana lidar system, Aeron. Rep. No. 94, Dep. Elec. Eng., Univ. Ill., Urbana, Ill.

Chimonas, G. [1969], Downward Movement of Ionization into the D Region, Aeron. Rep. No. 32, pp. 281-285, Dep. Elec. Eng., Univ. Ill., Urbana, Ill.

Chimonas, G. and W. I. Axford [1968], Vertical movement of temperate-zone sporadic E layers, J. Geophys. Res., 73, 111-117.

Chiu, Y. T. and B. K. Ching [1978], The response of atmospheric and lower ionospheric layer structures to gravity waves, Geophys. Res. Lett., 5, 539-542.

Clemesha, B. R., V. W. J. H. Kirchhoff and D. M. Simonich [1978], Simultaneous observations of the Na 5893 Å nightglow and the distribution of sodium atoms in the mesosphere, J. Geophys. Res., 83, 2499-2503.

Clemesha, B. R., V. W. J. H. Kirchhoff, D. M. Simonich, H. Takahashi and P. P. Batista [1980], Spaced lidar and nightglow observations of an atmospheric sodium enhancement, J. Geophys. Res., 85, 3480-3484.

Clemesha, B. R., V. W. J. H. Kirchhoff, D. M. Simonich and P. P. Batista [1981], Mesospheric winds from lidar observations of atmospheric sodium, J. Geophys. Res., 86, 868-870.

D'Altorio, A. and G. Visconti [1981], Lidar detection of volcanic aerosols in the atmosphere following the Mount St. Helens eruption, Geophys. Res. Lett., 8, 63-65.

Deliusi, J., V. Derr, R. Fegley and T. McNice [1980], Lidar observations of atmospheric debris from the Mt. St. Helens eruption at Boulder and Mauna Loa, Tenth International Laser Radar Conference Abstracts, 147, Silver Spring, MD.

Donahue, T. M. and R. R. Meier [1967], Distribution of sodium in the daytime upper atmosphere as measured by a rocket experiment, J. Geophys. Res., 72, 2803-2839.

Dudis, J. J. and C. A. Reber [1976], Composition effects in thermospheric gravity waves, Geophys. Res. Lett., 3, 727-730.

Eloranta, E. W. [1980], Lidar observations of stratospheric dust over Madison, Wisconsin after the Mt. St. Helens eruption, Tenth International Laser Radar Conference Abstracts, 144, Silver Spring, MD.

Frederick, J. E. [1979], Influence of gravity wave activity on lower thermospheric photochemistry and composition, Planet. Space Sci., 27, 1469-1477.

Gadsden, M. [1970], Metallic atoms and ions in the upper atmosphere, Ann. Geophys., 26, 141-149.

Gadsden, M. and C. M. Purdy [1970], Observations of the sodium dayglow, Ann. Geophys., 26, 43-51.

Gardner, C. S., C. F. Sechrist, Jr. and J. D Shelton [1980], Lidar observations of the Mount St. Helens dust layers over Urbana, Illinois, Appl. Opt., 19, A192-A193.

Gardner, C. S. and J. D. Shelton [1981], Spatial and temporal filtering technique for processing lidar photocount data, Opt. Lett., 6, 175-176.

Gault, W. A. and H. N. Rundle [1969], Twilight observations of upper atmospheric sodium, potassium and lithium, Can. J. Phys., 47, 85-98.

Gibson, A. J. and M. C. W. Sandford [1971], The seasonal variation of the nighttime sodium layer, J. Atmos. Terr. Phys., 33, 1675-1684.

Gibson, A. J. and M. C. W. Sandford [1972], Daytime laser radar measurements of the atmospheric sodium layer, Nature, 239, 509-511.

Grainger, J. F. and J. Ring [1962], Anomalous Fraunhofer line profiles, Nature, 185, 193-217.

Hake, R. D., Jr., D. E. Arnold, D. W. Jackson, W. E. Evans, B. P. Ficklin and R. A. Long [1972], Dye-laser observations of the nighttime atomic sodium layer, J. Geophys. Res., 77, 6839-6848.

Hauchecorne, A., J. Lefrere, G. Megie and M. L. Chanin [1980], Lidar observations of stratospheric aerosol layers over France after the Mount St Helens Eruption, Tenth International Laser Radar Conference Abstracts, 146, Silver Spring, MD.

Hines, C. O. [1960], Internal atmospheric gravity waves at ionospheric heights, Can. J. Phys., 38, 1441-1481.

Houghton, J. T. [1977], The Physics of Atmospheres, Cambridge University Press, New York.

Hunten, D. M. [1967], Spectroscopic studies of the twilight airglow, Space Sci. Rev., 6, 493-573.

Hunten, D. M. [1981], A meteor ablation model of the sodium and potassium layers, Geophys. Res. Lett., 8, 369-372.

Hunten, D. M. and L. Wallace [1967], Rocket measurements of the sodium dayglow, J. Geophys. Res., 72, 69-79.

Iwasaka, Y. and S. Hayashida [1980], Lidar measurements of dust-cloud particles loaded into the stratosphere by the volcanic eruption of St. Helens, Tenth International Laser Radar Conference Abstracts, 143, Silver Spring, MD.

Juramy, P., M. L. Chanin, G. Megie, G. F. Toulinov and Y. P. Doudoladov [1981], Lidar sounding of the mesospheric sodium layer at high latitudes, J. Atmos. Terr. Phys., 43, 209-215.

Kirchhoff, V. W. J. H. and B. R. Clemesha [1973], Atmospheric sodium measurements at 23° S, J. Atmos. Terr. Phys., 35, 1493-1498.

Kinter, T. M. [1977], A Laser Radar System Interface, MS Thesis, University of Illinois, Urbana, Ill.

Lefrere, J., J. Pelon, C. Cahen, A. Hauchecorne and P. Flamont [1981], Lidar survey of the post Mt. St. Helens stratospheric aerosol at Haute Provence Observatory, *App. Opt.*, *20*, A70-A71.

McCormick, M. P. [1975], The use of lidar for atmospheric measurements, *Remote Sensing Energy Related Studies*, T. N. Vezeroglu (ed.), 113-218, Wiley Publishing Co., New York.

McCormick, M. P., W. H. Fuller, Jr., W. H. Hunt and T. J. Swissler [1980], Lidar measurements of ash clouds from the St. Helens volcanic eruption, *Tenth International Laser Radar Conference Abstract*, 138, Silver Spring, MD.

McKinley, D. W. R. [1961], *Meteor Science and Engineering*, McGraw-Hill, New York.

McLeod, M. A. [1966], Sporadic E theory, I. Collision-geomagnetic equilibrium, *J. Atmos. Sci.*, *23*, 96-109.

Measures, R. M. [1977], Lidar equation analysis allowing for target lifetime, laser pulse duration, and detector integration period, *App. Opt.*, *16*, 1092-1103.

Megie, G. and J. E. Blamont [1977], Laser sounding of atmospheric sodium: interpretation in terms of global atmospheric parameters, *Planet. Space Sci.*, *25*, 1039-1109.

Meixner, F. X., H. W. Georgii and G. Ockelmann [1981], The arrival of the Mount St. Helens eruption cloud over Europe, *Geophys. Res. Lett.*, *8*, 163-166.

Nilssen, R. V. [1981], *Spectral Linewidth Measurements of a Pulsed Laser*, MS Thesis, University of Illinois, Urbana, Ill.

Noxon, J. F. [1968], Day airglow, *Space Sci. Rev.*, *8*, 92-134.

Oppenheim, A. V. and R. W. Schafer [1975], *Digital Signal Processing*, Prentice-Hall, Englewood Cliffs, N.J.

Pettifer, R. E. W. [1975], Signal induced noise in lidar experiments, *J. Atmos. Terr. Phys.*, *37*, 669-673.

Richter, E. S. and C. F. Sechrist, Jr. [1978], Theoretical and Experimental Studies of the Atmospheric Sodium Layer, *Aeron. Rep. No. 79*, Dep. Elec. Eng., Univ. Ill., Urbana, Ill.

Richter, E. S. and C. F. Sechrist, Jr. [1979a], A cluster ion chemistry for the mesospheric sodium layer, *J. Atmos. Terr. Phys.*, *41*, 579-586.

Richter, E. S. and C. F. Sechrist, Jr., [1979b], A meteor ablation-cluster ion atmospheric sodium theory, *Geophys. Res. Lett., 6*, 183-186.

Richter, E. S., J. R. Rowlett, C. S. Gardner and C. F. Sechrist, Jr. [1981], Lidar observations of the mesospheric sodium layer over Urbana, Illinois, *J. Atmos. Terr. Phys., 43*, 327-337.

Rosen, J. M. [1966], Correlation of dust and ozone in the stratosphere, *Nature, 209*, 1342-1351.

Rowlett, J. R., C. S. Gardner, E. S. Richter and C. F. Sechrist, Jr. [1978], Lidar observations of wave-like structure in the atmospheric sodium layer, *Geophys. Res. Lett., 5*, 683-686.

Rowlett, J. R. and C. S. Gardner [1979], Signal Processing of Sodium Lidar Photocount Data, *R.R.L. Publication No. 504*, Radio Res. Lab., Dept. Elec. Eng., Univ. Ill., Urbana, Ill.

Russel, P. B., T. J. Swissler and M. P. McCormick [1979], Methodology for error analysis and simulation of lidar aerosol measurements, *App. Opt., 18*, 3783-3797.

Saleh, B [1978], *Photoelectron Statistics*, Springer-Verlag, New York.

Shelton, J. D., C. S. Gardner and C. F. Sechrist, Jr. [1980], Density response of the mesospheric sodium layer to gravity wave perturbations, *Geophys. Res. Lett., 7*, 1069-1072.

SEAN Bulletin [1980], vol. 5, no. 5, pp. 2-12, National Museum of Natural History, Washington, D.C.

Teitelbaum, K. and C. F. Sechrist, Jr. [1979], A Microcomputer Control System for the Urbana Sodium Lidar, *Aeron. Rep. No. 88*, Dep. Elec. Eng., Univ. Ill. Urbana, Ill.

Tetenbaum, D. [1981], *Correlative Studies of the Mesospheric Sodium Layer at Urbana*, MS Thesis, University of Illinois, Urbana, Ill.

Thomas, L., A. J. Gibson and S. K. Bhattacharyya [1976], Spatial and temporal variations of the atmospheric sodium layer observed with a steerable laser radar, *Nature, 263*, 115-116.

Thomas, L., A. J. Gibson and S. K. Bhattacharyya [1977], Lidar observations of a horizontal variation in the atmospheric sodium layer, *J. Atmos. Terr. Phys., 39*, 1405-1409.

Weinstock, J. [1978], Theory of the interaction of gravity waves with $O_2('\Sigma)$ airglow, *J. Geophys. Res., 83*, 5175-5185.

VITA

John Davis Shelton was born on [redacted], [redacted] in [redacted] After graduating from Clear Creek High School in League City, Texas, he attended Texas A&M University as an electrical engineering student. During his undergraduate career, he was the recipient of a Texas A&M President's Scholarship and an Honorary Moody Scholarship. In 1972, he was drafted and spent several years with the U. S. Army in Germany as an electronics technician. In 1975 he was discharged from the armed forces and continued his educational career at Texas A&M. He graduated with a B.S. in electrical engineering in 1977 and began graduate work at the University of Illinois at Urbana-Champaign where he received an RCA Fellowship. In 1979 he received an M.S. in electrical engineering. The master's work included microprocessor system design and programming. Upon entering the Ph. D. program he joined the University of Illinois Aeronomy Laboratory as a member of the sodium lidar group. He is a member of Tau Beta Pi and Eta Kappa Nu.